

DISS. ETH NO. 24552

EVOLUTION OF THE AGN POPULATION IN THE UNIVERSE

A thesis submitted to attain the degree of
DOCTOR OF SCIENCES of ETH ZURICH

(Dr. sc. ETH Zurich)

presented by

Neven Čaplar

mag. phys., University of Zagreb

born on October 10th, 1986

citizen of Republic of Croatia

accepted on the recommendation of

Prof. Dr. Simon J. Lilly, examiner
Prof. Dr. Paul C. Hewett, co-examiner

2017

Contents

List of Figures	vii
List of Tables	ix
Abstract	xi
Kurzfassung	xiii
1 Introduction	1
1.1 Active galactic nuclei	1
1.1.1 AGN components and accretion	1
1.1.2 AGN luminosity	3
1.1.3 Measurement of black hole masses	4
1.2 Galaxy population	7
1.2.1 Two galaxy populations	7
1.2.2 Phenomenological approach to describe evolution of galaxy population	8
1.3 Co-evolution of black holes and their host galaxies	10
1.3.1 Cosmic density of mass accretion of black holes and galaxies	11
1.3.2 Black hole-galaxy correlations	11
1.3.3 Evolution of the galaxy-black hole mass relations	13
1.4 Variability of AGN	14
1.5 Organization and content of this thesis	17
2 AGN and galaxies: co-existence scenario	19
2.1 Ansätze	19
2.2 The origin of the quasar luminosity function	20
2.2.1 Convolution of Schechter functions with power law Eddington ratios	20
2.2.2 The simplest Eddington ratio distribution that reproduces the shape	
of the QLF	22
2.2.3 Broken power law Eddington ratio distribution and generalized duty	
cycle	23
2.2.4 Analytical derivation of the QLF	25
2.2.5 Predictions of the convolution model	28
2.3 Data	30
2.3.1 Mass function of star-forming galaxies	31
2.3.2 Quasar luminosity function	33

2.4	Results from comparing the evolution of the QLF and the galaxy mass function	35
2.4.1	The evolution of QLF normalization	35
2.4.2	The evolution of characteristic QLF luminosity	37
2.5	Testing the model with black hole mass data	39
2.5.1	The quasar mass-luminosity plane	39
2.5.2	Establishing the m_{bh}/m_* correlation in quenched systems	43
2.5.3	The m_{bh}/m_{bulge} correlation in quenched systems	46
2.5.4	Quenched galaxies as a function of galaxy and black hole mass	48
2.5.5	m_{bh}/m_* in AGN in the local Universe	50
2.6	Discussion	51
2.6.1	Comparing m_{bh}/m_* redshift evolution in active and quenched systems	52
2.6.2	Downsizing	53
2.7	Connection of the shape of Eddington distribution and mass ratio evolution	55
2.7.1	Coherent evolution of ϕ_{SF}^* and ϕ_{QLF}^*	56
2.8	Summary and conclusions	57
3	AGN and galaxies: quenching scenario	61
3.1	Is the mass ratio evolution consistent with the observed mass growth in the universe?	61
3.1.1	Mass growth of star-forming galaxies at low redshifts ($z \lesssim 0.7$)	62
3.1.2	Mass growth of star-forming galaxies and black holes in co-existence scenario	63
3.2	New convolution scenario	64
3.2.1	Qualitative explanation of the quenching scenario	64
3.2.2	Predictions for the mass function of AGN and AGN host galaxies	66
3.2.3	Connection between mass accretion and the mass function of galaxies and AGN	68
3.3	Observational determination of parameters describing AGN mass function and Eddington ratio function	71
3.4	Quantitative discussion	75
3.4.1	Description of the calculation	75
3.4.2	Predictions of the quenching scenario and comparison with the conclusions from the co-existence scenario	77
3.5	Summary and conclusions	79
4	Differentiating between AGN-galaxy co-evolution scenarios	81
4.1	Introduction	81
4.2	Galaxy properties as a function of AGN luminosity	82
4.3	AGN properties as a function of galaxy mass	84
4.4	Summary and conclusions	90
5	Optical variability	93
5.1	The sample & data	93
5.2	Re-calibration of the PTF AGN Light Curves	96
5.3	Analysis Methods	98

5.3.1	Construction of the structure functions	98
5.3.2	Wavelength correction	101
5.3.3	Fitting the structure function	102
5.3.4	Construction and testing of PSDs	105
5.4	Results of the SF analysis	110
5.4.1	The amplitude and the timescale of variability from the SF analysis	110
5.5	Results of the PSD analysis	115
5.5.1	Slope of PSDs in the (i)PTF sample	116
5.6	Discussion	121
5.7	Summary and conclusions	123
6	Summary and future prospects	125
6.1	Summary	125
6.2	Future prospects	129
6.2.1	Influence of steep PSD slope on detection of periodic AGN light curves	130
6.2.2	Variability as a method to measure spin and other physical parameters	130
6.2.3	Variability as AGN selection method	131
	Appendix to Chapter 5	133
A.1	Completeness and depth of the survey	133
A.2	Comparison of calibration with Ofek et al. (2012)	134
A.3	Colour dependence of the calibration	135
A.4	Reduction of SF ² residuals using the stellar sample	136
	Bibliography	139
	Acknowledgements	152

CONTENTS

List of Figures

1.1	Schematic illustration of AGN	3
1.2	Main Sequence of star-formation	8
1.3	The red fraction in SDSS as function of stellar mass and environment	10
1.4	Cosmic evolution of the star formation rate density and the black hole accretion rate density	12
1.5	Correlation between masses of black holes and galaxy bulges	13
2.1	Schematic representation of the procedure to create the QLF	21
2.2	Functional dependence of the factors $\Delta_L(\delta_1, \gamma_2)$ and $\Delta_\phi(\delta_1, \gamma_2)$	26
2.3	Comparison of the shape of the QLF and the result of the convolution	27
2.4	Shape of black hole and black hole host functions	28
2.5	Evolution of parameters describing mass function of star-forming galaxies	31
2.6	Fits of the results of the model to the QLF	34
2.7	Redshift evolution of parameters describing QLF; “full fit”	35
2.8	Redshift evolution of parameters describing QLF; normalization evolution fixed	36
2.9	Comparison of the redshift evolution of the normalization of star-forming galaxy mass function and the normalization of quasar luminosity function	38
2.10	Mass - luminosity plane; comparison with observations	40
2.11	Mass - luminosity plane, without luminosity cuts	43
2.12	m_{bh}/m_* relation in quenched galaxies today	44
2.13	Correlation of black hole mass with total and bulge mass in quenched galaxies	47
2.14	Scatter in the black hole - galaxy relation	48
2.15	Quenched fraction as a function of stellar and black hole mass	49
2.16	Simulated observation of m_{bh}/m_* relation in Stripe 82	51
2.17	Evolution of the mean m_{bh}/m_* relation in star-forming and quenched systems	53
2.18	Redshift evolution of comoving density of quasars at different luminosities	54
2.19	Evolution of the high-end slope of Eddington distribution	55
3.1	Maximal evolution of the m_{bh}/m_* relation in a star-forming galaxy on the Main Sequence	63
3.2	Schematic representation of the model in which AGN are connected with mass quenching	66
3.3	Mass function of AGN and AGN host galaxies in the quenching scenario	67
3.4	Redshift evolution of BHARD and SFRD	73
3.5	Redshift evolution of BHARD/SFRD	74
3.6	Redshift evolution of $(SFRD/BHARD) \cdot (L^*/M^*)$	75

LIST OF FIGURES

3.7	Mass - luminosity plane in quenching scenario; comparison with observations	78
3.8	m_{bh}/m_* relation in quenched galaxies today; quenching scenario	79
4.1	Star formation as a function of AGN luminosity I.	83
4.2	Star formation as a function of AGN luminosity II.	84
4.3	Effect of small field of view on the observational results	86
4.4	BHAR/SFR as a function of stellar mass of star-forming galaxies at $z \sim 2$.	88
4.5	BHAR/SFR as a function of stellar mass of star-forming galaxies at $z \sim 1$.	89
5.1	Distribution of observational cadence in the sample	94
5.2	Cumulative distribution of the number of observations for the objects in the sample	95
5.3	Cumulative distribution of the time span of the observations for the objects in the sample	96
5.4	SF ² split by redshift, luminosity and mass	100
5.5	Variability as a function of wavelength	102
5.6	Examples of PSD for four representative light curves	106
5.7	Result of the simulations to test accuracy of PSD estimation	108
5.8	Result of the simulations to test accuracy of PSD estimation; fraction of steep slopes	109
5.9	Value of the log(SF/mag) at a time scale of 100 days	110
5.10	The dependence of the SF ² as a function of the luminosity L	111
5.11	Time-scale at which the ensemble structure function reaches 0.071 mag . . .	112
5.12	The dependence of the SF ² as a function of the luminosity relative to the knee of the quasar luminosity function at that redshift	115
5.13	The dependence of the PSD slope, α , with mass and luminosity	117
5.14	The dependence of the PSD slope, α , with mass and luminosity for the SDSS Stripe 82 data	118
5.15	The short time-scale slopes of the structure function SF ² as a function of luminosity and mass	119
5.16	Simple model for the observed steepening of PSD slopes with mass in the observations	122
6.1	Periodicity in surveys as function of PSD slope	131
A.1	The completeness of the survey as a function of the observed magnitude of the source and the dimming of the observation	134
A.2	Comparison of the results for the quasar SF ² using the standard (i)PTF calibration and our re-calibration	135
A.3	Example of the light-curve using our re-calibration and using the standard (i)PTF calibration	136
A.4	The SF ² for stars (averaged over all Δt) as a function of their colour	137
A.5	Schematic representation of our procedure to create the final SF ² estimate for a quasar sample	137

List of Tables

- 2.1 Evolution of star-forming galaxy mass function, data from [Ilbert et al. \(2013\)](#) 32
- 2.2 Best fits to QLF data from [Hopkins et al. \(2007\)](#) 34

- 5.1 Fit of SF² with Equation (5.4), table of parameters 104
- 5.1 Fit of SF² with Equation (5.4), table of parameters 105
- 5.2 Fit to the time-scale of variability, Equation (5.7) 113
- 5.3 Dependence of the SF² slope, fit with Equation (5.14) 120

LIST OF TABLES

Abstract

Today, black holes are recognized to be ubiquitous in our Universe. It is thought that most if not all galaxies host a supermassive black hole in their centres. These black holes grow during luminous phases of accretion of matter, at which time they are called Active galactic nuclei (AGN). This thesis investigates the AGN population and the evolution of its properties.

First we investigate the evolution of the AGN population by studying connections between the galaxy and the AGN population in a phenomenological way. This approach allows us to use the most direct observables to identify the simplest connections present in the data. Where possible we seek to establish analytical expressions that connect various observables and use these expressions to identify the main processes affecting the AGN population. Our understanding of the galaxy population, the evolution of its mass function and its properties has increased immensely in the last several years, in no small part because of this phenomenological approach, which was developed at ETH Zurich. We use these recent insights to model co-evolution of black holes and galaxies.

We present a simple phenomenological model that links the evolving galaxy mass function and the evolving quasar luminosity function (QLF). We consider two scenarios of galaxy - black hole co-evolution. In the first case the black holes “co-exist” with their galaxies and grow intermittently during the time that the galaxy is creating stars. The second case involves the “quenching” scenario in which black holes accrete only during the final stages of the star-forming period of a galaxy. Both models reproduce the QLF and explain the appearance of downsizing and the so-called sub-Eddington boundary in observations.

We point out that strong evolution in the characteristic luminosity of AGN, L^* , can be produced by evolution in either the distribution of Eddington ratio, or the m_{bh}/m_* mass ratio, or both. To avoid this degeneracy in the first scenario, we look at the distribution

of AGN in the Sloan Digital Sky Survey (SDSS) (m_{bh}, L) plane, showing that an evolving ratio $m_{bh}/m_* \propto (1+z)^2$ reproduces the observed data and also reproduces the local relations that connect the black hole population with the host galaxies for both quenched and star-forming populations. When connected with the observed size evolution of the galaxies, this type of mass ratio evolution leads to a non-evolving $m_{bh} - \sigma$ and m_{bh}/m_{bulge} relationship.

We then explore whether this kind of mass ratio evolution is consistent with the evolution of star formation rate density and black hole accretion rate density i.e., the available information about the growth of mass of galaxies and black holes in the Universe. We find that, given the observational data, the quenching model is preferable. We then explore the quenching model and show analytically how the parameters describing the AGN population, such as the m_{bh}/m_* ratio, the normalization of the AGN mass function and the characteristic Eddington ratio λ^* , depend on the observed evolution of QLF, galaxy mass function and star formation rate density, avoiding the degeneracy encountered earlier.

As a final step in this part of the thesis, we consider the most direct observational evidence to differentiate between the co-existing and quenching scenarios. The main difference between these scenarios is that in the co-existence scenario, all of the star-forming galaxies have the same probability of hosting an AGN at any given time, whereas in the quenching scenario, AGN are preferentially hosted in more massive galaxies. We therefore compare our results for the evolution of the mean star formation rate as a function of AGN luminosity and consider the mean AGN luminosity as a function of galaxy mass with observational studies of these quantities. We point out how the small size of fields studied could significantly affect the observational results. When taking this effect into account, we again find that the quenching scenario of co-evolution is preferred.

While the previous approach studied the evolution of AGN mass and luminosity through their evolution on cosmological scales, optical variability is suitable to study the influence of AGN mass and luminosity on the local properties of the accretion disk. For this purpose, we characterise the optical variability of quasars in the Palomar Transient Factory and the intermediate Palomar Transient Factory (PTF/iPTF) surveys. We re-calibrate the r-band light curves for 28,000 luminous, broad-line AGN from the SDSS to produce a total of 2.4 million photometric data points. We utilise both the structure function (SF) and the power spectrum density (PSD) formalisms to search for links between the optical variability and the physical parameters of the accreting supermassive black holes. We find that the amplitude of variability at a given time-interval (or equivalently the timescale of variability to reach a certain amplitude) is most strongly correlated with luminosity with weak or no dependence on black hole mass and redshift. The PSD analysis also reveals that many quasar light curves are steeper than a damped random walk, which is commonly used to describe the variability of AGN. We find a correlation between the steepness of the PSD slopes, specifically the fraction of slopes steeper than 2.5, and the masses of the black holes, although we cannot exclude the possibility that either luminosity or the Eddington ratio are the drivers of this effect.

Kurzfassung

Schwarze Löcher sind in unserem Universum allgegenwärtig. Die meisten, wenn nicht sogar alle, Galaxien beherbergen ein supermassives Schwarzes in ihrem Zentrum. Schwarze Löcher wachsen durch die Akkretion von Materie. Während diesen Wachstumsphasen leuchten Schwarze Löcher und werden aktive galaktische Kerne genannt (englisch active galactic nuclei, abgekürzt AGN). Das Hauptthema dieser Arbeit ist die Erforschung der AGN-Population und die Entwicklung dieser Objekte.

Wir untersuchen die Entwicklung der AGN-Population, in dem wir Galaxien und ihre AGN auf phänomenologische Weise verknüpfen. Die Grundidee dieses Ansatzes besteht darin, Beobachtungen von offensichtlichen Eigenschaften zu verwenden, um die einfachsten Zusammenhänge in den Daten zu erkennen. Wir versuchen analytische Ausdrücke zu finden, die verschiedene Observablen miteinander verbinden, und verwenden diese dann, um die Hauptprozesse in der AGN-Population zu identifizieren. Unser Verständnis der Galaxienpopulation, insbesondere die Entwicklung der Massenfunktion, hat sich in den letzten Jahren enorm erweitert, nicht zuletzt aufgrund des an der ETH Zürich entwickelten, phänomenologischen Ansatzes. Wir verwenden diese Einsichten, um die Entwicklung von Schwarzen Löchern und Galaxien besser zu verstehen.

Wir präsentieren ein einfaches phänomenologisches Modell, welches die Galaxienmassenfunktion und die Quasar-Luminositätsfunktion (QLF) verbindet. Wir betrachten zwei Szenarien der Co-Evolution von Galaxien und Schwarzen Löchern. Im ersten Fall wachsen Schwarze Löcher parallel zu ihren Galaxien (Co-Evolutionsszenario), während im zweiten Fall schwarze Löcher nur während der letzten Stadien des Galaxienwachstums akkretieren, wenn Galaxien ihre Sternentstehung beenden (Beendigungsszenario). Beide Modelle reproduzieren die QLF und erklären das Auftreten von “Downsizing” und die so genannte “Sub-Eddington-Grenze” in Beobachtungen.

Wir zeigen, dass eine starke Entwicklung in der charakteristischen Leuchtkraft von

AGN, L^* , durch eine Evolution in der Verteilung der Eddington-Verhältnisse, eine Entwicklung des m_{bh}/m_* -Massenverhältnisses, oder durch beides erzeugt werden kann.

Wir brechen diese Entartung, indem wir die Verteilung der AGNs in der Sloan Digital Sky Survey in der (m_{bh}, L) Ebene betrachten. Die Beobachtungen werden gut durch die Relation $m_{bh}/m_* \propto (1+z)^2$ beschrieben, welches ebenfalls den lokalen Zusammenhang zwischen Schwarzen Löchern und sternformenden sowie passiven Galaxien reproduziert. Interessanterweise führt die Entwicklung des Massenverhältnisses zu einer sich nicht-entwickelnden, konstanten Beziehung von $m_{bh} - \sigma$, wenn die Grössenentwicklung der Galaxien mitbetrachtet wird.

Wir überprüfen, ob diese Entwicklung der Massenverhältnisses mit der Massenzunahme von Galaxien und Schwarzen Löchern konsistent ist. Dazu vergleichen wir die Evolution des Massenverhältnisses mit der Entwicklung der Dichte der Sternentstehungsrate und der Schwarzloch-Akkretionsrate. Unsere Ergebnisse zeigen, dass das zweite Szenario, in welchem Schwarze Löcher nur während der Beendigung der Sternentstehung wachen, die Daten besser beschreibt. Zudem zeigen wir analytisch, wie die Parameter der AGN-Population (m_{bh}/m_* -Verhältnis, die Normalisierung der AGN-Massenfunktion und das charakteristische Eddington-Verhältnis λ^*) von der beobachteten Evolution der QLF, der Galaxienmasse und der Dichte der Sternentstehung abhängen.

Als letzter Schritt in diesem Teil der Arbeit betrachten wir die Beobachtungen, die uns erlauben zwischen diesen beiden Szenarien zu unterscheiden. Der Hauptunterschied zwischen den Szenarien besteht darin, dass im Co-Evolutionsszenario alle sternbildenden Galaxien die gleiche Wahrscheinlichkeit haben, einen AGN zu einem beliebigen Zeitpunkt zu beherbergen. Im Beendigungsszenario werden dagegen AGN in massiveren Galaxien bevorzugt. Wir vergleichen daher unsere Ergebnisse mit Beobachtungen der Entwicklung der mittleren Sternbildungsrate als Funktion der AGN-Leuchtkraft und der mittleren AGN-Helligkeit als Funktion der Galaxienmasse. Wir weisen darauf hin, dass aufgrund des kleinen Beobachtungsvolumens die Beobachtungsergebnisse erheblich beeinträchtigen sein können. Wenn wir diesen Effekt mit einbeziehen, zeigen unsere Ergebnisse, dass das Beendigungsszenario der Co-Evolution bevorzugt wird.

Mit dem oben beschriebenen Ansatz haben wir die Entwicklung der AGN-Masse und Leuchtkraft auf kosmologischen Grössenordnungen analysiert. Die Erforschung der Variabilität eignet sich hingegen, um den Zusammenhang der AGN-Masse und Leuchtkraft mit den Eigenschaften der Akkretionsscheibe zu untersuchen. Zu diesem Zweck betrachten wir die optische Variabilität von Quasaren in der “Palomar Transient Factory” und “Intermediate Palomar Transient Factory” (PTF / iPTF). Wir kalibrieren die R-Band-Lichtkurven für ~ 28000 leuchtende, breitbandige AGNs aus der SDSS, die insgesamt 2.4 Millionen photometrische Datenpunkte erzeugen. Wir verwenden sowohl die Strukturfunktion (englisch structure function, abgekürzt SF) als auch die Leistungsspektrumdichte (englisch power spectrum density, abgekürzt PSD), um Beziehungen zwischen der optischen Variabilität und den physikalischen Parametern der akkretierenden supermassiven Schwarzen Löchern zu finden. Wir zeigen, dass die Amplitude der Variabilität in einem gegebenen Zeitin-

tervall, beziehungsweise einer Zeitspanne, um eine gewisse Amplitude zu erreichen, am stärksten mit der Helligkeit und nur schwach oder mit keiner Abhängigkeit von der Masse des Schwarzen Lochs und der Rotverschiebung abhängt. Die PSD-Analyse zeigt auch, dass die Lichtkurven vieler Quasare steiler sind als jene von gedämpften Zufallskurven, welche häufig für die Beschreibung der AGN-Variabilität benutzt werden. Wir finden eine Korrelation zwischen der Steilheit der PSD-Kurven, insbesondere zwischen jenen, welche steiler als 2.5 sind, und der Masse des Schwarzen Lochs, obwohl wir die Möglichkeit nicht ausschliessen können, dass die Helligkeit oder das Eddington-Verhältnis die Treiber dieses Effekts sind.

TEK ŠTO SU UTRNULE ZADNJE BOJE VEČERNJE RUMENI, ENO SE NA NEBU UŽEGLE MALE, ALI SJAJNE LUČI, TREPTANJEM SVOG SVJETLA ENO TE BAŠ ZOVU, DA BACIŠ OKO K NJIMA, A U DUŠI TI SE I NEHOTICE JAVLJAJU PITANJA: ŠTO SU TE LUČI, OTKUDA SU I ČEMU SU.

JUST AFTER THE LAST RED HUE OF THE EVENING HAS BEEN EXTINGUISHED, SUDDENLY SMALL, BUT POWERFUL, LIGHTS HAVE APPEARED IN THE SKY; WITH THEIR TWINKLING THEY ARE CALLING YOU TO GAZE AT THEM, AND IN YOUR SOUL THERE ARE INADVERTENTLY QUESTIONS: WHAT ARE THESE LIGHTS, WHERE ARE THEY FROM AND WHY.

Oton Kučera, *Naše nebo (Our sky)*, 1895

1 | Introduction

The discovery in 1959 that the 13th magnitude star-like object identified as the radio source 3C 273 had a unbelievably high redshift of $z=0.158$ was the dawn of the whole new area of research in astronomy. Assuming the Hubble expansion of the Universe, 3C 273 was the second most distant object known at the time and it was much more luminous than even the brightest known galaxies. Additionally, its rapid variability also indicated its small size. Discoveries of similar objects followed and it soon became clear that gravity rather than nuclear fusion served to power these compact and luminous bodies (Hoyle & Fowler, 1963; Salpeter, 1964; Lynden-Bell, 1969). Given that these luminous object reside in the centres of galaxies they were termed “active galactic nuclei” (AGN).

In this thesis we present the results of our effort to understand these systems by studying large samples of AGN. We discuss two quite different projects that use different methods to infer the evolution of AGN properties in the Universe. In the first approach we use demographical information to study AGN evolution on a cosmological time-scale and use recently acquired insights into the evolution of the galaxy population. In the second part we use variability to study AGN and their properties over days and years. Mirroring the topics covered in this thesis, in the Introduction below we present an overview of our knowledge about AGN and galaxies, their co-evolution, and AGN variability.

1.1 Active galactic nuclei

1.1.1 AGN components and accretion

The accepted picture of the origin of AGN (we will henceforth use terms AGN and quasar interchangeably) is that, as mass is accreted onto a supermassive black hole in the centre

of a galaxy, luminosity is released. An accretion disk forms naturally as infalling matter retains most of its angular momentum. The viscosity in the disk acts as a mechanism by which angular momentum is transported outwards while the mass moves towards the centre. Disks generally are divided according to their geometric properties (thin, slim or thick) and their optical properties i.e., their optical depth. For our purposes the most interesting is the geometrically thin, optically thick accretion disk which describes accretion during the periods of rapid mass growth.

It can be shown (Netzer, 2013) that the radial dependence of temperature in such a disk is given by the following Equation:

$$T(r) \sim 8.6 \times 10^6 \cdot \dot{m}_1^{1/4} m_8^{-1/2} f^{1/4}(r) (r/r_g)^{-3/4} \text{ K} \quad (1.1)$$

where \dot{m}_1 is the accretion rate in units of M_\odot/yr , m_8 is the mass of the black hole in units of $10^8 M_\odot$, r_g is gravitational radius, $r_g = 2Gm_{bh}/c^2$, and $f(r)$ is a highly nonlinear function that describes the dependence of the temperature on the spin of the accreting disk. Assuming that the local emission can be described by the perfect blackbody, we can construct the full spectrum of an AGN, which is broadly in agreement with what is seen in observations. For a typical black hole with $m_8 = 1$ the maximal temperature in the disk is roughly 10^5 K, so most of the energy is emitted in the ultra-violet part of the spectrum. The efficiency of the process - that is, the fraction of the accreting mass that is transformed into luminosity - depends on the spin of the system and is expected to range from 4% to 42%.

The optical spectra of AGN often exhibit prominent emission lines, resulting from accretion disk photons that ionise the surrounding gas. These lines are usually classified according to their width, which ranges from several hundred to several thousand km/s. The narrow lines are thought to be produced in lower density clouds located 30 - 100 parsecs from the accretion disk whereas the broad lines are produced in higher density regions within 0.001 - 0.01 parsec of the accretion disk. Although not all AGN exhibit broad lines, studies of polarized light have revealed that the broad line component is present even when it is not observed directly (Antonucci & Miller, 1985). This led to the “unified model” in which the difference among line widths exhibited by AGN can be attributed solely to orientation effects (Antonucci, 1993; Urry & Padovani, 1995; Urry, 2003). In this model, broad lines are not seen in some AGN because the line of sight to the nucleus is obstructed by optically thick material, which is usually described as being in a toroidal shape. We show this configuration in Figure 1.1. Large amounts of obscuration can significantly modify the observed spectrum because the optical emission is reprocessed by the dust and gas, and subsequently emitted in the infrared part of the spectrum.

AGN are some of the brightest X-ray sources in the Universe. Studying AGN in the X-ray band is also attractive because high energy photons are relatively unaffected by obscuration, giving us a less biased view of the AGN population. Though thin disk theory effectively describes the optical part of the AGN spectrum, the temperature in the accretion disk is not high enough to produce X-rays. This suggest the existence of an additional hot component, the corona, in which the ultraviolet and optical photons produced in the

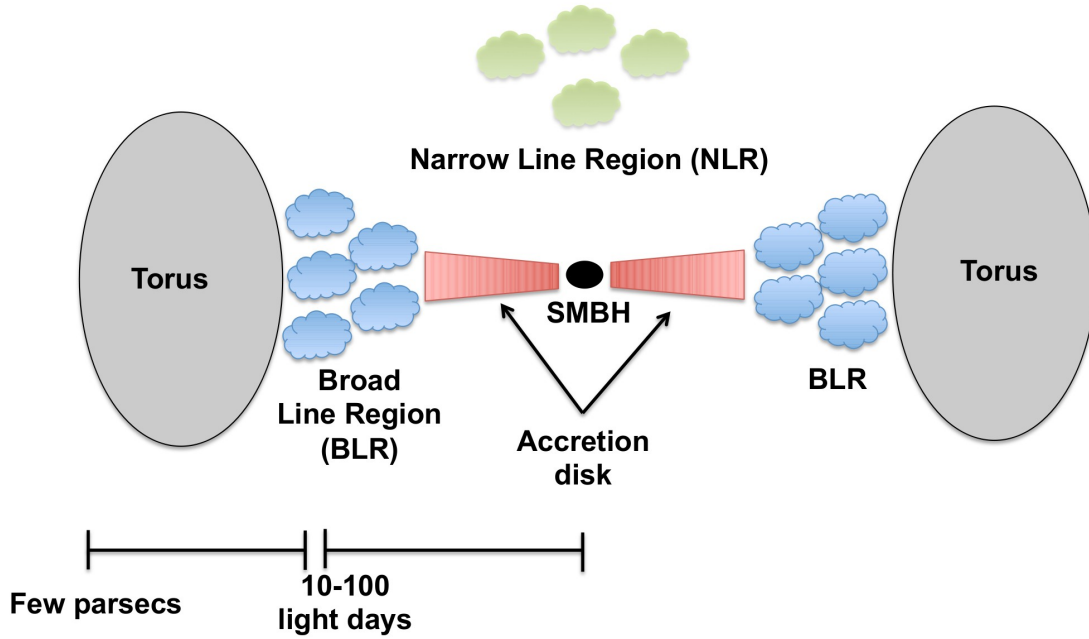


Figure 1.1: Schematic illustration of the components of an AGN. The supermassive black hole in the centre there is ringed by an accretion disk through which matter is transported into the black hole; here ultraviolet and optical components of the spectrum are produced. These structures are surround by regions which produce narrow and broad lines seen in optical spectrum. Region of dust, possibly in the shape of the torus, surrounds the system and obscures the view. Not shown is the corona, the region that produces the X-ray part of spectrum. Adopted from Ricci (2011).

disk undergo Compton upscattering by thermal electrons. This process leads to a power-law spectrum that extends to energies determined by the electron temperature (Sunyaev & Titarchuk, 1980; Haardt & Maraschi, 1991; Haardt et al., 1994; Veledina et al., 2011). Although this model explains the basic properties of the spectrum, the physical origin of such high temperature region and its spatial extent are still active areas of research.

1.1.2 AGN luminosity

In the accretion process discussed above, the pressure from the generated luminosity can act to counter the accretion caused by gravity. In a steady, spherically symmetric, case these two forces are balanced out at the “Eddington luminosity”, which is:

$$L_{edd} = \frac{4\pi G m_{bh} m_p c}{\sigma_T} = 10^{46.1} \cdot m_8 \text{ erg/s.} \quad (1.2)$$

where m_p is the mass of the proton, m_{bh} is the black hole mass, and σ_T is the Thomson scattering cross-section for the electron. Even though this luminosity is not a strict limit

for disk accretion, AGN are rarely observed to radiate at significantly higher luminosities; thus, L_{edd} is often a useful quantity to consider when studying accreting black holes.

The black growth is given by

$$\dot{m}_{bh} = \frac{(1 - \epsilon)\lambda L_{edd}}{\epsilon c^2}, \quad (1.3)$$

where L_{edd} is the Eddington luminosity, $\lambda = L/L_{edd}$ is the normalized quantity known as the Eddington Ratio and ϵ is the radiative efficiency, i.e., the fraction of the infalling mass that is converted to luminosity. Using the Eddington ratio definition, Equation (1.2) can be written in a simple form to emphasise the dependence between black hole mass and luminosity

$$L = 10^{46.1} \cdot \lambda m_8 \text{ erg/s}. \quad (1.4)$$

The average radiative efficiency in the Universe can be deduced from the simple argument first proposed by [Soltan \(1982\)](#). If most of the supermassive black hole mass is indeed accreted during the luminous accretion phases, then the local relic density should equal to the total luminosity radiated (with some efficiency ϵ) :

$$\rho_{local} = \int_0^\infty \frac{dt}{dz} dz \int_0^\infty \frac{1 - \epsilon}{\epsilon c^2} \Phi(L, z) dL \quad (1.5)$$

where $\Phi(L, z)$ is the bolometric quasar luminosity function (QLF). Early work on this topic suggested $\epsilon \approx 0.1$ ([Yu & Tremaine, 2002](#); [Shankar et al., 2004](#); [Marconi et al., 2004](#)) which is within the ranges expected in the thin disk theory.

The QLF quantity used above describes the number density of quasars per co-moving volume as a function of intrinsic luminosity and redshift. As such, it is a primary observational goal of any AGN survey and it has been characterized in a variety of bands and fields (e.g., [Boyle et al., 2000](#); [Richards et al., 2005](#); [Aird et al., 2010](#); [Masters et al., 2012](#); [Shen & Kelly, 2012](#)). The shape of the distribution is often described with the following broken power law function:

$$\Phi(L) \equiv \frac{dN}{d\log L} = \frac{\phi_{QLF}^*}{(L/L^*)^{\gamma_1} + (L/L^*)^{\gamma_2}}, \quad (1.6)$$

where ϕ_{QLF}^* is the normalization, L^* is a characteristic luminosity and γ_1 and γ_2 are, respectively, the faint and bright end slopes. One of the main goals of this thesis is to investigate the evolution of $\Phi(L)$'s properties and the consequences of this evolution for the AGN population.

1.1.3 Measurement of black hole masses

Mass is the primary physical variable that describes black holes. As such measurements of masses are crucial to the study of the interplay between supermassive black holes and their

host galaxies. We will use indeed black hole mass estimates in many, but not all parts of the thesis, e.g., as input for the scenario described in Chapter 2 and variability analysis in Chapter 5, and for comparison with the output of the scenario shown in Chapter 3. We note that, however, the major conclusions and findings of this thesis do not rely critically on the accuracy of black hole mass measurements. We review a few of the most important methods for measurement of black hole masses below.

By far the strongest case for the existence of the supermassive black holes is our Galaxy. The Galactic centre, at a distance of 8.28 ± 0.33 kpc (Genzel et al., 2010), is close enough that individual stars can be resolved and their proper motions and orbits followed. The orbital times of the stars near the galactic centre are short enough that they can be tracked during a human lifespan. The closest star to the centre, S2, has orbital period of 15.8 years and has already completed an orbit since measurements began. The modelling result for its mass is $m_{bh, MW} = 4.30 \pm 0.20(\text{stat}) \pm 0.30(\text{sys}) \times 10^6 M_{\odot}$. This is the gold standard for the measurement of black hole masses.

Supermassive black holes outside our Galaxy are too far away for us to be able to follow individual stars. Nevertheless, dynamical modelling can be used to understand the stellar dynamics in the vicinity of the central black hole. Both photometric and spectroscopic measurements of the central part of the galaxy are needed to properly model the system. Photometric measurements are used to determine the density distribution of the stars, and spectroscopy is used to derive their kinematic properties. This method, unfortunately, can be used only for a relatively small number of nearby galaxies. The central black hole is expected to dominate the local gravity and lead to observable effects only inside the “sphere-of-influence” radius $r_{inf} \equiv Gm_{bh}/\sigma^2$, where σ is the stellar velocity dispersion of the host bulge. This is on the order of 1 to 100 parsec for a typical galaxy. If we consider local galaxies, at distances of 1 - 20 Mpc, the necessary resolution is 0.1 to 1 arcsec. This resolution can be achieved by ground telescopes at prime observing locations or by space telescopes, such as the Hubble Space Telescope.

For actively accreting black holes there is another method to estimate the mass of the black hole at virtually any redshift. The main idea is that, because the broad lines in the ultraviolet and optical portions of the AGN spectra originate from the gravity-dominated regions close to the black hole, the width of the measured broad lines can be used to estimate the dynamics of the system. If the widths of the emission lines trace the virial velocity (V) of the region in which they are produced and this region is at the distance r from the black hole, then the mass is given by the following formula:

$$m_{bh} = \frac{fV^2r}{G}. \quad (1.7)$$

The factor f encapsulates our ignorance about exact astrophysical configuration of the system and it depends primarily on the geometry and detailed kinematic of the broad line region (see review by Peterson 2014).

The distances from the broad line region to the central engine range from a few light days to few light weeks and this distance cannot be probed by current facilities. Nonethe-

less, it is possible to estimate this distance using the reverberation mapping technique, which exploits the variability of AGN. The continuum of the AGN emission, which is generated close to the central black hole, exhibits stochastic variations. The same stochastic variations can be seen in the broad lines (they “reverberate”) after a time delay given by the light-travel time from the central engine. Observations which estimate these delays are relatively expensive because they require spectroscopic measurements with regular cadence. These work had yielded line-continuum lag measurements for approximately 50 objects, mainly lower luminosity objects in the nearby Universe (with the highest redshift object at $z = 0.29$) (Kaspi et al., 2000; Peterson et al., 2004; Bentz et al., 2009b,a; Denney et al., 2010; Barth et al., 2011; Grier et al., 2012). Much of this work has focused on measuring the response of the $H\beta$ line; for higher redshifts, the $Mg\ II\ \lambda 2798$ and $C\ IV\ \lambda 1549$ can be used, although there is great deal of debate about the validity of $C\ IV\ \lambda 1549$ for this kind of studies (Shen et al., 2008; Fine et al., 2008; Assef et al., 2011; Trakhtenbrot & Netzer, 2012; Coatman et al., 2017).

These results are then combined with velocity measurements to estimate the mass of the black hole. To estimate the virial velocity, V , in Equation (1.7) one usually uses the full-width-at-half-maximum (FWHM) of the emission line or the σ_{line} - that is, the second moment of the line profile. The largest uncertainty in the measurement comes from the factor f . Assuming a highly idealized spherical distribution of clouds in random, isotropic distribution we expect $f = 3/4$ if the FWHM of the lines is used; however if the measurement is done using σ_{line} , we expect $f = 3$ (Netzer et al., 1990). Efforts are under way to create observations of sufficient quality to directly estimate f (e.g., Denney et al. 2009; Grier et al. 2013). At the moment, the factor f is determined statistically by requiring that the sample of reverberation-mapped objects must follow the same $m_{bh} - \sigma$ relation as the galaxies that currently do not host an AGN. This approach yields estimates of $\langle f \rangle \sim 5$ with a spread of ~ 0.4 dex (Onken et al., 2004; Woo et al., 2010). In this work we will show that, even though we argue that m_{bh}/m_* evolves with redshift, when this is coupled with observed size evolution of galaxies, we expect no evolution in the $m_{bh} - \sigma$ and therefore $\langle f \rangle \sim$ should stay constant with redshift. Given how the factor f is derived, this method gives correct results only in a statistical sense and is highly uncertain for single objects.

As method described above is observationally expensive, in reality another short-cut is used. A number of previous studies found a correlation between r derived from reverberation mapping and the continuum luminosity of the AGN (Kaspi et al., 2000, 2005; Bentz et al., 2006). The intrinsic correlation, after contributions from the host galaxy are removed is $r \propto L^{0.519^{+0.063}_{-0.066}}$ where L is the AGN luminosity measured at $5100\ \text{\AA}$. This means that r in Equation (1.7) can be simply substituted with the measured continuum luminosity. This technique is known as “single-epoch mass measurement”, a name that reflects the fact that only a single measurement of an AGN spectrum, measuring the continuum luminosity and the width of the broad emission line, is enough, in principle, to estimate the virial mass of the object.

Given that this method has been tested only on relatively low-luminosity AGN in the

local Universe, it is not clear whether it is applicable for the whole AGN population. Theoretical work suggests that thin disk approximation fails below an Eddington ratio of $\lambda \approx 10^{-2}$, which could invalidate the simple correlations presented above. Similar arguments can be made for super-Eddington objects, for which the physical picture is even less clear. Observationally, very wide faint lines in very massive AGN can be harder to detect in typical noisy spectra (e.g., [Oh et al. 2011](#)). Nevertheless, this method provides crucial information about AGN masses at the present time, and is the only method practicable at high redshift.

1.2 Galaxy population

The basic physics behind galaxy formation and evolution is well understood. As the Universe evolves, primordial density fluctuations, driven by collisionless and cold dark matter grow until they collapse due to self-gravity. The distribution of these dark matter haloes and the number of these objects can be treated analytically - with some assumptions ([Press & Schechter, 1974](#)). Recently, a large number of simulations of different sizes and resolutions have been used to model the process with high accuracy ([Davis et al., 1985](#); [Dubinski & Carlberg, 1991](#); [Moore et al., 1999](#); [Springel et al., 2005, 2008](#); [Diemand et al., 2008](#); [Stadel et al., 2009](#); [Klypin et al., 2011](#)). Baryonic matter follows the dark matter until radiative, hydrodynamic and star-forming processes take over. As the baryonic matter falls into the collapsed dark matter halo it is shocked, heated, and then cools and settles into a disk to conserve angular momentum. The questions of how, exactly, the star-formation occurs and what are the critical parameters that control growth of galaxies remain still hotly debated.

1.2.1 Two galaxy populations

Observationally, the galaxies can be divided in two distinct populations (see [Figure 1.2](#)). When plotting the distribution of galaxies on the colour-absolute magnitude diagram, galaxies with primarily blue colours and disk morphologies are separated from galaxies with red colours and spheroidal morphologies ([Tully et al., 1982](#); [Blanton et al., 2003](#); [Baldry et al., 2004](#); [Driver et al., 2006](#)). Blue colours in galaxies indicate the existence of young, hot, blue stars and, therefore, recent star-formation.

The majority of these blue, star-forming galaxies have a star-formation rate (SFR) that is correlates strongly to their existing stellar masses, producing the so-called “Main Sequence” in which the specific SFR (sSFR) varies only weakly with stellar mass ([Brinchmann et al., 2004](#); [Daddi et al., 2007](#); [Elbaz et al., 2007](#); [Noeske et al., 2007](#)). The sSFR of the Main Sequence, however, increases strongly with look-back time ([Daddi et al., 2007](#); [Elbaz et al., 2007](#); [Pannella et al., 2009](#)) and is higher by approximately a factor of twenty at $z \sim 2$ compared with the present day value. Another interesting feature of the Main Sequence is its tightness; at any given redshift the galaxies are distributed with a very

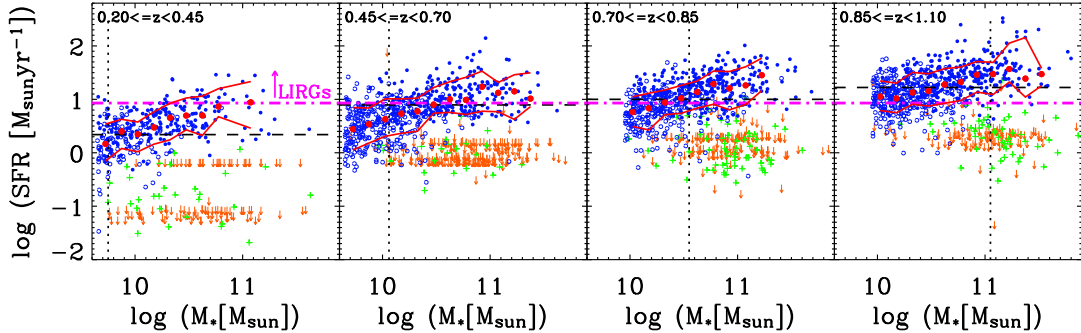


Figure 1.2: Star formation rate, determined from emission lines and $24\ \mu\text{m}$ data, as a function of stellar mass in four different redshift bins. Blue points show star-forming galaxies, green crosses represent galaxies with detections but with redder photometric colours, and orange arrows symbolise galaxies for which only the upper limits can be determined. Red lines and circles show the medians of $\log(SFR)$ and 1σ scatters. SFR is roughly linearly dependent on mass. Normalisation of the relation increases toward earlier cosmic times, approximately represented as $(1+z)^{2.5}$. Adopted from [Noeske et al. \(2007\)](#).

small scatter of $\sigma_{MS} \sim 0.2$ dex around the mean relation (e.g., review by [Speagle et al., 2014](#)). A small percentage of star-forming galaxies have significantly elevated sSFRs that are above the Main Sequence. It appears that the fraction of these “outliers” is more or less constant to $z \sim 2$ ([Sargent et al., 2012](#)) and that they represent 10% of the integrated star-formation that is occurring at any epoch.

The second part of the population consists of galaxies with significantly lower sSFRs. These galaxies are thought to have been star-forming in the past, but their star-formation has been “quenched”. Our understanding of the physical processes that lead to the quenching of star-forming galaxies is still limited, and a number of plausible physical mechanisms have been proposed (some of which directly involve AGN). However, the main empirical or phenomenological features of this quenching process are well understood based on the characteristic of the evolving populations of galaxies. We will explore connections between galaxy quenching and AGN activity, especially in [Chapter 3](#) in which we will study a scenario in which AGN activity is directly connected with the galaxy undergoing quenching.

1.2.2 Phenomenological approach to describe evolution of galaxy population

As the available data on galaxy populations at substantial look-back times have improved, new analysis techniques have been introduced that take an empirical approach to the data (see for example [Peng et al. \(2010\)](#) and [Behroozi et al. \(2013\)](#)). The approach in [Peng et al. \(2010\)](#) was to identify a few striking simplicities exhibited by the galaxy population(s) and to explore the consequences of these, where possible analytically, in terms of the most basic continuity equations linking the galaxy population(s) at different epochs.

The Peng et al. (2010) analysis was based on dividing the galaxy population into two components described above: the star-forming Main Sequence and the quenched population of passive galaxies. The number densities of star-forming galaxies at different masses can be well described by the Schechter function (Press & Schechter, 1974):

$$\Phi(m) \equiv \frac{dN}{d \log m} = \phi^* \left(\frac{m}{M^*} \right)^\alpha \exp \left(-\frac{m}{M^*} \right), \quad (1.8)$$

where ϕ^* is a normalization, α is the low mass slope and M^* is the characteristic Schechter mass. Much of the Peng et al. (2010) formalism is based on two salient observational results. The first is the observation that the effects of the mass and the density of the galaxy environment on the fraction of passive (quenched) galaxies are fully separable, as shown in Figure 1.3. This separability suggests that the quenching is a consequence of two processes: mass quenching which depends on the stellar mass and is independent of the environment, and environment quenching which is dependent on environment and is independent of stellar mass. The second observation is that the characteristic Schechter M^* of the mass-function $\phi(m)$ of the star-forming population has been more or less constant to at least $z \sim 2.5$ (and likely to $z \sim 4$) despite the substantial increase in stellar mass (by a factor of 10-30) of any galaxy that stays on the star-forming Main Sequence over this same time period (Bell et al., 2003; Bell et al., 2007; Ilbert et al., 2010; Pozzetti et al., 2010; Ilbert et al., 2013). This observation suggests that there is a connection between M^* and the termination of the mass growth of galaxies. The exponential drop-off of the mass function means that for a given star-forming galaxy, the mass-quenching rate, η_m , which reflects the probability that a given galaxy is quenching in unit time has to be proportional to the sSFR and the logarithmic gradient of the mass function, which is m for the case of the Schechter function. When these two relations are combined it follows that $\eta_m = (M^*)^{-1} \cdot SFR$, where M^* is a constant of proportionality. The equivalent statement is that for each galaxy a probability to grow to a certain mass is given by $P(m) = \exp[(M^*)^{-1} \cdot m]$. We note here that redshift independence of M^* requires the specific mass dependence of the quenching probability, but it does not put any constraint on the possible existence of the mass independent quenching process. Such mass-independent channel exists, and it is the environmental quenching process described above and seen in Figure 1.3.

As more and more galaxies reach M^* , mass quenching produces an accumulation of quenched galaxies at around the same mass. The mass-quenching rate described above produces a mass function of quenched galaxies that is also described with the Schechter function; however, the low mass slope, α_Q , is different from the low mass slope of star forming galaxies α_{SF} by 1 (i.e., $\alpha_Q = \alpha_{SF} + 1$). Environmental quenching also produces passive galaxies, but this process occurs in a manner which is independent of mass. Therefore the mass function of environmentally quenched galaxies has the same shape as that of the star-forming galaxies. This provides a natural explanation for the shape of the mass function of quenched galaxies, which can be described by the combination of two Schechter functions, with differing normalizations and low-mass slopes, but with the same characteristic Schechter mass as the star-forming galaxies.

The Peng et al. (2010) continuity formalism described above is very successful at repro-

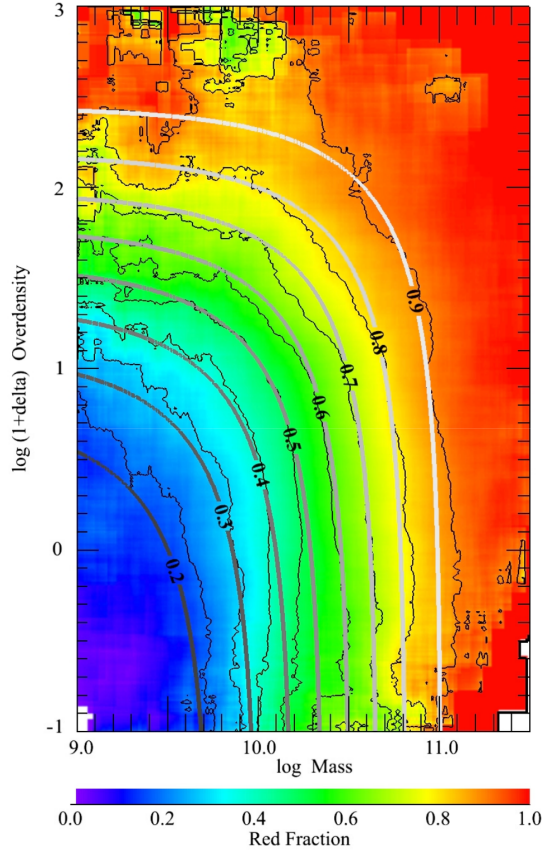


Figure 1.3: The red fraction in SDSS as a function of stellar mass and environment. The fraction of galaxies that are red is a fully separable effect of mass and environment. Adopted from Peng et al. (2010).

ducing mass functions of star-forming and passive galaxies in SDSS and also explains the quantitative relations between the Schechter parameters of these mass functions. This formalism allows easy computation of factors such as the quenching rate of galaxies and the mass function of galaxies that are undergoing quenching at any epoch. An alternative phenomenological approach of “abundance matching” (Behroozi et al., 2013) provides similar results, in terms of mass functions and star formation histories. With these recent developments, we now have a self-consistent, empirical (“phenomenological”) description of the evolving galaxy population at least back to $z \sim 4$ in terms of the evolving mass-functions of both the star-forming and quenched galaxy populations.

1.3 Co-evolution of black holes and their host galaxies

In the simplest sense, the black holes must “co-evolve” with their galaxies as they are embedded in them. It is not clear, however, whether black holes co-evolve with their

galaxies only in this strictest sense. They may share the physical environment but have little to no influence on the host galaxy or the black hole activity could have a profound effect on the host galaxies. Answer to this question is one of the main topic of this thesis that we discuss in Chapters 2, 3 and 4. There are several interesting correlations which hint at the strong connection, that we review below.

1.3.1 Cosmic density of mass accretion of black holes and galaxies

The black hole accretion rate density (BHARD) and the star formation rate density (SFRD) of the Universe roughly follow each other, but with some differences (see Figure 1.4). It is not immediately obvious whether the overall similarity of these two functions is indicative of the deep influence of black holes on their host galaxies or whether the similar evolutions of these quantities represent only a common availability of fuel for growth. We will show in Chapter 3 how the differences in the shape of these function are important and they can have a significant effect on the estimated evolution of the black hole mass function. It is also important to note that although the similarity of these functions exists in a global sense, black hole accretion and star formation histories of individual objects are very different. In a sample of star-forming galaxies, which are all on the Main Sequence and are therefore growing at a similar rate, there is a wide range of black hole accretion rates; some galaxies host extremely powerful AGN that accrete rapidly, whereas others host central black holes that are not growing at all. Typical duty cycle, i.e., fraction of galaxies which host an active black hole, ranges from 1% to 10%, depending on the exact definition of what constitutes an “active” black hole.

1.3.2 Black hole-galaxy correlations

The second line of evidence comes from observed correlations between the black hole masses and various galaxy properties. The most famous is the $m_{bh} - \sigma$ relation, which connects black hole masses with the stellar velocity dispersion σ of a galaxy bulge (Ferrarese & Merritt, 2000; Gebhardt et al., 2000). Modern work (Kormendy & Ho, 2013) suggests the following relationship:

$$\frac{m_{bh}}{10^9 M_{\odot}} = (0.309^{+0.037}_{-0.033}) \left(\frac{\sigma}{200 \text{ km s}^{-1}} \right)^{4.38 \pm 0.29}. \quad (1.9)$$

A similar correlation exists between black hole mass and the galaxy bulge (Magorrian et al., 1998), for which Kormendy & Ho (2013) suggests:

$$\frac{m_{bh}}{10^9 M_{\odot}} = (0.49^{+0.06}_{-0.05}) \left(\frac{m_{bulge}}{10^{11} M_{\odot}} \right)^{1.16 \pm 0.08}. \quad (1.10)$$

Both of these relationships show a surprisingly small intrinsic scatter, around 0.3 dex, suggesting that the quantities in the Equations above are deeply correlated (see Figure 1.5). However, correlation with a small scatter does not necessarily imply causation. For

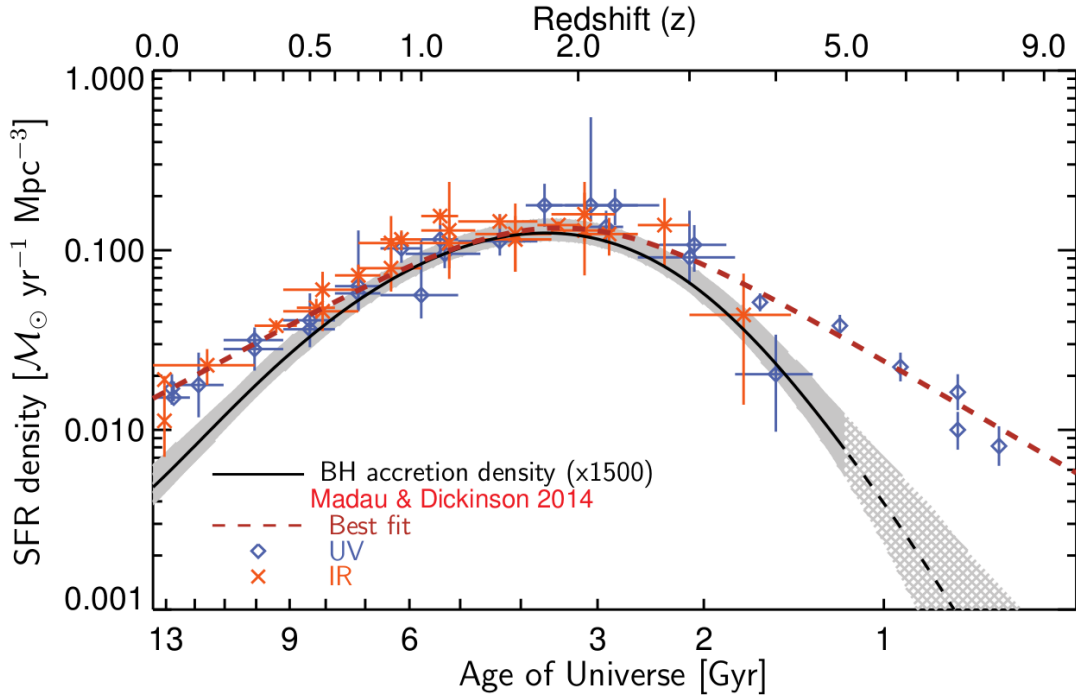


Figure 1.4: Cosmic evolution of SFRD and BHARD. The red line is the fit to SFRD given in review by [Madau & Dickinson \(2014\)](#), while blue and orange points are measurements done in ultraviolet and infrared bands, respectively. The black line and shaded region is BHARD and 1σ error estimated by [Aird et al. \(2015\)](#). The black line has been renormalised to ease the comparison. Adopted from [Aird et al. \(2015\)](#).

example, [Peng \(2007\)](#) and [Jahnke & Macciò \(2011\)](#) pointed out that even if the black hole mass and bulge masses are completely uncorrelated physically, galaxies that have undergone enough mergers would all have similar bulge to black hole ratio because of the averaging effect of the central limit theorem. We will also show that tightness of the m_{bh}/m_{bulge} relation in quenched galaxies can arise naturally, even if the m_{bh}/m_* is an intrinsic correlation for actively accreting black holes.

Other scaling relations have been proposed, such as $m_{bh} - n$ where n is Sersic index describing the light profile of the galaxy or m_{bh}/m_{halo} where m_{halo} is the mass of the dark matter halo. All these relations tend to show more scatter, but the basic difficulty in deducing the main parameters that drive these correlations is that most of these galaxy parameters are anyway strongly correlated with each other.

These correlation are primarily observed in relatively massive quenched galaxies with currently little or no AGN activity. For star-forming galaxies with active black holes in the local Universe, the primary correlation seems to be between the total mass of the galaxy and its black hole ([Sani et al., 2011](#); [Marleau et al., 2013](#); [Reines & Volonteri, 2015](#)). This would explain the observed AGN sources in bulgeless, pure-disk, galaxies ([Simmons et al., 2013](#)). We discuss the possible cosmic evolution of this relation in more detail below.

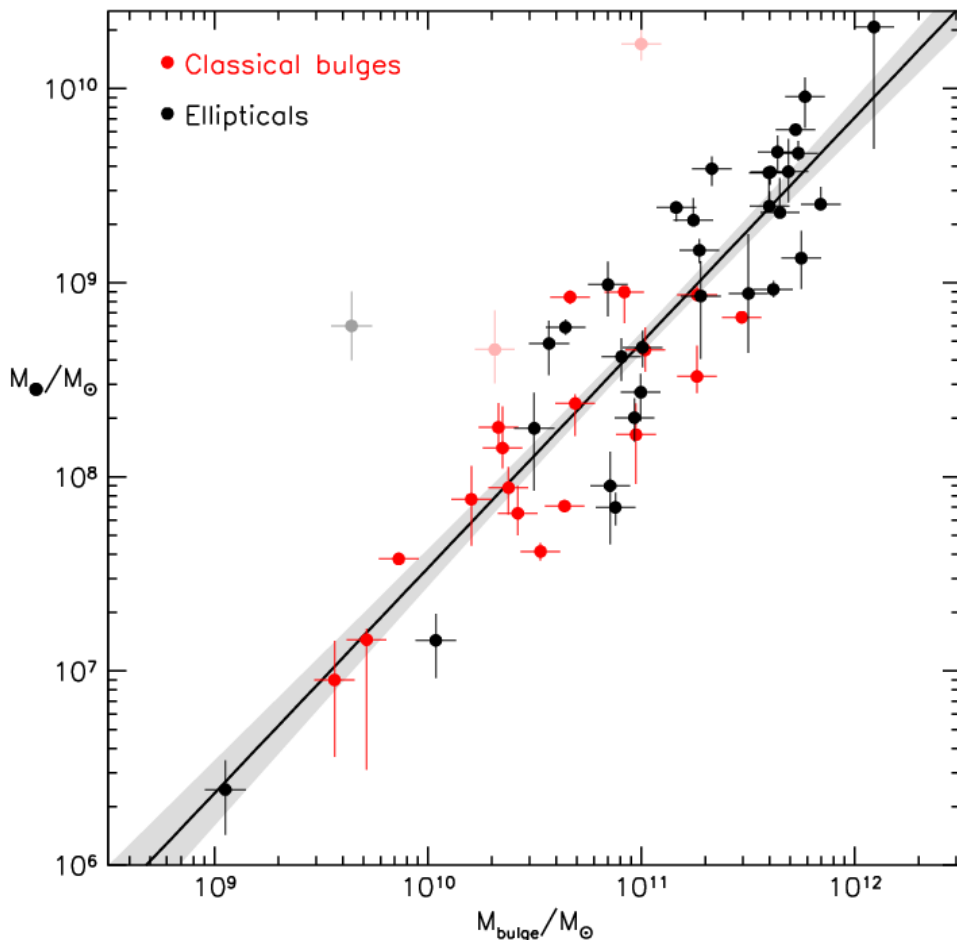


Figure 1.5: Black hole mass as a function of bulge mass. The black line is the relationship given in Equation (1.10), whereas the dashed line shows the error of the fit. Black points show elliptical galaxies, whereas the red points show “classical bulges” (i.e., elliptical galaxy-like bulges).

1.3.3 Evolution of the galaxy-black hole mass relations

Many studies have suggested that there is some redshift evolution in the m_{bh}/m_* relation (Peng et al., 2006; Decarli et al., 2010; Merloni et al., 2010; Trakhtenbrot & Netzer, 2010; Bennert et al., 2011; Sijacki et al., 2015), but others have found no significant evolution (Jahnke et al., 2009; Cisternas et al., 2011; Mullaney et al., 2012b; Schramm & Silverman, 2013) or argued that an observed evolution can be fully explained with selection effects (Schulze & Wisotzki, 2011; Schulze & Wisotzki, 2014). Recently, investigations in the local Universe have provided valuable insight on the topic of mass ratio evolution. Ferré-Mateu et al. (2015) and Ferré-Mateu et al. (2017) presented evidence for the existence of very compact quenched galaxies in the local Universe that have much larger black hole

masses than could be expected from the scaling relations. Given the compactness of these galaxies and their old mean mass-weighted ages, they can be interpreted as relics of a typical population quenched at $z \sim 2$. The fact that their central black holes are more massive than seen generally in the local Universe supports the idea that the m_{bh}/m_* ratio was larger at $z \sim 2$ than at lower redshifts. The same conclusion was reached by Barber et al. (2016) using the result from the Eagle simulation (Schaye et al., 2015; Crain et al., 2015). Different line of evidence for the mass ratio evolution comes from Reines & Volonteri (2015) who surveyed the m_{bh}/m_* in the active systems in the nearby universe ($z < 0.055$) and found the m_{bh}/m_* ratio in these systems to be more than an order of magnitude lower than the m_{bh}/m_* ratio found in the quenched systems. This finding is consistent with the evolving m_{bh}/m_* ratio in the scenario in which the quenched galaxies maintain a mass ratio representative of the active systems at the time of their quenching. This would naturally lead to quenched galaxies having larger m_{bh}/m_* than locally observed active galaxies.

The questions about the co-evolution, the influence of AGN on their host galaxies and the redshift evolution of the scaling relations still are hotly debated. In this thesis we explore different possibilities within a simple model framework and also emphasize the methodological issues that arise that are associated with the choice of samples.

1.4 Variability of AGN

Time variability is potentially one of the most interesting properties of quasars and AGN generally. The variability of quasars and AGN was recognized soon after the discovery of these objects (Matthews & Sandage, 1963). It is however still largely not understood and remains an active area of research. Variability in the brightness of AGN has been directly observed over a very wide range of time-scales, ranging from minutes and hours (e.g., Kasliwal et al., 2015; McHardy et al., 2016) up to several years (MacLeod et al., 2010) and even, by combining data from optical plates with modern surveys, to over 50 years (de Vries et al., 2003; Sesar et al., 2006). Indirect observational evidence exists for variability on scales of $\sim 10^5$ years (Schawinski et al., 2015) while simulations predict large scale variability during the AGN phase that may last $\sim 10^7$ years (Novak et al., 2011).

Quasar variability has been extensively studied in the optical waveband. The first study with very large numbers of objects used multiply-imaged regions of the SDSS survey (Vanden Berk et al., 2004). Further progress has been achieved by dedicated surveys of the variable sky, such as OGLE (Kozłowski et al., 2010), the Palomar-QUEST Survey (Bauer et al., 2009), the SDSS Stripe 82 (Sesar et al., 2007; MacLeod et al., 2010; MacLeod et al., 2012), PanStarrs (Morganson et al., 2014; Simm et al., 2016), SUDARE-VOICE (Falocco et al., 2015) and LaSilla-Quest (Cartier et al., 2015).

These studies have in general found an anti-correlation of the amplitude of variability (at a fixed rest-frame timescale) with luminosity, an increase of variability towards shorter wavelengths and little to no apparent dependence on redshift. The relationship with black hole mass remains unclear, with different studies finding either positive, negative or absent correlations (Wold et al., 2007; Wilhite et al., 2008; Kelly et al., 2009; MacLeod et al., 2010; Zuo et al., 2012). In the vast majority of cases (Andrae et al., 2013), the variability is found to be of a stochastic nature, with only a few recent claims of periodicity in a small number of objects (Graham et al., 2015a; Graham et al., 2015b; Charisi et al., 2016, but see also Vaughan et al., 2016). To describe the characteristics of this stochastic variability, the “damped random walk” model, first suggested by Kelly et al. (2009), is usually used. On short time scales, the variability is dominated by short-term random changes, producing a red noise spectrum. On longer timescales, the variation of brightness becomes uncorrelated, leading to a flattening of the spectrum towards white noise. The Kepler mission, with its precise photometry and continuous dense sampling of the optical light curves, has provided new insights and produced unambiguous power spectral density (PSD) curves for a small number of AGN. These individual PSD are often found to be inconsistent with the damped-random walk model, especially on short timescales (Kasliwal et al., 2015).

A range of possible explanations for brightness variations in quasars have been proposed. These include micro-lensing, accretion disk instabilities and variations in the accretion rate (Hawkins, 1993; Aretxaga et al., 1997; Kawaguchi et al., 1998; Trèvese & Vagnetti, 2002; Hawkins, 2007). The fact that the observed variability in the optical bands can be seen on scales of days to weeks is hard to reconcile with a model in which variability is caused by changes in the accretion rate. This is because the associated viscous time scales that should describe the radial migration or “drift” through the disk should be of order 10^4 years for typical AGN (Netzer, 2013). On the other hand accretion disk instabilities would be connected with the dynamical or orbital time scales, which are much shorter and will be of the order of ~ 1 yr for typical AGN. Thin accretion disk theory also predicts the dependence of these time scales with other physical parameters. Under the simplest assumptions the viscous time scale varies as, at a given rest-frame wavelength λ_{RF} , $\tau_{\text{vis}} \propto L^{7/60} \lambda_{RF}^{5/3} m_{bh}^{2/3}$, while the dynamical time scale should go as $\tau_{\text{dyn}} \propto L^{1/2} \lambda_{RF}^2$ (MacLeod et al., 2010).

Models with independent emitting regions that experience localized temperature variations, possibly created by instabilities in the accretion flow, are able to explain, in a qualitative manner, a wide range of features seen in optical variability surveys. In particular, they are also able to explain the measurements of large sizes of AGN disks from micro-lensing (Dexter & Agol, 2011; Cai et al., 2016).

Ground-based optical surveys generally suffer from irregular sampling, because of the realities of nightly, monthly and yearly observing periods. Therefore it is necessary to use alternative methods beyond Fourier analysis to characterize the variability. The most

commonly used approach is to construct the structure function (SF). The SF is defined to be the rms magnitude difference (in excess of observational noise) as a function of the time difference Δt between pairs of measurements. In this thesis we will generally use the SF^2 which is the excess variance (arising from variability) of the magnitude difference as a function of Δt :

$$SF^2(\Delta t) = \frac{1}{P} \sum_{i,j>i}^P (m_i - m_j)^2 - \sigma_i^2 - \sigma_j^2 \quad (1.11)$$

where the sum is over all P measurements which are separated by some time lag Δt , taking into account the measurement errors σ of the individual data points. The recent study of [Kozłowski \(2016\)](#) offers a good overview of the SF formalism, discusses different definitions used in the literature and points out a number of caveats. Using the SF formalism, it is possible to construct estimates of the ensemble variability of a set of objects. This implicitly assumes that an analysis of the variability of the members of a suitably defined set of quasars will reveal the same physical relations as studying individual objects.

AGN have been found to vary across all observational wavebands and PSD analysis has proved useful in the X-ray band because the time sampling is generally regular. The PSDs are in general found to be well described by a broken power law with a slope of roughly f^{-2} (as in a random walk) above a break frequency, f_{br} , and a flatter slope below the break frequency ([Lawrence & Papadakis, 1993](#); [Green et al., 1993](#)), broadly mimicking the behaviour of the SF at optical wavelengths. The exact nature of the phenomenological correlation found between the break frequency and the mass of the black hole (m_{bh}) is still unclear ([McHardy et al., 2006](#), [González-Martín & Vaughan, 2012](#), [Emmanoulopoulos et al., 2016](#)).

At optical wavelengths, the PSD formalism has been used in the case of the regularly and densely sampled Kepler data. These data suggest a wide spread of values for the high frequency slope of the optical PSD, with indicated slopes of between 2 and 4 ([Mushotzky et al., 2011](#), [Edelson et al., 2014](#)). The existence of a break frequency and associated flattening of the slope at low frequencies is still unclear, with various studies suggesting breaks occurring at scales of anywhere from ~ 10 to ~ 1000 days or longer ([Collier et al., 2001](#), [Kelly et al., 2009](#), [MacLeod et al., 2010](#)). Recently [Kelly et al. \(2014\)](#) introduced a flexible algorithm to estimate the PSD of light curves in the context of a broad family of continuous-time autoregressive moving average processes, which also enables estimates of PSD for sparsely sampled data to be obtained.

We will be using both of these methods (SF and PSD analysis) in Chapter 5 in which we study evolution of the AGN properties with the optical variability analysis.

1.5 Organization and content of this thesis

As indicated at the start of this chapter, in this thesis we present results of our two relatively disjoint investigations of the evolution of the AGN population and its properties. In Chapters 2, 3 and 4 we first present the results of our study of AGN based on our phenomenological exploration of the connections between the galaxy mass function, the AGN mass function and the QLF. Then, in Chapter 5 we present the results of our investigation into the evolution of AGN properties based on our examination of the variability of the AGN.

In Chapter 2 we develop a model in which black holes “co-exist” with their host galaxies and grow intermittently during the whole time that the galaxy is also star-forming. We point out the connections between the parameters of the galaxy mass function and QLF and make a number of testable predictions. We note that the results from analysis of the mass-luminosity plane suggest evolution in the m_{bh}/m_* ratio, which we argue was around ~ 10 times higher at $z \sim 2$ than it is today. This chapter is mostly based on a paper published in Caplar et al. (2015), with the addition of several modelling results.

We then investigate if the black hole mass accretion and star formation rates observed in the Universe could reproduce such a strong m_{bh}/m_* evolution and find that this is unlikely in the co-existence scenario described above. We therefore, in Chapter 3, discuss a scenario in which black hole accretion is associated with the mass-quenching of the galaxy’s star-formation. We use information about star-formation rate density and black hole accretion rate density to infer the evolution of m_{bh}/m_* and other parameters describing accretion. This scenario successfully reproduces observed m_{bh}/m_* evolution and we point out many similarities with the model developed in Chapter 2.

Given how both scenario lead to many comparable results even though they have very different physical origins we aim to find a observational diagnostic which can differentiate these two scenario. In Chapter 4 we point out that the biggest difference between the scenarios described in previous chapters is the mass dependence of the galaxies that host an AGN. We therefore select the observations which most directly probe this difference and conduct a comparison of the model predictions with the observations. We find that the second model, in Chapter 3, is to be preferred.

In Chapter 5 we present the results of our study on AGN variability in PTF/(i)PTF survey. We first discuss our procedure and the quality of our recalibration of the survey. We then show the results of the analysis conducted in the time domain using structure function formalism, and in the frequency domain, using power spectrum density analysis. This chapter is based on a paper published in Caplar et al. (2017).

In Chapter 6 we summarise our results and present an outlook for future research.

Throughout the thesis, we use a Λ CDM cosmology, with parameters $\Omega_M=0.3$, $\Omega_\Lambda=0.7$

and $H_0 = 70 \text{ km s}^{-1} \text{ Mpc}^{-1}$. Luminosities will be given in units of erg s^{-1} and will refer to bolometric luminosities, unless specified otherwise. Mass will be given in units of M_\odot , unless specified otherwise. We use the term “dex” to denote the antilogarithm, i.e., $n \text{ dex} = 10^n$. We also define all distribution functions, i.e., the star-forming galaxy mass function $\phi_{SF}(m_*)$, the black hole mass function $\phi_{BH}(m_{bh})$, AGN mass function, $\phi_{AGN}(m_{bh})$, the AGN luminosity function $\phi(L)$ and the probability distribution of Eddington ratio $\xi(\lambda)$, in \log_{10} space. This leads to power-law exponents that differ by unity relative to distribution functions defined in linear space. Units of $\phi_{SF}(m_*)$, $\phi_{BH}(m_{bh})$, $\phi_{AGN}(m_{bh})$ and $\phi(L)$ are $\text{Mpc}^{-3} \text{ dex}^{-1}$.

2 | AGN and galaxies: co-existence scenario

The content of this chapter is mostly based on [Caplar et al. \(2015\)](#).

2.1 Ansätze

The essence of our phenomenological approach is to make a limited number of simple Ansätze that allow us to construct a model using analytic techniques, or very elementary numerical modelling, based on straightforward representations of the most important features of the observational data. These Ansätze are in a sense “assumptions” and a decisive observational disproof of any of them would largely invalidate the model. Clearly they are very unlikely to be exactly true. Their value, as the basis for a simple “toy model”, is that we believe they are likely to be *broadly* true.

The three Ansätze which we use in the current chapter are as follows:

- radiatively efficient AGN are found in star-forming galaxies,
- the probability distribution of the Eddington ratio does not depend on the black hole mass of the system,
- the mass of the central black hole is linked to the stellar mass ($m_{bh} \propto m_*^\beta$), with some scatter, and we will for simplicity set $\beta \sim 1$. The ratio m_{bh}/m_* can however evolve with redshift.

The first Ansatz is motivated by the fact that, although there are undoubtedly some active AGN found in quenched galaxies, the bulk of radiatively efficient AGN reside in star-forming galaxies (Netzer, 2009; Silverman et al., 2009; Schawinski et al., 2010; Koss et al., 2011; Cimatti et al., 2013; Rosario et al., 2013; Matsuoka et al., 2014; Aird et al., 2017b), especially in those relatively low luminosity systems where the host galaxy can be most easily discerned. The second is the simplest assumption one can make about mass dependence of the Eddington ratio is supported by the studies such as Aird et al. (2013), Aird et al. (2017b) and Weigel et al. (2017). The final Ansatz is supported by observed correlations, as elaborated in Section 1.3.2. We will further justify these, and the choice of $\beta \sim 1$, further below.

Of course, there are a number of other implicit assumptions that are being made: observational data is not wildly wrong, individual black hole and stellar mass measurements are not systematically biased, the cosmological model is more or less correct and so on. We will not consider these further.

2.2 The origin of the quasar luminosity function

With our Ansätze, we can use our knowledge of the mass function of galaxies to construct the black hole mass function. To do this, we start with the mass function of star-forming galaxies and then impose a black hole to stellar mass ratio m_{bh}/m_* , with an additional log-normal scatter of η , to create a black hole mass function in star-forming hosts. This will serve as the basis for the radiatively efficient AGN population. In first part of this chapter, we will set the scatter $\eta = 0$ for initial analytic simplicity, before reintroducing it with $\eta \sim 0.5$ when we evaluate the model numerically.

If radiatively efficient accretion onto central black holes is only occurring in star-forming hosts, the quasar luminosity function can be created from a convolution of the black hole mass function in star-forming galaxies $\phi_{BH}(m_{bh}, z)$ with a probability distribution of the Eddington ratio λ ,

$$\phi(L, z) = \int \phi_{BH}(m_{bh}, z) \xi(\lambda, z) d \log \lambda, \quad (2.1)$$

where $\phi(L, z)$ is the resulting QLF, and $\xi(\lambda, z)$ is the probability distribution of the Eddington ratio, λ , as defined in Equation (1.3).

2.2.1 Convolution of Schechter functions with power law Eddington ratios

As noted above in Equation (2.1), the QLF will, with our Ansätze, be a convolution of the black hole mass function $\phi_{BH}(m_{bh})$ (itself derived from the stellar mass function of

star-forming galaxies $\phi_{SF}(m_*)$) and the distribution of Eddington ratios $\xi(\lambda)$, which gives the distribution of luminosities for black holes of a given mass. In this section we look at the general features of the $\xi(\lambda)$ distribution that are needed to produce a double power-law QLF from a Schechter-like mass function and explain qualitatively the connections that will exist between the parameters of these different functions. The exact calculation is presented in the following section.

First, we immediately note that in a model with a mass-independent $\xi(\lambda)$ and an input Schechter mass function, the only way to produce a power law at the bright end of the QLF (with slope γ_2) is to have a $\xi(\lambda)$ that is also a power law of the same slope at high values of the Eddington ratio. This power-law will then ensure that there is a high-end power-law in the QLF even as the mass function drops off exponentially. This is shown in Section 2.2.4. Given the limited dynamic range of the data, other representations of the QLF instead of a double power law are possible, e.g., a log-normal bright end or a modified Schechter function (e.g., Hopkins et al., 2007; Aird et al., 2012; Veale et al., 2014). We choose the conventional double power law for analytic simplicity and because it certainly provides a reasonable representation of the available data. Denoting the slope of the high end of Eddington ratio distribution by δ_2 we can thus equate

$$\gamma_2 = \delta_2, \quad (2.2)$$

with γ_2 the bright end slope of the QLF.

At the faint end, we may also expect a power-law QLF but now the QLF faint end slope γ_1 will be given by the steeper of the low end slope of $\phi_{BH}(m_{bh})$ and the low end slope of $\xi(\lambda)$, which we denote by δ_1 (see also discussion in Veale et al. 2014). Figure 2.1 illustrates what is happening with faint end of QLF (with slope) for different Eddington ratio assumptions.

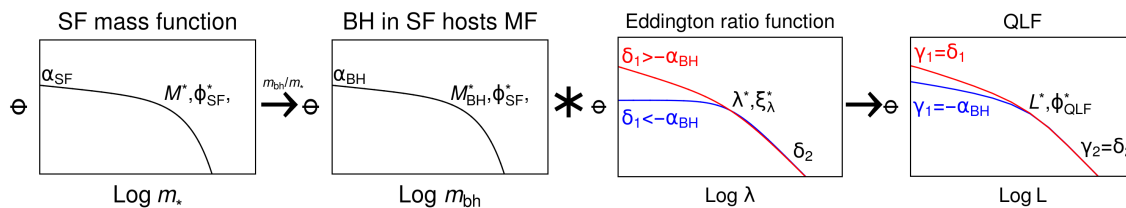


Figure 2.1: Schematic representation of our procedure to create the QLF. Starting from the star-forming mass function (leftmost) we use an m_{bh}/m_* scaling to get the mass function of SMBH in star-forming galaxies, with scatter as required (2nd panel). We convolve it with the Eddington ratio distribution (in the 3rd panel) to create QLF in the rightmost panel. Blue and red Eddington ratio distributions differ in the choice of parametrization of low end slope. The faint end slope of QLF will be same as low mass slope of galaxy mass function or low end slope of Eddington ratio distribution, depending on relative steepness of these two slopes. A short summary of the connections between parameters of the QLF and parameters of the contributing functions is given in Equation (2.10).

We can express this as

$$\gamma_1 = \max(-\alpha_{BH}, \delta_1). \quad (2.3)$$

The natural conclusion of a mass-independent Eddington rate distribution is that the faint end of QLF is set up by either the low end slope of the underlying black hole mass function or by the low end slope of the Eddington ratio function. If the logarithmic slope of the m_{bh} vs. m_* relation is β as above, then the faint end slope of the black hole mass function will be related to that of the star-forming galaxies by $\alpha_{BH} = \alpha_{SF}/\beta$.

We note at this point that there is good observational evidence that the faint end QLF slope, γ_1 , is similar to the observed low mass slope of the mass function of star-forming galaxies, α_{SF} , allowing for the reversal of sign in our definition. The QLF faint end slope, γ_1 is usually observed to be between 0.3 and 0.9 (Hasinger et al., 2005; Hopkins et al., 2007; Aird et al., 2010; Masters et al., 2012; Ueda et al., 2014). On the other hand the observed values of α_{SF} range from to -0.6 to -0.2 (Baldry et al., 2008; Pérez-González et al., 2008; Peng et al., 2010; González et al., 2011; Kajisawa et al., 2011; Baldry et al., 2012; Lee et al., 2012) with most newer studies converging around $\alpha_{SF} \sim -0.4$.

The data are therefore consistent with the idea that $\gamma_1 \sim -\alpha_{SF}$. This suggests, in the context of this model, that γ_1 may indeed being set by the low end slope of the black hole mass function (and not the low end of the Eddington ration distribution) and further that $\beta \sim 1$. We will henceforth assume that this is the case, i.e., that $\alpha_{BH} = \alpha_{SF} \approx -\gamma_1$. This then means that the low end slope δ_1 of $\xi(\lambda)$ can take any value that is shallower than this, i.e., $\delta_1 < -\alpha_{SF} \sim 0.4$. The high and low end power-laws of the Eddington ratio distribution will meet in a knee at a characteristic Eddington ratio which we denote by λ^* at which point the value of $\xi(\lambda)$ has a characteristic value ξ_λ^* .

2.2.2 The simplest Eddington ratio distribution that reproduces the shape of the QLF

To further demonstrate our approach we use the simplest function possible for the Eddington ratio distribution that reproduces, analytically, the required broken power law shape of QLF. We use a “triangular” distribution in which some fraction, f_d , of objects are active above a certain threshold value λ^* with an Eddington ratio distribution that is a single power law with slope δ_2 , while $(1-f_d)$ of objects are completely inactive. Effectively this sets the low end slope $\delta_1 = -\infty$.

The exact functional form of $\xi(\lambda)$ can then be written as

$$\xi(\lambda) = \frac{dN}{Nd \log \lambda} = \xi_\lambda^* \left(\frac{\lambda}{\lambda^*} \right)^{-\delta_2}, \quad \lambda > \lambda^*, \quad (2.4)$$

where ξ_λ^* is constrained by requirement that all of the objects have to be either active or inactive, so ξ in this case has to integrate to a duty cycle f_d .

In Section 2.2.4 we show that the knee of the QLF, L^* , will be related to the parameters of the original distribution functions through a formula describing the *population* which is analogous to Equation (1.4) of *individual* black holes, i.e.,

$$L^* = 10^{38.1} \cdot \lambda^* \cdot M_{BH}^* \cdot \Delta_L(\gamma_2), \quad (2.5)$$

where the Δ_L factor denotes a small multiplicative factor that is weakly dependent on γ_2 and varying by less than 0.15 dex.

In the same section, we also show that the ϕ_{QLF}^* normalization of the QLF, i.e., the value of ϕ_L at $L = L^*$ will be linked to the normalization of the galaxy mass function ϕ_{SF}^* and the normalization of the Eddington ratio distribution, ξ_λ^* ,

$$\phi_{QLF}^* = \phi_{SF}^* \cdot \xi_\lambda^* \cdot \Delta_\phi(\gamma_2), \quad (2.6)$$

where the Δ_ϕ denotes once again a small multiplicative factor, weakly dependent on γ_2 and varying by less than 0.15 dex. This is not surprising, and is stating the fact that the normalization of objects at given luminosity L^* is connected with the normalization of the contributing functions at M_{BH}^* and λ^* . Simply put, if there are more objects at mass M^* and more of them are active at λ^* , then we expect also more objects with corresponding luminosity L^* .

2.2.3 Broken power law Eddington ratio distribution and generalized duty cycle

Even though the triangular distribution of $\xi(\lambda)$ is a simple and analytically tractable one, it is unlikely to describe the real AGN population. For actual analysis we will adopt a more realistic broken power law distribution of Eddington ratio given by

$$\xi(\lambda) = \frac{dN}{Nd \log \lambda} = \frac{\xi_\lambda^*}{(\lambda/\lambda^*)^{\delta_1} + (\lambda/\lambda^*)^{\delta_2}}, \quad (2.7)$$

where we set $\delta_1=0$ for further analysis. This distribution diverges logarithmically at the low λ end. Since the integral of $\xi(\lambda)$ will therefore reach unity at some low value of

$\lambda \ll \lambda^*$, all black holes are “active” at some very low level and we need no longer consider “inactive” ones in this chapter.

As discussed in Section 2.2.1, this distribution will also reproduce the same shape of the QLF as the “triangular” distribution just discussed, provided that $\delta_1 < -\alpha_{BH}$.

We note that such a distribution, (with a sharp break at λ^* , instead of “smooth” version above), would naturally arise if individual AGN are boosted to some initial Eddington ratio above λ^* (the distribution of which is given by γ_2) and thereafter decay exponentially with a constant decay time τ . In this case, the concept of “duty cycle” f_d in the previous section is replaced by the value of ξ_λ^* . If the “boost plus decay” scenario is relevant, then it is easy to see that, if AGN are activated at some fractional rate η_{AGN} per star-forming galaxy per unit time (e.g., Hopkins et al., 2005), then

$$\xi_\lambda^* = \eta_{AGN} \cdot \tau, \quad (2.8)$$

so that ξ_λ^* is the fraction of black holes that are activated in the time interval corresponding to their subsequent decay time. This is quite a useful general definition of duty cycle.

Of course, other scenarios could also produce this $\xi(\lambda)$ distribution and even more general “duty cycle” could be defined as the fraction of black holes accreting above λ^* (as in the triangular distribution above). In this particular case, as shown in Section 2.2.4, this definition of duty cycle would be given by

$$f_d = \frac{\xi_\lambda^*}{\delta_2 \ln(10)} \quad (2.9)$$

The point is that the value of ξ_λ^* is a good indicator of a generalized duty cycle.

If $\delta_1 < -\alpha_{BH}$, then the exact choice $\xi(\lambda)$ below λ^* is of no great importance to the convolution model and the connections between the parameters, which we can derive analytically in the simplified model as in Equations (2.2), (2.3), (2.5) and (2.6) will still hold. Specifically, we can write

$$\begin{aligned} \gamma_2 &= \delta_2, \\ \gamma_1 &= \max(-\alpha_{BH}, \delta_1), \\ L^* &= 10^{38.1} \cdot \lambda^* \cdot M_{BH}^* \cdot \Delta_L(\delta_1, \gamma_2), \\ \phi_{QLF}^* &= \phi_{SF}^* \cdot \xi_\lambda^* \cdot \Delta_\phi(\delta_1, \gamma_2), \end{aligned} \quad (2.10)$$

where we have now also explicitly shown a δ_1 dependence in the Δ factors, because this corrective factor will also depend on our exact choice of low slope of the Eddington ratio distribution (see exact calculation in next section). Now using the m_{bh}/m_* relation, we can also connect the observed L^* of the QLF to the M^* of the star-forming galaxy mass function with

$$L^* = 10^{38.1} \cdot \lambda^* \cdot M^* \cdot \left(\frac{m_{bh}}{m_*} \right) \cdot \Delta_L(\delta_1, \gamma_2). \quad (2.11)$$

2.2.4 Analytical derivation of the QLF

In this subsection we will show analytically how the convolution of a Schechter mass function $\phi_{BH}(m_{bh})$ with a triangular Eddington ratio distribution $\xi(\lambda)$ in Equation (2.4) gives rise to a double power-law QLF and the simple relations between parameters given in (2.10). This section can be omitted by the readers who are not interested in the details of the mathematical procedure that give rise to convolution model of the QLF.

In this simplest case when $\xi(\lambda) = 0$ below λ^* , combining equations (2.1), (2.4) and (2.24) leads to

$$\begin{aligned} \phi(L) &= \int_{\lambda^*}^{\infty} \phi_{SF}^* \xi_{\lambda}^* \left(\frac{L}{10^{38.1} M_{BH}^* \lambda} \right)^{\alpha_{BH}} \exp \left[\frac{-L}{10^{38.1} M_{BH}^* \lambda} \right] \left(\frac{\lambda}{\lambda^*} \right)^{-\delta_2} \frac{1}{\ln(10)\lambda} d\lambda \\ &= \frac{\phi_{SF}^* \xi_{\lambda}^*}{\ln(10)} \left(\frac{10^{38.1} M_{BH}^* \lambda^*}{L} \right)^{\delta_2} \left(\Gamma[\alpha_{BH} + \delta_2] - \Gamma[\alpha_{BH} + \delta_2, \frac{L}{10^{38.1} M_{BH}^* \lambda^*}] \right), \end{aligned} \quad (2.12)$$

where $\Gamma[x]$ is Euler gamma function, given by $\Gamma[x] = \int_0^{\infty} t^{x-1} e^{-t} dt$ and $\Gamma[x, y]$ is incomplete gamma function, defined as $\Gamma[x, y] = \int_y^{\infty} t^{x-1} e^{-t} dt$. On the other hand we know that the integral of distribution of Eddington ratios has to be equal to f_d

$$\int_0^{\infty} \frac{\xi(\lambda)}{\log(10)\lambda} d\lambda = 1 \rightarrow \int_{\lambda^*}^{\infty} \xi_{\lambda}^* \left(\frac{\lambda}{\lambda^*} \right)^{-\delta_2} \frac{d\lambda}{\ln(10)\lambda} = f_d, \quad (2.13)$$

which gives

$$\xi_{\lambda}^* = f_d \delta_2 \ln(10). \quad (2.14)$$

Combining Equations (2.12) and (2.14) we arrive at an expression for the QLF

$$\phi(L) = f_d \phi_{SF}^* \cdot \left\{ \delta_2 \left(\frac{10^{38.1} M_{BH}^* \lambda^*}{L} \right)^{\delta_2} \left(\Gamma[\alpha_{BH} + \delta_2] - \Gamma[\alpha_{BH} + \delta_2, \frac{L}{10^{38.1} M_{BH}^* \lambda^*}] \right) \right\}, \quad (2.15)$$

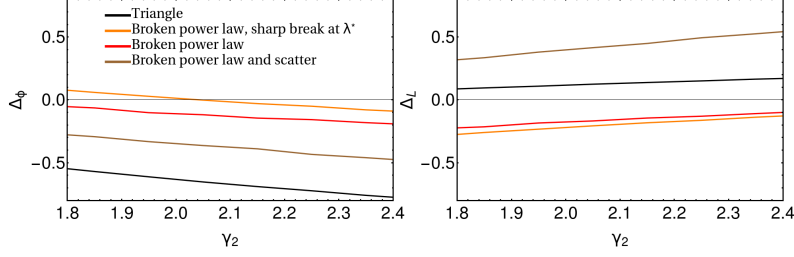


Figure 2.2: Functional dependence of the factors $\Delta_L(\delta_1, \gamma_2)$ and $\Delta_\phi(\delta_1, \gamma_2)$. Black line corresponds to the “triangle” distribution given with Equation (2.4). Orange line is showing the result for the distribution shown in Equation (2.21) (with $\delta_1 = 0$), red line is showing the result for the broken power law distribution, given in Equation (2.7) (with $\delta_1 = 0$), while brown line corresponds to previous case, but with added scatter when converting from the star-forming galaxy mass function to the mass function of black holes in star-forming galaxies.

where we separate the “normalization” from the rest of the expression in curly brackets. We can expand this expression at low and high L to show asymptotic power law behaviour.

Expanding around $L = 0$ gives

$$\phi(L \rightarrow 0) = f_d \phi_{SF}^* \delta_2 \cdot L^{\alpha_{BH}} \cdot \left(\frac{(10^{38.1} M^* \lambda^*)^{-\alpha_{BH}}}{\alpha_{BH} + \delta_2} - \frac{(10^{38.1} M^* \lambda^*)^{-\alpha_{BH}}}{10^{38.1} M_{BH}^* \lambda^* (1 + \alpha_{BH} + \delta_2)} L + \mathcal{O}(L^2) \right), \quad (2.16)$$

so we see that dominant term will be $L^{\alpha_{BH}}$ and that $\gamma_1 = -\alpha_{BH}$. This is special case of our formula $\gamma_1 = \max(-\alpha_{BH}, \delta_1)$ as in this case δ_1 is effectively minus infinity.

Expanding around $L \rightarrow \infty$,

$$\phi(L \rightarrow \infty) = f_d \phi_{SF}^* \delta_2 \cdot \left(\frac{10^{38.1} M_{BH}^* \lambda^*}{L} \right)^{\delta_2} \cdot \left(\Gamma[\alpha_{BH} + \delta_2] - \exp \left[-\frac{L}{10^{38.1} M_{BH}^* \lambda^*} \right] \left(\frac{L}{10^{38.1} M^* \lambda^*} \right)^{-1 + \alpha_{BH} + \delta_2} + \mathcal{O} \left(\frac{1}{L^2} \right) \right), \quad (2.17)$$

we see that dominant term is $L^{-\delta_2}$, giving rise to the equation $\gamma_2 = \delta_2$.

Defining the double power-law as in Equation (1.6), we find expression for L^* and ϕ^* is given by

$$\begin{aligned} L^* &\approx 10^{38.1} M_{BH}^* \lambda^* \\ \phi_{QLF}^* &\approx \phi_{SF}^* f_d \cdot \delta_2 (\Gamma[\alpha_{BH} + \delta_2] - \Gamma[\alpha_{BH} + \delta_2, 1]) \\ &\approx \phi_{SF}^* f_d. \end{aligned} \quad (2.18)$$

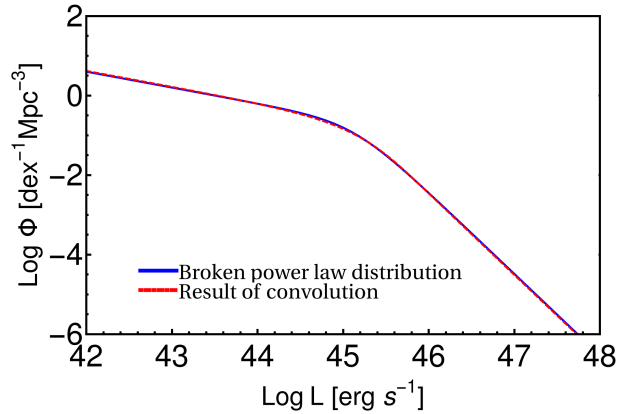


Figure 2.3: QLF in a shape of a broken power law distribution is show in blue, while in red we show results of convolution of Schechter mass function and simple “triangle” distribution of Eddington ratio (Equation (2.15)), with parameters set to reproduce the blue line which is barely visible below the red line. As we see, agreement is excellent.

As would be expected, the L^* and ϕ_{QLF}^* are related to the input M_{BH}^* and ϕ_{SF}^* via the characteristic λ^* and the normalization of ξ_λ^* given by f_d .

We have numerically fitted the resulting $\phi(L)$ around L^* with the broken power law given in equation (1.6) (with $\gamma_1 = -\alpha_{SF}$) for various γ_2 values and plot the resulting offsets Δ_L and Δ_ϕ in Figure 2.2 such that

$$\begin{aligned} L^* &= 10^{38.1} \cdot \lambda^* \cdot M_{BH}^* \cdot \Delta_L(\gamma_2), \\ \phi_{QLF}^* &= \phi_{SF}^* \cdot \xi_\lambda^* \cdot \Delta_\phi(\gamma_2). \end{aligned} \quad (2.19)$$

It can be seen that, as would be expected from Equation (2.15), the values of Δ_L and Δ_ϕ vary with γ_2 . The standard double power-law Equation (1.6) is a surprisingly good representation of the analytic result in Equation (2.15). Example of power-law shape and result from our convolution is shown in Figure 2.3.

We can also repeat this exercise with a second form of ξ_λ that is flat below λ^* , i.e., has $\delta_1 = 0$, replacing f_d by ξ_λ^* , i.e.,

$$\begin{aligned} L^* &= 10^{38.1} \cdot \lambda^* \cdot M_{BH}^* \cdot \Delta_L(\delta_1, \gamma_2), \\ \phi_{QLF}^* &= \phi_{SF}^* \cdot \xi_\lambda^* \cdot \Delta_\phi(\delta_1, \gamma_2), \end{aligned} \quad (2.20)$$

where we incorporate the fact that Δ factors depend on the assumed shape of the Eddington ratio. This can again be seen in Figure 2.2, where we also show results of fitting with Eddington ratio distribution which has sharp break at λ^* , i.e.,

$$\xi(\lambda) = \begin{cases} \xi_\lambda^* \left(\frac{\lambda}{\lambda^*}\right)^{-\delta_1} & \lambda < \lambda^* \\ \xi_\lambda^* \left(\frac{\lambda}{\lambda^*}\right)^{-\delta_2} & \lambda > \lambda^*. \end{cases} \quad (2.21)$$

2.2.5 Predictions of the convolution model

If the QLF is indeed produced by the convolution described in the previous two sections, then we can immediately see in general terms how the mass distribution of AGN, or host galaxies of AGN, selected at a given luminosity will vary with that selection-luminosity. This is shown in Figure 2.4 where we show the mass functions of galaxies and black holes. The masses and number densities are normalized, respectively, by the M^* and ϕ_{SF}^* of the input Schechter mass function of the star-forming galaxies. These distributions are plotted for different AGN luminosities relative to the knee luminosity L^* in the quasar luminosity functions (see also Equation (1.6)). To generate this plot we used the model for $\xi(\lambda)$ considered in the previous section, i.e., with a flat ξ below λ^* and with 0.5 dex scatter in the black hole to stellar mass relation. With this normalization the figures applies at all redshifts. Several points should be noted on this Figure.

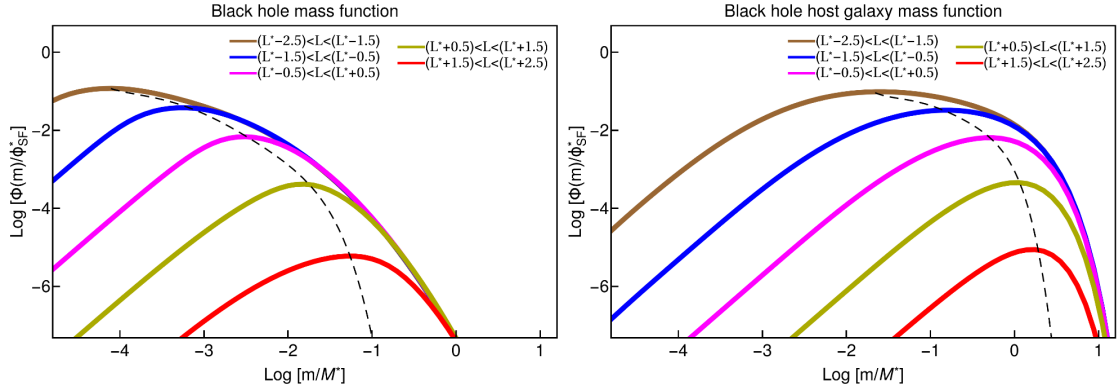


Figure 2.4: Expected shape of the black hole and the black hole host galaxy mass function, selected in different AGN luminosity bins. Mass are plotted relative to the Schechter M^* of the galaxy population ($M^* \sim 10^{10.85} M_\odot$) and Φ relative to the ϕ_{SF}^* of the galaxy population. All luminosities are relative to the L^* of the AGN luminosity function. The black dashed line is connecting the masses where the mass functions reach maximum value.

First, all of the mass functions (of both black holes and host galaxies) always show a peak at some mass. This is quite unlike the input mass function of star-forming galaxies, and thus also of black holes, which increase monotonically to lower masses. The peak arises because the low mass end of the input mass function is modulated by the high λ part of $\xi(\lambda)$, simply because it is the highest Eddington ratios that pull the lowest mass black holes (and hosts) into a given luminosity bin. The low mass end of these mass distributions should therefore have a slope of $\gamma_2 + \alpha_{SF}$, i.e., with $\alpha_{SF} \sim -0.4$ and $\gamma_2 \sim 2$ (see below), we predict a low mass slope of $+1.6$. This is a quite generic and robust prediction of the convolution model and is independent of the choice of δ_1 , the low λ behaviour of $\xi(\lambda)$ discussed above. This is because for most luminosities, the *high* mass end of the mass functions in Figure 2.4 is dominated by the exponential fall-off of the input mass function.

Second, at high luminosities, above L^* , the effect of the AGN luminosity on the host galaxy mass function is to change the numbers of hosts, but not to change the peak mass or, to first order, the shape of the mass function. This is because of the steep exponential fall off in the input mass function of galaxies above M^* . Above L^* , the peak host galaxy mass is always close to M^* because there are so few more massive galaxies. The numbers of M^* galaxies at the peak is determined by how high Eddington ratios are required to bring these objects into the luminosity range in question. For these high AGN luminosities, the shape of the mass function of (star-forming) hosts is very similar to that of passive galaxies except that the faint end slope is significantly steeper ($\alpha_{SF} + \gamma_2$, with $\gamma_2 \sim 2$) than of the passive galaxies which is given by $\alpha_{SF} + 1$ (see Peng et al., 2010). In mathematical form, the mass function of galaxies at any AGN luminosity above L^* will have a Schechter shape

$$\phi(m_*; L > L^*) \propto \left(\frac{m_*}{M^*}\right)^{\alpha_{SF} + \gamma_2} \exp\left(-\frac{m_*}{M^*}\right). \quad (2.22)$$

At lower luminosities, well below L^* , the behaviour changes and a region of intermediate slope appears. For black hole masses between $(10^{38.1})^{-1}(m_{bh}/m_*)^{-1}(\lambda^*)^{-1}L$ and $(10^{38.1})^{-1}(m_{bh}/m_*)^{-1}(\lambda^*)^{-1}L^*$, the mass function will have the slope given by $\alpha + \delta_1$. At very low masses we will again always recover the slope of $\alpha_{SF} + \gamma_2$.

The location of the peak in the black hole mass function therefore depends on the slopes of both underlying distributions (Eddington ratio and galaxy mass function), i.e., on the sign of $\alpha + \delta_1$. Not surprisingly, this intermediate zone also appears in the host galaxy mass function with the same slope. This produces a peak host galaxy mass of

$$\begin{aligned} m_{peak} &\sim \frac{M^*}{10^{38.1} m_{bh} \lambda^*} L & |\alpha_{SF}| > |\delta_1| \\ m_{peak} &\sim \frac{M^*}{10^{38.1} m_{bh} \lambda^*} L^* & |\alpha_{SF}| < |\delta_1|. \end{aligned} \quad (2.23)$$

This difference in behaviour can be understood as follows: In the $|\alpha_{SF}| > |\delta_1|$ case the dominant contribution to the luminosity function will come from low mass objects accreting at high Eddington ratio which are more numerous than high mass objects accreting at low Eddington ratios. In the second case, roles are simply reversed and main contributor to the QLF will be high mass AGN with low Eddington ratios.

If black hole masses were very tightly correlated with host galaxy masses, then clearly the same behaviour would be seen in the black hole mass function(s) since these would always be a simple (mass-)scaling of the galaxy mass function(s). However, the effect of scatter in the black hole to host galaxy mass relation is quite marked. This is visible in Figure 2.4. The reason is clear: the mass function of black holes will now be much smoother than that of the host galaxies since the log normal scatter smooths out the sharp exponential drop of the galaxies at high masses (recall that Figure 2.4 used a 0.5 dex scatter).

Of course, it might be argued that the black hole mass is somehow more fundamental, and that the galaxy mass function should be obtained by smoothing it. However, we know the galaxy mass function quite well, and it has an exponential cutoff (see Peng et al., 2010; Baldry et al., 2012). We do not, at this stage, know the underlying mass function of black holes in star-forming galaxies. With this scatter, there is a much smoother variation of the peak mass with AGN luminosity.

The dashed lines show the variation of the peak mass with luminosity. The fact that the difference between these dashed curves on the two panels decreases with luminosity illustrates the well known “Lauer effect” (Lauer et al., 2007) whereby the typical objects at high AGN luminosities will generally have been scattered above the mean black hole host mass relation. It should be noted, however, that there is no change in the low mass slope of the mass function(s) due to scatter and this remains a very robust prediction of our model.

It is worth noting in Figure 2.4 that the peak of the black hole mass distribution varies quite weakly with luminosity, i.e., a change in luminosity of 1 dex is associated with a smaller increase in the peak m_{bh} . This means that we will generally see higher Eddington ratios in higher luminosity quasars even though the Eddington ratio distribution is taken to be strictly independent of black hole mass. We return to this point in Section 2.5.1 below.

We stress that the (solid) curves in Figure 2.4 that show the mass functions of AGN host galaxies (with masses normalized to the Schechter M^*) at different AGN luminosities (computed relative to the knee of the luminosity function) are an easily testable prediction of the convolution approach, modulo the effects linked to the choice of α and δ_1 discussed above, which can shift the peak of $\phi(m)$. We will return to this topic in Chapter 4 when we compare predictions arising from different scenarios describing galaxy - black hole co-evolution.

2.3 Data

We next turn to demonstrate how our model relates to the observations of the mass function of star-forming galaxies and QLF. In this section, we will estimate the redshift evolution of parameters that describe these two populations.

2.3.1 Mass function of star-forming galaxies

As explained previously, we need to know the mass function of star-forming galaxies to deduce the SMBH mass function in star-forming galaxies, $\phi_{BH}(m_{bh})$, which is an integral part of predicting the QLF in Equation (2.1). We also want to verify the predictions of Peng et al. (2010) and Peng et al. (2012) for the time evolution of the parameters of the galaxy mass function (e.g., equation B3 from Peng et al., 2012).

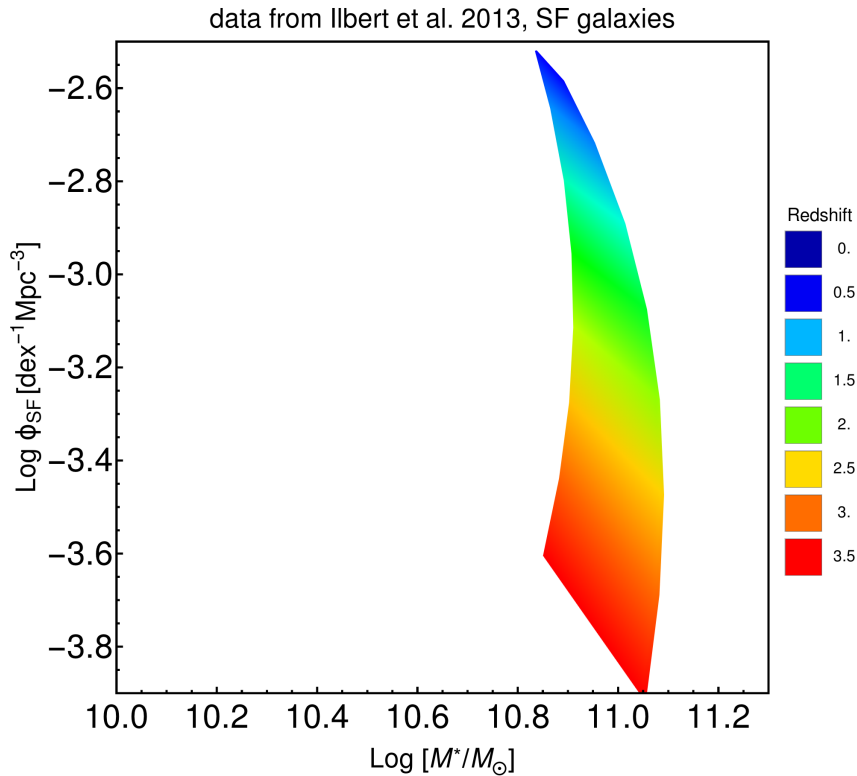


Figure 2.5: Evolution of ϕ_{SF}^* and M^* parameters in the Schechter mass function of star-forming galaxies. Data shows minimal evolution of M^* until at least $z \approx 2.5$, but significant evolution in ϕ_{SF}^* .

In order to do this, we fit the data for star-forming galaxies from Ilbert et al. (2013) at all redshifts with a single Schechter function in which the parameters ($\phi_{SF}^* \equiv \phi_{SF}^*(z)$, $M^* \equiv M^*(z)$) are smoothly varying functions of redshift. Fitting all the data in this fashion, instead of fitting at single redshifts, enables us to follow better the evolution of the parameters. It also reduces the sensitivity to small variations which may compromise fits at a single redshift and add to the degeneracies between parameters. This procedure of simultaneously fitting all of the data of the galaxy mass function at different redshifts is analogous to the standard procedure often used in determining the evolving QLF (e.g., Hopkins et al., 2007; Ueda et al., 2014). The functional form that we use for the redshift

Tab. 2.1 — Evolution of star-forming galaxy mass function, data from [Ilbert et al. \(2013\)](#)

parameter	fixed $\alpha_{SF} = -0.4$
a_0	-2.55 ± 0.04
a_1	-0.26 ± 0.06
a_2	-1.6 ± 0.12
a_3	-0.88 ± 0.16
b_0	10.9 ± 0.04
b_1	-0.53 ± 0.11
b_2	3.36 ± 0.11
b_3	-3.75 ± 0.13

evolution of the galaxy mass function is Schechter form introduced in (1.8)

$$\begin{aligned}
 \phi_{SF}(m_*, z) &= \frac{dN}{d \log m_*} \\
 &= \phi_{SF}^*(z) \left(\frac{m_*}{M^*(z)} \right)^{\alpha_{SF}} \exp \left(-\frac{m_*}{M^*(z)} \right),
 \end{aligned} \tag{2.24}$$

where we model the redshift dependence as

$$\begin{aligned}
 \log \phi_{SF}^*(z) &= a_0 + a_1 \kappa + a_2 \kappa^2 + a_3 \kappa^3, \\
 \log M^*(z) &= a_0 + b_1 \kappa + b_2 \kappa^2 + b_3 \kappa^3,
 \end{aligned} \tag{2.25}$$

with $\kappa \equiv \log(1+z)$. The slope of the low mass end, α_{SF} , was kept constant at the local value of $\alpha_{SF} = -0.4$ as there is considerable evidence that there is little or no change in the low mass slope for the redshift range considered ([Peng et al., 2014](#)). We give the results of the fit in Table 2.1.

The evolution of the parameters of the mass function in Figure 2.5 confirms that M^* is more or less constant up until at least redshift 2.5, i.e., it verifies the Ansatz of [Peng et al. \(2010\)](#) which establishes a single quenching mass scale M^* that does not change with redshift. It is important to stress that our results will not depend critically at this stage on the exact functional evolution of M^* above $z \gtrsim 2.5$, but will use the by now well established observational fact that M^* does not change at $z \lesssim 2.5$ and that the evolution in the galaxy population since that time is associated with a “vertical” evolution in ϕ_{SF}^* . We have also performed this analysis with the dataset from [Muzzin et al. \(2013\)](#) and the compilation of galaxy mass functions from [Behroozi et al. \(2013\)](#) and our conclusions presented in the rest of this work do not change.

2.3.2 Quasar luminosity function

Hopkins et al. (2007) combined measurements of quasar luminosity functions in different bands, fields and redshifts in order to characterise the bolometric QLF at epochs $0 < z < 6$. In their work, the best fit luminosity-dependant bolometric correction and luminosity and redshift-dependent column density distributions are used in order to construct an estimate of the bolometric QLF which should be consistent with all of the various individual surveys. Although now several years old, we believe that this synthesized QLF compilation remains the most comprehensive and it is used as the basis for the current analysis.

We proceed with fitting their tabulated data with a double power law QLF, as given by Equation (1.6). We fit both at each redshift individually, and carry out a “full fit” where the parameters (i.e., ϕ_{QLF}^* , L^* , γ_1 and γ_2) are all constrained to be smoothly varying functions of redshift, i.e., adopting a similar approach as we used earlier in our fitting of the galaxy mass function in Section 2.3.1. This “full” fitting of a redshift-dependent double power-law is essentially the same as the approach used in Hopkins et al. (2007), with one important difference. In order to avoid degeneracies in the fits it is necessary, both here and in Hopkins et al. (2007), to fix one or more of the parameters. Hopkins et al. (2007) chose to require a redshift-independent ϕ_{QLF}^* at a constant value. We now know that ϕ_{SF}^* of the galaxy population changes significantly over the redshift range of interest and, as developed in the previous section, the relationship of ϕ_{QLF}^* relative to ϕ_{SF}^* is of great interest in the context of the duty cycle. In contrast, γ_1 is set, in our convolution model, by the low mass slope α_{SF} of the mass function of star-forming galaxies. As mentioned before there is not much evidence (see Peng et al., 2014) that this changes significantly, if at all, over the redshift range of interest, nor compelling evidence for a change in γ_1 . Therefore, we choose to have a redshift-independent faint end slope of the luminosity function, γ_1 and to allow ϕ_{QLF}^* to vary with redshift. It should be noted that our fitting procedure is the same as a “luminosity and density evolution” model (e.g., Aird et al., 2010) except that we are allowing the bright end slope γ_2 to vary. We do this because, as we have seen, γ_2 is set by the high λ behaviour of the Eddington ratio distribution $\xi(\lambda)$.

The parameters in the luminosity function are allowed to vary as

$$\begin{aligned} \log \phi_{QLF}^* &= c_0 + c_1\kappa + c_2\kappa^2 + c_3\kappa^3, \\ \log L^* &= d_0 + d_1\kappa + d_2\kappa^2 + d_3\kappa^3 + d_4\kappa^4, \\ \gamma_1 &= e_0, \\ \gamma_2 &= f_0 + f_1z + f_2z^2, \end{aligned} \tag{2.26}$$

with again $\kappa = \log(1 + z)$. We follow Hopkins et al. (2007) in fitting γ_1 and γ_2 as a polynomial in z (rather than $\kappa = \log(1 + z)$), but this choice is not of great importance.

Additional degrees of freedom were added to the fit until we can find no appreciable

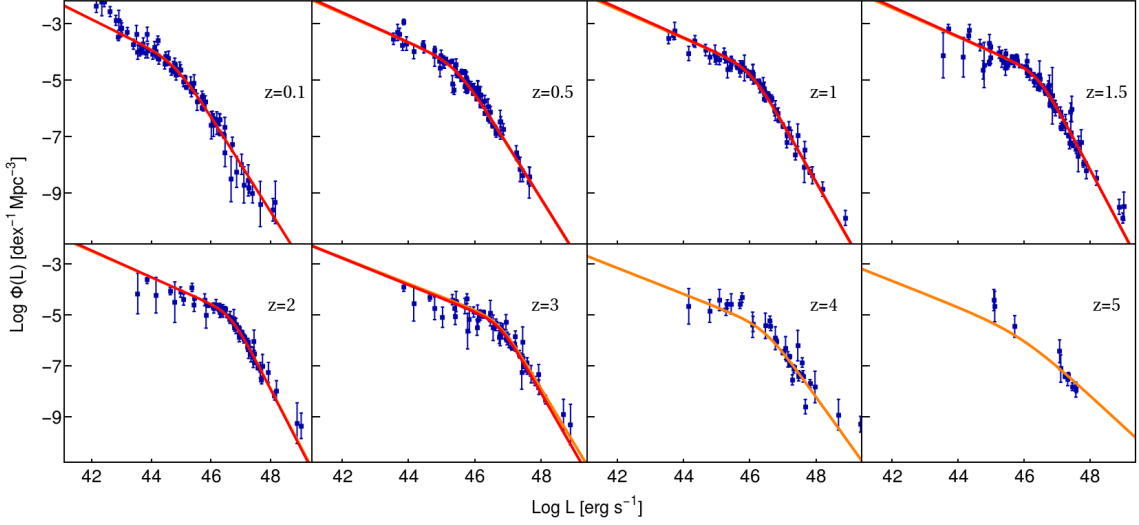


Figure 2.6: Fits to the bolometric dataset compiled in Hopkins et al. (2007), with the broken power law fit of Equation (1.6). The orange curve shows our “full fit” done with parametrization in Equation (2.26). Red curve shows fit in which redshift dependence of ϕ_{QLF}^* is set to be exactly the redshift dependence of ϕ_{SF}^* .

Tab. 2.2 — Best fits to QLF data from Hopkins et al. (2007)

parameter	“full fit”	with $\phi_{QLF}^* \propto \phi_{SF}^*$
c_0	-4.35 ± 0.06	-1.79 ± 0.04
c_1	0.059 ± 0.07	-
c_2	-3.2 ± 0.3	-
c_3	1.73 ± 0.2	-
d_0	44.67 ± 0.06	44.67 ± 0.04
d_1	4.02 ± 0.07	4.09 ± 0.09
d_2	3.78 ± 0.08	3.5 ± 0.07
d_3	-4.68 ± 0.1	-3.85 ± 0.07
d_4	-5.7 ± 0.2	-5.98 ± 0.15
e_0	0.5 ± 0.03	0.52 ± 0.04
f_0	1.64 ± 0.05	1.63 ± 0.06
f_1	0.54 ± 0.05	0.56 ± 0.06
f_2	-0.12 ± 0.01	-0.106 ± 0.03

quantitative difference in the quality of the fit. The values of the double power-law parameters in the smoothly varying “full-fit” are given in Table 2.2 and the fits are shown with orange curves in Figure 2.6.

The redshift dependences of ϕ_{QLF}^* and L^* are shown in the panels of Figure 2.7 and we discuss these results in the next section.

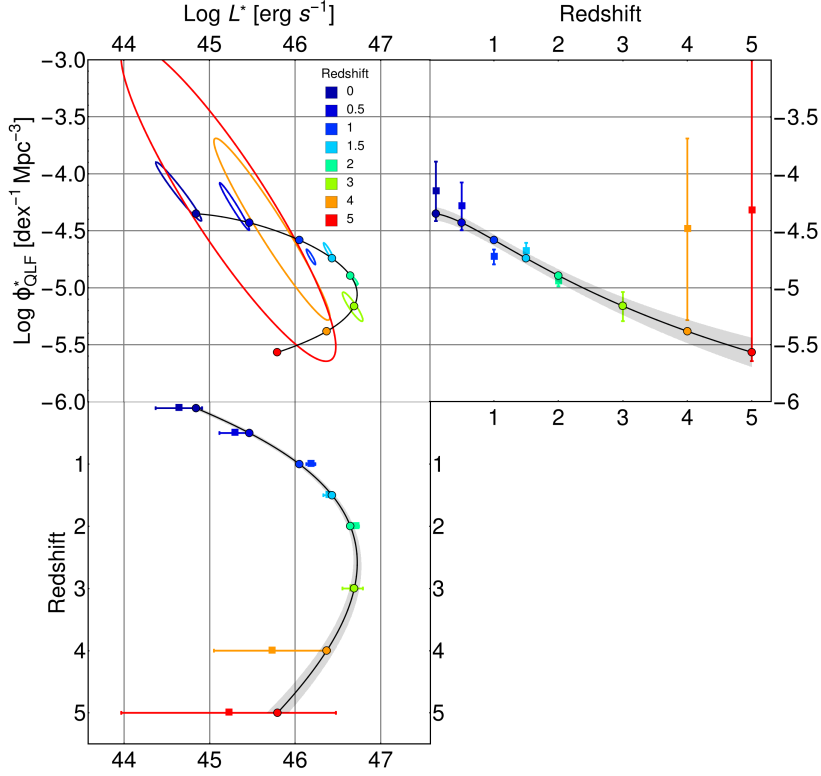


Figure 2.7: *Top left:* Redshift evolution of QLF parameters L^* and ϕ_{QLF}^* in our “full fit”. The contours are showing 1- σ allowed regions of parameter space for fits which were made with data at each individual redshift. The filled circles are the result of a global fit, for which the resulting QLF is shown in Figure 2.6. Uncertainty contours for this fit are not shown here for clarity. *Top right panel:* Projection showing explicitly the change of normalization ϕ_{QLF}^* with redshift. *Bottom left:* Projection showing explicitly change of L^* with redshift.

2.4 Results from comparing the evolution of the QLF and the galaxy mass function

2.4.1 The evolution of QLF normalization

The first result is that we notice a strong similarity between the observed redshift dependence of ϕ_{QLF}^* in Figure 2.7 and the observed ϕ_{SF}^* in Figure 2.5. Both drop by ~ 0.5 dex by redshift 2. Their relative evolution is explicitly compared in the bottom right panel

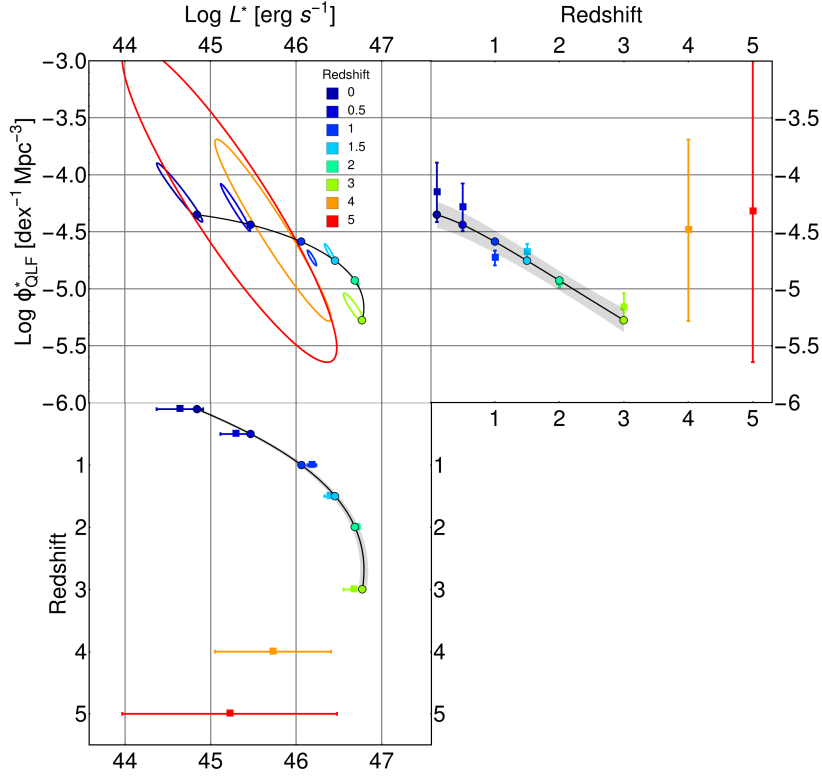


Figure 2.8: Same as Figure 2.7 for QLF fit at redshifts $z \leq 3$, in which we demanded that $\phi_{QLF}^* \propto \phi_{SF}^*$, i.e., that redshift dependence of these two variables is the same.

of Figure 2.9, which shows that a constant ratio between ϕ_{QLF}^* and ϕ_{SF}^* is perfectly consistent with the data. We note that the fact that the density normalization of the QLF decreases slowly with redshift has been seen in several previous analyses, for instance in the “luminosity and density evolution” model of Aird et al. (2010) and Aird et al. (2015), which have a 0.4 dex decrease in normalization between redshifts 0 and 2, Croom et al. (2009) shows a very similar decrease of normalization in his “luminosity and density evolution” model, while Hasinger et al. (2005) show a decrease in normalization of 0.5 dex between redshift 0.6 and 2.4. Here we highlight the striking similarity of this behaviour to the observed decline in ϕ_{SF}^* .

Referring back to Section 2.2.3, a constant ratio between ϕ_{QLF}^* and ϕ_{SF}^* implies a constant duty cycle, ξ_{λ}^* , of the black holes in the context of our convolution model. To explore this further, we now repeat the fitting procedure but set the evolution of ϕ_{QLF}^* to be exactly that of ϕ_{SF}^* , i.e., we impose that the evolution of the QLF normalization is exactly the same as the evolution of the normalization of star-forming galaxies in the redshift range where we have ϕ_{SF}^* available ($z < 3.5$), while the constant multiplicative

offset between these parameters remains a free parameter to be determined by the fitting procedure, i.e.,

$$\phi_{QLF}^* \propto \phi_{SF}^*. \quad (2.27)$$

The results of this fitting are given in Table 2.2 and the resulting QLF is shown with the red curve in Figure 2.6. It can be seen that the fit is extremely good, being only marginally worse than the full fit of Hopkins et al. (2007) ($\chi^2_{this\ work}/d.o.f. = 2.1$; $\chi^2_{Hopkins}/d.o.f. = 2.0$), both of which have a comparable number of free parameters. The main driver for the slightly worse fits in our work is the deviation of the fit from data for low luminosities at low redshifts. The data in this regime may be contaminated by contributions from the stellar populations of the hosts, as discussed in Hopkins et al. (2007).

The parameter evolution in this “ ϕ_{SF}^* -matched” fitting are shown as linked filled circles in Figure 2.8. As one can see, the points are typically situated on the edges of the individual 1- σ contours, which is to be expected given that $\chi^2/d.o.f. = 2.1$. We conclude that the change of normalization of the QLF is perfectly consistent with the change of normalization of the star-forming galaxy mass function over the entire redshift range for which we have the measurements of normalization of the star-forming galaxy mass function.

The fact that as far as we can tell the $\phi_{SF}^*(z)$ and $\phi_{QLF}^*(z)$ track each other throughout cosmic time (at least since $z \sim 3$, and quite possibly since earlier epochs also, is an interesting result. It means that the factor which is connecting these two quantities, which in the convolution model is ξ_λ^* (slightly modified by Δ_ϕ), remains constant.

As we have discussed above, this suggests that the general “duty cycle”, f_d , stays constant over cosmic time (e.g., Equations (2.6) and (2.9))(see also Conroy & White, 2013). Clearly, this would not be the case for other definitions of “duty cycle” that are based, for instance, on the fraction of black holes radiating above some luminosity or accreting above some Eddington ratio, if λ^* or L^* evolves with time, as it does (see below), but we believe that our definition of duty cycle is the most natural one (as discussed above).

2.4.2 The evolution of characteristic QLF luminosity

The other striking feature of the quasar luminosity function is the strong redshift evolution of L^* , which increases by almost two orders of magnitude back to $z \sim 2$. At higher redshifts, the $L^*(z)$ certainly flattens out and probably declines, although this cannot be

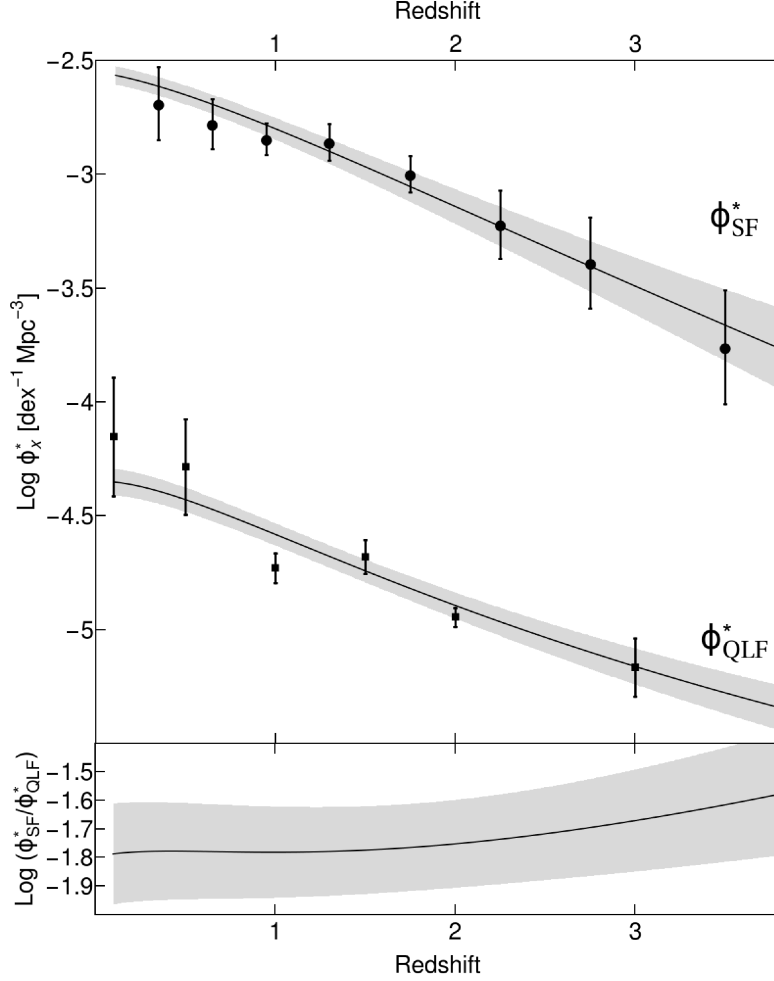


Figure 2.9: *Top:* Comparison of the redshift evolution of the normalization of star-forming galaxy mass function and the normalization of quasar luminosity function. Black circles show the values of ϕ_{SF}^* which were determined by fitting the data from Ilbert et al. (2013) at a single redshift. Black squares show the values of ϕ_{QLF}^* which were determined by fitting the QLF data at a single redshift and are also shown in Figures 2.7 and 2.8. *Bottom:* Redshift evolution of the ϕ_{SF}^*/ϕ_{QLF}^* . This ratio is remarkably constant over redshift range for which data is available.

established at high significance. The strong initial rise with redshift is seen independent of whether we use the full fit, or the fit constrained to have $\phi_{SF}^*(z)$ and $\phi_{QLF}^*(z)$ tracking each other.

In our convolution model, the steep rise in $L^*(z)$ (see Equation (2.11)) could have been caused in principle by one or more of (a) an evolution of λ^* , (b) an evolution of M^* of the

galaxy mass function or (c) an evolution of the mass ratio m_{bh}/m_* .

As discussed in Section 2.3.1, we know that the characteristic M^* of the galaxy population does not change, especially in the redshift range where increase of L^* is most prominent ($z \leq 2$), so case (b) will not apply. There is however complete degeneracy between cases (a) and (c), i.e., the distribution of specific accretion rates of AGN and the black hole to stellar mass ratio. This is clear in Equation (2.11) and has been pointed out also by e.g., [Veale et al. \(2014\)](#). This degeneracy can only be broken if we have information on the black hole masses of the AGN. We will explore this in the next section.

2.5 Testing the model with black hole mass data

2.5.1 The quasar mass-luminosity plane

In this part of the thesis we will compare predictions of how the black hole mass-luminosity plane of broad-line AGN should be populated in our model, and compare these with SDSS data. After creating a mock sample of star-forming galaxies in an SDSS volume, we will populate them with black holes assuming different redshift-dependent m_{bh}/m_* scaling relations and an assumed scatter. We will then assign Eddington ratios from the evolving $\xi(\lambda, z)$ distribution and apply an obscuration prescription from [Hopkins et al. \(2007\)](#). These two functions are chosen so that the QLF is reproduced as in the previous section: in other words the redshift evolution in m_{bh}/m_* and the redshift evolution in λ^* will be required to produce the observed evolution in the QLF L^* .

For the observational distribution, we use data from two observational studies ([Shen et al., 2011](#); [Trakhtenbrot & Netzer, 2012](#)) to show that our results do not depend critically on the data choice and to give the reader a graphical impression of the uncertainties involved in this kind of measurement. By comparing our mock data with the observed distribution we will be able to see which combination of redshift-dependent m_{bh}/m_* and $\xi(\lambda, z)$ best reproduces the observational data. We take into account the obscuration factor and the differences in bolometric correction between different works and apply the same bolometric correction to the data and model (namely the one used in [Shen et al., 2011](#)) to make them directly comparable.

By using this mock sample approach we can fully account for biases introduced by the luminosity-selection of the quasar samples. We recreate data only up to $z = 2$, as black hole mass estimates for higher redshifts are based on the broad C IV $\lambda 1549$ emission line, which was shown to be far less reliable for these purposes, as discussed in Introduction.

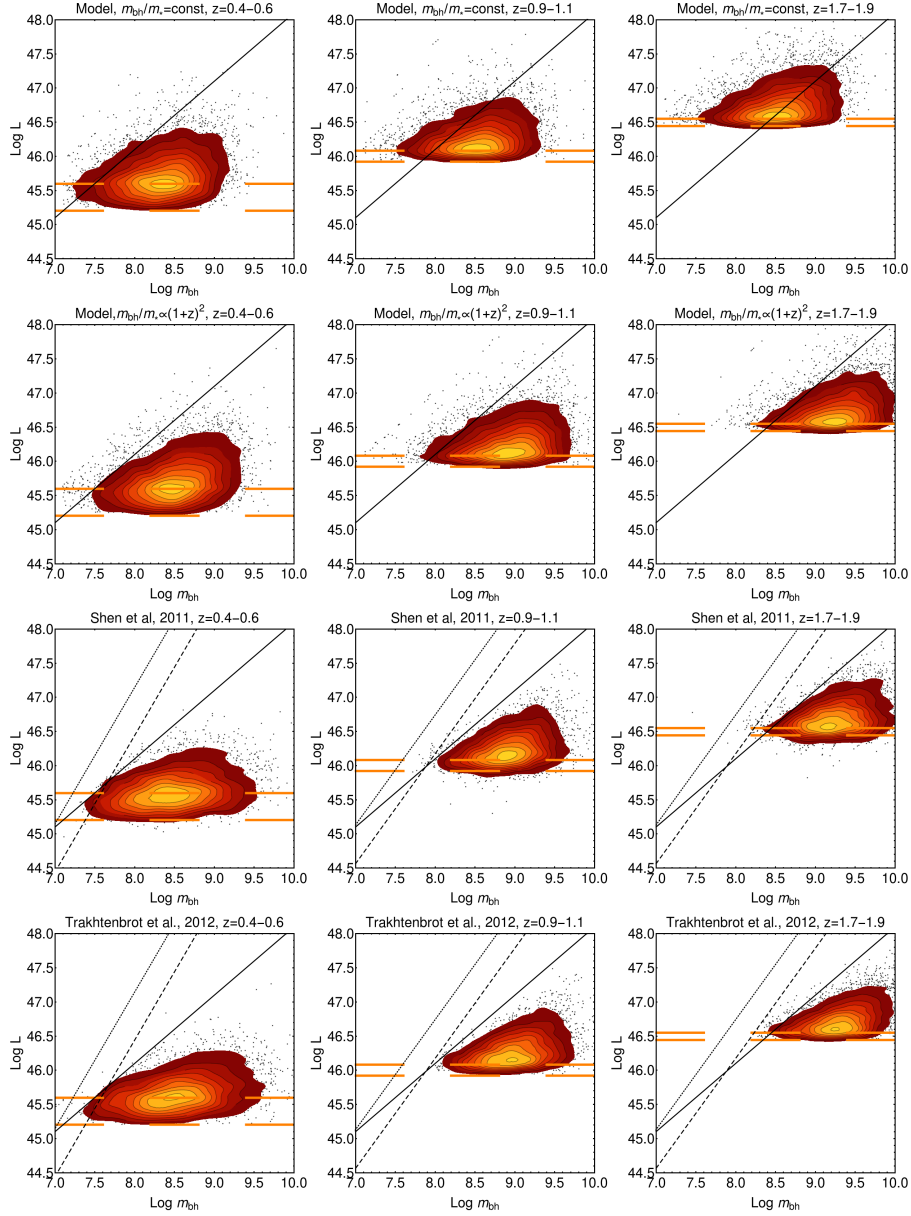


Figure 2.10: Mass-luminosity plane shown in 3 representative redshift bins. Our model with assumed non-evolving relation $m_{bh}/m_* = 10^{-2.8}$ is in the top row and our model with assumed evolving relation $m_{bh}/m_* = 10^{-3}(1+z)^2$ is in the row below. Observational data from Shen et al. (2011) and Trakhtenbrot & Netzer (2012) are shown in bottom two rows. The thick black line is the Eddington limit, dashed orange lines show the calculated luminosity selection limit for lowest and highest redshift in the bin. The dotted and dashed black lines represent FWHM=1000 km/s and 1500 km/s, respectively, and are shown here to indicate which objects could be missed in observations because of FWHM limit in quasar selection. Contours are set at 10%, 20% etc. values of estimated probability distribution of objects. Outermost objects are represented as individual dots.

We first show in the topmost panels of the Figure 2.10 the modelled distribution of quasars in the black hole mass-luminosity (m_{bh}, L) plane in three representative redshift bins if we assume a redshift independent m_{bh}/m_* with the standard value of $m_{bh}/m_* \approx 10^{-2.8}$. We introduce a log-normal scatter in this relationship of 0.5 dex to account for scatter in m_{bh}/m_* relationship. The solid diagonal line indicates the Eddington limit ($\lambda = 1$).

The data from Shen et al. (2011) and Trakhtenbrot & Netzer (2012) are plotted in the two bottom rows of panels in Figure 2.10. In these panels, the diagonal dashed and dotted lines indicate the locus of black hole masses for two constant FWHM (of 1000 km/s and 1500 km/s respectively) of the emission lines ($H\beta$ and $MgII$) that were used to infer the black hole masses. Systems of lower FWHM will not appear in the samples, e.g., the limit used in Shen et al. (2011) is set at 1200 km/s.

We see that there is good agreement of model with the data at low redshifts, which a consequence of the choosing a suitable m_{bh}/m_* ratio. We see, however, that a non-evolving m_{bh}/m_* relation produces far too many objects with masses that are too small or, equivalently, which have very high Eddington ratios, with around 50% being super-Eddington in the final redshift bin, while only around 2% of objects are super-Eddington in the data. This is a simple consequence of the fact that L^* is much higher then locally and is a reflection of the high λ^* implied for an unevolving m_{bh}/m_* relation shown in Figure 2.19.

We note that the comparison could not be expected to be perfect because our data is constrained to reproduce the QLF from Hopkins et al. (2007); although SDSS data and the optical QLF is the main contributor to the Hopkins QLF in this luminosity range, there are small contributions from other surveys as well as slightly different bolometric and obscuration corrections which will induce small differences. Nevertheless, the disagreement with a non-evolving m_{bh}/m_* ratio is too large to be due to this.

A much better agreement is obtained (second row of Figure 2.10) if we adopt an evolving m_{bh}/m_* relation. We adopt as a heuristic example the form $m_{bh}/m_* \propto (1+z)^n$ with $n = 2$. The agreement with the observed distribution is considerably better and there are now far fewer objects crossing the Eddington limit ($\sim 3\%$) at high redshifts. This means that the observed $\sim (1+z)^4$ increase in L^* back to $z \sim 2$ would be due to an equal split between a $(1+z)^2$ change in m_{bh}/m_* and a $(1+z)^2$ change in characteristic Eddington ratio λ^* , remembering that these two changes are degenerate in our convolution model without the m_{bh}/m_* data of Figure 2.10.

Finally we note that, quite independently of any assumptions about m_{bh}/m_* , our convolution model naturally recreates the apparent “sub-Eddington boundary” that has been

emphasized by [Steinhardt & Elvis \(2010\)](#), by which we mean the flat upper envelope. This refers to the fact that at all redshifts there seems to be a lack of objects at high masses close to the Eddington limit, which can also be seen in Figure 16 of [Trakhtenbrot & Netzer \(2012\)](#). This can be observed in the Figure 2.10 where the upper contours of the red regions have slopes that are noticeably shallower than the 45 degree slope that corresponds to a constant Eddington ratio, thereby giving the impression of an absence of high luminosity high λ sources.

This behaviour is quite counter-intuitive, and was interpreted by [Steinhardt & Elvis \(2010\)](#) as being caused by some new physical effect that somehow limits accretion onto more luminous quasars. Various authors have proposed alterations to the measurement methods in mass-luminosity plane which could reduce or eliminate this effect (e.g., [Rafiee & Hall, 2011a](#); [Rafiee & Hall, 2011b](#)). We show instead that this behaviour is actually expected from the convolution model presented in this chapter and is primarily a consequence of how the data is plotted!

We commented earlier in Section 2.2.5 that while the typical black hole mass increases with luminosity in our convolution model, it does so sub-linearly, so that the “typical” Eddington ratio must also increase with luminosity. This can be seen also in these plots: the ridge line that is defined by the peak in the mass distribution at a given L is indeed steeper than the 45 degree line of constant Eddington ratio, which is why the shallower slope of the boundary defined by the contours is so counter-intuitive. However, because the number of more massive black holes falls very steeply with mass, because of the decline of the galactic mass function above M^* , the contours of constant surface density, given by the contours in the plots in Figure 2.10 and in the [Steinhardt & Elvis \(2010\)](#) analysis, are actually shallower than the 45 degree line.

This is more clearly seen in Figure 2.11 were we show the appearance of our full sample, before the application of the SDSS luminosity cut. At lower luminosities the effect gets more and more pronounced and we expect that deeper surveys of a given area would find more super-Eddington objects at small masses.

We emphasize that the reproduction of the [Steinhardt & Elvis \(2010\)](#) effect in Figure 2.10 is achieved within our convolution model with an Eddington ratio distribution $\xi(\lambda)$ that is completely *independent* of black hole mass. The effect noted by [Steinhardt & Elvis \(2010\)](#) would not be seen (in our model) if the distribution of points in the (m_{bh}, L) plane was normalized to the total number of black holes (in star-forming galaxies) at a given *mass*, which is, of course, unfortunately not observable. Our explanation for the sub-Eddington boundary in [Steinhardt & Elvis \(2010\)](#) is therefore a kind of “plotting bias” arising from how the data is plotted, rather than a “selection effect” per se, coming through the construction of the sample via, e.g., emission line widths.

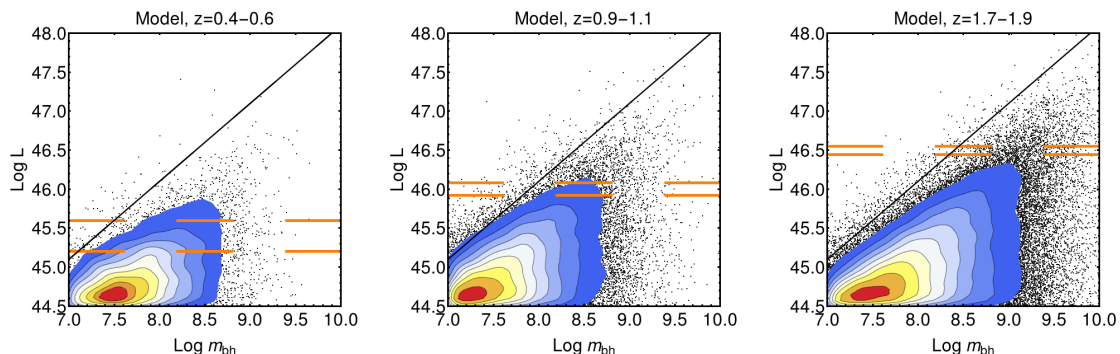


Figure 2.11: Full sample from our model, before applying the luminosity cuts to produce the second row in Figure 2.10. For clarity, only one out of every 25 points is shown.

2.5.2 Establishing the m_{bh}/m_* correlation in quenched systems

In this section we show how it is possible to reproduce the observed tight correlation between m_{bh}/m_* in the local Universe even if the black hole to stellar mass relation in the star-forming galaxies is strongly evolving (see also Croton, 2006; Hopkins et al., 2006a). We first consider the correlation between the black hole mass and the stellar mass in quenched objects. Given that we do not work with different galaxy component in this simple model, we initially do not consider the separation of the galaxy mass in the bulge/disk component, i.e., we treat the total galaxy mass at the moment of the quenching as an observable quantity in the local Universe. In the following section we will also explicitly consider, using the model from Lilly & Carollo (2016), m_{bh}/m_{bulge} relation in the local Universe.

For this analysis, we use results from the simple galaxy evolution model of Birrer et al. (2014) to construct a set of evolving star-forming galaxies and their quenched descendants. The details of the Birrer et al. (2014) model are not important for the present purpose since it reproduces well the overall evolution of the galaxy population, which is all that we require here.

For each quenched galaxy seen in the model at the present epoch, we know the mass and redshift at which it quenched and can therefore compute the black hole mass from the adopted redshift-dependent m_{bh}/m_* relation for (star-forming) galaxies, adding also the adopted scatter. We assume that there is no stellar mass growth after quenching and that there is no central SMBH mass growth after quenching

After this procedure we are left with a mock sample of quenched galaxies, with their

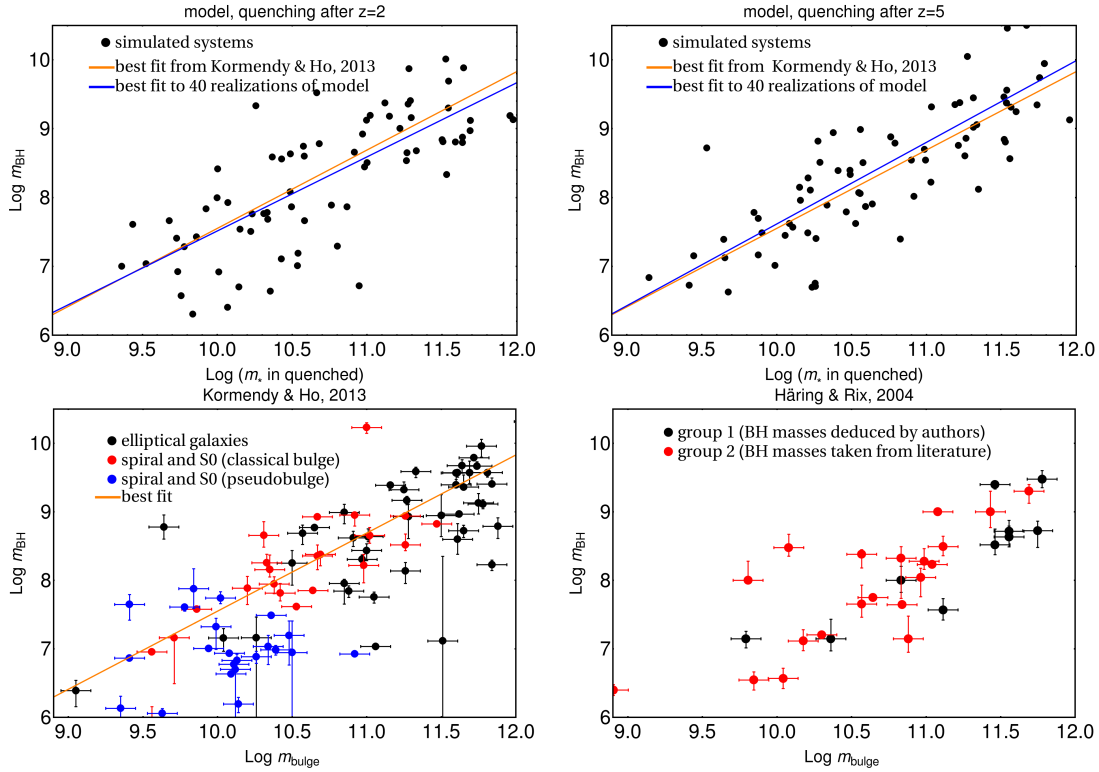


Figure 2.12: *Top left:* Resulting m_{bh}/m_* relation in quenched galaxy systems today, if we only take into account systems that have quenched after $z = 2$. Orange line shows best fit quoted in [Kormendy & Ho \(2013\)](#). Blue line shows best fit to the data generated from 40 realizations of the model. *Top right:* Resulting m_{bh}/m_* relation in quenched systems today, for full range of quenching history ($z < 5$). Orange and blue line are generated in same way as in previous panel. Merging, uncertain evolution in m_{bh}/m_* relation and errors in estimated rate of quenching at high redshift could bias this result, as discussed in text. *Bottom left:* Measured m_{bh}/m_{bulge} by [Kormendy & Ho \(2013\)](#). Orange line shows again best fit quoted in [Kormendy & Ho \(2013\)](#). *Bottom right:* Measured m_{bh}/m_{bulge} by [Häring & Rix \(2004\)](#).

black hole masses known, after which we can account for sample selection effects. This is not trivial, as measurements of masses of black holes are from heterogeneous sources and no single luminosity or other cut is possible.

We therefore decided to create an empirical selection in galaxy mass so that the distribution of galaxy masses in the mock sample broadly matches that of the passive early type galaxies which have had their SMBH mass measured. We show results for two situations, where we first only consider galaxies that quenched after $z = 2$ and then include all galaxies that have quenched since $z = 5$. We differentiate between these two cases since we expect merging, which is not explicitly accounted for here, to have a larger impact for galaxies that quench earlier, and because the assumed mass ratio scaling, which we think is reasonable approximation (see above) at redshift $z < 2$, may break down at higher red-

shifts. When we ignore quenching at $2 < z < 5$, we are losing only about 10% of today's quenched population, but the model is on a much firmer footing.

We have fitted the simulated data, derived from 40 random realizations of the model, with a relation of the form

$$100 \left(\frac{m_{bh}}{m_{*,quench}} \right) = a \cdot \left(\frac{m_{*,quench}}{10^{11} M_{\odot}} \right)^b \quad (2.28)$$

by regressing the black hole mass on the stellar mass, and compute the scatter of the simulated galaxies around this relation. We derive values of $(a, b) = (0.40, 0.09)$ and a scatter of 0.53 dex for the case of quenching only from $z=2$, and values of $(a, b) = (0.63, 0.18)$ with scatter of 0.6 dex for the case of quenching from $z=5$. These values should be compared with the observed values of $(a, b) = (0.49_{-0.05}^{+0.06}, 0.14 \pm 0.08)$ and a intrinsic scatter of 0.29 dex derived in [Kormendy & Ho \(2013\)](#). While the predicted scatter appears to be larger than observed, subsequent merging of galaxies, that has not been modelled here, will act to reduce the scatter ([Hirschmann et al., 2010](#), [Jahnke & Macciò, 2011](#)). Additionally, we are here considering the total galaxy mass, and we will show in the following subsection that scatter is smaller when considering only the bulge component of galaxies.

The origin of $m_{bh}/m_{*,quench}$ relation is the underlying m_{bh}/m_* relation in star-forming galaxies assumed in the model, with added scatter due to the fact that galaxies of a given stellar mass today have quenched at various redshifts and, for a given stellar mass, the spread in black hole masses is amplified by spread in the quenching redshifts. The mean of the m_{bh}/m_* relation in quenched objects is positioned roughly at the value of m_{bh}/m_* at the mean redshift of quenching at that mass, which is $z \sim 1 - 1.5$ over a wide range of galaxy masses.

It is interesting to note that objects that have quenched more recently would be expected on average to have a lower m_{bh}/m_* value, because of the evolution in m_{bh}/m_* . It is possible that these recently quenched galaxies could be associated with pseudo-bulges instead of bulges. [Kormendy & Ho \(2013\)](#) has indeed argued that pseudo-bulges do have a lower m_{bh}/m_{bulge} ratio.

We also note in passing that if there is a trend for the typical quenching redshift to increase with increasing stellar mass (e.g., because of interplay of mass and environment quenching, [Peng et al., 2010](#)) then this would introduce a tilt in the local m_{bh}/m_* relation ($b \neq 0$) even though the input m_{bh}/m_* in star-forming galaxies was perfectly linear.

The link with quenching redshift then prompts another interesting point. There is very good evidence that the sizes of galaxies, at a given mass, are smaller at high redshift ([Daddi et al., 2005](#); [Newman et al., 2012](#); [Carollo et al., 2013](#); [Shankar et al., 2013](#)). We

would therefore expect, through virial arguments, that the velocity dispersions, at a given mass, would also be higher. This has been directly observed in a few cases (e.g., [van Dokkum et al. 2014](#)). For analytic simplicity, we assume that the scale radius of galaxies scales as $(1+z)$ so that the usual Faber-Jackson-type scaling relation would be expected to evolve as

$$m_* \propto \sigma^4 (1+z)^{-2}. \quad (2.29)$$

If m_{bh}/m_* scales as $(1+z)^2$, as we have been exploring in this part of the thesis, then this naturally produces an $m_{bh} - \sigma$ relation that is *independent* of redshift.

This has two implications: first, we would not expect to see any significant evolution in the observed $m_{bh} - \sigma$ relation (see [Shen et al., 2015](#) for observational evidence). Second, we would expect the present-day $m_{bh} - \sigma$ relation for passive galaxies to be tighter than the $m_{bh} - m_*$ relation, because of the aforementioned broadening of the latter from the range of z_{quench} . We will explore this further, in the context of m_{bh}/m_{bulge} relation, in the next subsection.

We stress that this tighter $m_{bh} - \sigma$ relation would be present even if the velocity dispersion is not playing a direct role in the growth of black holes. Of course, it is also possible that the evolution in the m_{bh}/m_* is in fact *caused* by the constancy of an underlying $m_{bh} - \sigma$ causal connection. On the other hand, there could well be other causes for m_{bh}/m_* to evolve as $(1+z)^2$, in which case the tight $m_{bh} - \sigma$ relation would simply be a coincidence.

2.5.3 The m_{bh}/m_{bulge} correlation in quenched systems

In this section we will further expand our analysis of the scatter in the relation connecting galaxy properties and black holes masses in the quenched objects. We have already pointed out that the size evolution of galaxies will act to reduce scatter in the $m_{bh} - \sigma$ relationship, compared to the m_{bh}/m_* relation. We now consider the scatter in the m_{bh}/m_{bulge} relation.

How the bulges are formed and what dynamical processes are drivers of the bulge formation is still an open question and a topic of research (e.g., [Noguchi, 1999](#); [Steinmetz & Navarro, 2002](#); [Kormendy & Kennicutt, 2004](#); [Dekel et al., 2009](#)). However, phenomenological approach which we have been using so far, can provide some insights here as well. [Lilly & Carollo \(2016\)](#) studied correlation between sSFR and internal structure of galaxies. Their simple model uses observed evolution of the size-mass relation for star-forming galaxies to model build-up and radial dependence of stellar mass in galaxies. As galaxies grow along the Main Sequence the newly created stars are distributed in an azimuthally

symmetric exponential distribution with a scale length, h , which has a redshift dependence:

$$h(z) \propto (1+z)^{-1}. \quad (2.30)$$

For a typical galaxy at a given redshift and mass, the outer edges follow the exponential profile, while the inner parts have profile which rises above exponential due to the star formation which has happened at earlier epochs. This excess of the mass in the central parts of the galaxies can be operationally associated with the bulge component. In this model galaxies which have quenched at the earlier times have much denser core, due to scale length being smaller at earlier times, and a larger fraction of these galaxies can be identified as a “bulge”. This very simple model is quite successful in reproducing observed correlation between quenched fraction of galaxies and their mean surface mass densities, even though the quenching itself follows the prescription from Peng et al. (2010), i.e., it is only dependent on the mass and the environment, and it is not connected, in a direct way, with the surface mass density.

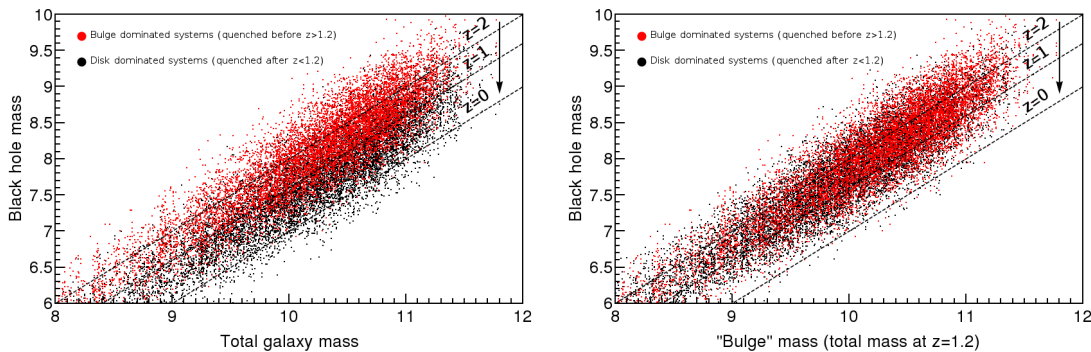


Figure 2.13: Correlation of black hole mass with total and bulge mass in quenched galaxies. In the left panel we show expected m_{bh}/m_* relation in quenched galaxies. We separate the population in the “bulge dominated systems”, i.e., the galaxies which have quenched before $z = 1.2$ which are shown in red and “disk dominated systems”, i.e., the galaxies which have quenched after $z = 1.2$, which are shown in black. We also show, in the dashed lines, evolution of the typical m_{bh}/m_* ratio with redshift. In the right panel we show expected m_{bh}/m_{bulge} relation in quenched galaxies. Bulge mass has been identified as a total stellar mass of a galaxy at $z = 1.2$.

Following this approach and to illustrate qualitatively the scatter expected in the m_{bh}/m_{bulge} relation, in the following analysis we simply identify, for each galaxy, the stellar mass which was created before $z > 1.2$ as bulge. More involved and no doubt more realistic scenario could be surely implemented but we use this simplest assumption following the spirit of our phenomenological modelling and to transparently illustrate the main effect. In Figure 2.13 we show our results. Comparison of the two panels clearly shows that the observed scatter is reduced when considering m_{bh}/m_{bulge} relation. This is because the “added scatter”, which is caused by the redshift evolution of m_{bh}/m_* relation, is virtually eliminated when considering just the bulge parts of the galaxies, which have all been built-up at higher redshifts. m_{bh}/m_{bulge} relation in quenched galaxies has therefore the scatter which is virtually the same as the intrinsic scatter of the m_{bh}/m_* relation in star-forming galaxies. We show also calculation of scatter as function of either total or

bulge mass in Figure 2.14. For this particular calculation we used intrinsic scatter of 0.3 dex - in this way contribution of the intrinsic scatter and the mass ratio evolution to the total observed scatter are of comparable magnitude.

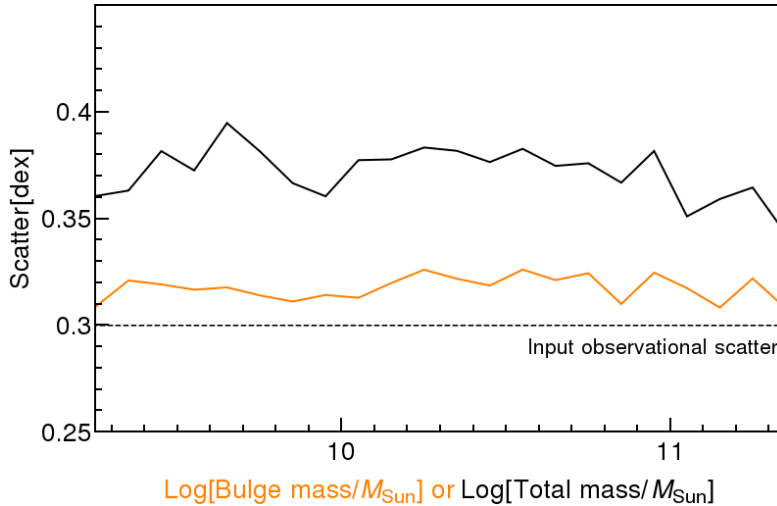


Figure 2.14: Scatter in the black hole - galaxy relation as a function total mass (in black) or as a function of “bulge” mass (in orange). Thin dashed line show the intrinsic scatter, which was set at 0.3 dex for this particular analysis. m_{bh}/m_{bulge} relation shows less scatter than the m_{bh}/m_* relation. This is because m_{bh}/m_{bulge} relation effectively eliminates the contribution of the m_{bh}/m_* evolution to the total scatter, which is present in the m_{bh}/m_* relation.

This analysis shows how the tight correlation between m_{bh}/m_{bulge} does not necessarily imply that there is deep causal connection between black hole and its bulge. Even though the intrinsic correlation in our model was between the black hole and the total stellar mass, the interplay between the sSFR evolution, the galaxy size evolution, and the m_{bh}/m_* evolution can mimic the tight m_{bh}/m_{bulge} relation. Of course, in the similar fashion as in the previous section, this analysis can not recover which physical process is the primary driver for correlations observed in the Universe. One could also conduct the analysis “in reverse”, by arguing that the m_{bh}/m_{bulge} in quenched galaxies is the most fundamental correlation and derive the mass quenching law, which we use as a premise.

2.5.4 Quenched galaxies as a function of galaxy and black hole mass

Following the discussion about the possibly misleading conclusions which can be derived from the data describing black hole - galaxy properties, in this section we show a similar effect when considering black hole mass and quenched fraction of galaxies. In the previous section we have briefly explained the basic assumption and ingredients of the model presented in Lilly & Carollo (2016). As we mentioned, the quenching law adopted in that work is the same that we discussed in Section 1.2.2, i.e., it is a function only of the galaxy mass and the environment. Yet, it successfully reproduces the observed correlation

between the quenching fraction and properties of the central regions of galaxies, which was the consequence of the size evolution in star-forming galaxies and the sSFR evolution (and therefore, as explained in Section 1.2.2, also the evolution in the quenching rate). We therefore expect a similar effect, in our model, when we look at the quenched fraction as a function of stellar mass and the black hole mass. We note that, if one uses the results from previous section in which we argued for tight connection between the black hole mass and the bulge mass, the reader can replace m_{bh} with m_{bulge} in what follows. We show our prediction for quenched fraction in Figure 2.15.

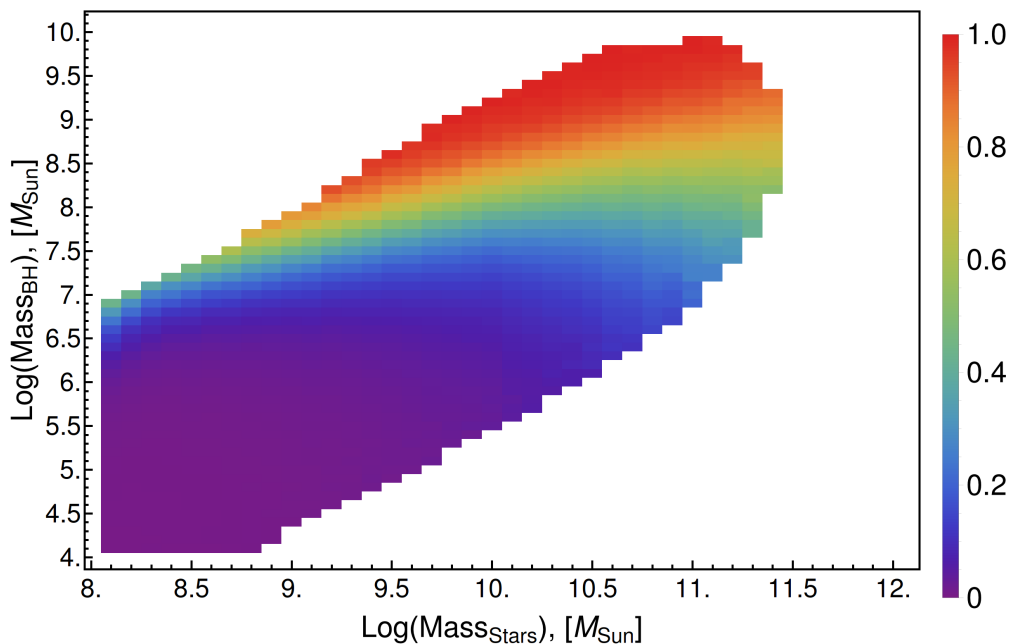


Figure 2.15: Quenched fraction as a function of stellar and black hole mass. The colour denotes the expected quenched fraction as shown on the label at the right hand side of the plot. Quenched fraction increases as a function of black hole mass, but this is due to the evolution of the m_{bh}/m_* ratio and the cosmic quenching rate. The black hole mass is not directly connected with the quenching in this model.

We note several features of this plot. First of all, if we concentrate ourselves solely on the stellar mass, we see the fraction of quenched objects as a function of stellar mass is rising. This is the trivial consequence of the quenching law which is galaxy mass dependent and reproduces star-forming and quenched galaxy mass functions in the local Universe which we discussed in Section 1.2.2.

Different view is to consider the quenched fraction as a function of black hole mass. We see that the quenched fraction rises suddenly around $10^8 M_\odot$, almost irrespective of the galaxy mass. This changes happens even though black hole mass was not directly connected with quenching of star-formation. The fact that the fraction of quenched objects is seemingly strongly related with black hole mass is consequence of the interplay of (i) rising quenched fraction as a function of galaxy mass, (ii) evolution of the quenched population, and (iii) m_{bh}/m_* ratio evolution.

For an example, consider all galaxies having similar stellar mass, e.g., $10^{10} M_{\odot}$. Galaxies which have low black hole mass, below $10^7 M_{\odot}$, are all likely to be star-forming as this ratio, because $m_{bh}/m_* = 10^{-3}$ is the typical ratio for the galaxies which are star-forming today. As the black hole mass rises we are probing higher and higher m_{bh}/m_* ratios which are tracking galaxies which have quenched at higher and higher redshifts and the number of currently star-forming galaxies which are scattered to these high ratios keeps dropping. Therefore, the fraction of quenched galaxies, at given galaxy mass, keeps rising with the black hole mass. On the other hand, given that fraction of quenched galaxies rises with stellar mass, the m_{bh}/m_* ratio needed to achieve the same fraction of quenched objects keeps changing in a way that constant quenching fraction roughly corresponds to the constant black hole mass. As discussed previously in Sections 2.5.2 and 2.5.3, this analysis shows how dangerous it is to associate the the correlations seen in the data with the causal relationship (e.g., [Bluck et al., 2014](#)).

We will return to the topic of connection between the m_{bh}/m_* ratio in star-forming and quenched galaxies when we discuss observation at higher redshifts in Section 2.6.1.

2.5.5 m_{bh}/m_* in AGN in the local Universe

Finally, we turn to estimates of the m_{bh}/m_* relations for AGN in the local Universe, where it is possible to estimate independently the mass of the galaxy that is hosting an optically active AGN. [Matsuoka et al. \(2014\)](#) made a careful decomposition into nuclear and host contributions of the images of $z < 0.6$ quasars in the SDSS Stripe 82. They found that the quasars are predominately hosted in massive star-forming galaxies, with relatively large m_{bh}/m_* ratios of around $10^{-2.5}$. [Matsuoka et al. \(2014\)](#) were aware of the possibility that selection effects could bias this value upwards but could not estimate their magnitude. We can now use our model to examine the expected size of this bias.

To do this we simulate sources within the same sky area as Stripe 82 and recreate objects above the AGN luminosity cut that would have been selected for quasar spectroscopy in the SDSS sample, with scatter of 0.4 dex. The results are shown in Figure 2.16, represented in the same way as in the original paper. We see that the observed quasars will have m_{bh}/m_* ratios that are indeed much higher than the mean value in the underlying sample, which is indicated by the shaded region in the figure.

Finally, we notice that even though we inserted $m_{bh}/m_* \propto (1+z)^2$ redshift evolution in our model, this evolution would be quite hard to detect in the sample of [Matsuoka et al. \(2014\)](#), owing to the large spread of points and the selection biases connected with such a study. Nevertheless, we do still see a slight change in the mean values of the simulated sample that is not seen in the actual data. We discuss evolution of the mass ratio at these low redshifts further in Section 3.1.1.

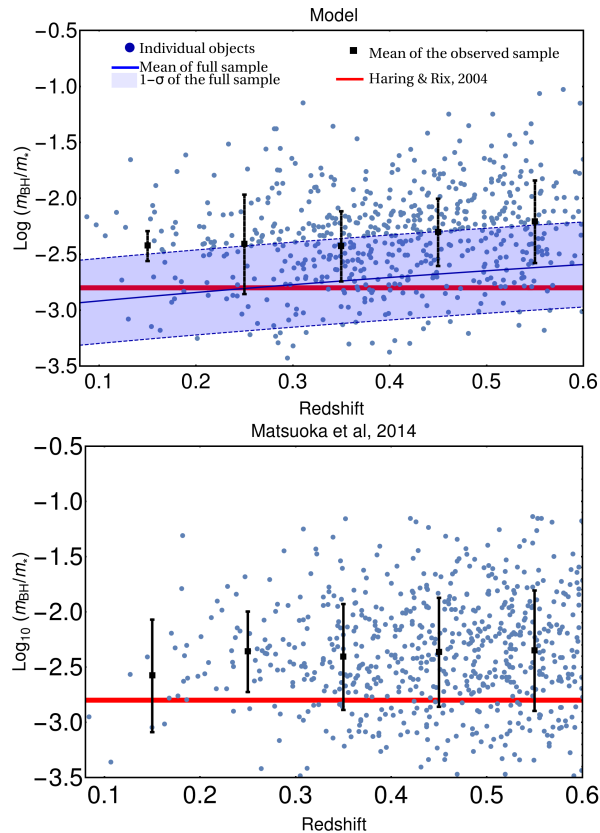


Figure 2.16: *Top panel:* Simulated observation of m_{bh}/m_* relation in Stripe 82, mimicking analysis of Matsuoka et al. (2014). Blue line shows mean m_{bh}/m_* relation in full sample (before luminosity cut was applied), while the shaded area shows $1 - \sigma$ spread around mean relation in our model. The black line shows mean and spread of distribution of points in 0.1 redshift slices. Red line is set to $10^{-2.8}$, which is approximately local relation from Haring & Rix (2004). *Bottom panel:* original data from Matsuoka et al. (2014).

2.6 Discussion

In the preceding sections of this thesis we have developed a simple generic model for obtaining the evolving AGN luminosity function from a convolution of the evolving galaxy mass function. This generic model makes testable predictions for quantities such as the shape of the mass distribution of host galaxies as a function of AGN luminosity and allows us to derive quantitative connections between the parameters describing the galaxy mass function and the AGN QLF. On the basis of these, we can derive powerful statements about the duty cycle of AGN. We then showed, in the framework of this general model, that a redshift-dependent m_{bh}/m_* and Eddington ratio distribution, $\xi(\lambda)$, successfully reproduces the observed quasar luminosity function (by construction) and also reproduces observations of the distribution of quasars in the (m_{bh}, L) plane, the black hole to bulge mass relation of quenched galaxies and measurements of m_{bh}/m_* for low redshift AGN. In

this Discussion, we develop further some of the astrophysical implications of the preceding results.

2.6.1 Comparing m_{bh}/m_* redshift evolution in active and quenched systems

It is important to appreciate that a quite rapid evolution in m_{bh}/m_* in *active* (star-forming) AGN systems does not imply an equally rapid evolution of m_{bh}/m_* in the *quenched* systems. This is because, when we are observing quenched systems, we are effectively observing the integrated population that was produced at earlier epochs. To illustrate this, we perform a simple heuristic exercise in which we determine m_{bh}/m_* in quenched systems at given epoch, assuming as above that quenching started at redshift 2. We make the same assumptions as before, namely that there is no stellar or black hole mass growth after quenching.

Our results are shown in Figure 2.17. Even though star-forming galaxies have changed their black-hole to stellar mass ratio by almost a factor of 10 from redshift $z \sim 2$ to today, the evolution in this ratio for *quenched* systems is much milder, more like a factor of 3 or even less (0.4 dex), simply because the quenched population includes galaxies that have quenched much earlier. This means that the redshift evolution in m_{bh}/m_* for quenched systems will always be much milder than the evolution in this quantity in active systems.

The distinction between active and passive populations becomes even more important if observational studies compare actively accreting systems at high redshift with data on the quiescent population at low redshift. This is unfortunately quite common practice (e.g., Jahnke et al., 2009; Decarli et al., 2010; Merloni et al., 2010; Bennert et al., 2011; Schramm & Silverman, 2013; Schulze et al., 2015), because of the current practicalities of observations. We stress that this approach automatically produces weaker evolution since neither m_{bh} nor m_* will have changed once a given object becomes inactive (i.e., passive/quenched). It is therefore clear that the mean m_{bh}/m_* relation in the quenched systems will reflect the mass ratio in the star-forming galaxies at the much earlier epochs when those galaxies actually quenched (as already discussed above). For the local population, this is typically around $z \sim 1-1.5$.

Clearly, if we compare the m_{bh}/m_* of star forming systems at $z \sim 1-1.5$ to the m_{bh}/m_* ratio of passive galaxies seen today that quenched at $z \sim 1-1.5$, then we would expect to see no change in m_{bh}/m_* , even if this ratio had changed a lot within the actively accreting population! Of course, if the high redshift active systems are luminosity-selected then their m_{bh}/m_* ratio will likely have been biased to higher values than the underlying population through the “Lauer effect” discussed in Section 2.2.5, which goes in the opposite direction (as shown by the parallel black lines in Figure 2.17). This figure shows that if Nature has

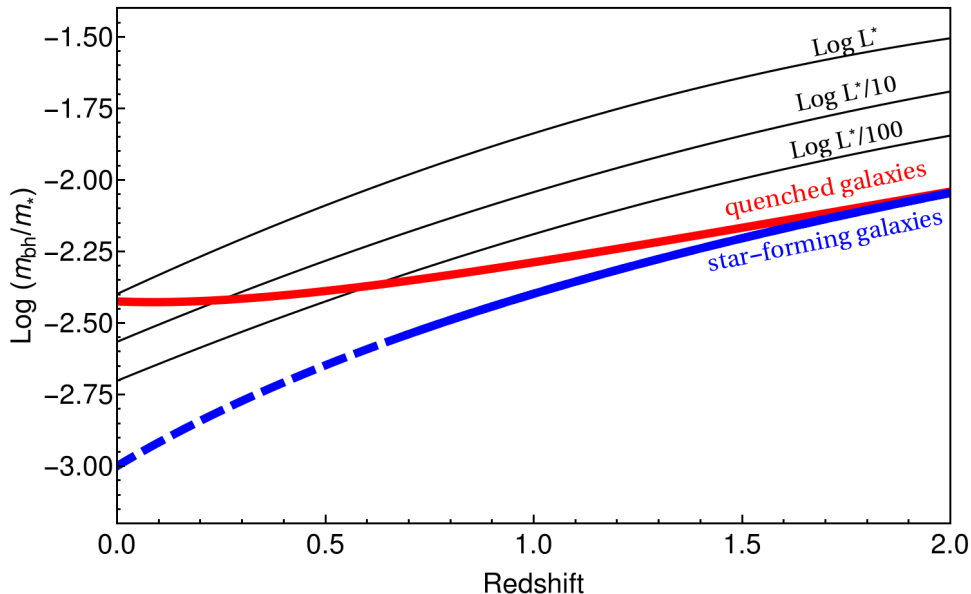


Figure 2.17: Evolution of the mean m_{bh}/m_* relation in star-forming (heavy blue line) and quenched systems (heavy red line). The dashed blue line shows the redshift range where this mean relation may not accurately represent star-forming galaxies, as it will be discussed in Section 3.1.1. The evolution in m_{bh}/m_* for the quenched (inactive nuclei) galaxies is always shallower than for the population of actively accreting systems, potentially leading to an underestimate of the evolution if the populations are mixed. On the other hand, the “Lauer effect” will bias the m_{bh}/m_* upwards in luminosity selected active samples, which goes in the opposite direction. This is indicated by the thin black lines which show the observed m_{bh}/m_* for active systems for luminosity-selection (labelled relative to L^*) for our standard assumption of $\sigma = 0.5$ dex.

an underlying m_{bh}/m_* scaling as $(1+z)^2$ for active systems, then we would expect to see $(1+z)^{0.8}$ if we compare comparisons of active systems at $z \sim 2$ with quenched systems at $z \sim 0$, once we correct for these observational biases. This is quite similar to the evolution seen in at least some of the observational studies cited above (e.g., Jahnke et al., 2009; Decarli et al., 2010; Merloni et al., 2010; Schramm & Silverman, 2013; Schulze et al., 2015).

We have already commented in Section 2.5.2 that we would also expect to see little or no evolution in $m_{bh} - \sigma$ for any population of galaxies, however selected. This is due to the higher σ associated with a given stellar mass at high redshift which cancels out the $(1+z)^2$ dependence in m_{bh}/m_* .

2.6.2 Downsizing

A number of authors (e.g., Hasinger et al., 2005; Barger et al., 2005; Labita et al., 2009; Li et al., 2011) have noted or discussed a “downsizing” of the quasar population. Although

different authors often use this term to mean different things, it is most often used to denote the observational fact that lower-luminosity AGN peak in comoving density at lower redshifts than higher-luminosity AGN.

It is worth stressing that this may not have much physical significance. We have shown that it is possible to reproduce the strong observed redshift evolution in the QLF with a model based on the observed mass function of star-forming galaxies coupled with a *mass-independent* (but redshift-dependent) Eddington ratio distribution $\xi(\lambda, z)$. This is shown more explicitly in Figure 2.18 where we show the comoving number density of quasars of different luminosity in the QLF which is reproduced by our model. This emphasizes that the apparent down-sizing signature in the AGN population can appear even though the distribution of Eddington ratios (and thus of specific black hole growth rates) is strictly *independent* of black hole mass at all redshifts in our model.

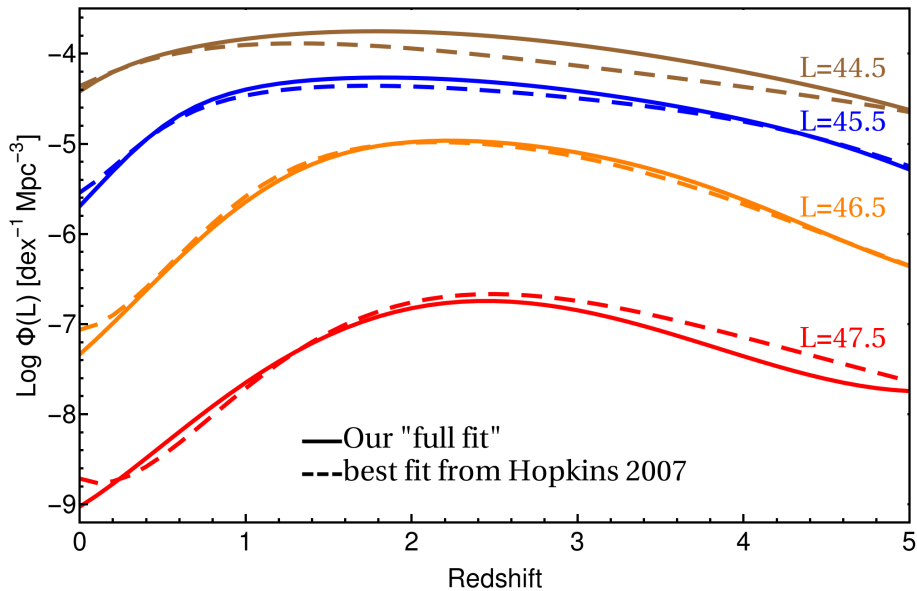


Figure 2.18: Redshift evolution of comoving density of quasars for several different luminosities. The density of lower luminosity AGN peaks at lower redshift than for high luminosity AGN. This behaviour is naturally produced in our model even though the distribution of Eddington ratios is completely independent of black hole mass.

It is clear that the apparent “downsizing” in our model arises as a natural consequence of two competing effects which are independent of mass. The first is the redshift evolution of the L^* which shifts the luminosity function *uniformly* in luminosity, but which therefore produces a differential change in number density with luminosity. This shift is produced by the degenerate combination of evolution of the m_{bh}/m_* mass ratio and characteristic Eddington ratio, λ^* . The second is the redshift evolution of ϕ_{QLF}^* that changes the number densities *uniformly* with luminosity. We have argued in this work that the evolution of ϕ_{QLF}^* is a direct consequence of the evolution of ϕ_{SF}^* , coupled with a constant duty

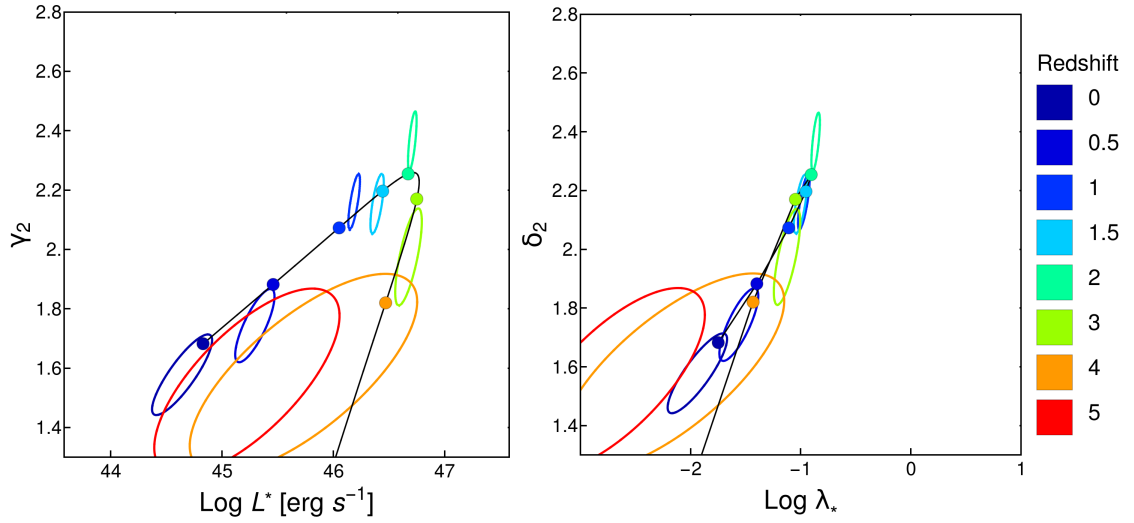


Figure 2.19: *Left:* $\gamma_2 - L^*$ redshift evolution. As in Figure 2.7, contours are showing 1- σ allowed regions of parameter space for fit which was made with data at each individual redshift, while filled circles are result of global fit. *Right:* $\delta_2 - \lambda^*$ evolution derived from $\gamma_2 - L^*$ evolution with our knowledge of redshift evolution of M^* and with assumed mass scaling $m_{bh}/m_* \propto (1+z)^2$. All of the points and contours seem to align along single line suggesting intimate link between these two quantities.

cycle. The combination of these two produces variation in the number density (at fixed luminosity) that changes with luminosity, producing a variation in the redshift of the peak in the number density as well as different rates of evolution at different luminosities.

2.7 Connection of the shape of Eddington distribution and mass ratio evolution

In this section we wish to point out one interesting and suggestive fact that arises from fits that were discussed in Section 2.4. We show on the left hand side of Figure 2.19 the relation obtained between L^* and the bright end slope of the QLF, γ_2 . There is a clear increase in the bright end slope γ_2 as L^* increases with redshift. At $z \geq 3$, as L^* stalls and then declines, we also see γ_2 decreasing again, although not in unison with L^* in the sense that the track in the (L^*, γ_2) plane is displaced. We can plot an equivalent diagram in the (λ^*, δ_2) plane by converting L^* to λ^* using an m_{bh}/m_* ratio and Equation (2.11) and setting $\delta_2 = \gamma_2$ (Equation (2.2)). The steepening of δ_2 as λ^* increases might qualitatively be expected if there was some maximum value of the Eddington ratio λ_{max} . As λ^* increased towards such a limit, then $\xi(\lambda)$ above λ^* would have to steepen, so as to get down to zero at the limiting λ_{max} .

An interesting question is then whether we can find an evolving (i.e., redshift-dependent)

m_{bh}/m_* ratio that will cause the “up” and “down” tracks in Figure 2.19 to lie on top of each other. We find that introducing $m_{bh}/m_* \propto (1+z)^2$ produces a good congruence in the (λ^*, δ_2) tracks associated with the rise and decline of L^* . This is shown in the right hand panel, where we show the (λ^*, δ_2) tracks obtained by using $m_{bh}/m_* = 10^{-3}(1+z)^2$. The congruence with this particular m_{bh}/m_* evolution is suggestive but cannot be taken as a strong indication of this particular evolution of m_{bh}/m_* .

2.7.1 Coherent evolution of ϕ_{SF}^* and ϕ_{QLF}^*

One of the most striking results of this chapter is that the observed evolution of ϕ_{QLF}^* of the QLF tracks the observed evolution of ϕ_{SF}^* of the star-forming galaxy mass function. This in turn implies that the ξ_λ^* knee of the Eddington ratio distribution $\xi(\lambda)$ has a more or less constant value, even though the change of the characteristic λ^* “knee” is dramatic. We have argued that ξ_λ^* is a good measure of a generalized “duty cycle” of quasars. Indeed, if the luminosity of individual quasars decays with a timescale τ then (Equation (2.8)) ξ_λ^* will be direct measure of the birth-rate of quasars in star-forming galaxies.

By applying simple continuity equations to the observed evolution of the star-forming galaxy mass function, Peng et al. (2010) derived an expression for the rate of the mass-quenching process, η_m , which may be written

$$\eta_m \sim sSFR(z) \cdot (m_*/M^*), \quad (2.31)$$

where $sSFR(z)$ is the redshift dependent specific star-formation rate of the star-forming Main Sequence. It has been well established that $sSFR$ was much higher in the past and a useful representation is (Lilly et al., 2013 and references therein)

$$sSFR \sim \begin{cases} (1+z)^3, & \text{when } z < 2 \\ (1+z)^{5/3}, & \text{when } z > 2. \end{cases} \quad (2.32)$$

AGN activity in “quasar-mode” is one of the many processes that have been proposed (e.g., Granato et al., 2004; Hopkins et al., 2008; King, 2010; Henriques et al., 2017) to drive the mass-quenching of galaxies. If a single quasar event is responsible for quenching, then this would require that η_{AGN} (from Equation (2.8)) to be equal to η_m . These can only be equated for our inferred constant ξ_λ^* for a particular redshift and mass dependence of the decay time τ .

$$\tau(m, z) \sim sSFR(z)^{-1} (m/M^*)^{-1} \xi_\lambda^*. \quad (2.33)$$

We would require quasars to fade faster at high redshift and at high galaxy masses. We could well imagine ways in which this would occur, e.g., because of the shorter dynamical timescales of galaxies at high redshift.

However, the above picture is probably over-simplistic. We could well expect the physics of quenching to be more complex. It is quite plausible that the energy source for quenching is AGN activity but that the effectiveness of this energy injection depends on the stellar or halo mass of the system (the Peng et al., 2010 quenching law can be written in terms of a redshift-independent survival probability that depends only on mass). This would then break the simple link between η_m and η_{AGN} .

We remind the reader that main feature of the model presented in this chapter is that all star-forming galaxies have the same chance to host an AGN, irrespective of their mass. That is the main reason why AGN quenching time in this scenario, expressed in Equation (2.33), has to incorporate mass dependence if AGN are the primary cause of mass-quenching. Of course, the model presented here is equally valid if the AGN activity is not the main driver for mass quenching, which in that case needs be driven by some other mass-dependent process. In the next chapter we will come back to this problem and investigate the scenario in which AGN activity is explicitly coupled with mass-quenching.

2.8 Summary and conclusions

In this chapter we have presented a simple, phenomenological model that aims to link the evolving galaxy population with the evolving AGN population. We use our observational knowledge of the evolving galaxy mass function and of the evolving quasar luminosity function (QLF) to connect these two populations and to create a global model to interpret the AGN population, including biases associated with sample selection.

Our model is based on three observationally motivated Ansätze, namely that

- radiatively efficient AGN are found in star-forming galaxies,
- the probability distribution of the Eddington ratio does not depend on the black hole mass of the system,
- the mass of the central black hole is linked to the stellar mass.

The QLF is then a straightforward convolution of the black hole mass function with the distribution of Eddington ratios $\xi(\lambda, z)$, while the former is itself a convolution of the galaxy mass-function with the m_{bh}/m_* relation. These heuristic assumptions ensure that our model is simple enough to be analytically tractable, while still capturing the main

characteristics of the galaxy and AGN population.

The main conclusions of this chapter can be summarized as follows:

1. The “broken” or “double” power law form of the quasar luminosity function is a consequence of the underlying Schechter mass function and a “double” power law, mass independent, Eddington ratio distribution. We show how the parameters of the QLF are straightforwardly connected with the input functions. Most importantly, the knee of the QLF, L^* , is proportional to the product of the M^* of the galaxy mass function, the ratio m_{bh}/m_* and the position λ^* of the break in the Eddington ratio distribution while the ϕ_{QLF}^* normalization of the QLF is proportional to the product of the ϕ_{SF}^* normalization of the star-forming galaxy mass function and the ξ_λ^* normalisation of the Eddington ratio distribution, which can be loosely interpreted as a “duty cycle”.

Our simple convolution model makes clear and testable predictions for the distribution of host galaxy masses (relative to the star-forming galaxy Schechter M^*) for different AGN luminosities (relative to L^*). At high luminosities (above the AGN L^*) this is a Schechter function with the star-forming M^* but a faint end slope given by $\alpha_{SF} + \gamma_2 \sim 1.5$.

2. There is a remarkable consistency in the redshift evolution of ϕ_{SF}^* normalization of SF mass function and the ϕ_{QLF}^* normalization of QLF. These two characteristic densities track each other closely out to redshifts of $z \sim 3$, and possibly to even higher redshifts. This implies that the generalised “duty cycle” of AGN is surprisingly constant with redshift.
3. In contrast, the QLF L^* evolves strongly with redshift, with evolution being at least $L^* \propto (1+z)^3$ up to $z \sim 2$. Given that there is strong evidence for no change in the galaxy M^* over this redshift range, this evolution in L^* is driven by an evolution in the characteristic “knee” in the Eddington ratio distribution λ^* or in the mass scaling between stellar mass and black hole mass, m_{bh}/m_* , or some combination of the two. The QLF evolution is degenerate in changes of these two quantities.

We then explore this degeneracy by comparing predictions of our model, incorporating the relevant selection cuts, for the distribution of systems in the SDSS AGN mass-luminosity plane(s) using black hole mass estimates for individual AGN. We find a good match with an evolving $m_{bh}/m_* \propto (1+z)^2$ in star-forming systems. This implies that the observed $\sim (1+z)^4$ increase in L^* back to $z \sim 2$ would be due to an equal split between a $(1+z)^2$ change in m_{bh}/m_* and a $(1+z)^2$ change in characteristic Eddington ratio λ^* .

We show that this is compatible with the observed m_{bh}/m_* relations in both quenched and in star-forming galaxies in the local Universe, both in terms of the mean relations and

the scatter.

We also make the important point that much weaker evolution, more like $m_{bh}/m_* \propto (1+z)^{0.8}$, would be deduced by observers, after correcting for the “Lauer bias”, if (as they usually of necessity do) they compare black hole masses in active (star-forming) systems at high redshift ($z \sim 2$) with those in quiescent systems at low redshift. Similarly, much weaker evolution would also be seen if black hole masses were to be compared solely within the passive population at different redshifts.

We make the point that an evolution of the form $m_{bh}/m_* \propto (1+z)^2$ would, when coupled with the observed changes in the sizes of galaxies which typically scale as roughly $(1+z)^{-1}$, have the feature of producing a $m_{bh} - \sigma$ relation that would be more or less *independent* of redshift. This could then explain why the present-day $m_{bh} - \sigma$ relation would have lower scatter than the m_{bh}/m_* relation, even if σ plays no direct role in black hole growth. Alternatively, a fundamental redshift-independent $m_{bh} - \sigma$ relation could be the physical origin of an apparent $m_{bh}/m_* \propto (1+z)^2$ evolution.

Following similar reasoning, and operationally identifying central stellar mass which was created at $z > 1.2$ as “bulge”, we show that the observed m_{bh}/m_{bulge} relation in quenched galaxies today would also be tighter than observed m_{bh}/m_* relation. This is again consequence of the size evolution of galaxies and m_{bh}/m_* ratio evolution. We finally show that the same evolution would also produce quenched fraction of galaxies which is seemingly independent of the galaxy stellar mass and strongly dependent on the black hole or bulge mass, even though the quenching in the model used is only directly connected with the stellar mass of galaxies.

We however stress that the most basic features of the model do not depend on the redshift dependence of m_{bh}/m_* , which is driven largely by the possibly uncertain observational estimates of black hole masses in high redshift AGN.

Not least, quite independent of the form of any evolution in m_{bh}/m_* , the generic model naturally reproduces the counter-intuitive “sub-Eddington boundary” in the (m_{bh}, L) plane that has been noted by [Steinhardt & Elvis \(2010\)](#) without the need to invoke any new physical effects. The generic model also produces the apparent “downsizing” of the AGN population (e.g., [Hasinger et al., 2005](#)). We stress that both of these apparently mass-dependent effects are achieved in the model with an Eddington ratio distribution that is completely *independent* of black hole mass at all redshifts.

3 | AGN and galaxies: quenching scenario

3.1 Is the mass ratio evolution consistent with the observed mass growth in the universe?

In the previous chapter, we found that the m_{bh}/m_* evolution was preferred to the scenario in which m_{bh}/m_* stays constant with redshift. This was based on the comparison of the models with the mass and luminosity SDSS data from [Shen & Kelly \(2012\)](#) and [Trakhtenbrot & Netzer \(2012\)](#). To explain both the QLF and the mass-luminosity plane at different redshifts, we investigated different mass scaling relations of the fiducial form $m_{bh}/m_* \propto (1+z)^n$. We found that the case of $n=0$ produced results that were inconsistent with the observations in the mass luminosity plane. If the mass ratio was set to reproduce the observations in the mass-luminosity plane at low redshifts and no evolution was allowed, we found that at $z \sim 2$, the majority of AGN need to be super-Eddington to produce correct QLF, given their relatively low black hole masses. This large fraction of super-Eddington objects would be clearly inconsistent with observations. We found much better agreement when setting $n=2$, that is with black holes being ~ 10 times more massive, relative to the host galaxy mass, at redshift 2 (see [Figure 2.10](#)). The inferred Eddington ratios are then also around 10 times smaller, with the simulated distributions agreeing with the observations and only a small fraction of observed black holes accreting at super-Eddington rates.

In the previous analysis, we have put in the needed mass ratio evolution “by hand”, i.e., we did not consider if the mass growth of the galaxies and black holes that we observe in the Universe is consistent with such an evolution. The evolution in the mass ratio that we suggest implies that the growth of star-forming galaxies would have to be much more vigorous than those of black holes at redshifts $z < 2$ to create such a change in the mass

ratio in the galaxies that remain star-forming throughout.

In this chapter we aim to expand the analysis from Chapter 2 by building a self-consistent model in which we include information about the mass accretion histories of both galaxy and black hole population. We will now use the star formation rate density (SFRD) and black hole accretion density (BHARD) in order to follow mass build up of both population over time. As such, observations in the mass-luminosity plane will now be a “consequence” of the model, rather than an input, and we will use them so check validity of our assumptions.

3.1.1 Mass growth of star-forming galaxies at low redshifts ($z \lesssim 0.7$)

This subsection has been presented in Caplar et al. (2015).

In this section we will show that mass ratio evolution of the type $(1+z)^n$, (with $n \sim 2$) is implausible at low redshifts in the co-existence scenario which we presented in previous chapter (see also Hopkins et al., 2006b). We consider the most extreme case in which black holes in star-forming galaxies are not growing at all and calculate what is the strongest possible evolution of the mass ratio in that case.

Assuming that a star-forming galaxy is on the Main Sequence we can track the increase of its stellar mass using the Main Sequence $rsSFR(z)$,

$$rsSFR(z) = \frac{\dot{m}_*}{m_*} = \left(\frac{-1}{H_0(1+z)\sqrt{\Omega_M(1+z)^3 + \Omega_\Lambda}} \right)^{-1} \frac{1}{m_*} \frac{dm_*}{dz}, \quad (3.1)$$

where $rsSFR$ is the “reduced specific star-formation rate” (see Lilly et al., 2013), $rsSFR = (1-R)sSFR$, where R is the fraction R of stellar mass that is returned during star formation $R \sim 0.4$, which is therefore the inverse mass doubling timescale of the stellar population. If we use $rsSFR(z) = 0.07(1+z)^3 \text{ Gyr}^{-1}$ from (e.g., Lilly et al. (2013) and references therein), this can be analytically integrated to give

$$m_*(z) = m_*(0) \left(\exp \left[\frac{2 \cdot 0.07 \sqrt{\Omega_M + \Omega_\Lambda}}{3H_0\Omega_M} - \frac{2 \cdot 0.07 \sqrt{\Omega_M(1+z)^3 + \Omega_\Lambda}}{3H_0\Omega_M} \right] \right). \quad (3.2)$$

This modest increase in stellar mass for a star-forming galaxy sets a maximal change in m_{bh}/m_* ratio even in the most extreme case that m_{bh} does not increase at all. We show this maximal evolution in Figure 3.1 and compare it with the $(1+z)^2$ evolution used before. It can be seen that the maximal evolution is actually slower than $(1+z)^2$ at

3.1. Is the mass ratio evolution consistent with the observed mass growth in the universe?

redshifts $z \lesssim 0.7$. Galaxies are growing so slowly at low redshifts that it is not possible to create a strong evolution in m_{bh}/m_* ratio in a given galaxy, even if their black holes are not growing at all.

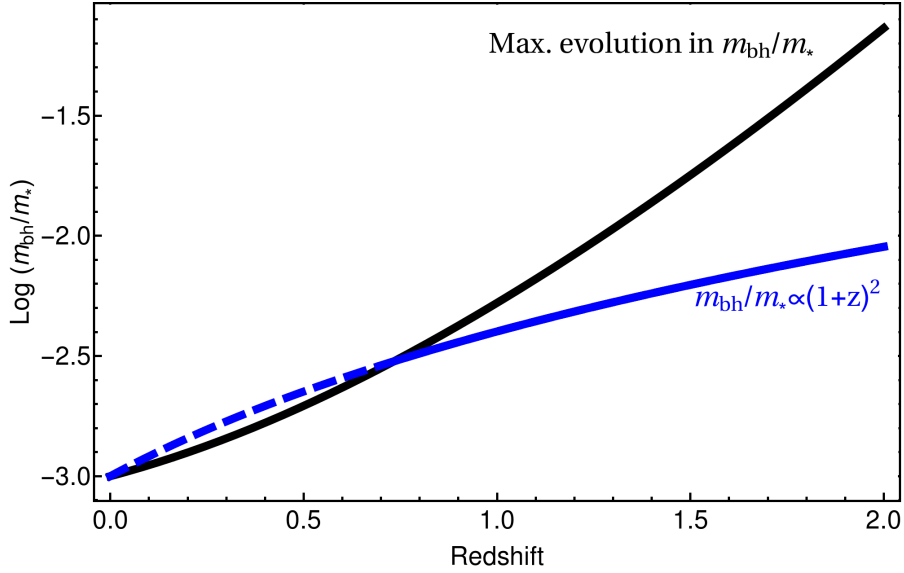


Figure 3.1: Comparison of the maximal evolution of the m_{bh}/m_* relation in a star-forming galaxy that stays on the Main Sequence, with our assumed $m_{bh}/m_* \propto (1+z)^2$. At low redshift galaxies are growing so slowly in the stellar mass that strong evolution in the m_{bh}/m_* ratio is not possible, even if the black hole does not grow at all.

3.1.2 Mass growth of star-forming galaxies and black holes in co-existence scenario

Of course, we know that the case we considered above, in which black holes do not accrete at all, is not realistic. We can estimate how the mass doubling time for the black holes would need to change if the m_{bh}/m_* ratio changes by the factor of ten from $z \sim 0$ to $z \sim 2$, this amount of change being implied by $m_{bh}/m_* \propto (1+z)^2$ evolution. We use an equation describing mass growth of AGN, which takes similar shape to Equation (3.1)

$$\frac{1-\epsilon}{\epsilon} \langle \lambda \rangle = \frac{\dot{m}_{bh}}{m_{bh}} = \left(\frac{-1}{H_0(1+z)\sqrt{\Omega_M(1+z)^3 + \Omega_\Lambda}} \right)^{-1} \frac{1}{m_{bh}} \frac{dm_{bh}}{dz}, \quad (3.3)$$

where $\langle \lambda \rangle$ is the mean Eddington ratio of the population. If we assume that both galaxy and black hole populations had the same mass doubling times at $z \sim 2$ and there is no change in efficiency of accretion, we find that mean Eddington ratio has to evolve as $\langle \lambda \rangle \propto (1+z)^{5.5}$ to create change of typical galaxy - black hole ratio by the factor of 10! This means that the black hole accretion has to fall rapidly to allow galaxies to “overtake” their black holes and create such a large change of in the m_{bh}/m_* ratio.

This change is a consequence of the fact that, as we have seen in the previous section, the galaxy growth is so slow at low redshifts that even in the case of no black hole growth, the mass ratio cannot change very much. Therefore, the black hole growth has to decline rapidly to allow for galaxy growth to overtake black hole growth sufficiently at $1 \lesssim z \lesssim 2$ so that the mass ratio can evolve. This rapid slowing down of mass doubling times implies that typical Eddington ratio would today have to be around ~ 500 times lower than at redshift 2, while we have pointed out in Section 2.8 that we expect characteristic Eddington ratio to experience mild evolution of $\lambda^* \propto (1+z)^2$ up until $z \sim 2$, i.e., change of factor ~ 10 .

Even if the efficiency does change, it is hard to imagine that it would change by a factor that would compensate for this difference. The minimal accretion efficiency in the standard thin disk model, for retrograde accretion disk, is 4%, and the maximal accretion efficiency is 42%. This maximal accretion efficiency cannot be achieved, and 31% is usually the quoted maximal canonical value, which is the consequence of the fact that the decelerating impact of radiation makes it impossible for the disk to achieve maximal spin (Thorne, 1974). Even the largest possible change of efficiency would not compensate for this difference and would imply that all accretion disks would have to change their spin rapidly, from being completely co-rotating with their black holes and having maximum efficiency (spin=1), to the state in which their spin is 0 or -1. In the following section we present an independent scenario that resolves this discrepancy in a much more plausible manner.

3.2 New convolution scenario

3.2.1 Qualitative explanation of the quenching scenario

It can be seen from the discussion above that the large evolutionary change of m_{bh}/m_* is hard to achieve in the co-existence scenario described in Chapter 2. This is a consequence of the fact that in this scenario, both the galaxy and the black hole mass have grown over a large spans of time so the changes in the ratio of the *current accretion rates* of the two populations will produce relatively small change in the ratio of *current total masses* in active black holes and galaxies. Therefore, to create mild evolution in the mass ratio, a much larger difference in the evolution of the accretion rates is needed.

We will now consider a model in which AGN are not continuously accreting during the whole time that the host galaxy is also creating stars, but the entire black hole accretion happens in single, almost δ -like, short burst of mass accretion just as the galaxy is about to mass-quench its star-formation. This clearly overcomes the problem. The black holes grow over a very short period of time, and the m_{bh}/m_* in these objects is unaffected by accretion in other systems that happened at earlier times. The *current mass ratio* between the total stellar mass and black hole mass is now not given by the integral over the long-term relation between mass accretion histories of galaxies and corresponding black

holes, but with a *current mass accretion rate*. We will explore and further clarify these statements below.

The starting point for our analysis is the mass function of galaxies that are being mass-quenched, which we will use as a mass function of AGN host galaxies. As elaborated in Section 1.2.2, the mass function of mass-quenched galaxies can be described with the Schechter formula defined in Equation (1.8):

$$\Phi_{Qing}(m_*) \equiv \frac{dN}{d \log m} = \phi_{Qing}^* \left(\frac{m_*}{M^*} \right)^{\alpha_{Qing}} \exp \left(- \frac{m_*}{M^*} \right) \quad (3.4)$$

where ϕ_{Qing}^* is the normalization, M^* is the Schechter mass and α_{Qing} is the low-mass end slope of the quenching population. The parameters of this function are directly connected with the mass function of star-forming galaxies (Peng et al., 2010); while the Schechter mass is the same for both populations, the low mass slope of galaxies that are being quenched differs from the low mass slope of star-forming galaxies by a factor of unity, i.e., $\alpha_{Qing} = \alpha_{SF} + 1$. To derive the normalization, we can use the fact that the rate by which galaxies are being quenched is proportional to the total number of star-forming galaxies and their quenching rate (Peng et al. (2010), see also Equation (2.31)). To get the normalization of quenching mass function (AGN host mass function), we multiply the rate with the time spent in the quenching phase τ , which describes the duration during which the galaxy is considered an AGN host. From this, it follows $\phi_{Qing}^* = \phi_{SF} \cdot sSFR \cdot \tau$.

As galaxies enter the quenching population we assume that black holes start accreting from some low “seed” mass and accrete until they reach their final mass. AGN grow exponentially which corresponds, in logarithmic space, to convolution of the AGN host mass function with the step-like function with lower limit set to reproduce the “seed” AGN mass. Mirroring the discussion in Section 2.2.1, the resulting function will be a Schechter function with the low mass slope given by the smaller of two power-law slopes of convolving functions, $\alpha_{AGN} = \min(\alpha_{Qing}, 0)$. Therefore the AGN mass function will have low mass end slope $\alpha_{AGN} = 0$. We show this schematically in Figure 3.2.

In the same figure we also show how the QLF is now a convolution of the AGN mass function and the Eddington ratio distribution:

$$\phi(L, z) = \int \phi_{AGN}(m_{bh}, z) \xi(\lambda, z) d \log \lambda, \quad (3.5)$$

where, when denoting AGN mass function, we used subscript *AGN* instead of *BH* used in Equation (2.1), to indicate that this mass function does not refer to all black holes hosted in star-forming galaxies, but only to the ones that are actually accreting. We see that this convolution is very similar to the one considered in Section 2.2, the only difference being the shape of the AGN mass function. Given that, all of our general conclusions about connections between AGN mass function, Eddington ratio distribution function and QLF can be carried across here as well.

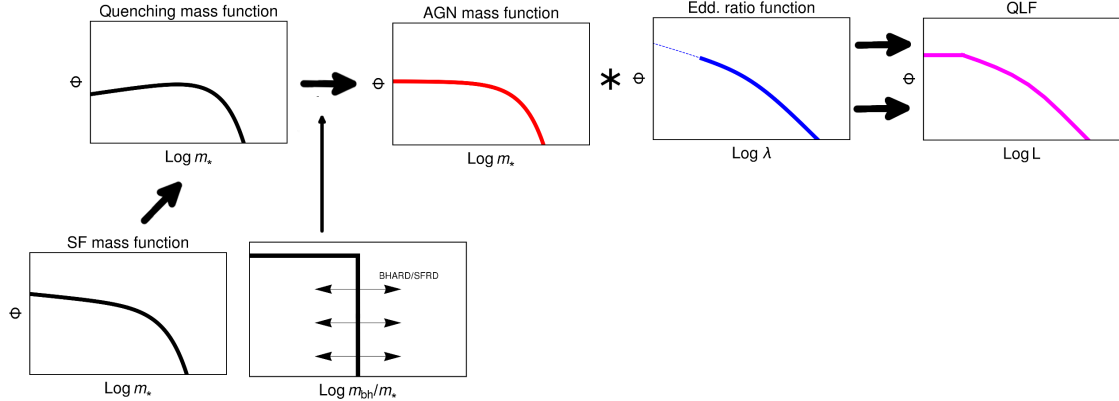


Figure 3.2: Schematic representation of the model used in this chapter. The quasar luminosity function is given by a convolution of the AGN mass function and the Eddington distribution. We also indicate that Eddington ratio function can not extended to arbitrarily low values and that this creates another break, below the “knee” or characteristic luminosity of the QLF. The AGN mass function is derived by convolving the galaxy mass function of galaxies undergoing quenching with the step-like function describing the m_{bh}/m_* relation. In the context of this model we show (see text) that the position of the step is given by $BHARD/SFRD$ ratio. Quenching mass function is derived from the star-forming mass function using formalism from Peng et al. (2010). In this scenario only star-forming galaxies that are undergoing mass-quenching host an AGN. Compare with Figure 2.1.

3.2.2 Predictions for the mass function of AGN and AGN host galaxies

Because the QLF is the product of the convolution of AGN mass function and Eddington ratio distribution, we can immediately calculate the predicted mass function of AGN and AGN host galaxies as a function of selection luminosity. Here, we present the analysis done for the quenching scenario presented above. This is the same analysis that we described in Section 2.2.5 and Figure 2.4 for the case of co-existence scenario. We will show that prediction for these two scenario differ substantially and we will use this extensively when trying to differentiate observable effects of two scenarios in Chapter 4.

To generate the plot, we used the AGN mass function described above and Eddington ratio distribution from Equation (2.7), with a lower limit on the Eddington distribution being $\lambda_{min} = \lambda^*/10$. We impose this limit to ensure that the AGN accretion mimics δ -like burst of mass accretion which is defining feature of the model. We do not add, at this point, any additional intrinsic scatter to the galaxy - black hole relation. We show our results in Figure 3.3. We follow the same procedure as we did when creating Figure 2.4, i.e., we normalize all our results to the parameters of the AGN host galaxy mass function, ϕ_{Qing}^* and M^* , and show results in bins of luminosity relative to the characteristic luminosity of QLF, L^* .

We see that for luminosities above L^* , results are virtually unchanged. This is a consequence of the fact that at these high luminosities the QLF is dominated by black

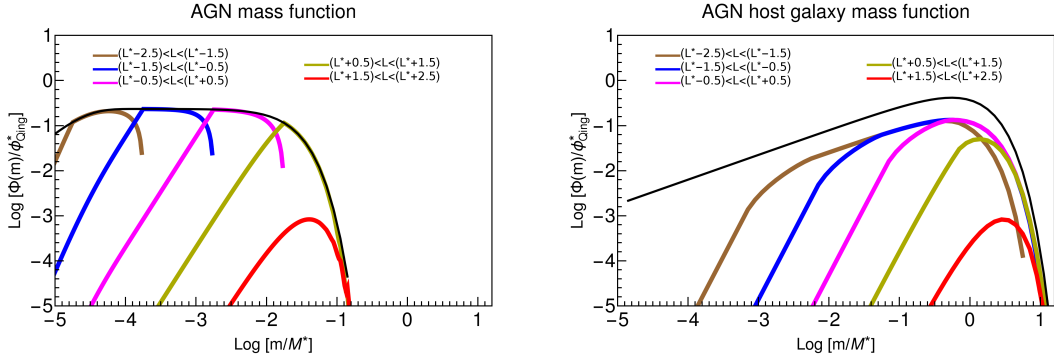


Figure 3.3: Expected shape of the black hole and the black hole host galaxy mass function, selected in different AGN luminosity bins. Mass are plotted relative to the Schechter M^* of the galaxy population ($M^* \sim 10^{10.85} M_\odot$) and Φ relative to the ϕ_{Qing}^* of the quenching galaxy population (AGN host population). All luminosities are relative to the L^* of the AGN luminosity function. L is given in logarithmic units. The black thick lines show the full AGN mass function (left) and AGN host mass function (right).

holes and galaxies that are at the Schechter mass of their respective mass functions and that are radiating at, or above, the characteristic Eddington ratio. Therefore, the mass function at these luminosities is dominated by an exponential drop off above the Schechter mass, and below the Schechter mass is it characterized with a low mass slope which is given with $\alpha = \alpha_{AGN} + \gamma_2$ (see Section 2.2.5). The difference between two scenarios is therefore only in the relatively small change of α_{AGN} slope ($\alpha_{AGN} = \alpha_{SF} = -0.45$ before and $\alpha_{AGN} \approx 0$ now).

Much more substantial differences arise when observing AGN at luminosities below L^* . In the left panel we see that different AGN luminosities are originating from different parts of the AGN mass function. This is a consequence of a fact that our Eddington ratio distribution is quite “narrow” so a given AGN luminosity is dominated by the black holes in a narrow range of mass. The AGN mass function always reaches its peak at

$$m_{peak,AGN} \sim \frac{L}{10^{38.1} \lambda^*}, \quad L < L_*. \quad (3.6)$$

We can again recognize that each individual mass function at a given luminosity has a low mass slope of $\alpha_{AGN} + \gamma_2$. This is caused by low mass AGN, described with low mass slope α_{AGN} , which are radiating at high Eddington ratios, described with high-end slope of γ_2 . Finally, the AGN mass function drops and disappears at a maximal mass of $m_{max,AGN} = L/(10^{38.1} \lambda_{min})$, reflecting the fact that these black hole are too massive to radiate at these low luminosities, given the λ_{min} of the distribution.

In case of galaxies at luminosities below L^* , we recognize three distinct regimes, similar to the co-existence case presented in Section 2.2.5. At low masses, below $10^{38.1} (m_{bh}/m_*)^{-1} (\lambda^*)^{-1}$, the mass function has slope $\alpha_{SF} + 1 + \gamma_2$, and then the slope of $\alpha_{SF} + 1$ until the M^* mass, after which an exponential drop takes over.

This is quite different relationship to the one presented before; AGN of all luminosities are mostly likely to be hosted in M^* galaxies. Perhaps surprisingly, even the low luminosity, low mass AGN are most likely to be in massive galaxies, simply because massive galaxies are dominating the quenching population and hosting AGN having wide range of black hole masses. As a conclusion, while AGN of *different luminosities* are hosted in systems with *different black hole masses*, systems with *similar galaxy mass*, $\sim M^*$, dominate the AGN distribution at *all luminosities*.

3.2.3 Connection between mass accretion and the mass function of galaxies and AGN

The star formation rate density (SFRD) and black hole luminosity density (BHLD) are the basic observational quantities describing mass accretion on galaxies and black holes in the Universe. BHLD can be used to infer the black hole accretion rate density (BHARD), as these are connected by a variable that describes the efficiency of accretion (see Equation 1.3). In the following we will assume that efficiency is constant with redshift and therefore BHLD and BHRD are effectively interchangeable quantities. Below we analyse analytically connections between SFRD and the BHARD to find the expected evolution of the active black hole mass function and Eddington ratio distribution.

Both of these integral quantities (SFRD and BHARD) can be derived computationally by knowing the underlying corresponding mass function and the corresponding law connecting mass and mass accretion. We first derive these relations, i.e., connections of SFRD and BHARD with the parameters of the appropriate mass functions and mass growth relations, before we attempt to connect the redshift evolution of SFRD and BHARD.

We first consider the SFRD. As noted above, the total star formation rate density at any given time in the Universe can be reproduced given the underlying mass function of star-forming galaxies and the law connecting star-formation and the mass of the galaxies. Integrating the Schechter function describing the star-forming mass function over the whole mass range we can derive the total mass of the star-forming population

$$\rho_{SF} = \frac{\phi_{SF}^*}{\ln 10} \cdot M^* \cdot \Gamma(1 + \alpha_{SF}) \quad (3.7)$$

where Γ is denoting the Gamma function, $\Gamma(x) = \int_0^\infty t^{x-1} \exp(-t) dt$.

As we discussed in Chapter 1, the vast majority of star-formation happens on the Main Sequence, a tight linear correlation between the stellar mass and the star-formation rate. This means that for galaxies on the Main Sequence, one can define the specific star-formation rate (sSFR), which is not strongly dependent on the stellar mass of a galaxy. We ignore in this analysis small tilt in Main Sequence, i.e., the fact that the correlation between the stellar mass and the star-formation rate is probably not perfectly linear (see Lilly et al. (2013), Speagle et al. (2014) and references within) for simplicity, but also note

that this small non-linearity would not make significant changes to our conclusions since they are driven by galaxies in a small range of mass.

Redshift evolution of the star-formation density is then given by a product of the mass density and sSFR so it follows that

$$SFRD \propto \frac{\phi_{SF}^*}{\ln 10} \cdot M^* \cdot \Gamma(1 + \alpha_{SF}) \cdot sSFR. \quad (3.8)$$

Given that we know that there is little to no evolution in the M^* and the slope α (e.g., Peng et al. 2014, Mortlock et al. 2015), the redshift evolution of the SFRD is primarily driven only by the evolution of the sSFR and the parameter ϕ_{SF}^* describing the overall normalization of the mass function, i.e.,

$$SFRD \propto \phi_{SF}^* \cdot sSFR. \quad (3.9)$$

We now follow the same procedure to investigate the evolution of BHARD, which can also be derived from the underlying AGN mass function and the relation describing its mass doubling rate. The mass density of the AGN population is given by an equation equivalent to Equation (3.7):

$$\begin{aligned} \rho_{AGN} &= \frac{\phi_{AGN}^*}{\ln 10} M_{AGN}^* \Gamma(1 + \alpha_{bh}) \\ &= \frac{\phi_{AGN}^*}{\ln 10} M^* \left(\frac{m_{bh}}{m_*} \right)_{AGN} \Gamma(1 + \alpha_{bh}), \end{aligned} \quad (3.10)$$

where in the first step we have denoted the Schechter mass of the AGN mass function with M_{AGN}^* , and in the second step we have explicitly written black hole - galaxy mass relation.

As we already discussed in Section 3.1.2, similarly to sSFR which describes the mass accretion for galaxies, the mass growth of the black holes is proportional to the mean Eddington ratio, $\langle \lambda \rangle$. Now we can write Equation for BHARD that is equivalent to (3.9) for SFRD:

$$BHARD \propto \phi_{AGN}^* \left(\frac{m_{bh}}{m_*} \right)_{AGN} M^* \cdot \langle \lambda \rangle, \quad (3.11)$$

We see that the evolution of BHARD has the same two parameters as the SFRD, which influence its dependence, normalization and mass growth rate. The only difference is the terms relating black hole and galaxy mass.

Because the AGN are now only active when the galaxy is mass-quenching, the number of AGN host galaxies is directly proportional to the number of galaxies that are undergoing quenching, $\phi_{AGN}^* \propto \phi_{Qing}^*$. As we have shown in Section 3.2, the number of galaxies

undergoing mass-quenching is given by $\phi_{Qing}^* = \phi_{SF} \cdot sSFR \cdot \tau$. Putting this normalization in Equation above leads to

$$BHARD \propto \phi_{SF}^* sSFR \tau \cdot \left(\frac{m_{bh}}{m_*} \right)_{Qing} \cdot \langle \lambda \rangle, \quad (3.12)$$

where we have used subscript *Qing* to remind the reader once again that the AGN accretion is happening as the galaxies are being quenched.

As τ denotes the time that the black grows from the seed mass to its final mass, it is inversely related with the $\langle \lambda \rangle$ that describes the mass accretion rate of the system. Therefore, Equation (3.12) can be simplified by removing τ and $\langle \lambda \rangle$, so that it now reads

$$BHARD \propto \phi_{SF}^* \cdot sSFR \cdot \left(\frac{m_{bh}}{m_*} \right)_{Qing} M^*. \quad (3.13)$$

When comparing Equations 3.9 and 3.13, and taking into account the fact that M^* does not evolve, we see that the mass ratio in the newly quenched objects is simply given by the ratio of BHARD and SFRD:

$$\left(\frac{m_{bh}}{m_*} \right)_{Qing} \propto \frac{BHARD}{SFRD}. \quad (3.14)$$

The equation above determines the redshift evolution of the black hole - galaxy mass ratio and therefore the evolution of the characteristic mass of the AGN mass function. In this case, the evolution of the mass ratio is given exactly by the ratio of BHARD and SFRD, i.e., changes in the black hole - galaxy mass ratio reflect, virtually instantaneously, changes in the black hole - galaxy mass accretion ratio and vice versa.

Using the same analysis we can also infer the connection of the normalization of the AGN mass function with the normalization of the star-forming galaxy mass function. As we pointed out when deriving Equation (3.11) the normalization of the AGN mass function is given by $\phi_{AGN}^* \propto \phi_{SF} \cdot sSFR \cdot \tau$. Using the fact that τ and $\langle \lambda \rangle$ are inversely related we immediately arrive to

$$\phi_{AGN}^* \propto \phi_{SF}^* \cdot \frac{sSFR}{\langle \lambda \rangle}. \quad (3.15)$$

This relation provides a direct link between normalization of mass function of star-forming galaxies and AGN, which is simply given by the ratio of the mass doubling times.

We note that if both $sSFR$ and $\langle \lambda \rangle$ have same redshift dependence the normalizations of respective populations will have also have the same redshift dependence. This is exactly the dependence that is seen at $z \lesssim 2$ in Section 2.4.1! This suggests that $sSFR$ and $\langle \lambda \rangle$ have the same, or similar, redshift dependence over this range of redshifts.

We have now derived the relation for the mass ratio between quenching galaxies and AGN (Equation (3.14)) and for the normalization of the AGN mass function which fully defines the evolving AGN mass function. To fully describe AGN evolution and its growth

we will now derive the evolution of the characteristic Eddington ratio. As the L^* , characteristic luminosity of the QLF, is proportional to the position of the Schechter break in AGN mass function and the break in Eddington ratio distribution, the second part of Equation (3.11) can be recognized as being proportional to L^*

$$L^* \propto \left(\frac{m_{bh}}{m_*} \right)_{Qing} M^* \lambda^*, \quad (3.16)$$

where we have used the simplifying assumption that $\langle \lambda \rangle \propto \lambda^*$, i.e., that the characteristic and mean Eddington ratio of the population are linearly related to one another. We can combine Equation above with Equation (3.14) to express λ^* fully as a function of evolving observable quantities

$$\lambda^* \propto \frac{SFRD}{BHARD} \cdot \frac{L^*}{M^*}. \quad (3.17)$$

Equation above provides clear prediction for the evolution of λ^* , which is given by the ratio of accretion rate densities and by evolution of the ratio between characteristic QLF luminosity and characteristic galaxy mass.

Equations (3.14), (3.15) and (3.17) fully describe the evolution of crucial parameters describing AGN mass function and Eddington ratio function once the evolution of SFRD and BHL(BHARD) is given.

We stress again that in this model the m_{bh}/m_* ratio in systems with AGN is set, virtually instantaneously, by the BHARD/SFRD ratio at that particular moment of time! This is a consequence of the fact that AGN accrete for a relatively brief time and as thus, all the relevant time-scales are short. This is different than in the co-existence scenario described in Chapter 2 in which AGN accrete during the whole lifetime that the host galaxy is also star-forming. This long co-existence means the m_{bh}/m_* ratio in the population is set by the integral over the whole accretion history of the host galaxy and AGN, and therefore m_{bh}/m_* does not respond instantaneously to the change of SFRD/BHARD ratio.

3.3 Observational determination of parameters describing AGN mass function and Eddington ratio function

In the previous section we pointed out the analytical connections between parameters describing AGN mass function and Eddington ratio function with the observed QLF and SFRD. Here, we aim to present the main observational constraints on the evolution of these quantities.

For evolution of the BHARD we use results from Hopkins et al. (2007), Ueda et al. (2014), and Aird et al. (2015). Even though the first study is somewhat older, it is arguably the most complete because it uses data from the rest-frame optical, soft and hard X-ray, and near- and mid-IR bands to infer bolometric QLF that is consistent with all the measurements in individual bands, at all of the redshifts. The second and third

studies use x-ray surveys with varying depths and sizes to constrain evolution of BHARD with redshift. X-ray surveys are especially suitable for this purpose because they can also probe moderately obscured AGN population and selection effects are relatively well understood.

To derive the BHARD from the observed luminosity densities reported in each paper, we use an efficiency $\epsilon = 0.04$ and the observational uncertainties reported in each paper as errors. We will show in Section 3.4 that the choice of $\epsilon = 0.04$ is most suitable as it reproduces the mass density of black holes seen in observations. Even though earlier works advocated higher values for efficiency, $\epsilon \sim 0.1$ (Merloni, 2004), re-normalization of the black hole - galaxy relation in the local Universe (Kormendy & Ho, 2013) suggest that lower values of efficiency are needed. We will show that our choice of efficiency is consistent with the observations in star-forming and quenched galaxies.

We also present results by using two different choices for SFRD. The first one is from Madau & Dickinson (2014), which uses surveys that have measured star-formation rates from rest-frame far-ultraviolet or mid- and far-infrared measurements to estimate the evolution of star-formation density. As noted in Madau & Dickinson (2014), this estimate is slightly inconsistent with measurements and evolution of the galaxy mass function. This could be due to a number of reasons, such as uncertainty in luminosity-weighted dust corrections for UV-measurements, changing initial mass function, influence of strong nebular lines and other systemic effects.

Although Madau & Dickinson (2014) is certainly the state-the-art compilation of star-formation density measurements we want to use the SFRD not just to follow the increase of total stellar mass in the Universe but also to have a self-consistent coupling of the sSFR and the number of mass-quenched objects at each redshift. To self-consistently model co-evolution of galaxies and AGN we also use an SFRD which was derived using a simplified assumption that the rsSFR of the Main Sequence evolves as $0.07 \cdot (1+z)^{2.5} \text{ Gyr}^{-1}$ and then following through the growth of the galaxy population using the model presented in Peng et al. (2010). This model reproduces growth of galaxy mass function from Ilbert et al. (2013), and will enable us later to self-consistently follow the growth of individual galaxies and their black holes, since to derive the number of quenching objects and galaxies that host an ANG, we use the same formalism. As for both choices of SFRD direct observational estimates of errors are not available, we assume, for plotting purposes only, that representative error is 0.15 dex and independent of redshift.

Figure 3.4 shows the redshift evolution of BHARD and SFRD, while the Figure 3.5 shows the redshift evolution of BHARD/SFRD ratio using the different choices for SFRD and BHARD described above. What we can see in Figures 3.4 and 3.5 is that all the panels suggest some amount of evolution in BHARD/SFRD ratio, with the ratio being smaller in the local Universe, then rising to $z \sim 2$ and then falling at higher redshifts. This points towards (see Equation (3.14)) an evolution of the m_{bh}/m_* ratio in galaxies which are hosting AGN, similar to the one which we pointed out in Chapter 2. The fact that both of these approaches yield similar results was not guaranteed as they have quite different

3.3. Observational determination of parameters describing AGN mass function and Eddington ratio function

reasoning. Most importantly, while in Chapter 2 m_{bh}/m_* evolution was promulgated as an input to the model in order to reproduce the data, now the m_{bh}/m_* ratio evolution arises as a simple consequence of the evolution of the observed integral quantities. Simply said, while in Chapter 2 m_{bh}/m_* ratio evolution was used as an “input” for the model, the m_{bh}/m_* ratio evolution now arises naturally as an “output”.

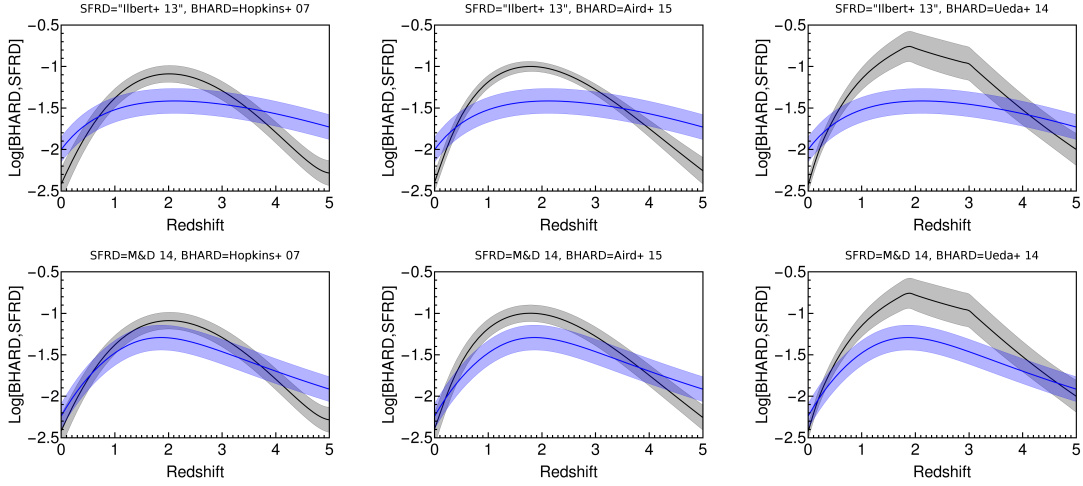


Figure 3.4: Observational determination of the redshift evolution of BHARD and SFRD. From left to right, we show BHARD from Hopkins et al. (2007), Aird et al. (2015), and Ueda et al. (2014). In the top row we show SFRD derived using model from Peng et al. (2010) and assuming that Main Sequence evolves as $rsSFR = 0.07 \cdot (1+z)^{2.5} \text{ Gyr}^{-1}$, which reproduces evolution of mass functions in Ilbert et al. (2013). In the bottom row we show results using SFRD from Madau & Dickinson (2014). In each panel the BHARD is shown in black and errors are taken from each individual observational study. BHARD has been derived from BHL D with $\epsilon = 0.04$ and multiplied by 10^3 to ease the comparison with the SFRD. In each panel the SFRD is shown in blue; errors are taken to be 0.15 dex and independent of redshift. Units of SFRD and BHARD are $M_\odot \text{ yr}^{-1} \text{ Mpc}^{-3}$.

Now we turn to the evolution of the Eddington ratio distribution. As we argued before (see Equation (3.17)), the characteristic Eddington ratio can be directly deduced from the evolution of BHARD/SFRD ratio, which we just established, and the evolution of the ratio of characteristic quantities L^*/M^* .

For evolution of L^* for QLF from Hopkins et al. (2007), we use the results of our “full” fit presented in Chapter 2, with the parameters given in Table 2.2. To estimate the L^* evolution in Aird et al. (2015) we use the results of their fit to the LADE model. This model describes QLF evolution with independent evolution of two parameters, “luminosity” and “density”. This is exactly the approach we adopt in this work, evolution of “luminosity” being evolution in L^* and evolution of “density” being the evolution in ϕ^* . Aird et al. (2015) provides for values of evolution of these quantities for observed hard and soft X-ray data, but unfortunately does not explicitly provide values for the evolution of total QLF with this model, which would include correction for obscuration. Therefore we estimate the evolution of L^* from the redshift evolution of ϕ_{QLF} in the LADE model and the total luminosity density, which includes obscured population. We use ϕ_{QLF} evolution in the

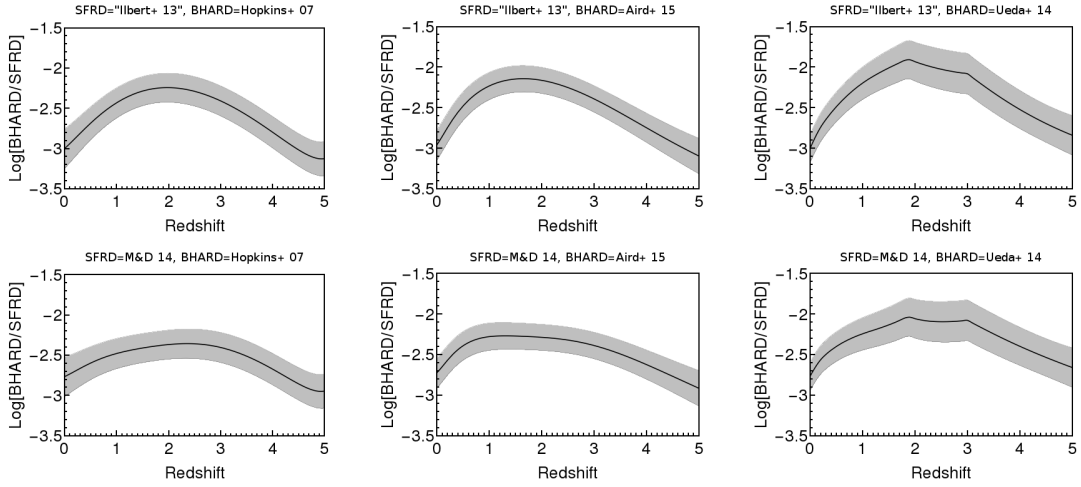


Figure 3.5: Observational determination of the redshift evolution of BHARD/SFRD ratio. From left to right, we show result derived with BHARD from Hopkins et al. (2007), Aird et al. (2015), and Ueda et al. (2014). In the top row we show SFRD derived using model from Peng et al. (2010) and assuming that Main Sequence evolves as $rsSFR = 0.07 \cdot (1+z)^{2.5} \text{ Gyr}^{-1}$, which reproduces evolution of mass functions in Ilbert et al. (2013) and in bottom row we show results using SFRD from Madau & Dickinson (2014).

observed hard band, but we note that evolution of both normalizations (in hard or soft band) are almost identical and thus this make little difference in our results. The fact that both of these normalizations, which are differently affected by obscuration, have the same redshift evolution makes us confident that the normalization of the total population behaves in the same way. Unfortunately, Ueda et al. (2014) does not parametrise the QLF as a simple broken power law function so we can not infer evolution of the L^* in this study. Still, we note that its results are broadly consistent with results presented in Aird et al. (2015).

Figure 3.6 shows the results of combining the evolution of SFRD/BHARD with the inferred evolution of L^* . The Eddington ratio rises with redshift, to $z \sim 2$ after which its evolutions flattens out. The change of the ratio up to $z \sim 2$ is around ~ 1.25 dex, which is what we would expect with the $\lambda^* \sim (1+z)^{2.5}$ evolution. This is very similar to the evolution of the sSFR relation at these redshifts. Additionally, we see that this flattening happens at a value at which characteristic Eddington ratio approaches the Eddington limit, i.e., $\lambda^* \sim 1$. This suggests that this is indeed the value above which accretion seems to be rare, and it represents a maximum value at which AGN can shine and accrete mass, at least in the cosmologically relevant sense. We stress that the flattening at higher redshifts at $\lambda^* \sim 1$ is again an output of the model and is not in any way motivated or dictated by any physical considerations. As such, there were no pre-existing requirements whatsoever which would dictate an evolution of the Eddington ratio which has same dependence as sSFR at low redshifts and flattens out at Eddington limit at $z \sim 2$.

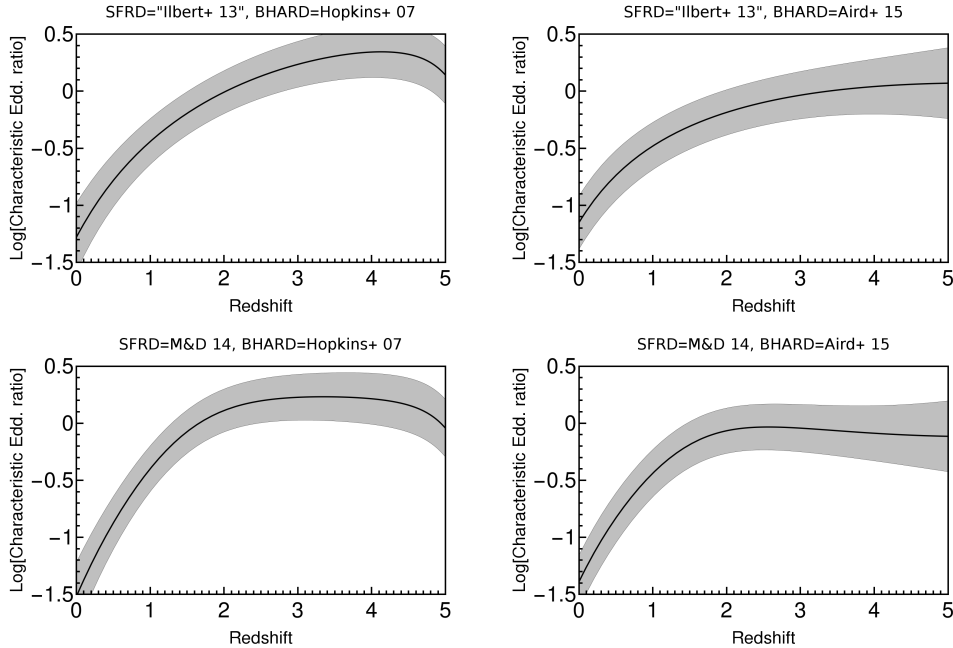


Figure 3.6: Redshift evolution of $(SFRD/BHARD) \cdot (L^*/M^*)$. The Figure uses same format at Figure 3.5. As we have argued in the text, $(SFRD/BHARD) \cdot (L^*/M^*)$ quantity is proportional to the characteristic Eddington ratio, λ^* . We see that it rises to $z \sim 2$, after which it flattens off at values corresponding to the Eddington limit.

3.4 Quantitative discussion

In previous sections, we have set up the model and derived analytic connections between parameters describing the galaxy mass functions, the AGN mass function, the Eddington ratio distribution and the QLF. We have then “derived” the redshift evolution of black hole - galaxy ratio and characteristic Eddington ratio by using observational constraints on the evolution of BHARD, SFRD and L^* . In this section, we adopt the specific choices for the evolution of all these variables, conduct a quantitative analysis and show our “predictions” for the black hole - galaxy relation in quenched galaxies in the local Universe and for star-forming galaxies at $z < 2$, which can be directly compared with observations.

3.4.1 Description of the calculation

We use the BHARD, presented in Hopkins et al. (2007) as we want to compare our results with the evolution of AGN mass-luminosity plane from SDSS. Because SDSS measurements are the main component of the analysis in Hopkins et al. (2007) this will ensure that comparisons are done using the same basic dataset. We then use the SFRD, which uses $rsSFR$ of the Main Sequence $rsSFR|_{MS} = 0.07 \cdot (1+z)^{2.5} \text{ Gyr}^{-1}$ and is prepared as discussed in Section 3.3. As noted, this functional form recreates the growth of galaxy

mass function and the evolution of the number of quenched objects.

The model is fully self-consistent because it uses the same inputs to determine both the evolution of galaxy and AGN population. As we discussed above, all of the choices for BHARD and SFRD will lead to same qualitative conclusions (see Figures 3.5 and 3.6) and the exact choice will not change our main findings.

Spurred by the results in Section 3.3 and especially those shown in Figure 3.6 we adopt a characteristic Eddington ratio which evolves as $\lambda^* = 0.048(1+z)^{2.5}$ below redshift 2 and then remains constant at higher redshifts. The fact that λ^* and $sSFR$ have the same redshift dependence automatically leads to same evolution of ϕ_S^* and ϕ_{QLF}^* below redshift 2, exactly as observed in the data (see Figure 2.9).

We start our simulation at redshift 6, assuming that all galaxies are star-forming at that redshift and that their mass distribution can be described by a Schechter function. We assume the same non-changing $M^* = 10^{10.85}$ and $\alpha_{SF} = -0.45$ seen in the data at lower redshifts. We use Equation (B1) from Peng et al. (2012) which provides the relationship for redshift evolution of normalization of star-forming galaxies:

$$\phi_{SF}^*(t) = \phi_{SF}^*(t_0) e^{\int_{t_0}^t -(1+\alpha_{SF})rsSFR(t') dt} \quad (3.18)$$

and search for value at redshift 6 which reproduces value of $\phi_{SF}^*(z=1) = 10^{-2.81} \text{ Mpc}^{-3} \text{ dex}^{-1}$ from the fit presented in Section 2.3.1. We find this value to be $\phi_{SF}^*(z=6) = 10^{-4.58} \text{ Mpc}^{-3} \text{ dex}^{-1}$. We then grow galaxies along the Main Sequence in consecutive bins of $\Delta z = 0.002$. In each redshift bin we also deduce which galaxies should quench, according to the mass-quenching law from Peng et al. (2010).

There are several ways that one could connect AGN accretion with quenching, either by requiring that AGN accretion happens just before galaxies quench, just after or with some part of accretion happening before and some part happening after quenching, which we assume to be an instantaneous event in the history of an galaxy. In this work, we set up the calculation in such a way that AGN start accreting from their seed mass and reach their final m_{bh} , which is given by BHARD/SFRD, at the moment that their host quenches. This is an operative choice, as both processes (AGN activity and quenching) are unlikely to be well defined, sharp transitions in the life of a galaxy but our results depend minimally on whether AGN accretion happens just before, during or after quenching of a galaxy.

When AGN start accreting, we assume that their initial mass function is of the shape as the mass function of “quenching” galaxies, i.e., that low mass slope is $\alpha_{AGN,1} = \alpha_{SF} + 1$, where with subscript 1 we denote that this is the low mass slope of the AGN that have started accreting in a single redshift step of the simulation. This choice of slope is the most logical one because it preserves the linear relation between galaxies that are quenching and their black hole mass. This shape is modified with assumed log-normal scatter, which we set at $\eta = 0.3$ dex for this analysis. To represent the seed mass of black holes, we assume that initial Schechter mass of AGN mass function of $M_{AGN,1}^* = 10^6 M_\odot$. In each step

we then increase the $M_{AGN,1}^*$ taking in account current $\langle\lambda\rangle$, until the maximal $M_{AGN,1}^*$ is reached. As we shown above, the maximal $M_{AGN,1}^*$ is given by the (non-evolving) M^* of the galaxy population and m_{bh}/m_* ratio which is reflecting evolving BHARD/SFRD ratio.

As we discussed in Section 2.2, the shape of the QLF is given by the combination of the underlying Eddington ratio distribution and the AGN mass function. The high luminosity end of the QLF is always equivalent to the high-end of the Eddington distribution, while the low luminosity end is given either by the low mass slope of the AGN mass function or the low end slope of the Eddington ratio distribution, whichever is steeper. While in Chapter 2 the low mass slope of AGN mass function had a slope of $\alpha_{AGN} = -0.45$ and was therefore steep enough to reproduce QLF, we have argued in Section 3.2.2 that this is not the case in this scenario ($\alpha_{AGN} \approx 0$) so we set up a low end slope of Eddington distribution function to reproduce low luminosity end of QLF ($\delta_1 = 0.45$). For simplicity and tractability of the model we set up the low and high Eddington ratio slopes to be constant with redshift. We chose the values representative of the QLF at $z \sim 2$ which corresponds to the peak of black hole accretion density. Following the results of our fit to the QLF given with Equation (2.26) and Table 2.2, we set the low Eddington slope to be $\delta_1 = -0.45$ and the high Eddington slope to be $\delta_2 = -2.45$. From this, it follows that the QLF will also have non-changing slopes and BHARD will only depend on the evolution of normalization and characteristic luminosity. We note that considering possible changes of the slopes would minimally influence our results. As an example, for a QLF with a given ϕ_{QLF}^* , L^* and $\gamma_1 = 0.45$, varying the high luminosity slope from the lowest value reported in Hopkins et al. (2007), which is $\gamma_2 = 1.8$ to the highest value, $\gamma_2 = 2.5$, changes the total luminosity density by the factor of 0.09 dex.

As we briefly mentioned above, to ensure that AGN growth happens in a quick, δ -like manner, we terminate the Eddington ratio at a given fraction of the characteristic Eddington ratio, λ^* , which we in this work set at tenth of λ^* , i.e., $\lambda_{min} = \lambda^*/10$. The choice of terminating the Eddington ratio distribution at a given fraction of λ^* is simplest possible, and is attractive as it leads to proportionally between the mean Eddington ratio of the population, $\langle\lambda\rangle$, and the characteristic Eddington ratio, λ^* .

3.4.2 Predictions of the quenching scenario and comparison with the conclusions from the co-existence scenario

We first present the black hole mass-luminosity plane, generated with the new, “quenching”, model. We follow exactly the procedure that we explained in detail in Section 2.5.1.

Figure 3.7 shows evolution of the mass-luminosity plane at three representative redshifts. Since the figure was produced using the same procedure it is directly comparable to Figure 2.10. We see that agreement with observational data, although not perfect, is far superior to the non-evolving case presented in upper panel of Figure 2.10. This is a consequence of the evolution in the mass ratio of roughly $m_{bh}/m_* \propto (1+z)^{1.5}$ and Eddington

ratio evolution of $\lambda^* \propto (1+z)^{2.5}$, quite similar to $(1+z)^2$ for both quantities which was postulated in Chapter 2. We remind the reader, that while in Chapter 2 we have put in m_{bh}/m_* evolution by hand, *any observed evolution in this ratio is now consequence of the observed galaxy and black hole growth in the SFRD and BHARD, respectively.*

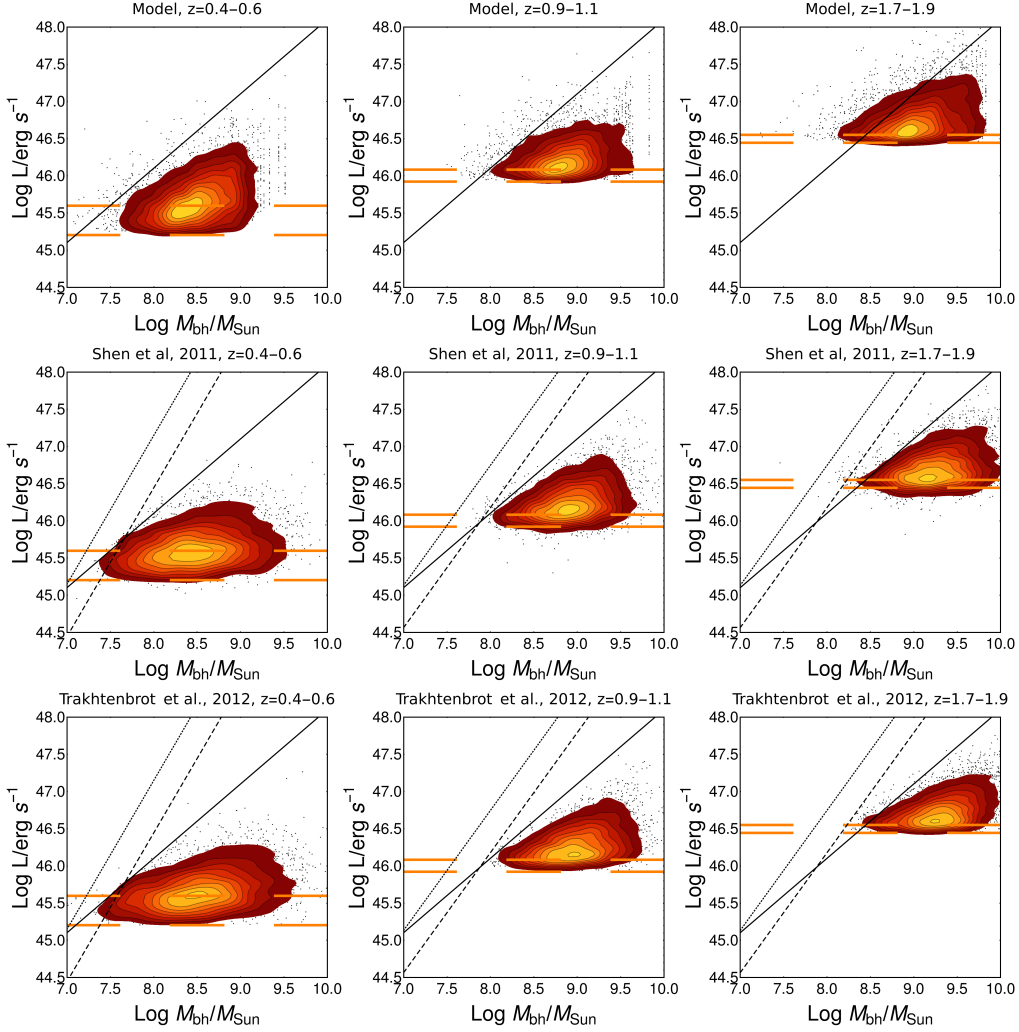


Figure 3.7: Mass-luminosity plane in the model in which AGN are connected with quenching, shown in 3 representative redshift bins. In the top row we show predictions from the quenching scenario of the model, and observational data from Shen et al. (2011) and Trakhtenbrot & Netzer (2012) are shown in bottom two rows. Colours and lines are the same as in Figure 2.10.

We also point out that most of the other conclusions that we made, such as pointing out that “sub-Eddington” boundary is a simple plotting effect, are still valid. That this particular effect is so similar in both cases is simply because the predictions for the two presented scenarios are very similar at high luminosities. SDSS probes luminosities of L^* and, as we argued when presenting black hole mass functions at different luminosities in Figures 2.4 and 3.3, the mass function of black holes at luminosities higher than L^* has basically the same shape in both scenarios we have considered. As a matter of fact, we

note that other conclusions from Chapter 2, such as expectation that $m_{bh} - \sigma$ relation is redshift independent and the explanation for weaker evolution of the mass ratio at $z \sim 1 - 2$ in direct observations are similarly not changed. These are both consequence of the mass ratio evolution, which is virtually unchanged in the new scenario, and galaxy evolution, which is unchanged. Finally, we note that since the new model was set to also reproduce QLF and BHARD it also automatically reproduces “downsizing”, even though the Eddington ratio distribution is again independent of the black hole mass.

Finally, we consider the prediction of the model for the black hole - galaxy relation for quenched objects in the local Universe. We follow the same procedure as when we produced the equivalent Figure 2.12 in Chapter 2. The only difference is, while before we used results from Birrer et al. (2014) to determine the quenching redshifts of passive galaxies, this information is not incorporated in the self-consistent manner in the model. Given how both reproduce well the overall evolution of the galaxy population this difference is in-consequential.

In the left panel of Figure 3.8 we show expected m_{bh}/m_* relation as measured in quenched galaxies in the local Universe, while in the right panel we show observational data from Kormendy & Ho (2013). We note excellent agreement, similar to the results shown in Figure 2.12. Given that both models employed the similar information about galaxy evolution and have similar m_{bh}/m_* evolution, this result is not surprising.

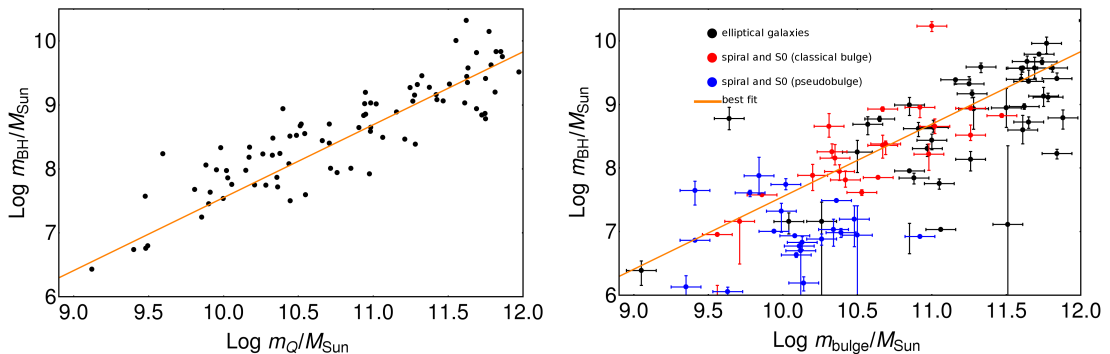


Figure 3.8: *Left:* Predicted m_{bh}/m_* relation in quenched galaxy systems in the local Universe. *Right:* Measured m_{bh}/m_{bulge} by Kormendy & Ho (2013). Orange line on both panels shows the best fit to the data reported in Kormendy & Ho (2013). The scenario in which AGN are associated with quenching, similarly to co-existence scenario, naturally reproduces the local relation in passive systems.

3.5 Summary and conclusions

In this chapter, we have presented a phenomenological model in which AGN were connected with the “mass-quenching” of galaxy star formation. This was motivated by the fact that significant change by a factor of ten in the black hole - galaxy mass ratio between red-

shifts 0 and 2, needed to reproduce observation in SDSS mass-luminosity plane, is hardly consistent with the observed mass growth rate in the co-existence scenario presented in Chapter 2. We have shown results of analysis that assumes that ANG accretion happens just as galaxies are mass quenched and whole AGN growth happens in one uninterrupted episode. Our main conclusion can be summarized as follows:

1. Black hole - galaxy mass relation for galaxies that are just about to be quenched is given explicitly by the BHARD/SFRD ratio at the moment of quenching. Observational data on BHARD and SFRD suggest that BHARD/SFRD ratio was higher at redshift 2 than today by 0.5 to 1 dex, i.e., it evolves with $\sim (1+z)^{1.5}$ dependence. This implies the same change of m_{bh}/m_* ratio in galaxies that host an AGN.
2. The characteristic Eddington ratio, λ^* is proportional to SFRD/BHARD ratio and the characteristic luminosity of QLF, L^* . Observations suggest a rise of this product with $\sim (1+z)^{2.5}$ dependence up to $z \sim 2$ which is similar to the redshift evolution of the cosmic sSFR. λ^* stabilizes around $z \sim 2$ at the value close to Eddington limit.
3. The normalization of the AGN mass function ϕ_{AGN}^* is proportional to the product of the normalization of the star-forming galaxy mass function ϕ_{SF}^* and $sSFR/\lambda^*$ ratio of mass doubling times for galaxies and AGN. If sSFR and λ^* have same redshift dependence as our analysis indicated for $z \sim 2$, the ratio between ϕ_{AGN}^* and ϕ_{SF}^* stays constant with time, as observed.

We have shown that this model in which AGN activity is connected with quenching also reproduces the SDSS mass-luminosity plane and the observed m_{bh}/m_* relation quenched galaxies in the local Universe. Similarly, other attractive conclusions from Chapter 2, such as (i) an explanation for the sub-Eddington boundary, (ii) a reproduction of downsizing with the Eddington ratio distribution being independent of mass, (iii) an explanation for weaker evolution mass ratio evolution at $z \sim 1$ in observations and (iv) an expectation that $m_{bh} - \sigma$ relation is redshift independent, are not modified.

This is not surprising as the m_{bh}/m_* and λ^* that we *derived* are very similar to the evolution we *postulated* in Chapter 2. We remind the reader that this congruence was not guaranteed or set up beforehand, but is a natural consequence of the evolution of BHLD(BHARD), SFRD and galaxy population. Given many similarities in the observational consequences arising from the two scenarios, even though their main assumptions and (presumably) physical drivers are quite disparate, in the next chapter we discuss explicitly their observational differences.

4 | Differentiating between AGN-galaxy co-evolution scenarios

4.1 Introduction

We have now presented a model for AGN-galaxy co-evolution with two quite different physical scenarios. While in the first scenario the AGN did not directly influence the galaxy and the co-evolution happens during the cosmological time-scales, in the second scenario AGN are active only when the galaxy is undergoing mass quenching, implying a close physical connection between the two. We have seen that both scenarios reproduce the QLF and other observables in the Universe. Even though we argued that only the scenario in which AGN are connected with quenching star-formation reproduces evolution in the mass-luminosity plane and m_{bh}/m_* relation in quenched galaxies once when the mass accretion histories are taken into account, we remind the reader that the mass ratio evolution difference is not defining feature of the model. Additionally, one could still imagine that effects such as obscuration and spin could conspire to create sufficient evolution in m_{bh}/m_* ratio even in the co-existence scenario considered in Chapter 2.

In this chapter, we directly compare two models, i.e., use a diagnostic that can conclusively differentiate between these two scenarios. We note that the main difference between the scenarios is in which galaxies host an AGN. In the first model all star-forming galaxies have an equal chance to host an actively accreting black hole and therefore the AGN host mass function has also the shape of the mass function of star-forming galaxies. In the second scenario, AGN are hosted only in galaxies undergoing mass-quenching, and therefore, the mass function of the AGN host galaxies has the same shape as the mass function of quenched galaxies. These two function differ in their low mass slope by the factor of 1, i.e., their mass function can be written as

$$\Phi_{host}(m_*) \propto \left(\frac{m_*}{M^*}\right)^{\alpha_{host}} \exp\left(-\frac{m_*}{M^*}\right) \quad (4.1)$$

with α_{host} is $\alpha_{host} = \alpha_{SF}$ in the co-existence scenario and $\alpha_{host} = \alpha_{SF} + 1$ in the quenching scenario. Simply stated, while in the first scenario AGN accretion is equally likely in all star-forming galaxies, in the later scenario AGN activity happens preferentially in the massive star-forming galaxies. Therefore we consider studies that test both AGN and galaxy properties in an independent and statistical manner.

Such studies are only possible in the fields with rich multi-wavelength data. As we argued in Chapter 1, X-ray surveys offer the best chance to trace AGN accretion in an unbiased way. Especially for studies in which we want to investigate AGN-galaxy dependence, the X-ray coverage is crucial because it is only band that allows to cleanly identify AGN accretion, as star formation cannot contribute significantly to the sources with luminosity of $L_x \gtrsim 10^{42}$ erg/s (e.g., [Aird et al., 2017a](#)). On the other hand mid- and far-infrared photometry are crucial for estimation of the SED of the objects and determination of the properties of galaxies, such as SFR and stellar mass. This restricts such studies to fields with deep X-ray coverage such as *Chandra* Deep Field North (CDF-N; [Alexander et al. 2003](#)), *Chandra* Deep Field South (CDF-S; [Xue et al. 2011](#)), COSMOS (C-COSMOS, [Elvis et al. \(2009\)](#)) and XMM-COSMOS, [Cappelluti et al. 2009](#)). The mid and far-infrared measurements for these fields with *Spitzer* and *Herschel* are described in [Elbaz et al. \(2011\)](#), [Lutz et al. \(2011\)](#) and [Oliver et al. \(2012\)](#).

4.2 Galaxy properties as a function of AGN luminosity

The first quantity we consider is the dependence of the star-formation rate as a function of the AGN luminosity. For this experiment, the AGN sample is divided into luminosity bins, and then the mean star-formation of the AGN hosts is determined. Assuming that the AGN hosts are star-forming galaxies that obey a linear relationship between their mass and star-formation, determining the mean star-formation rate is largely equivalent to determining the mean mass of the host galaxies. As we have argued in Section 3.2.2, this dependence is intrinsically different in two proposed scenarios. While in the co-existence scenario the typical galaxy mass of AGN hosts was dependent on the AGN luminosity, in the quenching scenario $\sim M^*$ galaxies dominate the host mass function at all luminosities.

We show our results in Figures 4.1 and 4.2. The data points in Figure 4.1 show results from [Ross et al. \(2013\)](#), while data points in Figure 4.2 show results from [Stanley et al. \(2015\)](#). These are directly comparable, but we avoided putting them in the same panel to improve the clarity of the presentation. We also show results from [Mullaney et al. \(2012a\)](#), using their Equation (4) which connects stellar mass and L_X . We transform stellar mass to SFR assuming the Main Sequence and show the result as a band with a width of 0.2 dex, corresponding to the scatter seen in the data. In both figures, we show on the x-axis labels for both X-ray and bolometric luminosity. We follow the suggestion from [Mullaney et al. \(2012b\)](#) and use, for a sake of simplicity, a constant bolometric correction to convert the X-ray luminosity to a bolometric luminosity using a correction factor of $k = 22.4$ ([Vasudevan & Fabian, 2007](#)). On the y-axis we show both the IR luminosity due

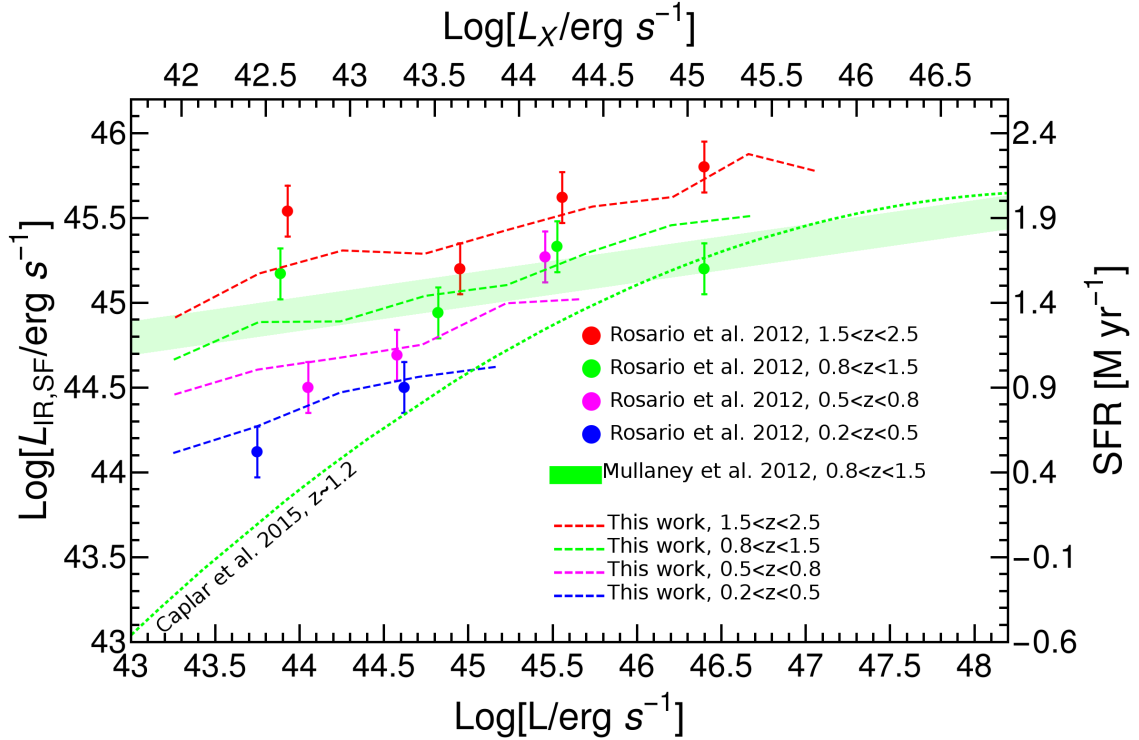


Figure 4.1: Star formation as a function of AGN luminosity. Dashed lines show predictions of our model, compared with data points and the filled area showing observational results listed in the Figure and explained in the text. Dotted line shows prediction from the co-existence scenario described in Chapter 2. We shows some of the results only at redshift $z \sim 1.2$ to improve clarity of the plot.

to star-formation, and the estimated SFR, using the constant scaling in which SFR of $1 M_{\odot}/\text{yr}$ correspond to $10^{43.6} \text{ erg s}^{-1}$, as used in Stanley et al. (2015). We show with dashed lines our predictions using the model in which AGN are connected with quenching in four different redshifts bins. We show with dotted line the expected results using the model from Caplar et al. (2015), i.e., from the model presented in Chapter 2. We show the last two outcomes (from Caplar et al. 2015 and Mullaney et al. 2012a) only at redshift $z \sim 1.2$, to reduce clutter on the plots and because the conclusions we derive are applicable to any redshift.

As Figures 4.1 and 4.2 show, the quenching model provides excellent agreement with observations. The predicted slope is almost flat as a consequence of the fact that in any AGN luminosity bin the sample is dominated by galaxies at the characteristic Schechter mass (see also Figure 3.3). Even though different luminosity bins have very different black hole masses, these are all hosted by the galaxies that are undergoing quenching, which are overwhelmingly massive galaxies around M^* . The slight tilt in the figures is a consequence of the fact that black hole accretion is not instantaneous - while black holes are growing their galaxies are also growing, although at a slower pace. This induces a weak dependence in which more luminous objects, corresponding to more massive black

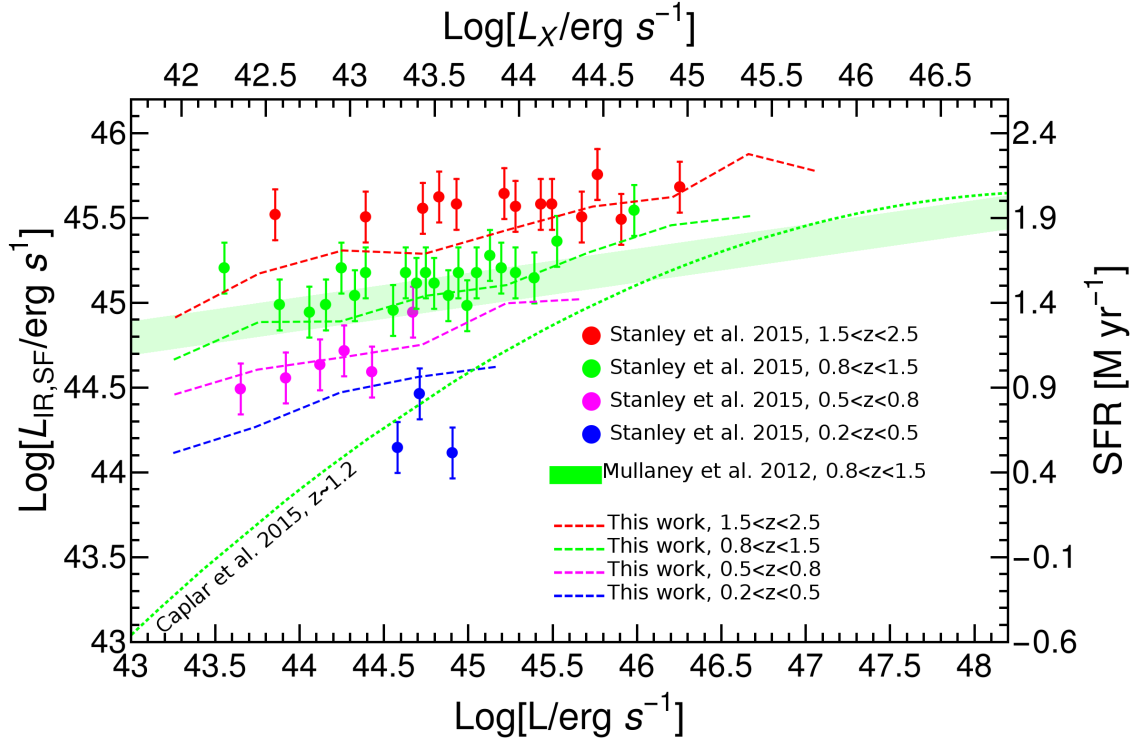


Figure 4.2: Star formation as a function of AGN luminosity. This plot is equivalent to the previous Figure but uses different observational results, indicated in Figure 4.1. We have separated presentation of observational results to avoid overcrowding on the Figures.

holes, reside in slightly more massive galaxies.

The co-existence scenario from Chapter 2 shows very different dependence. As we elaborated in Section 2.2.5 the dependence of host mass on AGN luminosity is quite different below and above L^* . Below L^* , the dependence of the galaxy mass and the AGN luminosity is linear, while above L^* this correlation can not continue given how steep the drop in the galaxy mass function is, and all AGN are hosted in M^* galaxies. This can be seen in Figures 4.1 and 4.2 as the dotted line flattens its linear dependence at higher luminosities towards what is seen in the quenching scenario (Chapter 3) at all luminosities.

4.3 AGN properties as a function of galaxy mass

An alternative view on the AGN - galaxy connection can be obtained if the data are not binned in bins of AGN luminosity but in bins of galaxy mass. In this analysis, all star-forming galaxies of a certain mass are considered and then the mean AGN luminosity is calculated by stacking the total X-ray flux at the positions of the objects, including the flux that would not be considered sufficient to a claim detection of an individual AGN. This analysis is of interest because, even though the underlying data are the same, different

projections can expose different trends in the population (e.g., [Volonteri et al. 2015](#)). Additionally, when selecting objects above a certain AGN luminosity, we are sensitive only to objects that are currently accreting. As we argued at the beginning of this chapter the main difference between two scenarios was in the mass dependence of the fraction of galaxies that host an AGN. This analysis is explicitly sensitive to this difference, as the mean luminosity of AGN in a bin containing all star-forming galaxies of a similar mass is obviously sensitive to the fraction of these galaxies that are hosting an AGN.

Before we compare the model predictions with the data we want to point out a salient effect that influences this analysis. Due to observational constraints, these types of analysis are done on still relatively small fields. These are not large enough to constraint a number of rare, very luminous, objects. If the luminous AGN are lacking in the sample of galaxies that can substantially change the conclusion about dependence of mean AGN luminosity with galaxy mass because the rare luminous objects are most likely to be hosted in more massive galaxies.

In [Figure 4.3](#), we schematically show predictions from our quenching model at redshift $z \sim 2$ and the effect we expect if more luminous objects are absent from the sample. On the x-axis, we have grouped galaxies in the bins of 0.5 dex, as such binning over relatively large range of masses is commonly done in observations. On the left y-axis we denote the mean x-ray luminosity over star formation rate for galaxies in the bin. On the right-hand side, we show the equivalent quantity, black hole accretion rate over star formation rate. We use a constant offset of a factor $10^{42.45}$, as used in [Rodighiero et al. \(2015\)](#). First, we consider the dark red line on the top of the figure that shows a non-biased sample, and follows the true distribution. For low masses, the slope has linear dependence, which is the consequence of the trend that the fraction of star-forming galaxies which are quenching is increasing linearly with the stellar mass (see [Equation \(4.1\)](#)). At the high mass end there is some flattening because the fraction saturates, i.e., the fraction of star-forming galaxies that host an AGN cannot continue to grow linearly as the high enough masses fraction of star-forming galaxies that host an AGN approaches unity.

We then start removing the most luminous objects from our sample, as indicated by the successive orange, yellow and blue lines. As we have pointed out, removing more luminous objects from the sample disproportionately affects measurement of mean AGN luminosities of high mass galaxies that are more likely to host these rare very luminous AGN. This effect causes flattening of the observed relation, because the inferred mean luminosity of AGN in high mass galaxies is underestimated. In the unrealistic extreme case in which we are only considering low luminosity AGN (e.g., dark blue line), the mean measured AGN luminosity in high mass galaxies is very low, since large black holes in those galaxies generally do not radiate at these low luminosities.

We now compare results of our models with two sets of observations. The first analysis mimics the results one would expect from a 0.9 deg^2 C-COSMOS field, analysed in [Rodighiero et al. \(2015\)](#). To do so, we use the results from our analysis in [Section 3.4](#) and create very large numbers (10^5) of AGN hosted in galaxies with $m_* > 10^8 M_\odot$, to-

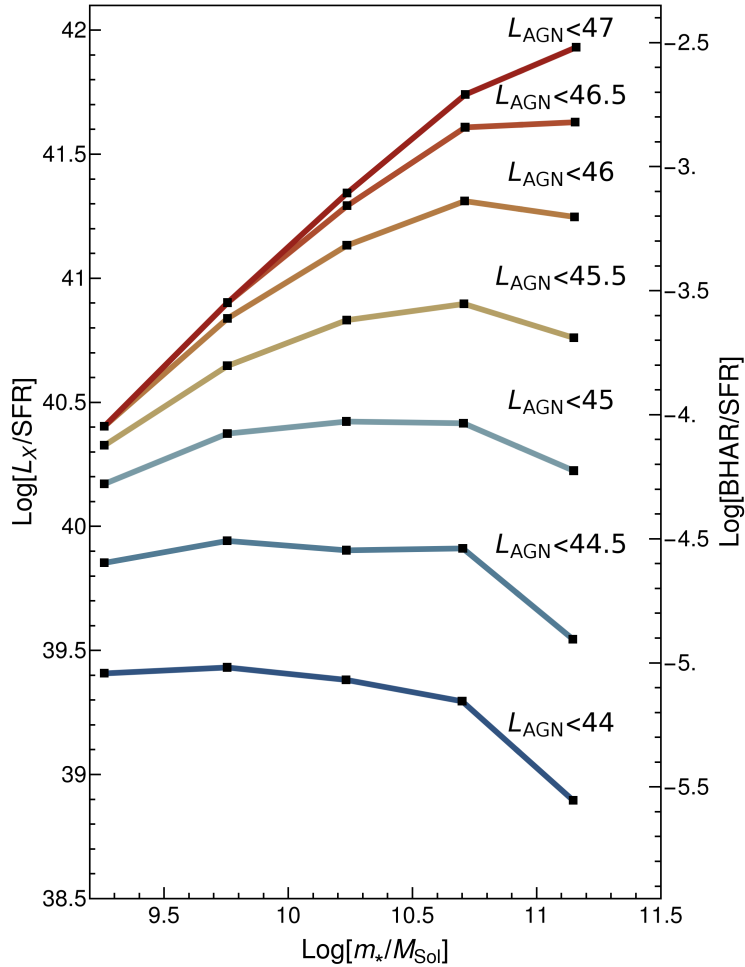


Figure 4.3: Schematic representation of the effect that removing AGN above certain luminosity has on the inferred L_x/SFR dependence with stellar mass. Lines show predicted L_x/SFR dependence if only AGN below bolometric luminosity indicated next to each line are kept in the sample. Luminosities on the Figure are logarithmic and expressed in units of erg/s. Figure has been created assuming that survey is at $z \sim 2$, when $L^* \approx 10^{46.7}$ erg/s.

gether with their black hole and galaxy masses at redshift intervals separated by $\Delta z = 0.1$. We estimate the number of objects that we expect in each redshift bin in a 0.9 deg^2 field and draw objects randomly. For the sample at $z \sim 2$ we simulate objects between $1.5 < z < 2.5$, and for the sample at $z \sim 1$ we simulate objects between $0.5 < z < 1.5$.

To make sure we capture the effect described in Figure 4.3, we estimate what are the most luminous objects seen in the COSMOS sample. We therefore create a function describing the redshift dependence of the brightest AGN found in the sample in the following manner. We consider the sample of COSMOS X-ray detections from Civano et al. (2012) between redshifts $0.5 < z < 2.5$ and search for brightest AGN in redshift bins of

$\Delta z = 0.25$. We then fit this upper envelope of the distribution in with functional form $\log L_{X,0} + n \log(1+z)$ and find best fit parameters to be $\log L_{X,0} = 43.5$ and $n = 2.14$, where unit of $L_{X,0}$ is erg/s. After that we apply the bolometric correction and raise the overall normalization of the relation so that all observed AGN are actually below it (apart from one object at $z \sim 1.2$). For our further analysis of the simulated sample we remove AGN, if there happen to be any, with luminosity larger than $L_{lim,COSMOS} = 44.8 + 2.14 \log(1+z)$, where $L_{lim,COSMOS}$ is now a bolometric luminosity and its unit is again erg/s. This procedure eliminates, on average, around 0.07% of the total simulated sample from the analysis.

The second analysis mimics results from the 0.11 deg² CDF-S field, analysed in [Mullaney et al. \(2012b\)](#) and [Yang et al. \(2017\)](#). We follow the same procedure as described above. For the sample at $z \sim 2$ we simulate objects between $1.3 < z < 2.0$, and for the sample at $z \sim 1$ we simulate objects between $0.5 < z < 1.3$, as it has been done in [Yang et al. \(2017\)](#). We also estimate a dependence of the maximal luminosity with redshift from the sample presented in [Yang et al. \(2017\)](#). We find upper envelope of the sample to be well described with $L_{lim,CDF-S} = 44.25 + 3.48 \log(1+z)$ and we remove objects with larger luminosities from the sample. With this procedure we remove, on average, $\sim 0.1\%$ of all galaxies that have been simulated. For a sample of 13114 galaxies considered in [Yang et al. \(2017\)](#) this correspond to ~ 13 objects. We can compare this with [Yang et al. \(2017\)](#), where 18 broad-line, generally more luminous, AGN were removed from the sample, as SFR measurements from SED fitting could be overestimated for these objects (e.g., [Ciesla et al., 2015](#)).

We show the results of our analysis in Figures 4.4 and 4.5. Figure 4.4 shows results at higher redshift of $z \sim 2$, while Figure 4.5 shows result at the lower redshift of $z \sim 1$. Both figures employ the same colour scheme. The red points show results from the analysis of COSMOS field presented in [Rodighiero et al. \(2015\)](#), black and grey points show results from analysing CDF-S field by [Mullaney et al. \(2012b\)](#), while light blue and blue points show CDF-S results by [Yang et al. \(2017\)](#). These different surveys have been scaled to the same K-correction for X-ray data as shown in [Rodighiero et al. \(2015\)](#). The thick lines show the intrinsic relationships, without considering the possible “small field effect” considering above. Brown thick line shows dependence with mass expected from the co-existence scenario elaborated in Chapter 2. The fact that this line is horizontal is a natural consequence of the model in which all star-forming galaxies have an equal chance to host an AGN, regardless of their mass. On the other hand the diagonal thick orange line shows the idealized expectation of mass dependence from the quenching scenario from Chapter 3, in which the probability of hosting an AGN increases linearly with galaxy mass. The line saturates at high masses as the fraction of star-forming galaxies which are considered to be quenching starts to approach unity. The red and blue lines show our expectation for the actually observed relations, after the “small field effect” correction, in COSMOS and CDF-S field, respectively. With dotted lines we show results from co-existence model in Chapter 2, while with dotted lines we show results from the quenching model described in Chapter 3. The shaded regions were created by running the simulation of the results from quenching model 100 times and selecting the 16th and 84th quantile to indicate the possible spread of the results. Because COSMOS field is much larger and contains more

galaxies, the spread is naturally smaller, as seen in the figures.

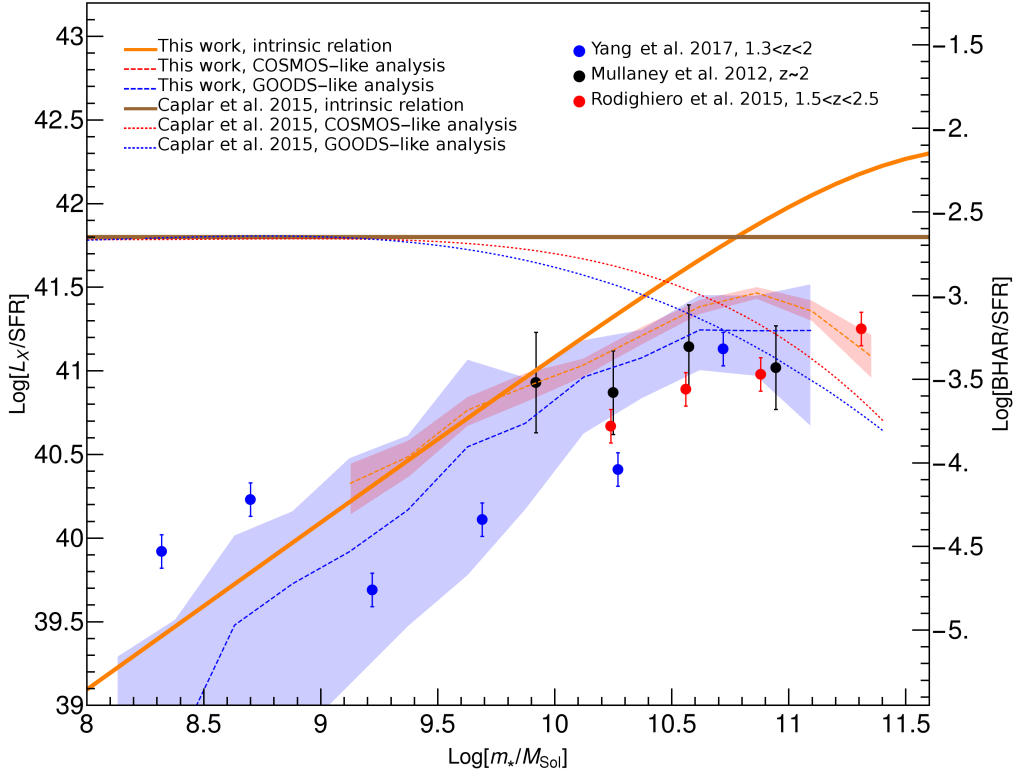


Figure 4.4: Dependence of L_X/SFR on the stellar mass, prediction from our model and the data at $z \sim 2$. The points are from observational studies indicated in the Figure and the lines show our predictions from using co-existence scenario (denoted with “Caplar et al. 2015”) and the quenching scenario (denoted with “This work”). Full lines are showing schematically the difference of the mass dependence between these two scenarios, while red and blue lines show our predictions for observational results in realistic surveys. See text for more details.

The quenching model is fully consistent with the observational data once the fact that the very luminous objects are likely missing in the available surveys is considered. The effect is such that it can easily recreate the observed lack of mass dependence in the $\langle L_X/SFR \rangle$ relationship at relatively high masses ($m_* > 10^{10} M_\odot$) as seen in Mullaney et al. (2012b), even though intrinsic relation has almost linear dependence with stellar mass. Rodighiero et al. (2015) argues, from analysing COSMOS field, for a steeper relationship, with $\langle L_X/SFR \rangle \propto m_*^{0.43 \pm 0.09}$. This steeper relationship is exactly what we would expect in the quenching scenario when considering a larger, less biased field!

The second difference that we expect to see between the analysis in the COSMOS and CDF-S fields is the normalization. As shown in Figure 4.3, our prediction is that normalization of the $\langle L_x/SFR \rangle$ relation should be higher in the larger field which is less affected by the “small field effect”. That is not what is seen in Figure 4.5 where the normalization of studies in both fields is seen to be comparable. However, these studies

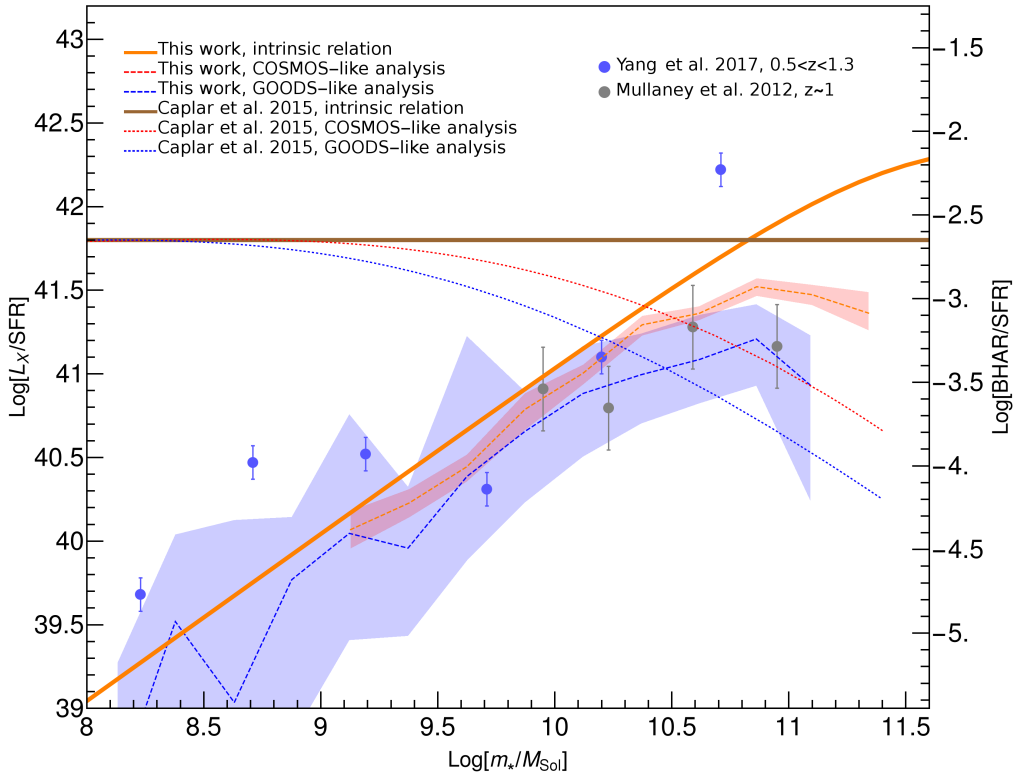


Figure 4.5: Dependence of L_X/SFR on the stellar mass, prediction from our model and the data at $z \sim 1$. See Figure 4.4 for explanation of labels.

have been done on different datasets and using different methods to estimate the SFR. Given these differences we believe it would be unwise to attach too much significance to this disparity.

At lower galaxy masses our predictions follow the intrinsic correlation as these galaxy host black hole that accrete at luminosities that are well probed by surveys. We see that the data points from Yang et al. (2017), which is the only study covering these masses, are below the results measured from galaxies with larger masses, qualitatively in accordance with our predictions. Yang et al. (2017) notes that contribution of the X-ray background, not explicitly modelled here, acts to flatten out the dependence at low stellar masses and this is probably the reason why the data at low stellar masses do not continue to follow linear trend with the stellar mass.

This mass dependence in these results is already in contradiction with the co-existence scenario, in which no mass-dependence is expected. If we also take into account the maximal luminosities observed in the fields, we would expect that the observed $\langle L_X/SFR \rangle$ should actually fall towards higher galaxy masses. To look at it another way, in general, we expect the difference in the slope of $\langle L_X/SFR \rangle - m_*$ dependence between two scenarios to be of an order of unity. This will be the case not only for the intrinsic relations, but also

for the relations with observational effects included. As we have shown that the quenching scenario produces an apparent lack of correlation in the observations of small, possibly biased, fields, the difference of slope of order of unity suggests the negative correlation in observation for the co-existence scenario, as shown in Figures 4.4 and 4.5.

As a final note, we mention that the results in this section are somewhat preliminary as there are several other ways to test these observational results. In the near future we aim to confirm our reasoning with (i) statistically evaluating model predictions expected from COSMOS and CDF-S sized fields, without special luminosity cuts, and (ii) by modelling non-stacked data, i.e., modelling $\langle L_X/SFR \rangle$ only for the AGN which are actually detected in X-ray surveys. This is the most direct way to test the different scenarios as it avoids possible problems due to stacking and it automatically fully accounts for the peculiarities of the observational surveys and their relatively small fields which might bias the result.

4.4 Summary and conclusions

In this chapter we have presented direct comparison between two possible scenarios characterizing galaxy - black hole co-evolution that we described in Chapters 2 and 3. We have pointed out that the main difference between the co-existence and quenching scenario was in the mass function of galaxies that are hosting AGN. We have therefore conducted this comparison with the studies that follow simultaneously evolution of mean properties of both galaxy and AGN population. Our main findings can be summarized as follows:

1. Mean star-formation in AGN host galaxies is only weakly dependent with the luminosity of AGN in the quenching scenario, which is in excellent agreement with the observed relations from Rosario et al. (2012), Mullaney et al. (2012a), and Rodighiero et al. (2015) that show little luminosity dependence in the observed range. The co-existence scenario, on the other hand, predicts linear correlation between the star-formation rate and AGN luminosity in the luminosity range covered by the observations.
2. When studying dependence of mean AGN luminosity as a function of galaxy mass, the observed mass dependence can substantially differ from the actual relation in the Universe if the small fields studied do not include high luminosity AGN.
3. We make predictions for the mean AGN luminosity/SFR ratio as a function of galaxy mass in the quenching and co-existence scenarios in COSMOS and CDF-S fields, using actual maximal luminosities of AGN in those fields. We find that the quenching scenario offers better description than the co-evolution scenario for the observed galaxy mass dependence of $\langle L_X/SFR \rangle$ in Rodighiero et al. (2015) and Yang et al. (2017). Quenching scenario is also consistent with Mullaney et al. (2012b), once the actual maximal luminosities of AGN in the survey are modelled. The quenching model also correctly predicts a steeper observed slope in the COSMOS field,

$\langle L_X/SFR \rangle \propto m_*^{0.5}$, rather than no dependence with galaxy mass (at relatively high stellar masses, $M^* > 10^{10} M_\odot$) that is seen in CDF-S field. This is a consequence of less bias affecting the intrinsic relation in the larger and more representative COSMOS field.

With this we conclude our study of the co-evolution of galaxies and black holes. In Chapters 2, 3, and 4 we have presented a simple phenomenological model which, despite its simplicity, is capable of explaining the number of observations in the local and high-redshift Universe. We have pointed out a number of predictions and possible misconceptions which can arise from interpretations of the data which involves redshift-evolving quantities. Full summary of our results is presented in Chapter 6.

5 | Optical variability

The content of this chapter is based on [Caplar et al. \(2017\)](#).

In this chapter we adopt a very different approach to study the AGN population. We will still use large datasets and explore the evolution of the same AGN properties, such as mass and luminosity, but with the data collected through synoptic surveys. While in the previous chapter AGN properties have been inferred indirectly from the AGN-galaxy co-evolution on cosmological time-scales, this new approach will be directly testing the accretion disk and its structure. Overview of the topic of AGN variability has been given in Section 1.4. Several of the more technically involved sections are presented in dedicated Appendix.

5.1 The sample & data

Our main dataset comes from the Palomar Transient Factory (PTF) and intermediate Palomar Transient Factory (iPTF). The PTF/iPTF is studying the transient sky using the 48'' telescope on Mount Palomar. It employs the former Canada-France-Hawaii Telescope 12K \times 8K camera with 11 active chips which together cover an effective 7.26 deg² field of view ([Rahmer et al., 2008](#), [Law et al., 2009](#), [Rau et al., 2009](#)). Most of the PTF/iPTF observations, which started in the March 2009, are taken in the Mould $\langle r \rangle$ filter ($\lambda = 6580 \text{ \AA}$). The median seeing of the images is about 2.2''. Individual exposures are 60 seconds and the surveys cover $\sim 8000 \text{ deg}^2$ of the northern sky above declination of -30° . Further information about the performance of the survey and the data preparation procedures are available in [Law et al. \(2009\)](#) and [Laher et al. \(2014\)](#). Initial calibration for the survey was reported in [Ofek et al. \(2012\)](#), but we decided to recalibrate the quasar data with our specific scientific goals in mind. This re-calibration is presented below in

Section 5.2.

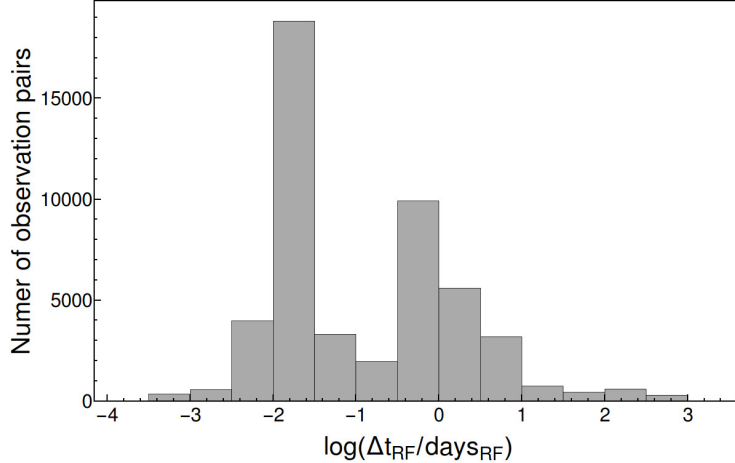


Figure 5.1: Distribution of observational cadence in the sample. The time differences have been transformed into the quasar restframe.

This analysis is based on all the observations that were taken in the r -band in the six year interval between the start of the survey in March 2009 and April 2015. A small fraction of images were taken with g -band and $H\alpha$ filters, but these were not included due to the low number of available observations. We only use images which are not significantly affected by clouds, i.e., if the mean observed instrumental magnitudes of our reference objects (see below) are within 0.2 mag of the instrumental magnitudes in the 5 best observations of that field. This cut removes a significant fraction of the available data ($\sim 30\%$), but is necessary in order to achieve a high quality of calibration (see also Appendix A.1), not least because, with such a large field of view and short exposure, the effects of clouds can vary significantly across the field of view. The survey consists of a large number of images of specific regions of the sky, or “fields”, each-defined by a single field-center. Our work only includes those fields for which images at more than 10 epochs are available.

The sample of quasars was constructed from the homogeneous sample of AGN identified in the Sloan Digital Sky Survey Data Release 7 (SDSS-DR7) by Shen et al. (2011). All physical quantities are taken from the accompanying catalog, except for black hole masses which are taken from a catalog with improved estimates in Trakhtenbrot & Netzer (2012). In cases where mass estimates from Trakhtenbrot & Netzer (2012) are not available, we retain the Shen et al. (2011) mass estimates. We have verified that the choice of the black hole mass catalog makes no significant difference to our final conclusions. In both of the catalogs, black hole masses are estimated using the single-epoch method in which the mass is estimated from the width of the broad emission lines ($H\beta$, $\text{Mg II } \lambda 2798$ or $\text{C IV } \lambda 1549$) combined with the monochromatic luminosity at 5100, 3000 or 1450 Å, respectively. The exact choice of the line and monochromatic luminosity that is used depends on the redshift of the source.

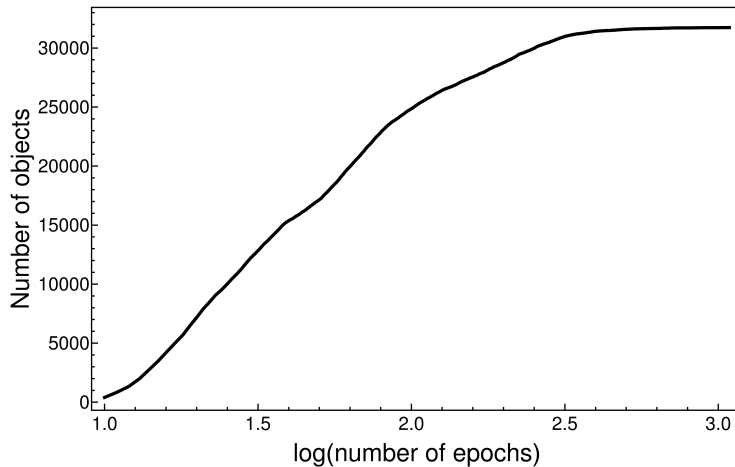


Figure 5.2: Cumulative distribution of the number of observations for the objects in the sample. There are $\sim 14,500$ quasars with light curves with more than 50 observations, and $\sim 1,750$ light curves with more than 250 observations.

We have then selected only quasars for which the median instrumental magnitude in the PTF/iPTF was brighter than -9 mag which corresponds broadly to $r = 19.1$ mag.¹ We impose this conservative cut in order to be sure that we can fully capture the variability of the AGN, both through their bright and their faint phases. This choice is discussed further in Appendix A.1. We also exclude objects in areas around the bad columns on the chips. To accommodate small variations in the pointing of each field, these are chosen to be 100 pixels wide, leading to a loss of about $\sim 6\%$ of the field of view.

Our final sample consists of 28,096 AGN with the total of 2.4 million photometric data-points. The PTF/iPTF survey also has a number of special fields which were configured for specific projects. Some of the selected AGN therefore appear in different PTF-fields and CCD chips. As our recalibration is chip and field specific (see Section 5.2), we treat these duplicated AGN as completely separate objects for calibration and analysis purposes. There are 3634 such objects, so our sample in fact consists of 31,730 calibrated light curves. In Figures 5.1, 5.2 and 5.3 we present the distributions of the survey’s observational cadence, the number of observations per light curve and the total duration of the light curves.

At two points in our analysis, we also use light curves from the SDSS Stripe 82 survey. The first is when we estimate, and correct, the wavelength dependence of AGN variability. The second is to compare with the results of our PSD analysis. The Stripe 82 survey covered an area of 290 deg^2 and provides 5-band photometric measurements, with an average of 60 observations in each band per quasar. Photometric accuracy of the SDSS is

¹Instrumental magnitudes refer to the measured brightness of the sources, as obtained from the automatically generated catalogs provided by the PTF collaboration. Details regarding these measurements are given in [Laher et al. \(2014\)](#).

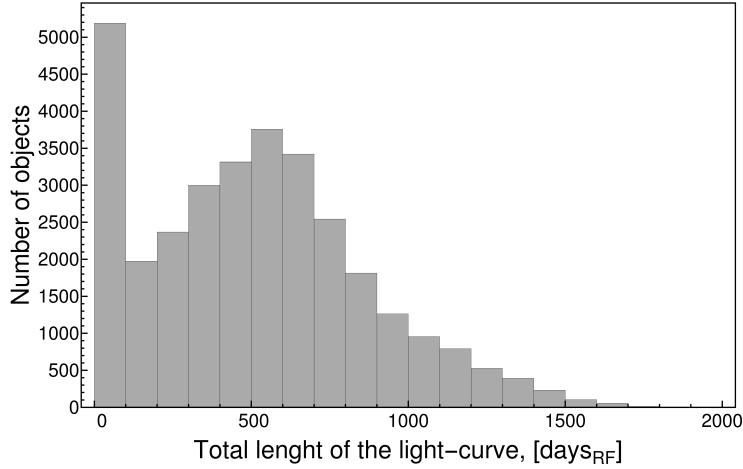


Figure 5.3: Cumulative distribution of the time span of the observations for the objects in the sample, i.e., the total length of the light curve between the first and the last observation. The time spans have been transformed into the quasar restframe.

excellent, with the photometric errors smaller than $\sigma=0.018$ mag in the g , r and i bands and 0.04 mag in u and z bands for sources with $r < 19$ mag. We refer the reader to [MacLeod et al. \(2012\)](#) for an extensive discussion of this survey and data products.

5.2 Re-calibration of the PTF AGN Light Curves

Although the initial calibration from [Ofek et al. \(2012\)](#) is available for all of the AGN in our sample, we decided to recalibrate all of the AGN photometry in a way that was optimized to our scientific goals. This led to a significant reduction in the systematic errors. A more detailed comparison of the calibrations is presented in [Appendix A.2](#).

In general, we use a relative calibration as we are primarily interested in the differences in the brightness of the quasars as a function of time rather than the absolute measurements. We broadly follow the procedure and philosophy in [Levitan et al. \(2011\)](#) and [Ofek et al. \(2011\)](#), for which we give a brief overview below. The main idea is to minimize the scatter in a set of reference objects, similar to the targeted quasars, that are available in the same images.

We first identify, in each field, the five “best” observations, i.e., epochs, simply in terms of the number of detected objects. A set of potential “reference” objects is then constructed to be all objects that (a) were observed in at least 4 out of these 5 best observations for a given field and chip combination, (b) have SExtractor CLASS_STAR value larger

than 0.9 and (c) do not have any SExtractor quality flags set in any of the observations (Bertin & Arnouts, 1996). Potential reference objects that were selected in this fashion were cross checked against the AGN SDSS-DR7 catalog and known AGN were removed. We then assign an initial value of brightness to each of these reference objects, calculated as the mean instrumental magnitude of the object in these best observations.

For each object for which we want to create a calibrated light curve, we then select a subsample of up to 50 reference objects which are in the same chip and same field. These are chosen to be within 0.25 mag of the median magnitude of the five “best” observations of the target in question. If, as was usually the case, there are more than 50 objects that satisfy this criteria then we select the 50 spatially nearest ones (in the same chip) to the source that we are calibrating. If there are fewer than ten available reference objects, the target is discarded.

Using these reference objects we then fit, using standard least-squares, the following relation for each of the targets:

$$m_{ij} \cong z_i + \bar{m}_j, \quad (5.1)$$

where m_{ij} is a $p \times q$ matrix that contains all the p measured magnitudes of the q reference objects, and i is the epoch index and the j is the index of reference object. From the results of the fit we can determine \bar{m}_j which is the mean magnitude of the j th reference object and the z_i which is the zero-point of the i th epoch observation (Ofek et al., 2012). We apply the method iteratively, by removing reference objects which are highly variable ($\chi^2/\text{d.o.f.} > 3$ for the constant magnitude fit) and adding “cosmic error” term to all the measurement in the epoch for which the residuals are deemed to be too large (as suggested in Ofek et al., 2012).

We then use the final zeropoints, z_i , determined for this target for each epoch, to calibrate the relative light curve for the quasar. For each observation of a target at a given epoch, we also estimate the measurement errors σ_i from the spread of the reference objects around their respective means. We do not include specifically any color dependant terms in our calibration as we demonstrate that for stars there is no dependence of residuals on colour. We shown this in Appendix A.3.

Clearly, the estimate of the zero point z_i at a given epoch will have uncertainties since it is based on data from a finite number of reference objects (maximum 50). This estimate will introduce a spurious apparent variability to the target quasar that must be included in calculating the SF. It is easy to show that the additional variance in the quasar variability will be equivalent to $\sigma^2/(N - 1)$ where N is the number of reference objects used and σ^2 is initially estimated variance. This additional variance can therefore be easily included in the final estimate of the measurement error.

Following the procedure in [Schmidt et al. \(2010\)](#) we clean our resulting quasar light curves to remove spurious outliers. We do this by applying a 5-point median filter to the light curves and removing individual observations which satisfy the criterion

$$|m_i - m_{m,i}| > 0.3 \text{ mag} \times (\Delta t_{i,i-1}/100)^{1/2} + 5\sigma_i, \quad (5.2)$$

where m_i is the observed magnitude, $m_{m,i}$ is the resulting magnitude after applying 5-point median filter, $\Delta t_{i,i-1}$ is the temporal separation of i th and $i-1$ observation measured in days in the quasar rest frame and σ_i is the estimated error of the i th observation. Given that the light curves have large seasonal gaps, the time-dependent term ensures that we do not remove variability which is not spurious, but which might have occurred during the long observational break. We have compared our results with and without the time-dependent term in the Equation (5.2) and we find that our main conclusions are unchanged. This cleaning removes 0.1% of the data points. Visual inspection of the images associated with these discrepant data-points confirms that they were often compromised by satellite or aircraft trails ².

5.3 Analysis Methods

5.3.1 Construction of the structure functions

In order to study the correlation of variability with the physical parameters of the quasars, we construct the ensemble structure functions. We split our quasar sample into 64 bins defined by the physical properties of redshift, luminosity and black hole mass, as follows. Firstly we split our sample into 4 redshift bins that each contain the same number of quasars. Each of these 4 redshift bins is then subdivided equally into 4 luminosity bins, and finally each of these bins is further divided into 4 mass bins. Mean values for redshift, mass and luminosity in each of these bins are shown in the Figure 5.4 and in the Table 5.1. Although the bins are different in size and are irregularly spaced in parameter space, this procedure ensures that each of the final 64 bins contains the same number of quasars and consequently also approximately the same number of photometric observations. Since the uncertainty in the mean properties is driven by scatter within the population, this means that the uncertainty in the mean behaviour should be comparable in all of the bins.

In each bin, we then construct the structure function using Equation (1.11), modified as described in Section 5.2. Firstly we transform all of the quasar observations into the quasar rest-frame, i.e., we divide all of the observation times by the time-dilation factor of $(1+z)$, where z is the redshift of the quasar. For each of the 64 bins, we then create the structure function in 20 time bins of time interval Δt , chosen so that each time bin contains the same number of pairs of observations. Outside of the Δt associated with the seasonal gaps in the survey observations, the spacing of these bins is roughly equidistant

²Re-calibrated data is available at https://github.com/nevencaplar/PTF_AGN

in units of $\log \Delta t$, with a typical width of ~ 0.13 dex.

This divides the whole survey, which consists of 250 million pairs of photometric observations, into 1280 bins of the structure function which contain, on average, 150,000 observational pairs each. However, it should be realised that, within each structure function, the number of objects which are contributing to the different Δt bins varies with Δt . While time-bins describing short-term Δt (~ 1 day) contain typically 400-500 objects, because essentially all quasars in a given redshift-luminosity-mass bin will be present, the number contributing to the longest-term time bins drops to ~ 150 . This is a consequence of the inhomogeneous observing strategy in which objects are usually observed multiple times during the same or adjacent nights and only a subset of the sky was observed repeatedly during the full duration of the survey.

Because our data sample is quite heterogeneous, with different quasars represented by a very different number of observations, there is some danger of the results being dominated by a small number of objects that were observed very often. In the case of the SF, each light curve comprising p data points will contribute p^2 times to the structure function. Given that quasars display a wide range of variability properties, this could significantly bias our results, further exacerbating the problem that individual quasars may contribute to the SF² with different weights at different Δt . To minimise this, when constructing the SF² in each of the time bins Δt , we restrict the number of observational pairs from each quasar in a given Δt bin to be a maximum of 20 (randomly chosen) pairs. If the quasar does not contribute with 20 data-pairs to the particular time bin its contribution is discarded. This limits the weight given to the most densely sampled quasars.

To estimate the uncertainties in the SF² arising from the scatter in the population and from the variations in the observational data described in the previous paragraphs, we employ resampling procedures. We repeat the SF² construction procedure 100 times using N randomly selected objects from the N available objects, allowing repetition. When an object is included twice, it is treated as “new”, e.g., with a different randomly chosen set of 20 observational pairs. We estimate the mean SF² and error on the SF² from the distribution of the results.

The quasar SF² constructed in this way show a significantly non-zero value of the SF² at short time scales, where the SF² should in principle converge towards zero for zero Δt . For example, within a single night the SF² is typically $10^{-3.5}$, i.e., a residual variability of about 0.01-0.02 mag. This could well be the signature of unrecognised systematic uncertainties, and similar samples of stars might be expected to show similar effects. We have therefore constructed control samples of stars which were matched in brightness to the AGN samples. These stellar samples were processed, using the above procedure, in exactly the same way as if they were quasars. Of course, this control sample of stars could show

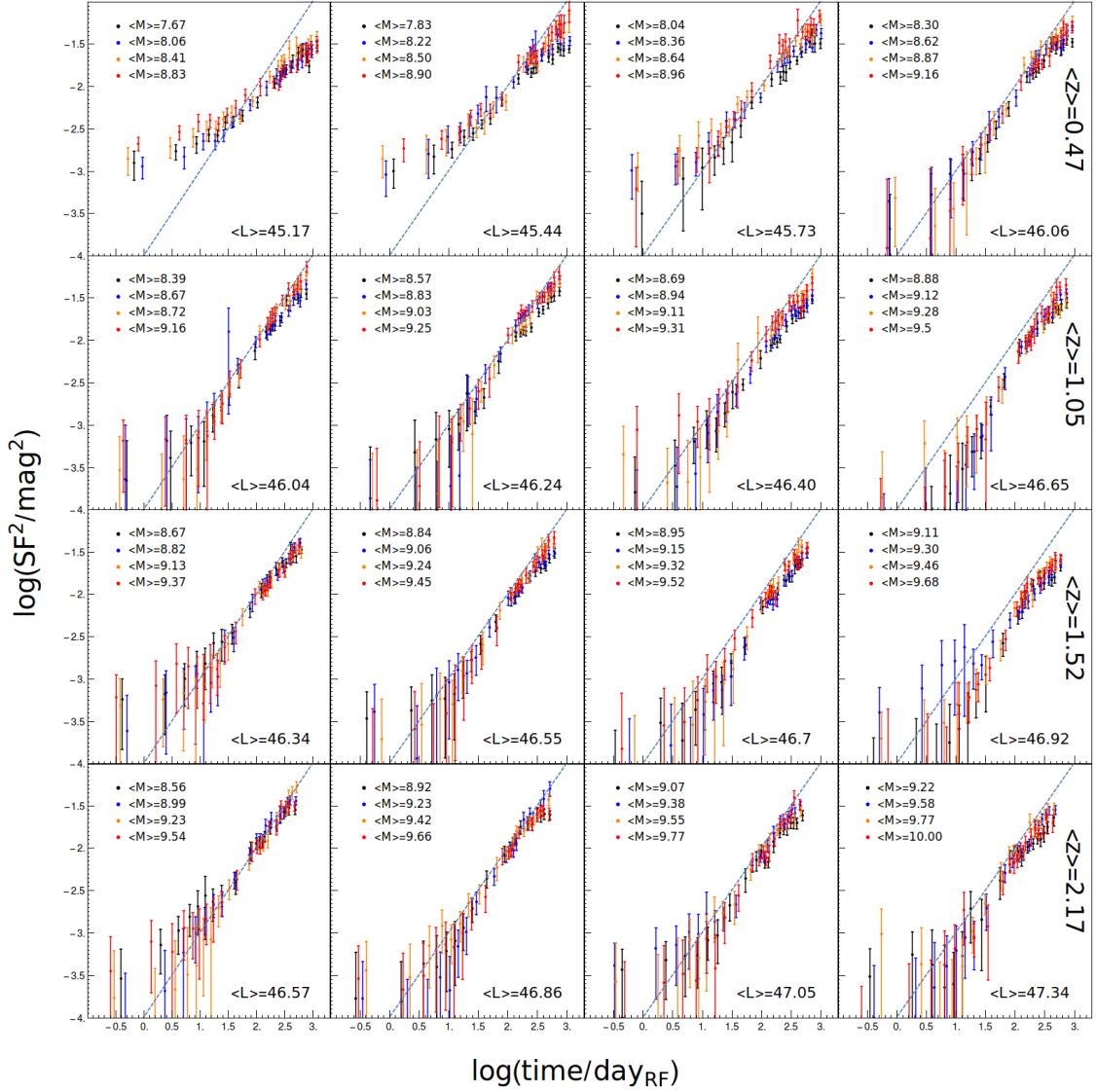


Figure 5.4: SF^2 split by redshift, luminosity and mass. Each row shows structure functions taken from the same redshift bin, as indicated on the right-hand side. Each panel within each row, then shows the structure functions of quasars in a given luminosity bin, which is then further split within each panel into black hole mass by denoting the points in different colors. In each panel, we show the mean luminosity and the mean mass is given in the key, both in logarithmic units. The dashed line, which is the same on all of the panels, has a functional dependence of $-4 + \log t$ and is given to help guide the eye in comparing panels. Except at the lowest redshifts and luminosities, where the photometry could be affected by the host galaxy, the structure functions are consistent with zero as Δt tends to zero.

genuine stellar variability effects. This procedure is explained and discussed in detail in Appendix A.4, but we provide brief overview here. What is seen is that the stellar SF^2 is flat over a wide range of Δt , with a similar amplitude to that of the quasars at very small Δt . The stellar SF^2 is independent of the colour of the stars. It is therefore likely that the

estimate of the observational errors on each photometric point has slightly underestimated the observational uncertainties in the survey (they appear to capture around 90% of the variance). In order to account for this effect we simply subtract the stellar SF² from the initial AGN SF², to yield a final estimate of the AGN SF².

We show the corrected SF² in Figure 5.4. We see that we are able to capture the variability for the vast majority of objects from shortest ($\lesssim 1$ day) to very long (several years) scales. Except for a small excess variance at small Δt at the lowest redshifts and luminosities, the SF² generally converge towards zero as Δt approaches zero, as expected. The two lowest redshift and lowest luminosity bins may contain residual calibration errors, possibly due to host galaxy contributions. When conducting the analysis below we take special care to verify that none of our results is being driven by these two bins.

5.3.2 Wavelength correction

When comparing the measurements of SF² of quasars of different properties, we would ideally compare them at the same rest-frame wavelength, given that variability is known to be wavelength dependent (e.g., MacLeod et al., 2010). Since our data is only taken in a single (observed) band, this involves a redshift-dependent correction to the observed amplitudes, on top of correction to the timescales from the cosmological time-dilation. This correction cannot be estimated from our data alone but can be estimated from the multi-wavelength quasar data from the SDSS Stripe 82 in MacLeod et al. (2012).

We separate the available SDSS data into 5 redshift bins and then split each redshift bin into 5 luminosity bins. In each of the resulting 25 bins we estimate the ratios of the SF² in the g - and r - bands, and in the r - and i - bands. We estimate this ratio with all of the available data in the single bin as we assume that the color dependence of variability is independent of time. We do not use the u and z bands because of the larger errors associated with the photometric measurements in these bands. This procedure, done in a single redshift bin, enables us to estimate the dependence of the SF² across the gri wavelength range which spans the r -band data of the (i)PTF. Splitting the redshift bin into different luminosity bins allows us to check if this wavelength dependence changes with luminosity, but we do not in fact detect any such luminosity trends and can treat these five luminosity bins as independent estimates of a luminosity-independent relation.

In order to connect these single-redshift estimates across a range of redshift, we construct a redshift ladder, as shown in the Figure 5.5. We first force the gri SF² curves from the five luminosity bins at the lowest redshift to be coincident at a rest-frame 4000 Å by making small vertical adjustments. We then require the SF² variance curves from the next two redshift bins to overlap with each other and with the ones from the lowest

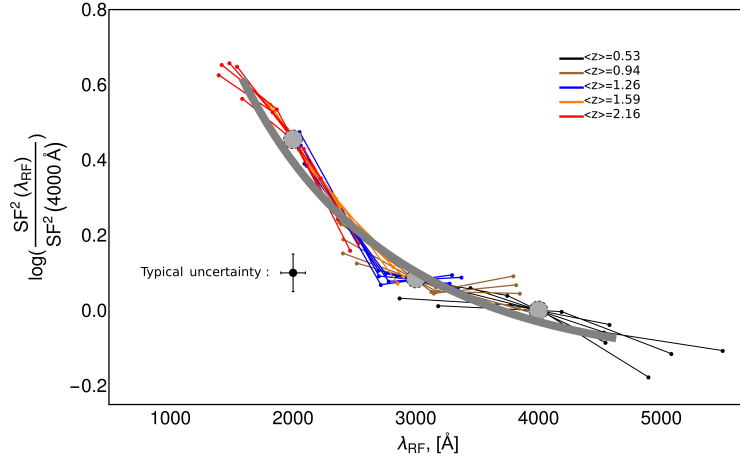


Figure 5.5: The redshift ladder constructed to determine the dependence of variability as a function of wavelength. We estimate the ratio of excess variance (SF^2) between the g-r band and r-i band in the SDSS Stripe 82 in different redshift bins and then demand that these estimates agree at the fixed points of 2000, 3000, and 4000 Å. The grey line, which we show in the wavelength range that is probed in this survey, shows a fit to the data (Equation 5.3) which we use in further analysis to characterize the dependency of variability with wavelength. See text for more details.

redshift bin at the shorter rest-frame wavelength of 3000 Å. Finally, we can add the two highest redshift bins, now normalising at 2000 Å. We then fit a second order polynomial to these normalized estimates of SF^2 at different wavelengths to infer:

$$\log \frac{SF^2(\lambda_{RF})}{SF^2(4000\text{\AA})} = -0.03 - 0.815 \log \left(\frac{\lambda}{4000\text{\AA}} \right) + 1.989 \log \left(\frac{\lambda}{4000\text{\AA}} \right)^2. \quad (5.3)$$

We will use the function in Equation (5.3) to renormalise all of our estimates of variability at different redshifts to the value expected at 4000 Å. This choice of rest-frame wavelength corresponds to what is observed within (i)PTF for $z \sim 1$ quasars - typical of our sample. We note that our prescription is consistent with other estimates of the wavelength dependence of quasar variability from the same dataset (MacLeod et al., 2010; Meusinger et al., 2011; Zuo et al., 2012).

5.3.3 Fitting the structure function

As was seen in Figure 5.4, the SF^2 rise uniformly with time, with slopes similar to that expected from a random walk and with possible breaks at long time-scales in some cases. We therefore model the ensemble SF^2 , constructed in each bin of quasar properties and after applying the wavelength correction derived above, with the functional form of a

broken power law. Namely we use

$$\text{SF}^2(\Delta t) = \begin{cases} \phi_0 + \phi_1 \cdot (\Delta t)^{g_1} & \Delta t \leq \Delta t_{br} \\ (\phi_0 + \phi_1 \cdot (\Delta t_{br})^{g_1}) \cdot \left(\frac{\Delta t}{\Delta t_{br}}\right)^{g_2} & \Delta t > \Delta t_{br} \end{cases} \quad (5.4)$$

where the Δt_{br} is the timescale associated with a break in the structure function. We fit the SF^2 function with a double power law to allow for potential changes of slope at long timescales which can be caused by either a real flattening or by statistical fluctuations in the sample (remembering that not all quasars contribute at the longest timescales). The term ϕ_0 in Equation (5.4) allows for the possibility of a time-independent term associated with lingering systematic effects in the calibration. All of the inferred parameters are shown in Table 5.1.

Tab. 5.1 — Fit of SF² with Equation (5.4), table of parameters

$\langle z \rangle$	$\langle \log L \rangle$	$\langle \log M \rangle$	ϕ_0	ϕ_1	g_1	g_2	t_{br}	$\chi^2/\text{d.o.f}$
0.26	45.15	7.67	-2.88±0.12	-3.94±0.24	0.83±0.098	0.242±0.11	2.70±0.088	0.75
0.28	45.17	8.06	-3.02±0.15	-4.08±0.26	0.93±0.12	0.531±0.071	2.18±0.085	0.37
0.29	45.17	8.41	-2.77±0.10	-4.29±0.31	1.04±0.13	0.348±0.14	2.49±0.14	0.42
0.30	45.18	8.83	-2.67±0.083	-3.80±0.25	0.78±0.10	0.461±0.081	2.25±0.12	0.66
0.38	45.42	7.83	-3.68±0.61	-3.83±0.26	0.86±0.11	0.393±0.074	2.35±0.083	0.85
0.40	45.44	8.22	-4.37±0.71	-3.34±0.13	0.67±0.057	0.327±0.10	2.54±0.15	0.57
0.40	45.44	8.50	-2.77±0.094	-4.78±0.37	1.29±0.17	0.699±0.11	2.18±0.098	0.81
0.40	45.44	8.90	-2.82±0.14	-4.01±0.20	0.96±0.082	0.455±0.20	2.73±0.19	0.56
0.51	45.71	8.04	-5.66±1.8	-4.04±0.20	0.96±0.11	0.519±0.081	2.33±0.19	0.70
0.54	45.72	8.36	-10.7±1.4	-3.68±0.11	0.82±0.052	0.391±0.11	2.53±0.098	1.1
0.56	45.74	8.64	-15.8±2.2	-3.58±0.13	0.80±0.058	0.387±0.14	2.60±0.11	1.1
0.55	45.74	8.96	-3.68±0.58	-4.15±0.29	1.12±0.15	0.453±0.14	2.36±0.16	0.46
0.64	46.01	8.30	-4.33±0.78	-4.27±0.21	1.04±0.088	0.266±0.15	2.60±0.082	0.34
0.67	46.05	8.62	-4.72±1.6	-4.36±0.26	1.13±0.12	0.482±0.13	2.43±0.11	0.73
0.69	46.08	8.87	-7.53±0.85	-4.86±0.25	1.43±0.13	0.695±0.082	2.15±0.078	0.44
0.66	46.11	9.21	-4.30±0.50	-4.45±0.21	1.19±0.11	0.751±0.074	2.10±0.080	0.28
0.90	45.99	8.39	-4.43±0.60	-4.20±0.18	1.03±0.079	0.364±0.19	2.57±0.12	0.42
0.91	46.02	8.67	-4.19±0.57	-4.05±0.17	0.98±0.086	0.676±0.081	2.25±0.12	0.56
0.95	46.05	8.87	-4.29±0.56	-4.60±0.30	1.29±0.15	0.719±0.090	2.16±0.11	0.29
0.97	46.07	9.16	-11.3±1.3	-4.37±0.23	1.16±0.11	0.635±0.17	2.45±0.17	0.43
1.02	46.24	8.58	-3.69±0.44	-4.84±0.28	1.34±0.14	0.787±0.053	2.08±0.049	0.37
1.03	46.25	8.84	-4.51±0.67	-4.95±0.28	1.49±0.14	0.707±0.057	2.07±0.050	0.35
1.06	46.25	9.03	-8.03±1.0	-4.35±0.22	1.11±0.10	0.530±0.20	2.56±0.15	0.35
1.05	46.25	9.25	-5.89±0.65	-4.63±0.28	1.32±0.14	0.692±0.095	2.19±0.096	0.30
1.08	46.39	8.69	-3.93±0.66	-4.56±0.37	1.16±0.18	0.746±0.087	2.15±0.16	0.46
1.10	46.40	8.94	-5.40±1.1	-4.31±0.19	1.05±0.086	0.455±0.17	2.49±0.092	0.26
1.12	46.41	9.11	-7.75±0.84	-4.89±0.32	1.40±0.16	0.794±0.12	2.15±0.12	0.57
1.11	46.41	9.31	-6.46±0.47	-4.08±0.24	1.02±0.12	0.481±0.14	2.30±0.12	0.81
1.09	46.59	8.88	-14.0±0.92	-5.07±0.27	1.41±0.15	0.631±0.080	2.19±0.10	0.26
1.14	46.61	9.12	-6.11±1.3	-5.03±0.19	1.35±0.089	0.664±0.17	2.46±0.098	0.30
1.15	46.65	9.28	-9.72±1.0	-4.68±0.31	1.20±0.14	0.499±0.17	2.42±0.085	0.58
1.16	46.69	9.51	-10.9±1.7	-4.84±0.19	1.28±0.091	0.889±0.20	2.43±0.28	0.38
1.45	46.29	8.67	-7.20±2.2	-3.83±0.21	0.90±0.096	0.419±0.13	2.39±0.12	0.35
1.45	46.34	8.92	-3.64±0.36	-4.72±0.31	1.32±0.15	0.770±0.080	2.09±0.068	0.34
1.44	46.37	9.13	-4.11±0.81	-4.08±0.22	0.98±0.10	0.365±0.17	2.60±0.15	0.59
1.45	46.37	9.37	-4.21±0.87	-4.26±0.23	1.08±0.10	0.654±0.14	2.24±0.17	0.64
1.51	46.55	8.84	-16.7±1.7	-4.27±0.19	1.07±0.094	0.602±0.12	2.22±0.11	0.21
1.49	46.55	9.06	-10.4±0.82	-4.23±0.18	1.04±0.082	0.467±0.20	2.47±0.085	0.46
1.47	46.56	9.24	-10.2±0.92	-4.28±0.16	1.08±0.071	0.451±0.19	2.57±0.064	0.38
1.50	46.55	9.45	-8.60±1.4	-4.79±0.28	1.34±0.14	0.880±0.089	2.11±0.071	0.20
1.55	46.70	8.95	-10.1±0.82	-4.65±0.21	1.22±0.11	0.759±0.096	2.16±0.095	0.24
1.53	46.70	9.15	-5.22±0.72	-4.49±0.16	1.10±0.069	0.480±0.22	2.68±0.15	0.79
1.55	46.71	9.32	-8.35±1.0	-5.06±0.31	1.45±0.15	0.850±0.086	2.13±0.11	0.30
1.55	46.71	9.52	-12.2±0.85	-4.07±0.15	0.96±0.065	0.408±0.19	2.64±0.13	0.71
1.59	46.89	9.11	-5.63±1.1	-5.09±0.38	1.38±0.18	0.492±0.17	2.25±0.084	0.26
1.59	46.89	9.30	-4.27±1.5	-4.43±0.39	1.06±0.18	0.591±0.19	2.41±0.20	0.61
1.60	46.94	9.46	-4.36±0.51	-4.69±0.24	1.19±0.11	0.506±0.20	2.48±0.087	0.70
1.59	46.99	9.68	-6.20±1.0	-5.15±0.23	1.46±0.12	0.649±0.11	2.18±0.074	0.28

Tab. 5.1 — (cont'd)

$\langle z \rangle$	$\langle \log L \rangle$	$\langle \log M \rangle$	ϕ_0	ϕ_1	g_1	g_2	t_{br}	$\chi^2/\text{d.o.f}$
2.04	46.48	8.56	-8.71±1.8	-3.59±0.14	0.80±0.066	0.324±0.17	2.49±0.16	0.33
1.96	46.57	8.99	-4.31±0.53	-4.00±0.17	1.01±0.080	0.426±0.17	2.44±0.11	0.37
1.97	46.61	9.23	-6.80±1.1	-4.30±0.20	1.12±0.090	0.616±0.24	2.57±0.21	0.42
2.03	46.64	9.54	-3.86±0.61	-4.10±0.24	1.02±0.11	0.343±0.17	2.47±0.086	0.40
2.05	46.85	8.92	-6.65±0.84	-4.39±0.22	1.18±0.11	0.420±0.13	2.20±0.079	0.33
1.98	46.85	9.23	-4.86±0.57	-4.69±0.23	1.29±0.12	0.732±0.22	2.37±0.17	0.53
2.06	46.86	9.42	-10.1±1.3	-4.00±0.17	0.98±0.085	0.522±0.19	2.40±0.18	0.44
2.05	46.88	9.66	-6.57±0.73	-4.40±0.26	1.17±0.13	0.484±0.15	2.25±0.097	0.31
2.22	47.04	9.07	-5.57±1.6	-4.29±0.26	1.04±0.12	0.423±0.19	2.45±0.13	0.95
2.17	47.05	9.38	-3.29±0.16	-4.84±0.30	1.35±0.14	0.633±0.15	2.28±0.065	0.34
2.13	47.05	9.57	-4.41±0.99	-4.61±0.39	1.27±0.19	0.522±0.13	2.19±0.089	0.33
2.21	47.08	9.77	-6.41±1.5	-4.48±0.21	1.17±0.095	0.549±0.21	2.43±0.11	0.66
2.56	47.28	9.22	-8.46±0.73	-4.57±0.31	1.22±0.16	0.548±0.12	2.05±0.049	0.44
2.30	47.27	9.58	-4.93±0.85	-4.53±0.21	1.18±0.092	0.582±0.23	2.41±0.12	0.42
2.44	47.31	9.77	-12.9±1.1	-4.61±0.28	1.25±0.14	0.707±0.16	2.20±0.14	0.78
2.61	47.40	10.0	-7.85±1.3	-4.67±0.30	1.25±0.16	0.484±0.18	2.19±0.10	0.32

We note that while we use a broken power law to describe our SF² functions by ensuring a good fit, we do not think it is safe to ascribe physical meaning or significance to the timescales of the possible breaks which we always find on the scales comparable to the total length of the survey. The main reason for this is that, as noted above, different quasars will contribute with different weights to the SF² at different Δt , because of the heterogeneous temporal coverage of the (i)PTF survey in different fields. Only a relatively small number of quasars have photometric data covering the full length of the survey. In quite general terms, it is clear that features in the SF on timescales comparable to the length of the survey should be treated with some caution because of limited sampling at these timescales, even for individual objects (e.g., [Emmanoulopoulos et al., 2010](#)).

5.3.4 Construction and testing of PSDs

Power spectrum analysis presents a powerful alternative to structure function analysis. In this section we describe the analysis of the data using this independent method. While the SF² analysis was used on the ensemble of objects, the PSD analysis can be only used on individual light curves. We will be using the code presented in [Kelly et al. \(2014\)](#) that estimates the PSD of a light curve by modelling it as a continuous auto-regressive moving average (CARMA) process. This method is suitable for use even when using data with non-uniform time sampling with large gaps, as in (i)PTF. The tool includes an adaptive MCMC sampler, maximum likelihood estimators and the basic tools for representing the final results of the estimate. We refer the reader to [Kelly et al. \(2014\)](#) for a detailed explanation of the procedure and the code. Previous examples of the AGN variability studied using this algorithm can be found in [Edelson et al. \(2014\)](#) and [Simm et al. \(2016\)](#).

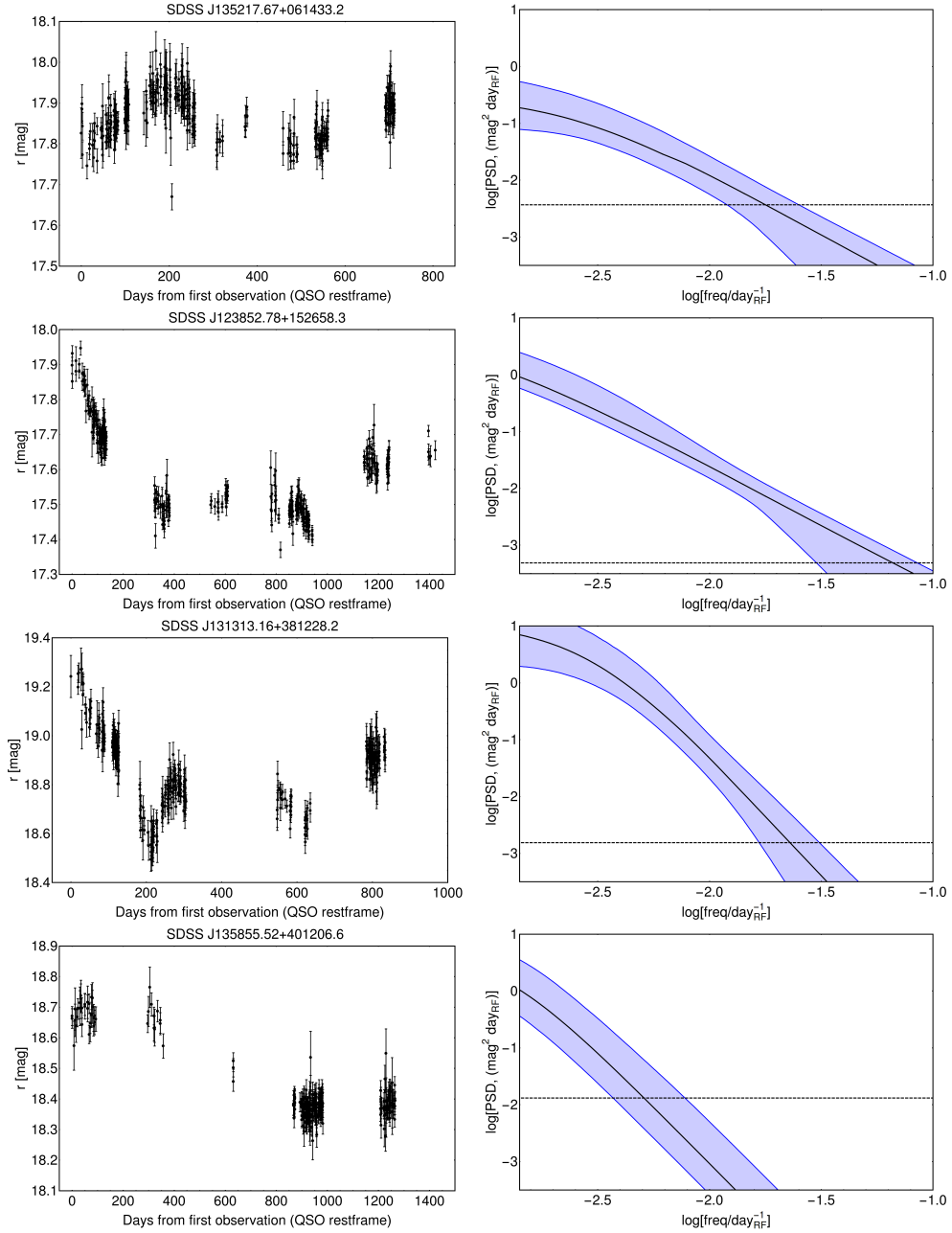


Figure 5.6: Four representative light curves (left) and the resulting PSD spectra (right) obtained using the code presented in Kelly et al. (2014). In the latter, the solid lines show the maximum-likelihood estimate, while the shaded regions shows the 95% confidence interval. The dashed lines show the approximate level of noise in the photometric measurements. All of the right hand panels have the same scaling to ease comparison. The upper two panels show examples of quasars that are well modelled with with power-law PSD, $\text{PSD} \propto f^{-\alpha}$, with slope of $\alpha \sim 2$, while the lower two panels shows two quasars with a steeper PSD, $\alpha \sim 3$.

For setting up the algorithm we use the standard procedure described in Kelly et al. (2014) and further elaborated in Simm et al. (2016). We let the algorithm freely choose the order of the CARMA(P,Q) process on the grid of values P=1,2,3 and Q=0,1,2. It was not found to be necessary to include higher order processes as the light curves were adequately modelled in the vast majority of cases. After choosing the optimal CARMA(P,Q) process we then run the sampler for 75,000 iterations. We show examples of the results in Figure 5.6.

Following testing of this algorithm, we restricted the analysis to well-sampled, extended light curves. Specifically, we include only light curves with more than 60 data points and more than 300 days separation between the first and last observations. Light curves with lower quality tend to perform poorly and often produce results which are of little value due to the large inferred errors on the estimates. Imposing these conditions reduces our sample ten-fold to $\sim 2,200$ quasars.

We performed extensive simulations to see how well we are able to infer the parameters of the light curves with this particular method in this particular data-set. In order to do so we simulate light curves with the same cadence and observational errors as in the real data-set. We use the algorithm from Timmer & Koenig (1995) to generate light curves with the PSDs which are described with single power-law slope of $\alpha = 1.75, 2, 2.25, 2.5, 2.75, 3$ (no connection with low mass slope of the Schechter mass function, α , defined in Equation (1.8)). We then try to recover the slope by fitting a power law to the PSD estimated with the CARMA procedure. In order to eliminate red-noise leak effects (see e.g., Emmanoulopoulos et al., 2010) we generate ten times longer light curves than needed and then select a random segment having the desired length. To match the observed ensemble behaviour of our sample (see Section 5.4) we normalize the variability by increasing or decreasing the simulated variability so that the SF² for the whole sample of simulated AGN at 100 days is equal to 0.01 mag².

When fitting the PSD we only fit the values which are above the estimated level of measurement noise in the data. Following Kelly et al. (2014) and Simm et al. (2016), the measurement noise is set to $2 \text{ med}(\delta t) \cdot \text{med}(\sigma^2)$ where $\text{med}(\delta t)$ is the median cadence and $\text{med}(\sigma^2)$ is the median of the measured noise variance. We tested also the results when using the means of the cadence and variance instead of the medians, but find that choosing medians reproduces better the input values in the simulation.

We show the results of these simulations in Figure 5.7. The error bars represent the 25 and 75 percentiles of the distribution of the recovered parameters from the population and not the inferred errors for a single object. Although the spread is large the basic trend is recovered. The large spread highlights the fact that the estimated parameters for a single light curve are quite uncertain and that conclusions can be only made by

using a statistically significant number of objects. We also note that the slopes are better recovered for slopes around two (corresponding to random walk), than for steeper slopes. This reflects the fact that for intermediate values of the slope (~ 2.5), the algorithm tends to sometimes run away and converge to extremal values of either 2 or 4 (see also Figure B.1. from [Simm et al., 2016](#)). In Figure 5.8, we show an alternative way of representing the results, which partially alleviates these effects. Here we represent the fraction of sources that are inferred to have a power law slope steeper than $\alpha > 2.5$. In the ideal case we would want to see a clear step function, with a step at the input value of $\alpha = 2.5$ (as represented with a dashed line in the Figure). In practice, we do recover the basic trends, but do not reproduce the step function exactly. The error bars in the Figure are derived by bootstrapping the sample and as such represent the statistical uncertainty in the number of quasars with PSD slopes larger than 2.5, given the number of quasars in the sample, which is set to be representative of the actual data.

We remark that we tried fitting the PSDs from both the data and the simulated light

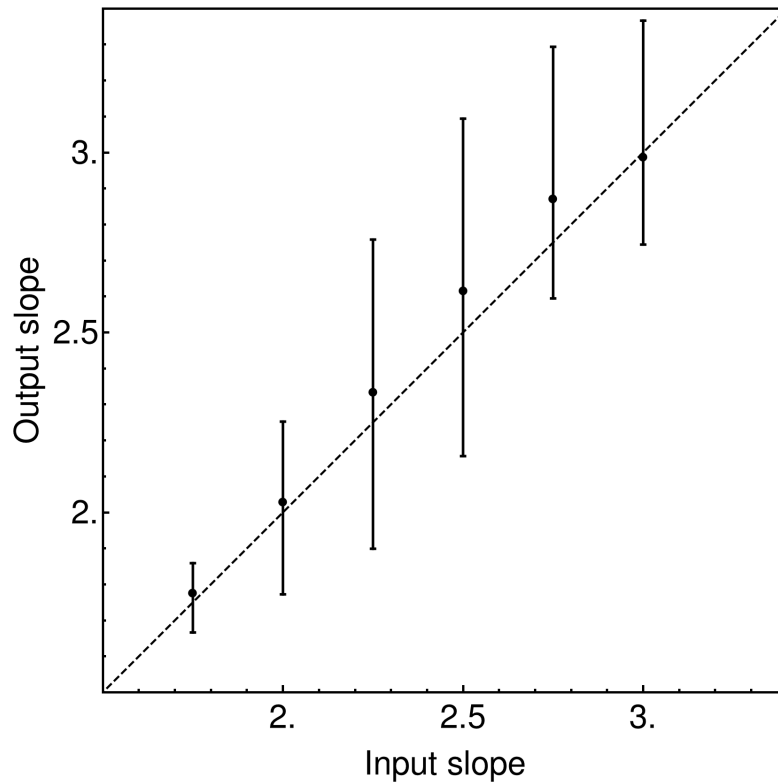


Figure 5.7: Result of the simulations in which we attempt to recover the slope of the PSD of a set of quasars whose mock photometry was generated using a power-law PSD of known slope, as described in the text. The mock observations are constructed to have the same errors and cadence etc. as the actual data. While the PSD analysis recovers the mean slope well, there is significant dispersion in the output for a given input slope. The error bars represent the 25 and 75 percentile of the distribution of the resulting output slopes.

curves with a broken power-law fit, but found the results to be unreliable. Specifically, when running our simulations, which as input had pure power-law PSDs, we found that

the inferred (rest-frame) time scale of the break was perfectly correlated with the redshift i.e., effectively with the (rest-frame) duration of the observations. This is due to the fact that the algorithm is modelling the PSD as a weighted sum of Lorentzian functions (Kelly et al., 2014) which means that the function which is used to model the PSD must have a turnover at some point. The model is forced to locate this turnover at or near to the minimal frequency available in the observations. We see exactly the same effect when fitting the real data, with a clear dependence on redshift but not on mass or luminosity, from which we conclude that this is an artificial effect. In general, we find that with the double power-law, the algorithm tends to overestimate the steepness of the low-frequency slopes and to give relatively unreliable estimates of the high-frequency slope. Therefore we conclude that the details of the PSD are unreliable, and that we are only able to estimate, at least with the (i)PTF data, the global shape of the PSD for statistical samples of objects.

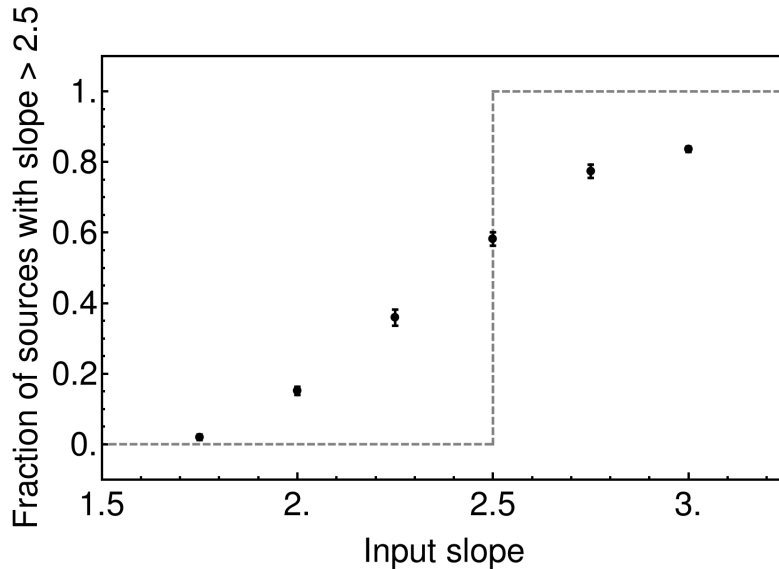


Figure 5.8: An alternative way to show the results of the simulations in Figure 5.7 is to plot the fraction of sources that are inferred to have steep slope $\alpha > 2.5$, where $\text{PSD} \propto f^{-\alpha}$, including sampling errors derived from bootstrapping the mock sample (as with the real data). Ideally, we would recover the dashed line step function, which represents a case in which the input and the output slopes would agree perfectly. Uncertainties in determining the slope produce a blurring of this.

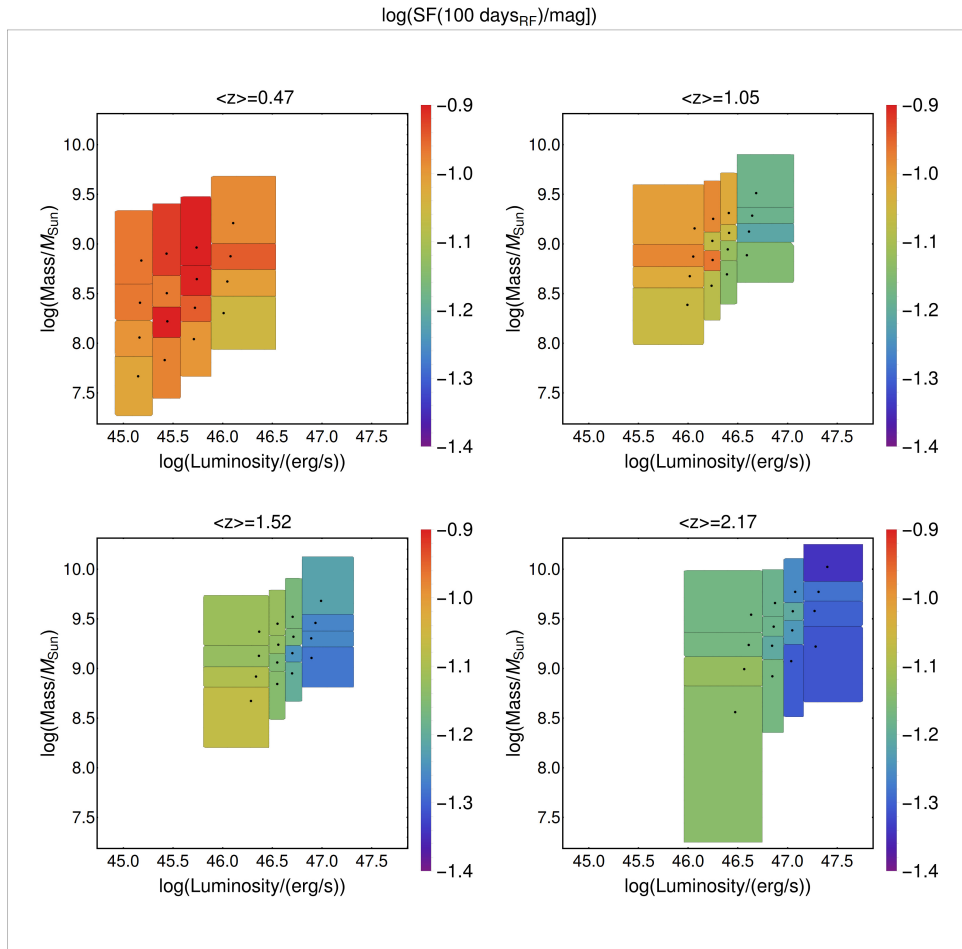


Figure 5.9: Value of the $\log(\text{SF}/\text{mag})$ at a time scale of 100 days, in the quasar restframe as a functions of the black hole mass and the luminosity, as observed in the four redshift intervals (the four panels). The dots inside each bin show the mean values of mass and luminosity for the quasars in that bin. A clear anti-correlation with luminosity can be observed, with more luminous objects varying less. This dependence is seen in individual redshift bins and also across the whole redshift range.

5.4 Results of the SF analysis

5.4.1 The amplitude and the timescale of variability from the SF analysis

In Figure 5.9 we show the amplitude of variability at a time-scale of 100 days (in the quasar rest frame) for the 64 bins in redshift, luminosity and black hole mass. This timescale is chosen as the associated level of variability is well above the noise level of the survey (see Figure 5.4) and because it lies well within the most densely sampled parts of the survey (significantly shorter than the total length of the survey).

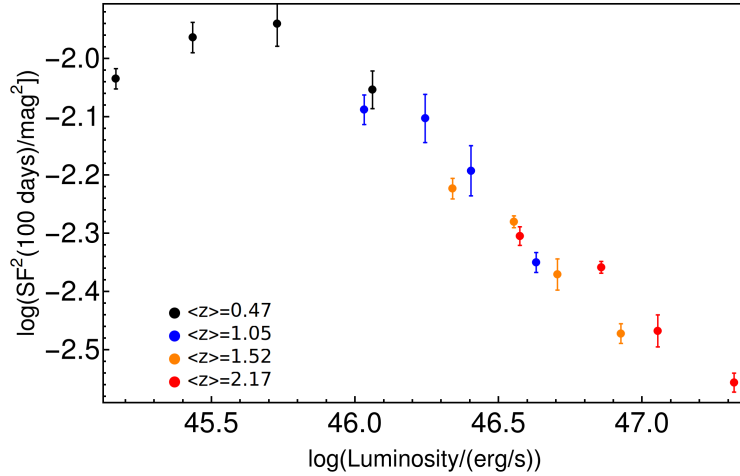


Figure 5.10: The dependence of the SF^2 , measured at 100 days, as a function of the luminosity L . The strong anti-correlation with luminosity, and the weak or absent dependence on redshift, are obvious.

A strong anti-correlation is seen between the amplitude of variability and luminosity - more luminous sources are less variable. This effect is visible in every redshift bin and is even more obvious when comparing different redshift panels, as the distribution of the sample shifts in luminosity. We explicitly show this result in Figure 5.10, where we have suppressed the mass information and show the variability amplitude at 100 days (rest-frame) in bins defined in redshift and luminosity. We observe the clear and tight anti-correlation of variability with luminosity, i.e., the effect that we already discussed above. We note that the flattening on the low-luminosity side is possibly spurious - as mentioned before, the largest residuals in our estimation of SF^2 are in the lowest luminosity and lowest redshift bins. Apart from that, the trend with luminosity is well established and continuous across redshift bins. This clear dependence with luminosity has been seen before several times in smaller surveys (e.g., Vanden Berk et al., 2004; Bauer et al., 2009; MacLeod et al., 2010) but is very clearly seen in the very large data set presented here. A comparison of the panels in Figure 5.9 or examination of Figure 5.10 shows that the variability at a given luminosity is more or less constant with redshift. Although the dependence on luminosity is obvious, any dependence with black hole mass is much less pronounced.

In Figures 5.9 and 5.10 we followed the conventional practice of considering the amplitude of variability at a given (rest-frame) timescale. A more or less equivalent diagram results from what we might suspect is a possibly more physically intuitive representation, which is to consider the timescale τ at which the variability reaches some given amplitude (note that τ is different than the one used in Chapter 3). This is shown in Figure 5.11. We set this amplitude to be 0.071 mag, equivalent to the SF^2 reaching 0.005 mag². This value

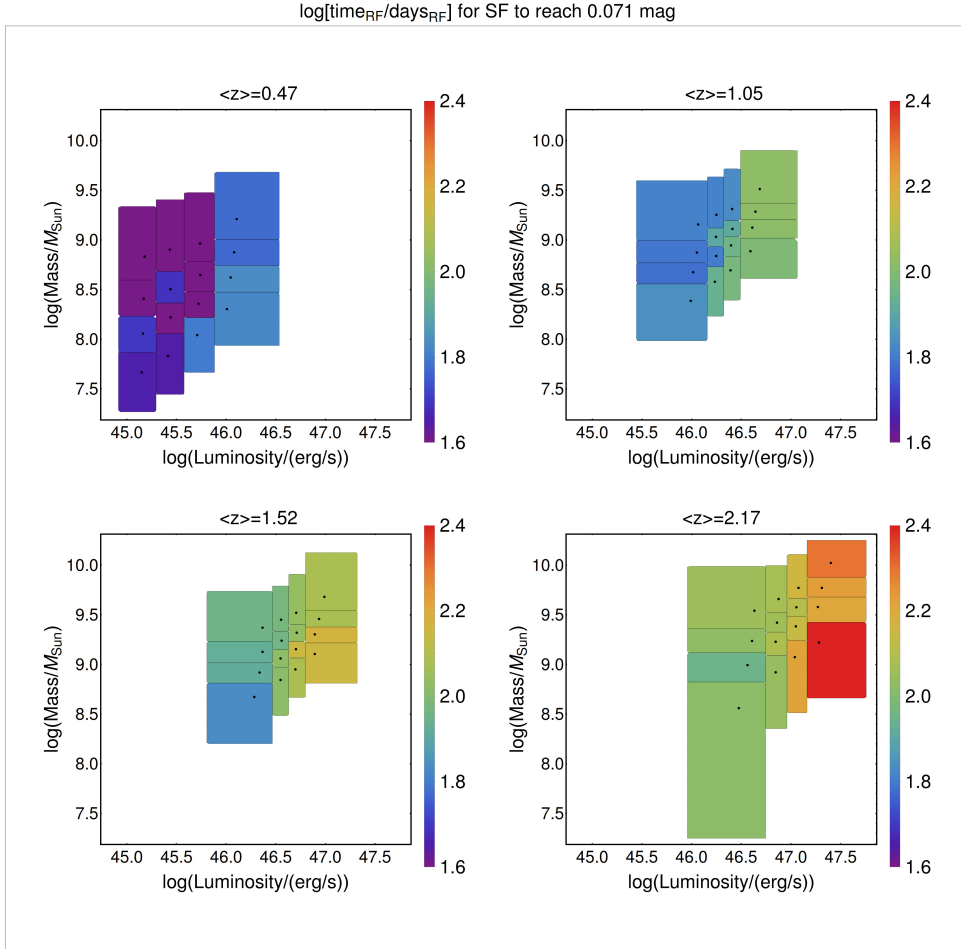


Figure 5.11: The logarithm of the rest-frame time-scale, in days, at which the ensemble structure function reaches 0.071 mag. The dots inside the bins show the mean value of mass and luminosity for the objects in the bin. This figure contains similar information to that in the Figure 5.9 but offers a different interpretation of the variability properties. The clear dependence with luminosity can be observed, with more luminous objects needing more time to achieve the same level of variability. This dependence is seen in individual redshift bins and also across the whole redshift range.

is similarly chosen as it is far above the noise level of the survey and because this level of variability is reached between 50 to 250 days, ensuring that our estimates are again within very densely sampled parts of the survey. It is to be also noted that this timescale is of the order of the typical dynamical time-scales expected for the AGN in our sample (e.g., [Netzer, 2013](#)).

Formally, for each of our AGN samples we search for τ that is the solution to the simple equation

$$\text{SF}^2(\tau_C) = C \text{ mag}^2. \quad (5.5)$$

where $C=0.005$. We note that for short enough times, where SF^2 is fully described with

Tab. 5.2 — Fit to the time-scale of variability, Equation (5.7)

a_0	a_1	a_2	a_3	$\chi^2/\text{d.o.f}$
1.46 ± 0.02	0.02 ± 0.16	0.41 ± 0.04	-0.09 ± 0.03	2.93
1.46 ± 0.02	$\equiv 0$	0.41 ± 0.04	-0.09 ± 0.03	2.89

a single power law (see Equation (5.4)) this connection can be expressed as

$$\tau_C = \left(\frac{C}{\phi_1} \right)^{g_1}. \quad (5.6)$$

Not surprisingly, the two Figures 5.9 and 5.11 are similar. Again, we see a clear positive correlation between luminosity and τ_C , and little variation with black hole mass or redshift (recall that the analysis is performed in the rest-frame). The statement that more luminous sources vary on longer timescales is largely equivalent to the previous statement that they are less variable at a given timescale.

To investigate the dependence of τ_C on quasar parameters we fit the data³ with a function of the form:

$$\log \tau_C = a_0 + a_1 \log(1+z) + a_2(\log L - 45) + a_3(\log M - 8). \quad (5.7)$$

The results of these fits are shown in Table 5.2. Noticing that the returned dependence on redshift is negligible, we also fit the same functional form with the redshift term forced to be zero, and find no significant change to the other two terms. These fits confirm that the main dependence of variability is with luminosity, with a much weaker dependence on black hole mass. We also note here that although the details of the fit will change with the choice of amplitude of variability, C, the exact choice of C is inconsequential for our main conclusions (the clear dependence with L, little to no dependence with mass or redshift).

The lack of redshift evolution in the link between variability (whether in terms of amplitude or timescale) with luminosity is interesting. The quasar luminosity function can be represented by a double power-law with a characteristic break luminosity L^* . This break luminosity increases with redshift roughly as $L^* \propto (1+z)^{3-4}$ up to $z \approx 2$ and then plateaus or even decreases at higher redshifts (e.g., Hopkins et al., 2007, Ueda et al., 2014). In a simple phenomenological model presented earlier, we suggested that this L^* arose from the combination of a characteristic Eddington ratio, λ^* , the characteristic Schechter mass

³Here we treat masses and luminosities as independent quantities, although in practice both are based, to some extent, on the observed monochromatic luminosities.

of the host galaxies, M^* , and the m_{bh}/m_{star} ratio. It was suggested that the $(1+z)^4$ evolution in L^* was produced by a roughly equal $(1+z)^2$ evolution in λ^* and m_{bh}/m_* . In the model, the luminosity of an AGN relative to the L^* of the population (for $L > L^*$) emerges as a useful diagnostic of luminous AGN. The above fits make clear however that quasar variability seems to be linked to L and not to L/L^* . This is illustrated graphically in Figure 5.12. We see that if the amplitude of variability is plotted against L/L^* , there is no agreement across different redshifts bins, as expected as we do not see any significant redshift evolution in the SF (see Table 5.2), while L^* is known to strongly evolve with redshift (as noted above).

It is intriguing that the timescale of variability is most strongly correlated with luminosity, with the scaling $\tau \propto L^{0.4}$, rather than black hole mass. This can be compared with the inferred time-scale of variability in the thin-disk accretion model. For an accretion disk around a black hole with a mass m_{bh} and a given luminosity L the temperature of the disk is given by (Netzer (2013), see also Equation (1.1))

$$T \propto L^{1/4} m_{bh}^{-1/2} \left(\frac{r}{r_g} \right)^{-3/4}, \quad (5.8)$$

where the r_g is the gravitational radius of the black hole, $r_g \propto m_{bh}$. This expression ignores the spin term.

From this we can follow MacLeod et al. (2010) to derive a characteristic location within the accretion disk that is connected with a certain temperature, and thus with a corresponding emission wavelength:

$$r_\lambda \propto m_{bh}^{1/3} L^{1/3} \lambda_{RF}^{4/3}. \quad (5.9)$$

From Kepler’s law we have that

$$t_{\text{dyn}} \propto r^{3/2} m_{bh}^{-1/2}. \quad (5.10)$$

Combining these two expressions and identifying t_{dyn} as the time-scale of variability, we could expect that the timescale of variability at a single wavelength should depend on luminosity alone as

$$\tau \propto L^{1/2}. \quad (5.11)$$

This is not dissimilar to the fitted $\tau \propto L^{0.4} m_{bh}^{-0.1}$ behaviour we find in (i)PTF data (see Table 5.2). Obviously this is the simplest possible model. In reality, the observed flux at given wavelength is produced from a wide range of radii and therefore mixing various time-scales. Such kind of “mixing” could significantly weaken any underlying luminosity dependencies, making them harder to identify in our data.

We note that this line of argument was already explored in MacLeod et al. (2010), who however noted that the de-correlation timescales in their damped random walk model did *not* appear to correlate with luminosity in this simple way. As noted above, we prefer not to ascribe a physical significance to the (possible) breaks in the SF, because of the

observational artefacts that can easily produce them. Rather, we instead point out that the simple luminosity-only dependence is observed, with approximately the correct index, if we interpret the relevant “timescale” to be the time taken to reach a given level of variability. One caveat is that while the luminosities of the quasars used in the above analysis are nominally bolometric luminosities, they are in fact ultimately derived from, and are proportional to, the monochromatic luminosities L_λ at 5100, 3000 or 1350 Å. Consideration of L_λ in the context of a thin accretion disk would modify the expected relation and introduce a mass dependence of the form

$$\tau \propto L_\lambda^{3/4} m_{bh}^{-1/2}. \quad (5.12)$$

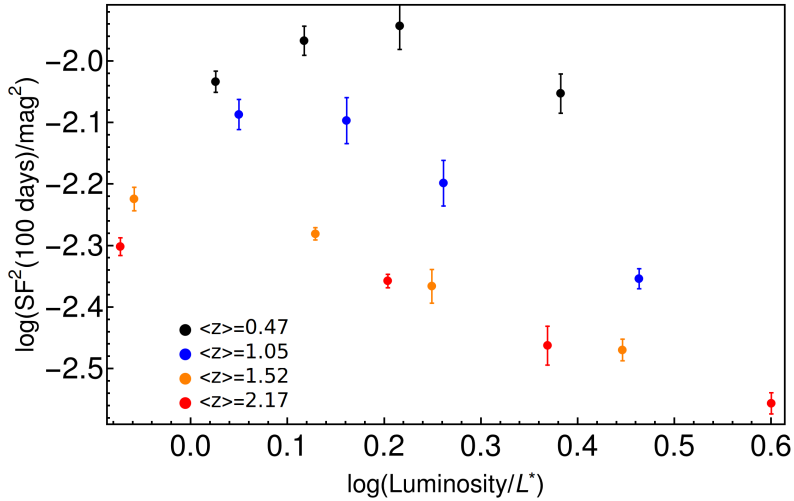


Figure 5.12: The dependence of the SF^2 , measured at 100 days in the rest-frame, as a function of the luminosity relative to the knee of the quasar luminosity function at that redshift, L/L^* . While the anti-correlation with luminosity at a given redshift is still obvious, there is no longer the independence with redshift in this L/L^* plot compared with that for simply L as in Figure 5.10.

5.5 Results of the PSD analysis

In this section we will investigate the slopes of the PSD of objects, which may contain information on the process driving the variability. We model the PSD with a simple power-law $PSD \propto f^{-\alpha}$. Different values of α will correspond to different correlation properties of the driving process. For instance, $\alpha = 0$ corresponds to the white noise of a completely random process without memory, while $\alpha = 2$ is indicative of a random walk process. Since the PSD and SF are closely connected quantities, we would expect the effects visible in a PSD analysis to also be seen in the SF analysis described above, although possibly modified due to the different types of systematics affecting each type of analysis. One difference is that the PSD analysis is more readily carried out on an object by object basis

whereas the SF is ideally suited to combining observations of objects within a sample. In general, for a PSD described with a power law $PSD(f) = \kappa f^{-\alpha}$ and $1 < \alpha < 3$ the SF² will have the following analytical form (e.g., [Emmanoulopoulos et al., 2010](#)):

$$SF^2(\Delta t) = -2^\alpha \kappa \pi^{\alpha-1} \Gamma(1 - \alpha) \sin\left(\frac{\alpha\pi}{2}\right) \Delta t^{\alpha-1}. \quad (5.13)$$

where $\Delta t = f^{-1}$. From this we can see that a PSD with slope of α should correspond to a SF² with slope of $\alpha - 1$.

5.5.1 Slope of PSDs in the (i)PTF sample

Fitting the PSDs of the 2,200 available objects for which the PSD can be constructed (see Section 5.3.4 above) yields a range of slopes between $1.5 < \alpha < 4$. In Figure 5.13 we show the fraction of quasars with slopes steeper than $\alpha = 2.5$, choosing this threshold to be significantly above the random walk value of $\alpha = 2.0$. The whole sample was first split in 4 redshift bins with the same procedure as described in Section 5.3.1, so that each redshift bin contains the same number of objects. We show results for two ways in which we further split the sample. In the case shown on the left hand side of Figure 5.13, we have further divided each redshift subsample into 4 luminosity bins. Alternatively, in the right hand side of Fig. 5.13 we have instead divided each redshift subsample into 4 mass bins. We find this binning approach to be preferable, at this stage, to creating the larger number of 64 bins in mass-luminosity space, as we did in the structure function analysis, simply due to our desire to maintain statistical robustness given the much smaller number of objects for which the PSD can be determined. We will explicitly discuss the mass/luminosity dependence below. We have also discarded objects whose PSD appear to be inconsistent with the single power law description, i.e., which show strong bending. Specifically, we discard any object for which the best fit single power-law fit deviates beyond the 95% confidence regions of the PSD analysis. This removes 20% of the quasars. We also show in the lower two panels of Figure 5.13 the results that would be obtained from the observational uncertainties if all sources were in reality described by the $\alpha = 2.0$ PSD of a pure random walk. These simulations were prepared as described in Section 5.3.4. After the simulated data was created, exactly the same analysis procedure was applied to it as to the real data.

There is a clear trend in Figure 5.13 for quasars with higher luminosity and/or black hole mass to have, on average, steeper PSD. The simulations with uniform $\alpha = 2$ do not show this steepening effect, and the fraction of (apparently) steep PSDs among simulated light curves stays at roughly 10% independent of luminosity or mass. While the lowest luminosity/mass systems are consistent with this fraction, i.e., with all sources having $\alpha = 2$ in reality (given the observational uncertainties), the quasars at higher luminosity/mass have systematically “redder” PSDs. The effect can be seen across redshifts, but it is also visible in individual redshift bins, making clear that it is not a bias caused by the shifting time-dilated observing window. This is further verified as the effect is still visible when we construct samples that have exactly the same span of rest-frame time.

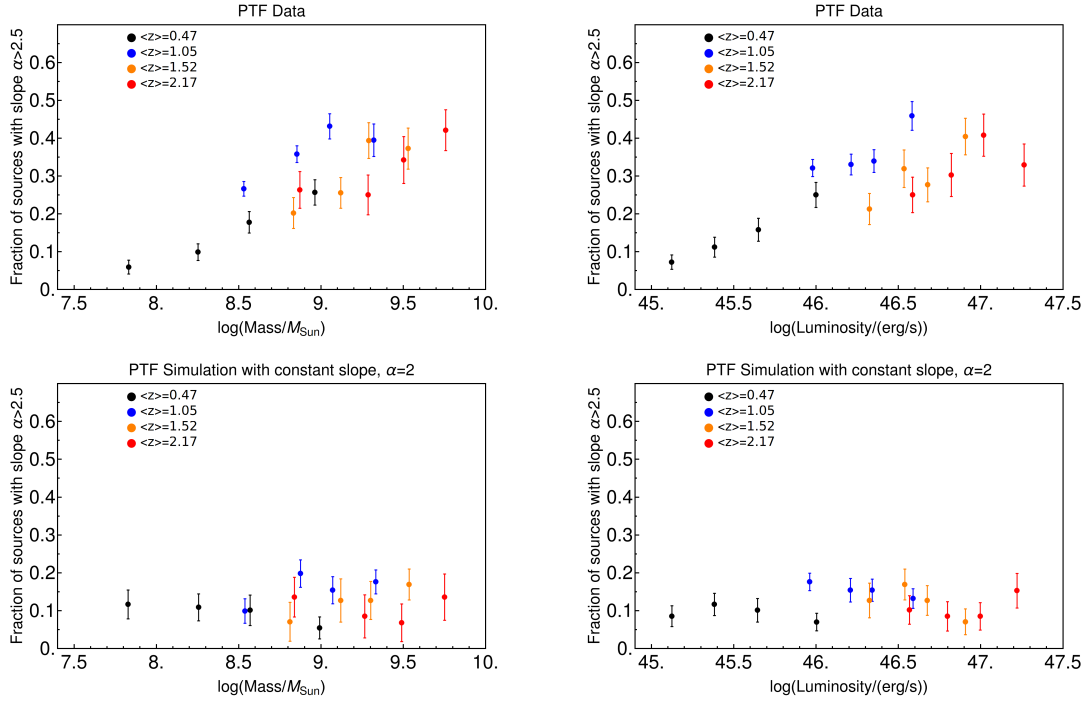


Figure 5.13: The dependence of the PSD slope, α , with mass (left) and luminosity (right). In each panel, the colours denote different redshift bins. We show the fraction of sources for which the CARMA modelling gives a slope $\alpha > 2.5$. In the upper panels we show the results from the (i)PTF data, while in the lower panels we show the results from the simulation in which artificial sources with a fixed input slope of $\alpha = 2$ were observed with the cadence and photometric uncertainties of the actual data. Whereas the real data shows a systematic increase with luminosity and/or black hole mass, the artificial data shows no such effect, suggesting that we are observing a real effect of steepening of the PSD slope with luminosity and mass in the quasars.

This effect should be visible in the larger ensemble SF analysis described above. In Figure 5.15 we show the slope g_1 of the SF, i.e., the slope of the short timescale variability (see Equation (5.4)), using the same binning and symbols as for the PSD analysis in Figure 5.13. The grey dashed lines show the SF² slope that would be expected from the PSD analysis using Equation (5.13). When doing this we have for simplicity assumed that all of the quasars in a single bin have exactly the same PSD dependence, defined by the median α in that bin. This is the simplest assumption one can make and is used here to check the consistency of the results and should not be interpreted as a precise physical statement.

We see that the results are quite consistent. The same dependence of slope on luminosity and mass is seen in the SF², with the more luminous/massive systems having steeper slopes on average. The results from the SF² analysis alone are however not conclusive, and the dashed line offers only a 25% improvement when measuring $\chi^2/\text{d.o.f.}$ compared to the best horizontal of constant slope, ($\chi^2/\text{d.o.f.}$ (constant) = 3.72, against $\chi^2/\text{d.o.f.}$ (dashed line) = 2.82). However, we find it encouraging that both types of analy-

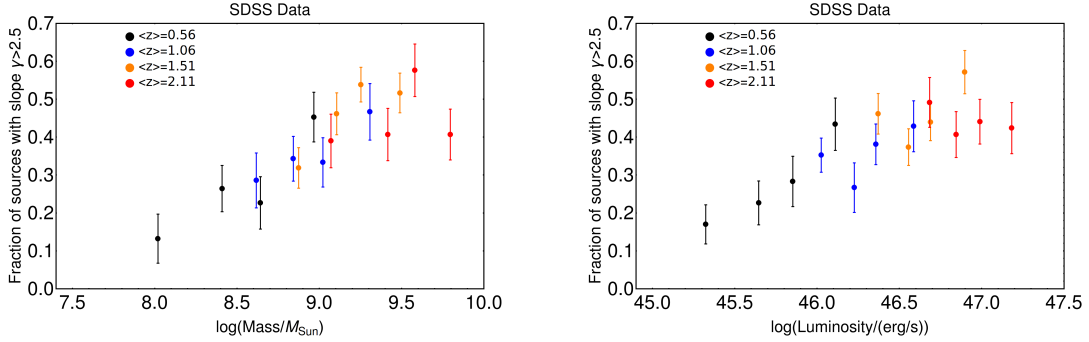


Figure 5.14: This plot is the same as the upper panels of Figure 5.13, but with the analysis done for the SDSS Stripe 82 data. The same effect, with more massive and more luminous quasars displaying steeper slopes of their PSD, is observed.

sis show consistent results. We again emphasize that the dashed line in Figure 5.15 is not the fit to the data - it is an *expectation* derived from the PSD analysis.

As an additional check on the reality of this result, we perform the same PSD analysis with the r band observations in the sample of SDSS Stripe 82 quasars. We perform exactly the same procedure as for our (i)PTF sample, selecting only well sampled light curves and splitting into the four redshift and then four mass or luminosity bins. The results are shown in Figure 5.14. We see that we recover exactly the same trends as in our (i)PTF analysis, showing the strong dependence and the steeping of the slopes with luminosity and mass. We conclude that this is likely to be a real effect.

To investigate further the connection between the steepness of the slope and mass and luminosity, we fit the dependence of the slope with a functional form

$$g_1 = b_0 + b_1(\log L - 45) + b_2(\log m_{bh} - 8). \quad (5.14)$$

Given the weak effects of redshift in Figures 5.13, 5.14 and 5.15, we do not include redshift as one of the parameters in order to reduce the degeneracy in our fits. In Table 5.3 we show our results for different binning and analysis techniques. We have first fitted the dependence of the SF² slopes, as derived in Section 5.3.1, using the full sample split in redshift, luminosity and mass. Second, we have suppressed the information about the redshift and created new bins which were split only in luminosity and mass and for which we fitted the SF² with the same procedure. Third, we fit the results from the PSD analysis using 64 bins of redshift, luminosity and mass. We report the inferred values for the SF² slope by using the Equation (5.13), i.e., by assuming that PSD slopes and the SF² slopes differ by one. This is represented in the table with the (+1) symbol at the relevant position. Finally, case (4) shows our fit to the results from our PSD analysis of the SDSS Stripe 82 sample using the same 64-bin approach.

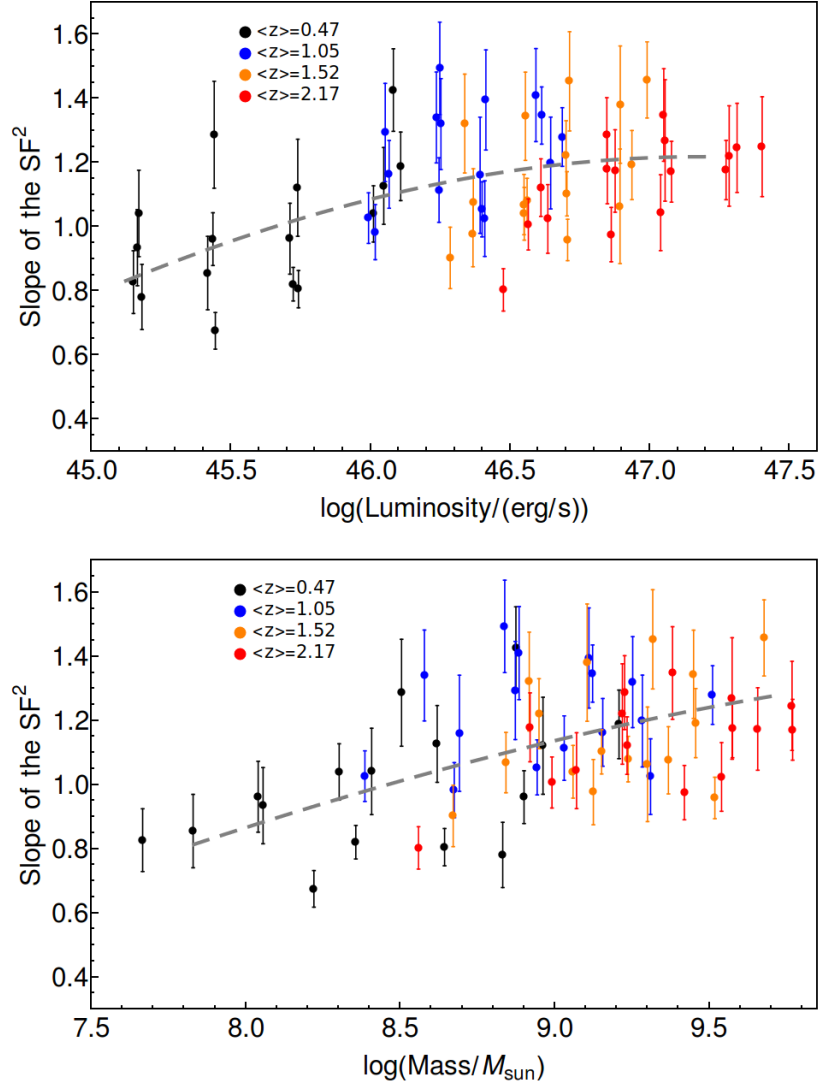


Figure 5.15: The short time-scale slopes of the structure function SF^2 , i.e., g_1 , as a function of luminosity and mass. The dashed line we show the *expected* dependence from the PSD results. We see that the SF^2 results are consistent, albeit with greater noise, supporting the reality of this effect.

All of these results point towards a stronger dependence on the mass of the black hole than on the quasar luminosity. The fact that all these different types of analysis lead to similar conclusions is reassuring given the uncertainties and the different systematics affecting each method.

The existence of the strong degeneracy between the mass and luminosity in quasar samples means that, even though the dependence appears preferentially to be with mass, there will inevitably be an apparent secondary correlation with luminosity (and thus Eddington ratio). The uncertainties are large enough that a primary dependency on luminosity is

Tab. 5.3 — Dependence of the SF² slope, fit with Equation (5.14)

case ¹	b_0	b_1	b_2	$\chi^2/\text{d.o.f}$
1	0.82 ± 0.05	0.05 ± 0.06	0.13 ± 0.07	2.72
2	0.93 ± 0.05	-0.02 ± 0.06	0.20 ± 0.06	3.10
3	$0.88 (+1) \pm 0.05$	0.04 ± 0.06	0.19 ± 0.06	1.71
4	$0.87 (+1) \pm 0.06$	0.0 ± 0.08	0.33 ± 0.09	1.50

¹Procedure of how each sample was prepared and which methods were used is described in the text

only excluded at the $\sim 2 \sigma$ level, depending on the type of analysis used. We also note that if the data taken from two lowest luminosity bins are removed the confidence contours enlarge enough that even pure luminosity dependence is allowed within 1σ level when using the SF data shown in Figure 5.15 (described as Case 1 in the text above).

The variation of the PSD and SF slopes has previously been hinted at in the recent Pan-Starrs study of [Simm et al. \(2016\)](#). In that study PSDs were constructed for a sample of X-ray selected AGN in the COSMOS field. That work showed differences in the high frequency slopes of the PSD as a function of mass, although the small number of objects in the sample and the uncertainties associated with the measurement and the PSD method prohibited any strong conclusions. The PSDs were modelled as a broken power law, with two slopes. As discussed above, we prefer to fit a single power-law to the PSD. Clearly the much larger number of sources and greater time sampling of the (i)PTF observations relative to the Pan-Starrs coverage of COSMOS makes this effect much clearer.

Less directly, [Kozłowski \(2016\)](#) recently conducted a re-analysis of the SDSS Stripe 82 data using the SF approach. When using the full sample without any cuts (in redshift, mass or luminosity), this study tentatively found a somewhat steeper slope of the SF ($g_1 = 1.1 \pm 0.16$) than would be expected from the pure random walk. This is also consistent with our results since only in the lowest luminosity/mass bins are the sources consistent with all having random walk PSDs (see Figures 5.13, 5.14 and 5.15). More interestingly, that study also reported a weak correlation of the SF slope and the luminosity of the AGN, ranging from $g_1 \approx 0.9$ for the lowest luminosity and lowest redshift objects ($\log(L/\text{erg s}^{-1}) \sim 45$), reaching $g_1 \approx 1.3 - 1.4$ for the high luminosity objects in the sample ($\log(L/\text{erg s}^{-1}) \sim 47.5$). We also note in passing that the effect can in fact be seen, although it was not extensively discussed, in the early analysis of the SDSS Stripe 82 data by [Voevodkin \(2011\)](#), as a difference in the SFs of high and low mass quasars in his Figure 8.

The fact that this effect is clearly seen using two different analysis techniques in our very large (i)PTF data set, and is also present at lower significance in other data sets using both the PSD and SF approaches (i.e., the PSD method in PanStarrs (Simm et al., 2016), the SF method in SDSS - Stripe 82 (Kozłowski, 2016)) makes us confident that this subtle effect is nevertheless real.

5.6 Discussion

In the preceding section we have pointed out several interesting results linking quasar variability with their physical properties, using both the SF and PSD formalisms to describe the variability. Using the SF formalism we were able to show that the amplitude of variability, defined as the value of SF^2 at a particular rest-frame timescale (100 days), or, largely equivalently, the timescale to reach a certain value (0.005 mag^2), is most strongly correlated with the luminosity of the quasar, with little or no dependence with with we black hole mass or redshift. When using the PSD approach, we find clear evidence for variations of the PSD slope, with quasars powered by the higher mass black holes exhibiting steeper PSDs. We also find that the slopes from the SF analysis are also consistent with this steepening trend. The effect is seen when splitting the sample in either luminosity or mass bins, but a combined analysis tentatively suggests that mass is the driver of the effect, although luminosity (or Eddington ratio) can not be conclusively excluded.

This work, as well as several others (Mushotzky et al., 2011, Edelson et al., 2014, Kozłowski, 2016) have highlighted observational shortcomings in the damped random walk model of quasar variability, in which a random walk at short timescales flattens at longer timescales in the damped part. In particular, there is now rather good evidence that a non-negligible fraction of quasars exhibit variability which have significantly redder PDSs at low frequencies than expected from the random walk, with this fraction depending on the black hole mass.

Could this behaviour reflect a situation in which quasars display damped random walk behaviour at medium and long time scales and a steeper spectrum at short time scales? The time scale at which the model switches from the "steep" to the random walk behaviour would need to be connected with the mass of the black hole, in order to reproduce the mass dependence of the slope that we see in the data. This time scale would need to be at quite short time-scales, below our detection threshold (~ 0.1 -10 days) for the low mass AGN where we do not observe any steepening, and much longer (~ 10 -1000 days) for massive systems where we observe steeper slopes. For instance, in low mass ($10^7 M_{\odot}$) AGN, Zw 229-15, which was monitored by Kepler, the time-scale of switching from steep slope to the random walk slope is at ~ 5 days and as such the steep part of the PSD would not be observed in our data (Edelson et al., 2014). We show this schematically in Figure

5.16.

In this scenario it might be thought that the shift in timescale to achieve the steepening was associated with the shift in timescale that we have argued is equivalent to the change in variability amplitude. It is not easy to make such a model work in practice, the change in slope being effectively too large. This suggests that two separate processes may be involved in the change in amplitude/timescale, and the spectra steepening, as also implied by the apparently different dependences on luminosity and mass.

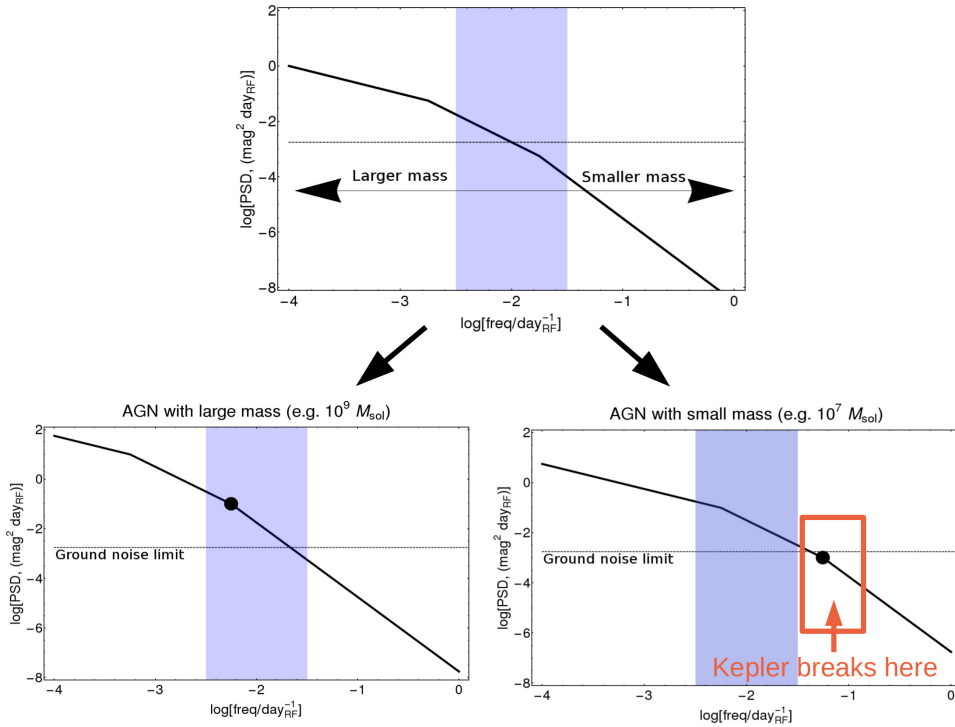


Figure 5.16: Schematic representation of the simple model which could explain the observed steepening of PSD slopes with mass in the observations. In the top we show a general PSD which is steep at higher frequencies and gets flatter towards lower frequencies. With blue shaded region we show the range of frequencies which is covered in a typical time-domain survey and the dashed line show the limiting variability that one could expect from a ground based observatory. In bottom we show two panels, in which we denote where the steep part of PSD spectrum ($\text{PSD} \propto f^{-3}$) breaks and continues as random walk with a big black point. The positions of this break is dependent on the mass. For massive AGN, large parts of the steep PSD are observable, while for the low mass AGN this is not the case. Breaks on short-time scales in the low mass AGN, observed by Kepler, are beyond the capabilities of ground surveys which are limited by noise and cadence.

5.7 Summary and conclusions

The main aim of this chapter has been to characterise the AGN properties through the optical variability of a very large number of quasars in the Palomar Transient Factory (PTF) and intermediate Palomar Transient Factory (iPTF) surveys. We have analysed light curves from 28,096 AGN with the total of 2.4 million photometric data-points. All of these light curves were re-calibrated specifically for this work. The quality of the (re-)calibration is very high with the vast majority of the AGN sample not showing any excess variability at the shortest scales. We have used both the structure function (SF) and power spectral density (PSD) formalism to characterize the variability of the quasars and to search for connections of the variability with redshift, black hole mass and luminosity. Our main conclusions can be summarized as follows:

- The amplitude of variability, defined in this work as the value of the SF^2 at a rest-frame time scale of 100 days, exhibits a clear anti-correlation with luminosity and little or no variation with mass or redshift. We find that simple epoch-independent anti-correlation with luminosity is clearly preferred over connections of variability with the normalised luminosity L/L^* , where L^* is the break in the quasar luminosity function.
- The time scale τ at which the variability reaches a given amplitude, which in this work we set at $SF^2(\tau) = 0.005 \text{ mag}^2$, is closely connected to the variability amplitude described above. We again find that $\tau \propto L^{0.4} M^{-0.1}$, without any redshift dependence. We note that this trend is broadly consistent with the expectation from a simple Keplerian accretion disk model, where the orbital time scale follows $\tau_{\text{dyn}} \propto L^{0.5}$, with no mass dependence.
- There is a clear variation of the slopes of the PSDs, with many quasars that are steeper than what is expected from a random walk model. Quasars with high mass and/or luminosity tend to have steeper PSD slopes. The steepening of the PSD slopes is consistent with the observed slopes of the SF functions, and substantially strengthens the indications of this effect in other recent variability studies. There is some evidence in our own data that the dependence is primarily with the black hole mass rather than the luminosity.
- The observed dependence of the PSD slope with the black hole mass or AGN luminosity could be reproduced in a model in which PSD exhibits steeper slopes below a certain time-scale, with this time-scale being dependent on mass/luminosity, but this would require a strong compensating effect on the amplitude.

6 | Summary and future prospects

In this final part of the thesis, we present a short summary of the main results and point out several avenues for continuation of this research.

6.1 Summary

This thesis presented results from a study of evolution of AGN population and its properties. It consisted of two parts representing two different approaches that we employed to study AGN. The first approach used known evolution of galaxies and simple observables like galaxy mass function and QLF to determine the evolution of AGN mass function and Eddington ratio distribution. The second approach used AGN variability to study the interplay between AGN mass, luminosity and redshift. In both cases, we have studied a large number of objects in a statistical manner and searched for the most important properties that describe AGN.

In the first part of the thesis, we presented a simple phenomenological model that connected galaxy and AGN population. We presented two scenarios: (i) a co-existence scenario, in which AGN grew intermittently during the whole time a galaxy was forming stars and (ii) quenching scenario, in which AGN were associated only with the final stages of galaxy growth, just as the galaxy is about to be mass-quenched.

The co-existence scenario was based on three observationally motivated Ansätze: (i) radiatively efficient AGN are found in star-forming galaxies, (ii) the probability distribution of the Eddington ratio does not depend on the black hole mass and (iii) the mass of the central black hole is linearly related to the stellar mass. We show that normalization of the QLF, ϕ_{QLF}^* is a product of the normalization of the star-forming galaxy mass function, ϕ_{SF}^* , and the normalization of the Eddington ratio function, ξ_{λ}^* . Similarly, characteristic

luminosity of the QLF, L^* is the product of the galaxy Schechter mass M^* , mass ratio m_{bh}/m_* and characteristic Eddington ratio λ^* .

Comparison with the observational data (Shen et al., 2011; Trakhtenbrot & Netzer, 2012) suggests strong evolution of $L^* \propto (1+z)^4$ up to $z \sim 2$. Given that M^* does not evolve, this change can be produced by either change in m_{bh}/m_* ratio of characteristic Eddington ratio, but the QLF evolution is degenerate in changes of these two quantities. To break this degeneracy we compared our predictions with the mass-luminosity plane and found that $m_{bh}/m_* = 10^{-3}(1+z)^2$ provides the best match to the observed data.

We explored the physical consequences of this model. We first showed that it reproduces the m_{bh}/m_* observed in quenched and star-forming galaxies in the local Universe (Kormendy & Ho, 2013; Matsuoka et al., 2014). We point out that m_{bh}/m_* ratio evolves slower in quenched population as it consists of galaxies which have quenched at different redshifts and therefore have different m_{bh}/m_* ratios. Ratio in quenched galaxies ($m_{bh}/m_* \sim 10^{-2.5}$) is representative of the mass ratio in star-forming galaxies at $z \sim 1 - 1.5$, which is the median redshift of quenching for galaxy population.

Because of the same reason, we have pointed out the danger in measuring the m_{bh}/m_* in the galaxy harbouring AGN at higher redshifts and trying to infer the evolution of this relation by comparing it to the m_{bh}/m_* relation observed in the quenched galaxies locally. Even if the mass ratio evolution had very strong redshift dependence, we would expect, simply from the redshift evolution of the galaxy population, that the observed m_{bh}/m_* at $z \sim 1$ in ANG and at $z \sim 0$ in quenched galaxies is identical.

We showed that, when coupled with observed size evolution of galaxies, the mass ratio evolution automatically produces non-evolving $m_{bh} - \sigma$ relation with less scatter than in m_{bh}/m_* relation. We then utilized the reasoning from the phenomenological model for galaxy size evolution by Lilly & Carollo (2016) which identifies dense cores of galaxies as “bulges” and performed the analysis of expected scatter in the m_{bh}/m_{bulge} by making a simplifying assumption that the stellar mass in quenched galaxies at $z = 1.2$ would be recognized as “bulge” today. We show that m_{bh}/m_{bulge} exhibits less scatter than m_{bh}/m_* relation, because the effect of the m_{bh}/m_* ratio evolution which increases the scatter in the local observations, is virtually eliminated. We emphasized that this effect (tighter correlation in m_{bh}/m_{bulge} than in m_{bh}/m_*) was achieved without any direct connection between the bulge and the black hole.

We pointed out that a similar effect can happen when observing the quenched fraction of galaxies as a function of galaxy and black hole mass. Given that m_{bh}/m_* ratio was larger at higher redshifts, when observing at given stellar mass the quenched fraction rises with black hole mass, even though black hole mass is not necessarily a parameter which is crucial for quenching. Additionally, when this effect is coupled the rise of quenched fraction with stellar mass the quenched fraction of galaxies seems to be driven completely by the black hole mass. This analysis emphasizes the risk of determining the physical driver of quenching by comparing properties of star-forming and quenched galaxies at a

single redshift without considering evolutionary effects.

Our model naturally reproduces the “downsizing” of the AGN luminosity (the fact that number density of high luminosity AGN peaks at earlier time than the number density of lower luminosity AGN) even though the distribution of Eddington ratio was mass-independent. This was a natural consequence of the higher characteristic Eddington ratio and lower number density of AGN at higher redshifts.

We also provided explanation for the “sub-Eddington” boundary seen in the mass luminosity plane. “Sub-Eddington” boundary describes the upper envelope of the data seen in the mass-luminosity plane which is below Eddington limit and seems to fall towards higher mass AGN. We have shown that this is “plotting” effect - there are many more low mass AGN, so even though all AGN have same Eddington ratio distribution, iso-density contours are connecting low mass AGN with higher Eddington ratios and high mass AGN with lower Eddington ratios.

We then expanded our analysis and used information about mass growth of galaxies and black holes to test whether these are consistent with such a change in the mass ratio. While the observed mass growth is inconsistent with such an evolution of the mass ratio in the co-existence scenario, we found that such a change is much more naturally produced in a quenching scenario. We showed that in this model m_{bh}/m_* evolution is determined by BHARD/SFRD evolution, while the normalization of the AGN mass function is proportional to the product of normalization of the mass function of star-forming galaxies and ratio of mass doubling times for galaxies and black holes, $\phi_{ANG}^* \propto \phi_{SF}^* \cdot sSFR/\lambda^*$. Finally, the λ^* of the QLF is given by BHARD/SFRD evolution and the evolution of characteristic quantities describing galaxy mass function and the QLF, $\lambda^* \propto (SFRD/BHARD) \cdot (L^*/M^*)$. These relations allow us to determine the parameters which fully describe the AGN population from relatively easily observable quantities.

We then determine the evolution of the AGN populations parameters using the observations from Hopkins et al. (2007), Peng et al. (2010), Ilbert et al. (2013), Madau & Dickinson (2014), Ueda et al. (2014) and Aird et al. (2015). We find that, from redshift $z=0$ to $z=2$, the evolution of the mass ratio is given by $m_{bh}/m_* \propto (1+z)^{1.5}$, while the characteristic Eddington ratio evolves as $\lambda^* \propto (1+z)^{2.5}$. We stress that, while in the first part of the work mass ratio evolution and Eddington ratio evolution were put in the model to satisfy QLF evolution and the observation in the mass luminosity plane, these dependencies were now derived from the observations of the SFRD and the BHARD. These quantities are now the “output” of the model, rather than “input” like in the co-existence scenario - yet both approaches yield similar redshift dependencies.

The fact that the characteristic Eddington ratio evolves in the same fashion as the $sSFR$ at $z < 2$ demands, in our model, that the normalizations of the QLF and the star-forming galaxy mass function should follow each other; this is exactly what is seen in the observations. Above redshift $z=2$, deduced characteristic Eddington ratio flattens off at

the value close to the Eddington limit, suggesting that this is indeed the fundamental limit above which AGN accretion is rare.

Many of the results, such as the appearance of “downsizing”, sub-Eddington boundary and the tightness of the $m_{bh} - \sigma$ relation and the m_{bh}/m_{bulge} relation, are naturally explained by the general model, irrespective of the exact scenario used (co-existence or quenching).

Given the many similarities of the results, even though the physical origin for each scenario is quite different, we conducted an analysis to directly differentiate between them. The main difference between two scenarios is that in the co-existence scenario all the star-forming galaxies have the same chance to host an AGN, while in the quenching scenario the mass function of AGN host galaxies had a shape of mass-quenched galaxies, i.e., AGN are predominately hosted in massive galaxies. We therefore compared the model prediction with the data showing (i) galaxy properties (mean SFR) as a function of AGN luminosity (Rosario et al., 2012; Mullaney et al., 2012a; Stanley et al., 2015), and (ii) AGN properties (mean L_x/SFR) as a function of galaxy mass (Mullaney et al., 2012b; Rodighiero et al., 2015; Yang et al., 2017).

The observation that the mean SFR is only weakly dependent on the AGN luminosity, for the wide range of AGN luminosities, is suggesting that AGN of all luminosities are predominately hosted in the galaxy of the same mass. This is what is expected from the quenching scenario, in which galaxies at M^* are dominating AGN population at all black hole masses and luminosities.

We showed that the lack of bright AGN in the fields of small size which are observed can significantly change the expected results when studying the mean L_x/SFR as a function of galaxy mass. When using the actual maximal luminosities of AGN observed in the surveys, we again found that the quenching scenario offers better explanation of the data. We attribute the difference in the results derived from COSMOS and smaller CDF-S field to the fact that AGN in the samples have different maximal luminosities.

In the second part of the thesis we studied optical variability in order to study directly the evolution of AGN parameters such as mass and luminosity. We have used data from the PTF/(i)PTF survey. We conducted a major re-calibration effort in order to be able to constrain variability at short time-scales where AGN show little intrinsic variability. We showed that the quality of recalibration of light curves of $\sim 28,000$ AGN is very high with the vast majority of AGN not showing any excess variability at the shortest time-scales.

We then analysed the sample using the SF formalism. We have divided the whole sample in the 64 bins in redshift, mass and luminosity and found that the amplitude of variability shows clear anti-correlation with luminosity, without any or weak dependence on mass or redshift. When studying the closely related quantity, the time-scale τ it takes for an AGN to reach a given amplitude, in this work set at $\text{SF}^2 = 0.005 \text{ mag}^2$, we find that $\tau \propto L^{0.4}M^{-0.1}$.

Finally, we have studied AGN variability in frequency space and constructed PSD slopes for a subset of well-sampled objects. We showed that AGN with higher mass and/or luminosity tend to have steeper PSD slopes. We confirmed that this effects is consistent with the results from the SF analysis and tested, with simulations, that is not a consequence of observational biases. Additionally, we confirmed this effect in the independent sample of AGN from Stripe 82 variability study.

6.2 Future prospects

We have seen how powerful the phenomenological modelling is in providing insights for the evolution of the AGN population. There are several consequences and implications that are worth further exploration. For example, although we have shown that the evolution of the m_{bh}/m_* mass ratio should follow the BHARD/SFRD ratio it is not clear from the current phenomenological model why the BHARD/SFRD ratio has the exact shape that is has. One of the first figures in this thesis, Figure 1.4, showed this difference of shape that is present at all redshifts. One explanation could be, at least at redshifts below $z \lesssim 2$, that this is due to size-evolution of galaxies, which become larger at lower redshifts and therefore less gas accretion is available for central processes. If BHARD is connected with the part of SFRD originating from the parts of the galaxies close to the black hole (e.g., within 1 kpc), BHARD would fall towards lower redshifts as smaller fraction of total star-formation is happening within these central regions. This would also automatically create a stronger correlation of black holes with the properties describing central regions of galaxies than with properties connected with the whole galaxy. For an example, this could provide an explanation for the correlations with bulge or central surface density in quenched systems that we discussed in Section 2.5.3.

Different explanation are, of course, possible. King (2003) suggested, from modelling the interaction of the AGN outflow and the host galaxy, that the mass at which the BH will blow away any residual gas around itself is $m_{bh} \propto \sigma^4$, independent of redshift. This is the same conclusion as the one we arrived at, using very different arguments. Energetic arguments i.e., studying the amount of energy needed to be produced by the black hole in order to quench the galaxy, could also be used to infer black hole - galaxy mass evolution. Obviously, the physical explanation for the phenomenological connections we have shown is rather rich area for the future research.

Below we will focus on the possible extensions and prospect of studying AGN variability. Analysis in Chapter 5 showed that, while the current variability data is providing interesting insights on its own right, the quality of the data is not yet high enough to provide insights which would be widely useful to the AGN and astronomical community in general. This is, however, soon to change as in the moment number of advanced surveys capable of studying variability, such as zPTF, GAIA, LSST, are either running or are nearing to the start of scientific operations (Ivezic et al., 2008; Eyer et al., 2011; Bellm, 2014). Therefore, it is safe to say that we are entering the golden age of time domain

astronomy with many possible projects which will provide unique insight into physics associated with supermassive black hole fuelling. Below we give a short description of just a couple of ways to study AGN with optical variability, which are already possible today or will be possible in the near future.

6.2.1 Influence of steep PSD slope on detection of periodic AGN light curves

In Introduction we have indicated great amount of interest in the community for detecting periodic AGN light curves. The main issue is that stochastic variability of AGN, coupled with realities of observational surveys with irregular cadence and large measurement uncertainties, means that non-periodic AGN can sometimes mimic periodic signal. Therefore, of crucial importance is to estimate, in statistical manner, how likely it is that any detected periodic light curve is indeed periodic, and not consequence of stochastic AGN variability.

The calculation discussed above depends crucially on the correlation properties of AGN variability, i.e., on the slopes of PSD. While uncorrelated white noise is extremely unlikely to mimic a periodic light curve, more correlated noise with steeper slope PSD is more likely to create quasi-period behaviour. We show this in Figure 6.1.

In our work we have argued that many AGN have PSDs with steeper slopes than expected from the random walk model which is commonly used for these estimates. We therefore expect that large number of period-like light curves currently reported are false positives. As a straightforward continuation of work presented in this thesis we could recalculate these estimates using our new insights about PSD slopes of the AGN.

6.2.2 Variability as a method to measure spin and other physical parameters

Even though the details of AGN variability are still unclear, we mentioned in Introduction that a large number of features can be described with the basic phenomenological models, which have proven to be very successful in the past several years (Dexter & Agol, 2011; Cai et al., 2016). The main premise of these models is that the observed optical variability of AGN can be explained as the superposition of the temperature variations in the parts of the accreting disk. By measuring the total variability for the ensemble of AGN (e.g., by constructing structure function for which luminosity and mass are known) we can immediately deduce the dependence of spin on the mass and the luminosity, considering that all these parameters influence the temperature and variability of the AGN. These estimates would be of great use for the models of the AGN population which currently marginalize the possible influence of the spin (our model included). Influence of spin is larger in bluer bands, so it would be beneficial to study the variability properties of AGN

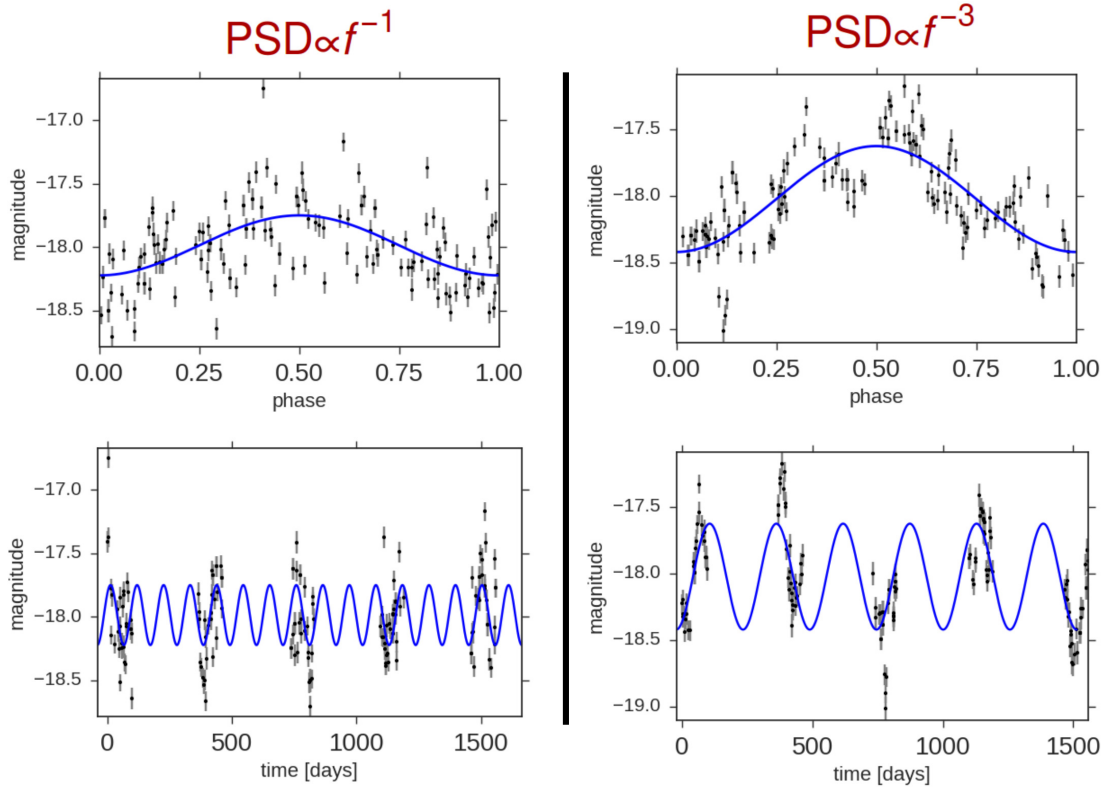


Figure 6.1: Example of the effect that PSD has on the periodicity found in surveys. We simulate 100 realistic light curves with the $\text{PSD} \propto f^{-1}$ and $\text{PSD} \propto f^{-3}$ and show in the panels the best “periodic” curve that has been found with Lomb-Scargle algorithm (Lomb, 1978; Scargle, 1982). In upper panels we show folded light curves and in lower panels we show actual “data” with the periodic solution plotted in blue. The false “periodicity” is more likely to be found in curves produced with steep PSD.

in rest-frame NUV and u- and g- wavebands. Currently the best sample for this purpose is the sample of objects in u-band from the Stripe 82 SDSS variability survey at redshift ~ 1 .

6.2.3 Variability as AGN selection method

Our knowledge about AGN is still mostly based on samples which have been selected largely by photometric criteria, which are designed to select intrinsically blue objects (Richards et al., 2002). At the same time, this strategy results in only “normal” AGN being found, given that unusual types of SEDs will be automatically excluded from any AGN survey (e.g., Bertemes et al. 2016). Therefore, every existing survey is biased against black holes with red SEDs caused by low temperatures of the disk (black holes with high mass, low Eddington ratio, and low or retrograde spin), especially at higher redshifts. As

such, we can never be certain if we have a full census of the total accreting population of black holes. Finding or constraining the fraction of extremely massive black holes that are still accreting would be also of importance for galaxy - black hole co-evolution studies like the one we conducted.

Even though these rare high-mass low-spin objects can not be found using normal AGN colour-selection techniques there is no obvious reason suggesting that variability would be suppressed in such objects. Therefore, we can construct and investigate the sample of variable “red” objects that can not be selected with usual photometric AGN selection but show AGN-like variability properties. By exploring candidate objects that show promising photometric variability properties, one would be able for the first time to discover and unambiguously deduce the fraction of active extremely massive black holes.

Appendix to Chapter 5

A.1 Completeness and depth of the survey

In this part of Appendix, we wish to characterize the completeness of the (i)PTF survey. In Figure A.1 we show the completeness, i.e., the probability that an object is detected as a function of its “reference magnitude”, as defined in the main body of the text and below, and the atmospheric absorption (mostly due to clouds) of the observation. For simplicity, only sources in chip 0 are shown - all of the other chips display similar behaviour. As described in Section 5.2, we assign to each object its reference magnitude as a mean value of the measurements from the 5 brightest observations, while the dimming of the observation is deduced as the median difference of the observed brightness of the reference objects to their reference values in that particular observation. As expected, the completeness stays roughly constant along the lines of constant observed brightness, i.e., along the line defined by subtracting the dimming of the observation from the reference magnitude. The dashed line delineates the region from which we select our AGN sample. We select only objects which are brighter than $r = 19.1$ magnitude and we only take into account observations taken in the clear conditions, i.e., with atmospheric dimming below 0.2 magnitude. This conservative cut is applied in order to make sure that we are only minimally biased in our estimate of variability; if we included fainter objects in our selection we would not be able to observe them during their fainter phases, biasing the results. We also see evidence that, when there is significant cloud absorption, the absorption varies significantly over the large field of view of the camera, as might be expected given the short exposure times.

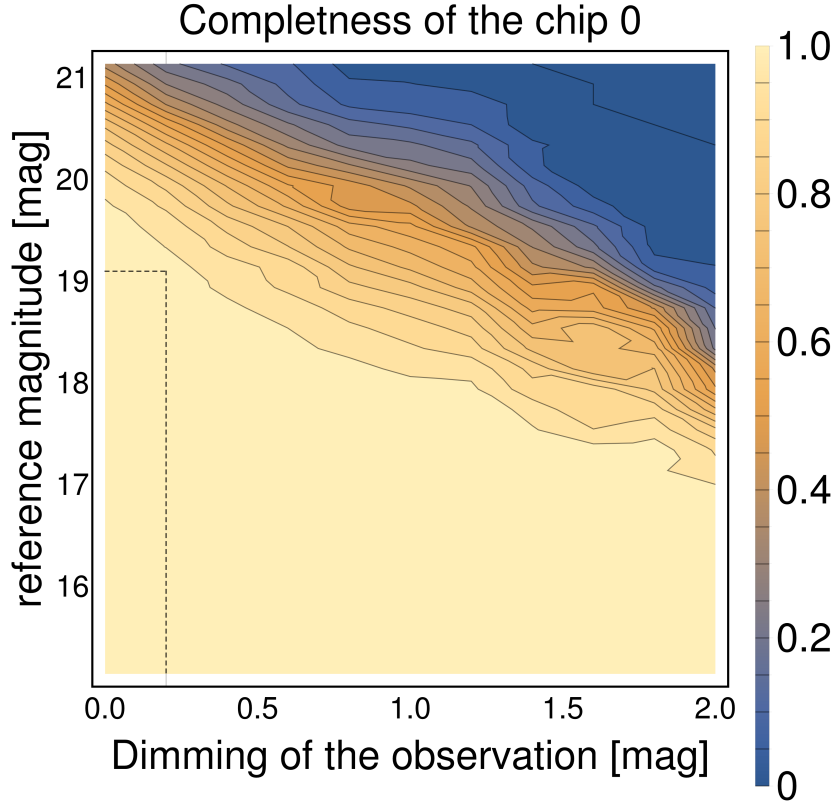


Figure A.1: The completeness of the survey, as in the single representative Chip 0, as a function of the observed magnitude of the source and the dimming of the observation (see text for details). Each contour denotes 5% change in the probability that a given object is included in the SExtractor sample. The dashed lines show the region from which we select the observations to be used in this work.

A.2 Comparison of calibration with Ofek et al. (2012)

In this part of the Appendix we will briefly compare the calibration used in this work and the original calibration of the (i)PTF survey presented in Ofek et al. (2012). As an example, in Figure A.2 we show the initial AGN SF² for the sample constructed at redshift $\langle z \rangle = 1.05$, luminosity of $\langle \log(L/\text{erg s}^{-1}) \rangle = 46.04$ and mass $\langle \log m_{bh}/M_{\odot} \rangle = 8.72$. Note that, for ease of comparison, this is the same sample as considered in Appendix A.3. The residuals are large when using original calibration, while when using our improved methods we see significant reduction. The small excess at short times that can be seen also when using our calibration can be accounted for in statistical sense by correcting with stellar sample, as described in Appendix A.3.

This difference can be attributed to two factors. Firstly, we find that our error estimates, which are taken from the spread of the calibrator objects around their means, are

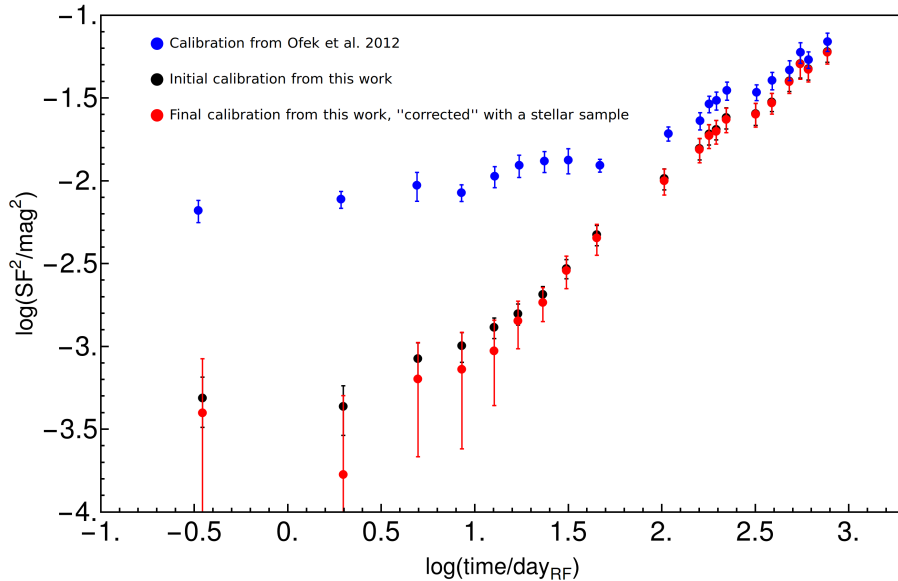


Figure A.2: Comparison of the results for the quasar SF^2 constructed using the standard (i)PTF calibration described in Ofek et al. (2012), the re-calibration described in this work and the final correction using the stellar SF^2 . The re-calibration is successful in significantly reducing the systematics which can dominate the variability at short time scales. After correction by the stellar SF^2 , the final quasar SF^2 is generally consistent with zero as Δt approaches zero, as required.

consistently around 30 % larger than pure SExtractor error estimates used in Ofek et al. (2012), indicating that the SExtractor does not capture fully the measurements uncertainties in the survey. Additionally, we have significantly improved the stability of the survey; data points taken with small time separation are highly consistent with each other, which is often not the case when using the original calibration. Example of this is shown in Figure A.3.

A.3 Colour dependence of the calibration

Given that there were no explicit color terms in the calibration (see Section 5.2) we investigate if there are significant color-dependant trends in the final calibration product used. In order to do this we construct the SF^2 for the sample of stars for which the color is known from the SDSS. We select 28667 available reference objects (stars) from 100 randomly selected fields (for conditions to be selected see Section 5.2). We calibrated these objects with the same procedure with which we calibrated AGN. We then split our sample into 20 bins given their u-g color and created ensemble SF^2 functions for each sub-sample, using the method described in Section 5.4. Finally we calculate the “Mean SF^2 ” as:

$$\langle SF^2 \rangle = \frac{1}{N} \sum_i^N SF^2(t_i) \quad (\text{A-1})$$

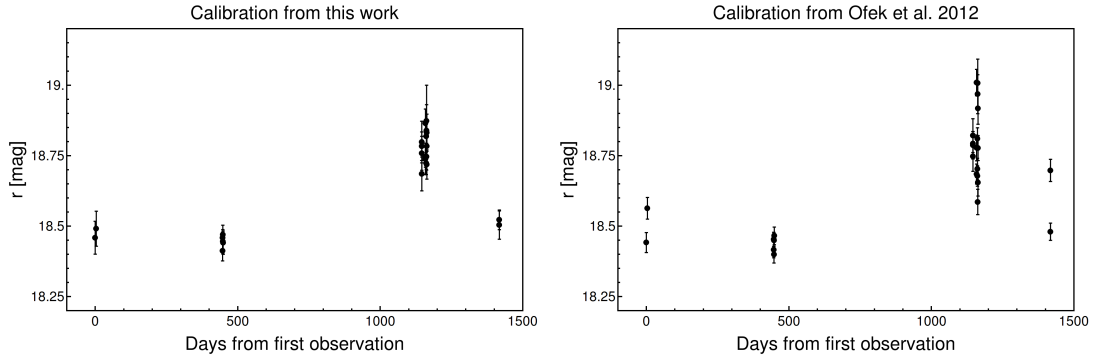


Figure A.3: Light curve for the representative (randomly chosen) quasar SDSS J102255.21+172155.7. On the left hand side we show the light-curve using the recalibration from this work and on the right hand side we show the light-curve with the original calibration from Ofek et al. (2012). The increased consistency of same-night observations is apparent. Notice also the smaller scatter of the group of the points at ~ 1150 days. The calibration improvements have been critical in enabling us to measure the variability at short (~ 10 days) time scales.

where we averaged over all $N = 20$ time bins in which we estimated SF^2 . Errors are indicating the spread of the $SF^2(t_i)$ measurements. In an ideal case, and if there was no underlying stellar variability, all of the points would be at exactly zero, indicating that we have perfectly captured and subtracted errors in the sample. We see that the values of $\langle SF^2 \rangle$ are slightly positive indicating that there are some residuals in our SF^2 estimation, but these do not depend on colour, suggesting that stellar variability effects are small. In general our estimated errors account for around 90% observed variance. Our procedure for dealing with this problem when constructing AGN SF^2 is further elaborated in Appendix A.4.

A.4 Reduction of SF^2 residuals using the stellar sample

As explained in Section A.3, our estimated errors on the measurements during (re-)calibration account for around $\sim 90\%$ of the observed variance, causing our estimated SF^2 to be slightly above zero. In order to account for this when analysing the AGN SF^2 we construct an equivalent sample of stars which are matched to the AGN in terms of their brightness. We construct the SF^2 for these stars using the same procedure as for the AGN. To take into account that some stars are also variable we do the analysis for the full sample of stars and also for the sample of stars for which we are sure that are non-variable, i.e., that have Stetson J index smaller than 4. The Stetson J -index is defined as (Stetson,

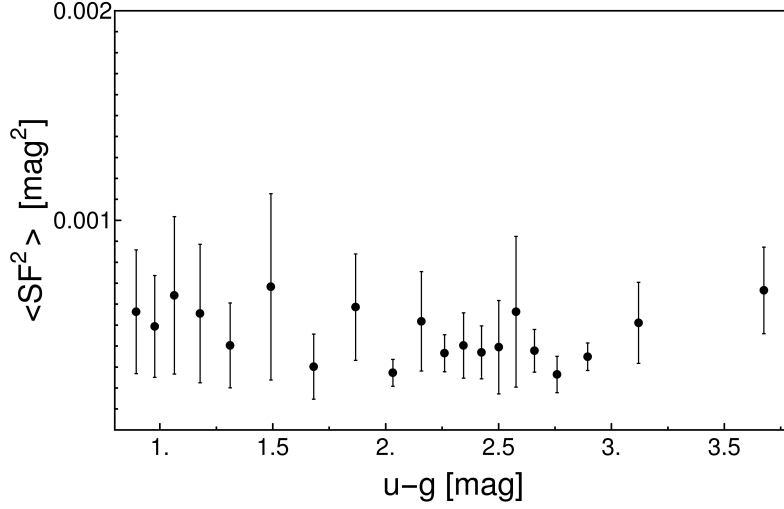


Figure A.4: The SF^2 for stars (averaged over all Δt) as a function of their colour, as constructed using the procedure described in the text. There is no significant color-dependence, suggesting (a) that instrumental effects are likely not colour-dependent and (b) that the stellar SF^2 is probably not dominated by intrinsic stellar variability but rather by uncontrolled systematic uncertainties in the photometry that presumably would also be present in the quasar data. It should be noted that strongly varying sources, with Stetson variability parameter $J > 4$ were removed from the staple sample - see text for details.

1996, Price-Whelan et al., 2014)

$$J = \sum_i^{N-1} \text{sign}(\delta_i \delta_{i+1}) \sqrt{|\delta_i \delta_{i+1}|} \quad \text{where} \quad \delta_i = \sqrt{\frac{N}{N-1}} \frac{x_i - \mu}{\sigma_i} \quad (\text{A-2})$$

where x_i are measurements values, μ mean value and σ_i are measurements errors. Stetson J tends to 0 for non-variable stars and is large when there are adjacent measurements are discrepant. We then construct the final SF^2 as the mean of these two samples in each time bin and conservatively assume largest possible errors from these two samples.

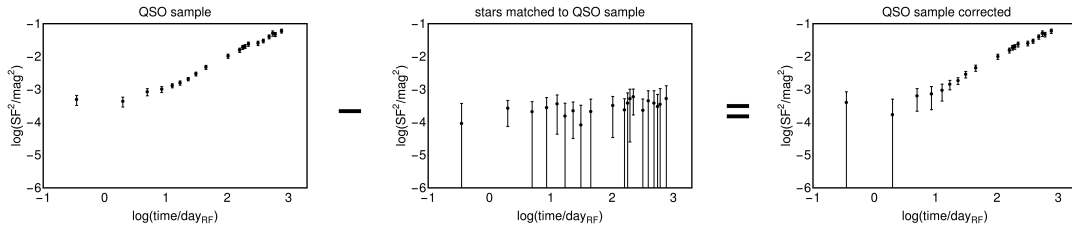


Figure A.5: Schematic representation of our procedure to create the final SF^2 estimate for a quasar sample. Starting from the initial SF^2 (shown on the left) we subtract the stellar SF^2 constructed from stars of similar magnitude, to reach the final, corrected quasar SF^2 shown on the right. It should be noted that strongly varying sources, with Stetson variability parameter $J > 4$, are treated as described in the text.

When constructing the final AGN SF^2 for the quasars we subtract the SF^2 observed

for the stars to get a final estimate of the AGN SF², which we then use in the analysis described in the main body of the manuscript. The errors in the final AGN SF² are derived by adding in quadrature the errors from the initial AGN SF² and from the stellar sample SF². The procedure is sketched in Figure A.5 for the sample constructed at redshift $\langle z \rangle = 1.05$, luminosity of $\langle \log(L/\text{erg s}^{-1}) \rangle = 46.04$ and mass $\langle \log m_{bh}/M_{\odot} \rangle = 8.72$. Using this procedure we are able to fully capture the uncertainty in our estimates of SF² for a large number of AGN SF² in a sense that our final estimates are consistent with zero on the shortest time scales probed.

Bibliography

- Aird, J., Coil, A. L., & Georgakakis, A. 2017a, MNRAS, 465, 3390 [4.1](#)
- . 2017b, ArXiv e-prints, arXiv:1705.01132 [2.1](#)
- Aird, J., Coil, A. L., Georgakakis, A., et al. 2015, MNRAS, 451, 1892 [1.4](#), [2.4.1](#), [3.3](#), [3.4](#), [3.3](#), [3.5](#), [6.1](#)
- Aird, J., Nandra, K., Laird, E. S., et al. 2010, MNRAS, 401, 2531 [1.1.2](#), [2.2.1](#), [2.3.2](#), [2.4.1](#)
- Aird, J., Coil, A. L., Moustakas, J., et al. 2012, ApJ, 746, 90 [2.2.1](#)
- . 2013, ApJ, 775, 41 [2.1](#)
- Alexander, D. M., Bauer, F. E., Brandt, W. N., et al. 2003, AJ, 126, 539 [4.1](#)
- Andrae, R., Kim, D.-W., & Bailer-Jones, C. A. L. 2013, A&A, 554, A137 [1.4](#)
- Antonucci, R. 1993, ARA&A, 31, 473 [1.1.1](#)
- Antonucci, R. R. J., & Miller, J. S. 1985, ApJ, 297, 621 [1.1.1](#)
- Aretxaga, I., Cid Fernandes, R., & Terlevich, R. J. 1997, MNRAS, 286, 271 [1.4](#)
- Assef, R. J., Kochanek, C. S., Ashby, M. L. N., et al. 2011, ApJ, 728, 56 [1.1.3](#)
- Baldry, I. K., Glazebrook, K., Brinkmann, J., et al. 2004, ApJ, 600, 681 [1.2.1](#)
- Baldry, I. K., Glazebrook, K., & Driver, S. P. 2008, MNRAS, 388, 945 [2.2.1](#)
- Baldry, I. K., Driver, S. P., Loveday, J., et al. 2012, MNRAS, 421, 621 [2.2.1](#), [2.2.5](#)
- Barber, C., Schaye, J., Bower, R. G., et al. 2016, MNRAS, 460, 1147 [1.3.3](#)
- Barger, A. J., Cowie, L. L., Mushotzky, R. F., et al. 2005, AJ, 129, 578 [2.6.2](#)

BIBLIOGRAPHY

- Barth, A. J., Pancoast, A., Thorman, S. J., et al. 2011, *ApJL*, 743, L4 [1.1.3](#)
- Bauer, A., Baltay, C., Coppi, P., et al. 2009, *ApJ*, 696, 1241 [1.4](#), [5.4.1](#)
- Behroozi, P. S., Wechsler, R. H., & Conroy, C. 2013, *ApJ*, 770, 57 [1.2.2](#), [1.2.2](#), [2.3.1](#)
- Bell, E. F., McIntosh, D. H., Katz, N., & Weinberg, M. D. 2003, *ApJS*, 149, 289 [1.2.2](#)
- Bell, E. F., Zheng, X. Z., Papovich, C., et al. 2007, *ApJ*, 663, 834 [1.2.2](#)
- Bellm, E. 2014, in *The Third Hot-wiring the Transient Universe Workshop*, ed. P. R. Wozniak, M. J. Graham, A. A. Mahabal, & R. Seaman, 27–33 [6.2](#)
- Bennert, V. N., Auger, M. W., Treu, T., Woo, J.-H., & Malkan, M. A. 2011, *ApJ*, 742, 107 [1.3.3](#), [2.6.1](#)
- Bentz, M. C., Peterson, B. M., Netzer, H., Pogge, R. W., & Vestergaard, M. 2009a, *ApJ*, 697, 160 [1.1.3](#)
- Bentz, M. C., Peterson, B. M., Pogge, R. W., Vestergaard, M., & Onken, C. A. 2006, *APJ*, 644, 133 [1.1.3](#)
- Bentz, M. C., Walsh, J. L., Barth, A. J., et al. 2009b, *ApJ*, 705, 199 [1.1.3](#)
- Bertemes, C., Trakhtenbrot, B., Schawinski, K., Done, C., & Elvis, M. 2016, *MNRAS*, 463, 4041 [6.2.3](#)
- Bertin, E., & Arnouts, S. 1996, *A&AS*, 117, 393 [5.2](#)
- Birrer, S., Lilly, S., Amara, A., Paranjape, A., & Refregier, A. 2014, *ApJ*, 793, 12 [2.5.2](#), [3.4.2](#)
- Blanton, M. R., Hogg, D. W., Bahcall, N. A., et al. 2003, *ApJ*, 594, 186 [1.2.1](#)
- Bluck, A. F. L., Mendel, J. T., Ellison, S. L., et al. 2014, *MNRAS*, 441, 599 [2.5.4](#)
- Boyle, B. J., Shanks, T., Croom, S. M., et al. 2000, *MNRAS*, 317, 1014 [1.1.2](#)
- Brinchmann, J., Charlot, S., White, S. D. M., et al. 2004, *MNRAS*, 351, 1151 [1.2.1](#)
- Cai, Z.-Y., Wang, J.-X., Gu, W.-M., et al. 2016, *ApJ*, 826, 7 [1.4](#), [6.2.2](#)
- Caplar, N., Lilly, S. J., & Trakhtenbrot, B. 2015, *ApJ*, 811, 148 [1.5](#), [2](#), [3.1.1](#), [4.2](#)
- . 2017, *ApJ*, 834, 111 [1.5](#), [5](#)
- Cappelluti, N., Brusa, M., Hasinger, G., et al. 2009, *A&A*, 497, 635 [4.1](#)
- Carollo, C. M., Bschorr, T. J., Renzini, A., et al. 2013, *ApJ*, 773, 112 [2.5.2](#)
- Cartier, R., Lira, P., Coppi, P., et al. 2015, *ApJ*, 810, 164 [1.4](#)
- Charisi, M., Bartos, I., Haiman, Z., et al. 2016, *MNRAS*, 463, 2145 [1.4](#)

- Ciesla, L., Charmandaris, V., Georgakakis, A., et al. 2015, *A&A*, 576, A10 [4.3](#)
- Cimatti, A., Brusa, M., Talia, M., et al. 2013, *ApJL*, 779, L13 [2.1](#)
- Cisternas, M., Jahnke, K., Bongiorno, A., et al. 2011, *ApJL*, 741, L11 [1.3.3](#)
- Civano, F., Elvis, M., Brusa, M., et al. 2012, *ApJS*, 201, 30 [4.3](#)
- Coatman, L., Hewett, P. C., Banerji, M., et al. 2017, *MNRAS*, 465, 2120 [1.1.3](#)
- Collier, S., Crenshaw, D. M., Peterson, B. M., et al. 2001, *ApJ*, 561, 146 [1.4](#)
- Conroy, C., & White, M. 2013, *ApJ*, 762, 70 [2.4.1](#)
- Crain, R. A., Schaye, J., Bower, R. G., et al. 2015, *MNRAS*, 450, 1937 [1.3.3](#)
- Croom, S. M., Richards, G. T., Shanks, T., et al. 2009, *MNRAS*, 399, 1755 [2.4.1](#)
- Croton, D. J. 2006, *MNRAS*, 369, 1808 [2.5.2](#)
- Daddi, E., Renzini, A., Pirzkal, N., et al. 2005, *ApJ*, 626, 680 [2.5.2](#)
- Daddi, E., Dickinson, M., Morrison, G., et al. 2007, *ApJ*, 670, 156 [1.2.1](#)
- Davis, M., Efstathiou, G., Frenk, C. S., & White, S. D. M. 1985, *ApJ*, 292, 371 [1.2](#)
- de Vries, W. H., Becker, R. H., & White, R. L. 2003, *AJ*, 126, 1217 [1.4](#)
- Decarli, R., Falomo, R., Treves, A., et al. 2010, *MNRAS*, 402, 2453 [1.3.3](#), [2.6.1](#)
- Dekel, A., Sari, R., & Ceverino, D. 2009, *ApJ*, 703, 785 [2.5.3](#)
- Denney, K. D., Peterson, B. M., Pogge, R. W., et al. 2009, *ApJL*, 704, L80 [1.1.3](#)
- . 2010, *ApJ*, 721, 715 [1.1.3](#)
- Dexter, J., & Agol, E. 2011, *ApJL*, 727, L24 [1.4](#), [6.2.2](#)
- Diemand, J., Kuhlen, M., Madau, P., et al. 2008, *Nature*, 454, 735 [1.2](#)
- Driver, S. P., Allen, P. D., Graham, A. W., et al. 2006, *MNRAS*, 368, 414 [1.2.1](#)
- Dubinski, J., & Carlberg, R. G. 1991, *ApJ*, 378, 496 [1.2](#)
- Edelson, R., Vaughan, S., Malkan, M., et al. 2014, *ApJ*, 795, 2 [1.4](#), [5.3.4](#), [5.6](#)
- Elbaz, D., Daddi, E., Le Borgne, D., et al. 2007, *A&A*, 468, 33 [1.2.1](#)
- Elbaz, D., Dickinson, M., Hwang, H. S., et al. 2011, *A&A*, 533, A119 [4.1](#)
- Elvis, M., Civano, F., Vignali, C., et al. 2009, *ApJS*, 184, 158 [4.1](#)
- Emmanoulopoulos, D., McHardy, I. M., & Uttley, P. 2010, *MNRAS*, 404, 931 [5.3.3](#), [5.3.4](#), [5.5](#)

BIBLIOGRAPHY

- Emmanoulopoulos, D., McHardy, I. M., Vaughan, S., & Papadakis, I. E. 2016, *MNRAS*, 460, 2413 [1.4](#)
- Eyer, L., Suveges, M., Dubath, P., et al. 2011, in *EAS Publications Series*, Vol. 45, *EAS Publications Series*, ed. C. Turon, F. Meynadier, & F. Arenou, 161–166 [6.2](#)
- Falocco, S., Paolillo, M., Covone, G., et al. 2015, *A&A*, 579, A115 [1.4](#)
- Ferrarese, L., & Merritt, D. 2000, *ApJL*, 539, L9 [1.3.2](#)
- Ferré-Mateu, A., Mezcua, M., Trujillo, I., Balcells, M., & van den Bosch, R. C. E. 2015, *ApJ*, 808, 79 [1.3.3](#)
- Ferré-Mateu, A., Trujillo, I., Martín-Navarro, I., et al. 2017, *MNRAS*, 467, 1929 [1.3.3](#)
- Fine, S., Croom, S. M., Hopkins, P. F., et al. 2008, *MNRAS*, 390, 1413 [1.1.3](#)
- Gebhardt, K., Bender, R., Bower, G., et al. 2000, *ApJL*, 539, L13 [1.3.2](#)
- Genzel, R., Eisenhauer, F., & Gillessen, S. 2010, *Reviews of Modern Physics*, 82, 3121 [1.1.3](#)
- González, V., Labbé, I., Bouwens, R. J., et al. 2011, *ApJL*, 735, L34 [2.2.1](#)
- González-Martín, O., & Vaughan, S. 2012, *A&A*, 544, A80 [1.4](#)
- Graham, M. J., Djorgovski, S. G., Stern, D., et al. 2015a, *Nature*, 518, 74 [1.4](#)
- . 2015b, *MNRAS*, 453, 1562 [1.4](#)
- Granato, G. L., De Zotti, G., Silva, L., Bressan, A., & Danese, L. 2004, *ApJ*, 600, 580 [2.7.1](#)
- Green, A. R., McHardy, I. M., & Lehto, H. J. 1993, *MNRAS*, 265, 664 [1.4](#)
- Grier, C. J., Peterson, B. M., Pogge, R. W., et al. 2012, *ApJ*, 755, 60 [1.1.3](#)
- Grier, C. J., Peterson, B. M., Horne, K., et al. 2013, *ApJ*, 764, 47 [1.1.3](#)
- Haardt, F., & Maraschi, L. 1991, *ApJL*, 380, L51 [1.1.1](#)
- Haardt, F., Maraschi, L., & Ghisellini, G. 1994, *ApJL*, 432, L95 [1.1.1](#)
- Häring, N., & Rix, H.-W. 2004, *ApJL*, 604, L89 [2.12](#), [2.16](#)
- Hasinger, G., Miyaji, T., & Schmidt, M. 2005, *A&A*, 441, 417 [2.2.1](#), [2.4.1](#), [2.6.2](#), [2.8](#)
- Hawkins, M. R. S. 1993, *Nature*, 366, 242 [1.4](#)
- . 2007, *A&A*, 462, 581 [1.4](#)
- Henriques, B. M. B., White, S. D. M., Thomas, P. A., et al. 2017, *MNRAS*, 469, 2626 [2.7.1](#)

- Hirschmann, M., Khochfar, S., Burkert, A., et al. 2010, MNRAS, 407, 1016 [2.5.2](#)
- Hopkins, P. F., Cox, T. J., Kereš, D., & Hernquist, L. 2008, ApJS, 175, 390 [2.7.1](#)
- Hopkins, P. F., Hernquist, L., Cox, T. J., et al. 2005, ApJ, 630, 716 [2.2.3](#)
- . 2006a, ApJS, 163, 1 [2.5.2](#)
- Hopkins, P. F., Richards, G. T., & Hernquist, L. 2007, ApJ, 654, 731 ([document](#)), [2.2.1](#), [2.2.1](#), [2.3.1](#), [2.3.2](#), [2.3.2](#), [2.6](#), [2.2](#), [2.4.1](#), [2.5.1](#), [3.3](#), [3.4](#), [3.3](#), [3.5](#), [3.4.1](#), [3.4.1](#), [5.4.1](#), [6.1](#)
- Hopkins, P. F., Robertson, B., Krause, E., Hernquist, L., & Cox, T. J. 2006b, ApJ, 652, 107 [3.1.1](#)
- Hoyle, F., & Fowler, W. A. 1963, MNRAS, 125, 169 [1](#)
- Ilbert, O., Salvato, M., Le Floch, E., et al. 2010, ApJ, 709, 644 [1.2.2](#)
- Ilbert, O., McCracken, H. J., Le Fèvre, O., et al. 2013, A&A, 556, A55 ([document](#)), [1.2.2](#), [2.3.1](#), [2.1](#), [2.9](#), [3.3](#), [3.4](#), [3.5](#), [6.1](#)
- Ivezic, Z., Axelrod, T., Brandt, W. N., et al. 2008, Serbian Astronomical Journal, 176, 1 [6.2](#)
- Jahnke, K., & Macciò, A. V. 2011, APJ, 734, 92 [1.3.2](#), [2.5.2](#)
- Jahnke, K., Bongiorno, A., Brusa, M., et al. 2009, ApJL, 706, L215 [1.3.3](#), [2.6.1](#)
- Kajisawa, M., Ichikawa, T., Yoshikawa, T., et al. 2011, PASJ, 63, 403 [2.2.1](#)
- Kasliwal, V. P., Vogeley, M. S., & Richards, G. T. 2015, MNRAS, 451, 4328 [1.4](#)
- Kaspi, S., Maoz, D., Netzer, H., et al. 2005, APJ, 629, 61 [1.1.3](#)
- Kaspi, S., Smith, P. S., Netzer, H., et al. 2000, APJ, 533, 631 [1.1.3](#)
- Kawaguchi, T., Mineshige, S., Umemura, M., & Turner, E. L. 1998, ApJ, 504, 671 [1.4](#)
- Kelly, B. C., Bechtold, J., & Siemiginowska, A. 2009, ApJ, 698, 895 [1.4](#), [1.4](#)
- Kelly, B. C., Becker, A. C., Sobolewska, M., Siemiginowska, A., & Uttley, P. 2014, ApJ, 788, 33 [1.4](#), [5.3.4](#), [5.6](#), [5.3.4](#), [5.3.4](#)
- King, A. 2003, ApJL, 596, L27 [6.2](#)
- King, A. R. 2010, MNRAS, 402, 1516 [2.7.1](#)
- Klypin, A. A., Trujillo-Gomez, S., & Primack, J. 2011, ApJ, 740, 102 [1.2](#)
- Kormendy, J., & Ho, L. C. 2013, ARA&A, 51, 511 [1.3.2](#), [1.3.2](#), [2.12](#), [2.5.2](#), [3.3](#), [3.4.2](#), [3.8](#), [6.1](#)
- Kormendy, J., & Kennicutt, Jr., R. C. 2004, ARA&A, 42, 603 [2.5.3](#)

BIBLIOGRAPHY

- Koss, M., Mushotzky, R., Veilleux, S., et al. 2011, *ApJ*, 739, 57 [2.1](#)
- Kozłowski, S. 2016, *ApJ*, 826, 118 [1.4](#), [5.5.1](#), [5.6](#)
- Kozłowski, S., Kochanek, C. S., Udalski, A., et al. 2010, *ApJ*, 708, 927 [1.4](#)
- Labita, M., Decarli, R., Treves, A., & Falomo, R. 2009, *MNRAS*, 396, 1537 [2.6.2](#)
- Laher, R. R., Surace, J., Grillmair, C. J., et al. 2014, *PASP*, 126, 674 [5.1](#), [1](#)
- Lauer, T. R., Tremaine, S., Richstone, D., & Faber, S. M. 2007, *ApJ*, 670, 249 [2.2.5](#)
- Law, N. M., Kulkarni, S. R., Dekany, R. G., et al. 2009, *PASP*, 121, 1395 [5.1](#)
- Lawrence, A., & Papadakis, I. 1993, *ApJL*, 414, L85 [1.4](#)
- Lee, K.-S., Ferguson, H. C., Wiklind, T., et al. 2012, *ApJ*, 752, 66 [2.2.1](#)
- Levitan, D., Fulton, B. J., Groot, P. J., et al. 2011, *ApJ*, 739, 68 [5.2](#)
- Li, Y.-R., Ho, L. C., & Wang, J.-M. 2011, *ApJ*, 742, 33 [2.6.2](#)
- Lilly, S. J., & Carollo, C. M. 2016, *ApJ*, 833, 1 [2.5.2](#), [2.5.3](#), [2.5.4](#), [6.1](#)
- Lilly, S. J., Carollo, C. M., Pipino, A., Renzini, A., & Peng, Y. 2013, *ApJ*, 772, 119 [2.7.1](#), [3.1.1](#), [3.2.3](#)
- Lomb, N. R. 1978, *MNRAS*, 185, 325 [6.1](#)
- Lutz, D., Poglitsch, A., Altieri, B., et al. 2011, *A&A*, 532, A90 [4.1](#)
- Lynden-Bell, D. 1969, *Nature*, 223, 690 [1](#)
- MacLeod, C. L., Ivezić, Ž., Kochanek, C. S., et al. 2010, *ApJ*, 721, 1014 [1.4](#), [1.4](#), [5.3.2](#), [5.3.2](#), [5.4.1](#), [5.4.1](#), [5.4.1](#)
- MacLeod, C. L., Ivezić, Ž., Sesar, B., et al. 2012, *ApJ*, 753, 106 [1.4](#), [5.1](#), [5.3.2](#)
- Madau, P., & Dickinson, M. 2014, *ARA&A*, 52, 415 [1.4](#), [3.3](#), [3.4](#), [3.5](#), [6.1](#)
- Magorrian, J., Tremaine, S., Richstone, D., et al. 1998, *AJ*, 115, 2285 [1.3.2](#)
- Marconi, A., Risaliti, G., Gilli, R., et al. 2004, *MNRAS*, 351, 169 [1.1.2](#)
- Marleau, F. R., Clancy, D., & Bianconi, M. 2013, *MNRAS*, 435, 3085 [1.3.2](#)
- Masters, D., Capak, P., Salvato, M., et al. 2012, *ApJ*, 755, 169 [1.1.2](#), [2.2.1](#)
- Matsuoka, Y., Strauss, M. A., Price, III, T. N., & DiDonato, M. S. 2014, *ApJ*, 780, 162 [2.1](#), [2.5.5](#), [2.5.5](#), [2.16](#), [6.1](#)
- Matthews, T. A., & Sandage, A. R. 1963, *ApJ*, 138, 30 [1.4](#)
- McHardy, I. M., Koerding, E., Knigge, C., Uttley, P., & Fender, R. P. 2006, *Nature*, 444, 730 [1.4](#)

- McHardy, I. M., Connolly, S. D., Peterson, B. M., et al. 2016, *Astronomische Nachrichten*, 337, 500 [1.4](#)
- Merloni, A. 2004, *MNRAS*, 353, 1035 [3.3](#)
- Merloni, A., Bongiorno, A., Bolzonella, M., et al. 2010, *ApJ*, 708, 137 [1.3.3](#), [2.6.1](#)
- Meusinger, H., Hinze, A., & de Hoon, A. 2011, *A&A*, 525, A37 [5.3.2](#)
- Moore, B., Ghigna, S., Governato, F., et al. 1999, *ApJL*, 524, L19 [1.2](#)
- Morganson, E., Burgett, W. S., Chambers, K. C., et al. 2014, *ApJ*, 784, 92 [1.4](#)
- Mortlock, A., Conselice, C. J., Hartley, W. G., et al. 2015, *MNRAS*, 447, 2 [3.2.3](#)
- Mullaney, J. R., Pannella, M., Daddi, E., et al. 2012a, *MNRAS*, 419, 95 [4.2](#), [1](#), [6.1](#)
- Mullaney, J. R., Daddi, E., Béthermin, M., et al. 2012b, *ApJL*, 753, L30 [1.3.3](#), [4.2](#), [4.3](#), [4.3](#), [3](#), [6.1](#)
- Mushotzky, R. F., Edelson, R., Baumgartner, W., & Gandhi, P. 2011, *ApJL*, 743, L12 [1.4](#), [5.6](#)
- Muzzin, A., Marchesini, D., Stefanon, M., et al. 2013, *ApJ*, 777, 18 [2.3.1](#)
- Netzer, H. 2009, *MNRAS*, 399, 1907 [2.1](#)
- . 2013, *The Physics and Evolution of Active Galactic Nuclei* [1.1.1](#), [1.4](#), [5.4.1](#), [5.4.1](#)
- Netzer, H., Maoz, D., Laor, A., et al. 1990, *ApJ*, 353, 108 [1.1.3](#)
- Newman, A. B., Ellis, R. S., Bundy, K., & Treu, T. 2012, *ApJ*, 746, 162 [2.5.2](#)
- Noeske, K. G., Weiner, B. J., Faber, S. M., et al. 2007, *ApJL*, 660, L43 [1.2.1](#), [1.2](#)
- Noguchi, M. 1999, *ApJ*, 514, 77 [2.5.3](#)
- Novak, G. S., Ostriker, J. P., & Ciotti, L. 2011, *ApJ*, 737, 26 [1.4](#)
- Ofek, E. O., Frail, D. A., Breslauer, B., et al. 2011, *ApJ*, 740, 65 [5.2](#)
- Ofek, E. O., Laher, R., Law, N., et al. 2012, *PASP*, 124, 62 [5.1](#), [5.2](#), [5.2](#), [A.2](#), [A.2](#), [A.3](#)
- Oh, K., Sarzi, M., Schawinski, K., & Yi, S. K. 2011, *ApJS*, 195, 13 [1.1.3](#)
- Oliver, S. J., Bock, J., Altieri, B., et al. 2012, *MNRAS*, 424, 1614 [4.1](#)
- Onken, C. A., Ferrarese, L., Merritt, D., et al. 2004, *ApJ*, 615, 645 [1.1.3](#)
- Pannella, M., Carilli, C. L., Daddi, E., et al. 2009, *ApJL*, 698, L116 [1.2.1](#)
- Peng, C. Y. 2007, *APJ*, 671, 1098 [1.3.2](#)
- Peng, C. Y., Impey, C. D., Rix, H.-W., et al. 2006, *ApJ*, 649, 616 [1.3.3](#)

BIBLIOGRAPHY

- Peng, Y., Lilly, S. J., Renzini, A., & Carollo, C. M. 2014, ArXiv e-prints, arXiv:1406.7291 [2.3.1](#), [2.3.2](#), [3.2.3](#)
- Peng, Y.-j., Lilly, S. J., Renzini, A., & Carollo, M. 2012, ApJ, 757, 4 [2.3.1](#), [3.4.1](#)
- Peng, Y.-j., Lilly, S. J., Kovač, K., et al. 2010, ApJ, 721, 193 [1.2.2](#), [1.2.2](#), [1.2.2](#), [1.3](#), [2.2.1](#), [2.2.5](#), [2.2.5](#), [2.3.1](#), [2.3.1](#), [2.5.2](#), [2.5.3](#), [2.7.1](#), [2.7.1](#), [3.2.1](#), [3.2](#), [3.3](#), [3.4](#), [3.5](#), [3.4.1](#), [6.1](#)
- Pérez-González, P. G., Rieke, G. H., Villar, V., et al. 2008, ApJ, 675, 234 [2.2.1](#)
- Peterson, B. M. 2014, Space Sci. Rev., 183, 253 [1.1.3](#)
- Peterson, B. M., Ferrarese, L., Gilbert, K. M., et al. 2004, ApJ, 613, 682 [1.1.3](#)
- Pozzetti, L., Bolzonella, M., Zucca, E., et al. 2010, A&A, 523, A13 [1.2.2](#)
- Press, W. H., & Schechter, P. 1974, ApJ, 187, 425 [1.2](#), [1.2.2](#)
- Price-Whelan, A. M., Agüeros, M. A., Fournier, A. P., et al. 2014, ApJ, 781, 35 [A.4](#)
- Rafiee, A., & Hall, P. B. 2011a, MNRAS, 415, 2932 [2.5.1](#)
- . 2011b, ApJS, 194, 42 [2.5.1](#)
- Rahmer, G., Smith, R., Velur, V., et al. 2008, in Proc. SPIE, Vol. 7014, Ground-based and Airborne Instrumentation for Astronomy II, 70144Y [5.1](#)
- Rau, A., Kulkarni, S. R., Law, N. M., et al. 2009, PASP, 121, 1334 [5.1](#)
- Reines, A. E., & Volonteri, M. 2015, ApJ, 813, 82 [1.3.2](#), [1.3.3](#)
- Ricci, C. 2011, http://www.isdc.unige.ch/~ricci/Website/Active_Galactic_Nuclei.html, accessed: 2017-28-6 [1.1](#)
- Richards, G. T., Fan, X., Newberg, H. J., et al. 2002, AJ, 123, 2945 [6.2.3](#)
- Richards, G. T., Croom, S. M., Anderson, S. F., et al. 2005, MNRAS, 360, 839 [1.1.2](#)
- Rodighiero, G., Brusa, M., Daddi, E., et al. 2015, ApJL, 800, L10 [4.3](#), [4.3](#), [4.3](#), [1](#), [3](#), [6.1](#)
- Rosario, D. J., Santini, P., Lutz, D., et al. 2012, A&A, 545, A45 [1](#), [6.1](#)
- . 2013, ApJ, 771, 63 [2.1](#)
- Ross, N. P., McGreer, I. D., White, M., et al. 2013, ApJ, 773, 14 [4.2](#)
- Salpeter, E. E. 1964, APJ, 140, 796 [1](#)
- Sani, E., Marconi, A., Hunt, L. K., & Risaliti, G. 2011, MNRAS, 413, 1479 [1.3.2](#)
- Sargent, M. T., Béthermin, M., Daddi, E., & Elbaz, D. 2012, ApJL, 747, L31 [1.2.1](#)
- Scargle, J. D. 1982, ApJ, 263, 835 [6.1](#)
- Schawinski, K., Koss, M., Berney, S., & Sartori, L. F. 2015, MNRAS, 451, 2517 [1.4](#)

- Schawinski, K., Urry, C. M., Virani, S., et al. 2010, *ApJ*, 711, 284 [2.1](#)
- Schaye, J., Crain, R. A., Bower, R. G., et al. 2015, *MNRAS*, 446, 521 [1.3.3](#)
- Schmidt, K. B., Marshall, P. J., Rix, H.-W., et al. 2010, *ApJ*, 714, 1194 [5.2](#)
- Schramm, M., & Silverman, J. D. 2013, *ApJ*, 767, 13 [1.3.3](#), [2.6.1](#)
- Schulze, A., & Wisotzki, L. 2011, *A&A*, 535, A87 [1.3.3](#)
- . 2014, *MNRAS*, 438, 3422 [1.3.3](#)
- Schulze, A., Bongiorno, A., Gavignaud, I., et al. 2015, *MNRAS*, 447, 2085 [2.6.1](#)
- Sesar, B., Svlković, D., Ivezić, Ž., et al. 2006, *AJ*, 131, 2801 [1.4](#)
- Sesar, B., Ivezić, Ž., Lupton, R. H., et al. 2007, *AJ*, 134, 2236 [1.4](#)
- Shankar, F., Salucci, P., Granato, G. L., De Zotti, G., & Danese, L. 2004, *MNRAS*, 354, 1020 [1.1.2](#)
- Shankar, F., Weinberg, D. H., & Miralda-Escudé, J. 2013, *MNRAS*, 428, 421 [2.5.2](#)
- Shen, Y., Greene, J. E., Strauss, M. A., Richards, G. T., & Schneider, D. P. 2008, *ApJ*, 680, 169 [1.1.3](#)
- Shen, Y., & Kelly, B. C. 2012, *ApJ*, 746, 169 [1.1.2](#), [3.1](#)
- Shen, Y., Richards, G. T., Strauss, M. A., et al. 2011, *ApJS*, 194, 45 [2.5.1](#), [2.10](#), [3.7](#), [5.1](#), [6.1](#)
- Shen, Y., Greene, J. E., Ho, L. C., et al. 2015, *ApJ*, 805, 96 [2.5.2](#)
- Sijacki, D., Vogelsberger, M., Genel, S., et al. 2015, *MNRAS*, 452, 575 [1.3.3](#)
- Silverman, J. D., Lamareille, F., Maier, C., et al. 2009, *ApJ*, 696, 396 [2.1](#)
- Simm, T., Salvato, M., Saglia, R., et al. 2016, *A&A*, 585, A129 [1.4](#), [5.3.4](#), [5.3.4](#), [5.5.1](#)
- Simmons, B. D., Lintott, C., Schawinski, K., et al. 2013, *MNRAS*, 429, 2199 [1.3.2](#)
- Soltan, A. 1982, *MNRAS*, 200, 115 [1.1.2](#)
- Speagle, J. S., Steinhardt, C. L., Capak, P. L., & Silverman, J. D. 2014, *ApJS*, 214, 15 [1.2.1](#), [3.2.3](#)
- Springel, V., White, S. D. M., Jenkins, A., et al. 2005, *Nature*, 435, 629 [1.2](#)
- Springel, V., Wang, J., Vogelsberger, M., et al. 2008, *MNRAS*, 391, 1685 [1.2](#)
- Stadel, J., Potter, D., Moore, B., et al. 2009, *MNRAS*, 398, L21 [1.2](#)
- Stanley, F., Harrison, C. M., Alexander, D. M., et al. 2015, *MNRAS*, 453, 591 [4.2](#), [6.1](#)
- Steinhardt, C. L., & Elvis, M. 2010, *MNRAS*, 402, 2637 [2.5.1](#), [2.8](#)

BIBLIOGRAPHY

- Steinmetz, M., & Navarro, J. F. 2002, *New A*, 7, 155 [2.5.3](#)
- Stetson, P. B. 1996, *PASP*, 108, 851 [A.4](#)
- Sunyaev, R. A., & Titarchuk, L. G. 1980, *A&A*, 86, 121 [1.1.1](#)
- Thorne, K. S. 1974, *ApJ*, 191, 507 [3.1.2](#)
- Timmer, J., & Koenig, M. 1995, *A&A*, 300, 707 [5.3.4](#)
- Trakhtenbrot, B., & Netzer, H. 2010, *MNRAS*, 406, L35 [1.3.3](#)
- . 2012, *MNRAS*, 427, 3081 [1.1.3](#), [2.5.1](#), [2.10](#), [3.1](#), [3.7](#), [5.1](#), [6.1](#)
- Trèvese, D., & Vagnetti, F. 2002, *ApJ*, 564, 624 [1.4](#)
- Tully, R. B., Mould, J. R., & Aaronson, M. 1982, *ApJ*, 257, 527 [1.2.1](#)
- Ueda, Y., Akiyama, M., Hasinger, G., Miyaji, T., & Watson, M. G. 2014, *ApJ*, 786, 104 [2.2.1](#), [2.3.1](#), [3.3](#), [3.4](#), [3.5](#), [3.3](#), [5.4.1](#), [6.1](#)
- Urry, C. M., & Padovani, P. 1995, *PASP*, 107, 803 [1.1.1](#)
- Urry, M. 2003, in *Astronomical Society of the Pacific Conference Series*, Vol. 290, *Active Galactic Nuclei: From Central Engine to Host Galaxy*, ed. S. Collin, F. Combes, & I. Shlosman, 3 [1.1.1](#)
- van Dokkum, P. G., Bezanson, R., van der Wel, A., et al. 2014, *ApJ*, 791, 45 [2.5.2](#)
- Vanden Berk, D. E., Wilhite, B. C., Kron, R. G., et al. 2004, *ApJ*, 601, 692 [1.4](#), [5.4.1](#)
- Vasudevan, R. V., & Fabian, A. C. 2007, *MNRAS*, 381, 1235 [4.2](#)
- Vaughan, S., Uttley, P., Markowitz, A. G., et al. 2016, *MNRAS*, 461, 3145 [1.4](#)
- Veale, M., White, M., & Conroy, C. 2014, *MNRAS*, 445, 1144 [2.2.1](#), [2.2.1](#), [2.4.2](#)
- Veledina, A., Vurm, I., & Poutanen, J. 2011, *MNRAS*, 414, 3330 [1.1.1](#)
- Voevodkin, A. 2011, *ArXiv e-prints*, arXiv:1107.4244 [5.5.1](#)
- Volonteri, M., Capelo, P. R., Netzer, H., et al. 2015, *MNRAS*, 452, L6 [4.3](#)
- Weigel, A. K., Schawinski, K., Caplar, N., et al. 2017, *ArXiv e-prints*, arXiv:1707.05323 [2.1](#)
- Wilhite, B. C., Brunner, R. J., Grier, C. J., Schneider, D. P., & vanden Berk, D. E. 2008, *MNRAS*, 383, 1232 [1.4](#)
- Wold, M., Brotherton, M. S., & Shang, Z. 2007, *MNRAS*, 375, 989 [1.4](#)
- Woo, J.-H., Treu, T., Barth, A. J., et al. 2010, *ApJ*, 716, 269 [1.1.3](#)
- Xue, Y. Q., Luo, B., Brandt, W. N., et al. 2011, *ApJS*, 195, 10 [4.1](#)

Yang, G., Chen, C.-T. J., Vito, F., et al. 2017, *ApJ*, 842, 72 [4.3](#), [4.3](#), [3](#), [6.1](#)

Yu, Q., & Tremaine, S. 2002, *MNRAS*, 335, 965 [1.1.2](#)

Zuo, W., Wu, X.-B., Liu, Y.-Q., & Jiao, C.-L. 2012, *ApJ*, 758, 104 [1.4](#), [5.3.2](#)

BIBLIOGRAPHY

Acknowledgements

First of all, I would like to acknowledge my fellow Ph.D. students. I would like to especially thank Ana Weigel and Sandro Tacchella. Ana's arrivals in my office, usually late in the evening, always meant that a productive discussion about mass functions is about to take place. On the other hand, my arrivals in Sandro's office meant that Sandro would have to explain to me, patiently and repeatedly, basics of galaxy observations, spectroscopy or similar.

I would like to thank Christian Knobel. He was the person with whom I had first contact at ETH Zurich and who encouraged me to apply for the Ph.D. program. For this I am immensely grateful.

Benny Trakhtenbrot worked with me closely and I benefited extensively from his knowledge about AGN observations and theory. He is also the person who ignited my interest in AGN spins and accretion disk physics which are the topics that fascinate me and which I hope to be able to study more in the future. I am grateful for his help.

I would also like to express my deepest gratitude to my parents, Vesna and Roman. Without their support during my Ph.D. and especially in the difficult period beforehand, this thesis would surely not exist. I am grateful for the continuous support that I had in my life and for many doors and possibilities that they have provided me with. They have always backed all of my decisions and assisted in any way they could.

ACKNOWLEDGEMENTS

Finally, I would like to thank my Ph.D. advisor, Simon Lilly. I would like to especially thank him for his incredible patience. I cannot count how many times I came into his office claiming that something cannot be done, only to be proven wrong hours later. I cannot count how many times I came to his office with mangled plots, half-baked ideas or silly comments, yet every time I received understanding and learned something. I also wish to acknowledge the freedom I have been given to explore and satisfy my scientific curiosity with various projects. Simon's calmness, level of knowledge and critical spirit is something I will strive to achieve in my future.

Zurich, July 2017

Neven Caplar

Neven Caplar

Swiss Federal Institute of Technology
Department of Physics
8093-Zurich
Wolfgang-Pauli Strasse 27
HIT J-33.3

Phone: +41 44 63 33826
Phone2: +1 609 787 8425
Web: <http://people.phys.ethz.ch/~caplarn>
Email: caplarn@phys.ethz.ch
Email2: ncaplar@princeton.edu

Education

2013 - 2017, Ph.D., ETH Zurich

Advisor: Dr. Simon J. Lilly, ETH Zurich

Thesis: Evolution of the AGN population in the Universe

2005 - 2010, MSc, University of Zagreb

Advisor: Dr. Hrvoje Stefancic, Institut Ruder Boskovic

Thesis: Unification models of dark energy and dark matter

Research

Main topics of my work include black hole-galaxy co-evolution, AGN physics and time domain astronomy.

Peer-Reviewed Journal Articles in Astronomy

- 2017, A. Weigel, K. Schawinski, **N. Caplar**, A. Carpineti, R. Hart, S. Kaviraj, W. Keel, S. Kruk, C. Lintott, R. Nichol, B. Simmons, R. Smethurst
Galaxy Zoo: Major galaxy mergers are not a significant quenching pathway, submitted to ApJ
- 2017, A. Weigel, K. Schawinski, **N. Caplar**, O. I. Wong, T. Ezequiel, B. Trakhtenbrot
Two mass independent Eddington ratio distribution functions regulate black hole growth of blue and red galaxies in the local Universe, accepted to ApJ
- 2017, **N. Caplar**, S. J. Lilly, B. Trakhtenbrot
Optical variability of AGN in the PTF/iPTF survey, ApJ, 2017, 834, 111C
- 2015, **N. Caplar**, S. J. Lilly, B. Trakhtenbrot
AGN evolution from a galaxy evolution viewpoint, ApJ, 2015, 811, 148C
- 2013, **N. Caplar**, H. Stefancic
Generalized models of unification of dark matter and dark energy, Phys. Rev. D, 2013, 87, 023510

Other Publications

These publications are not directly connected to Astronomy. However, they are both “big-data” papers for which I collected and reduced the data.

6. 2016, **N. Caplar**, S. Tacchella, S. Birrer
Quantitative evaluation of gender bias in astronomy, 2017, NatAs, 1E, 182C
7. 2013, **N. Caplar**, M. Suznjevic, M. Matijasevic
Analysis of players’ in-game performance vs rating: Case study of Heroes of Newerth, Foundation of Digital games 2013, pp. 237-244

Telescope Proposals

2013, F. Miniati, S. J. Lilly, **N. Caplar**

The connection between magnetised galactic outflows and high Faraday effect in the circumgalactic environment of intermediate redshift galaxies

Awarded 24 hours with VIMOS instrument on VLT

2013, S. J. Lilly, F. Miniati, **N. Caplar**, B. Gaensler, J. Farnes

Testing the association of magnetized plasma with high redshift galaxies along the line of sight

Awarded 5 nights at NTT telescope

Seminar and Conference Presentations

2017: Weizmann Institute of Science/ University of Geneva/ Unveiling the Physics Behind Extreme AGN Variability, St. Thomas, USA (conference, talk)/ Models of Gravity workshop, Hannover, Germany (workshop, talk)

2016: Caltech/ University of Washington/ Stanford/ University of Maryland/ Shining from the heart of darkness: black hole accretion and jets, Katmandu, Nepal (conference, talk)/ AGN: what’s in a name, Munich, Germany (conference, talk)

2015: Black Hole Accretion and AGN Feedback, Shanghai, PRC (conference, talk)/ Inaugural Zwicky Symposium, Braunwald, Switzerland (conference, talk-organizer)/ Demographics and environment of AGN from multi-wavelength surveys Chania, Greece (conference, talk)/ Unveiling the AGN-Galaxy Evolution, Puerto Varas, Chile (conference, talk)

2014: COSMOS team meeting, Zagreb, Croatia (workshop, talk)/ Multiwavelength-surveys, Dubrovnik, Croatia (conference, poster)/ Powerful AGN, Port Douglas, Australia (conference, talk)/ The Formation and Growth of Galaxies in the Young Universe, Obergurgl, Austria (conference, talk)

2012: Karl-Franzens University/ Jagellonian University/ European Summer Campus, Strasbourg, France (conference-school, poster)

Special skills and computing

Programming Languages: Mathematica, Python, L^AT_EX, CIAO

Experience in working with X-ray, optical and time-domain data

Experience in data reduction, survey calibration, “big data” and machine learning techniques

Since April 2015 I run astrodataiscool.com website, where I publish analysis of the data from astronomical and popular sources. The website gathered ~20000 unique views.